University of Sussex

A high-performance, multi-frequency micro-controlled Electrical Impedance Mammography (EIM) excitation and phantom validation system

Ali Zarafshani

Submitted for the degree of Doctor of Philosophy

Biomedical Engineering, School of Engineering and Informatics

University of Sussex, Brighton, UK

I hereby declare that this dissertation, whether in the same or different form, has not been previously submitted to this or any other university for a degree.

Ali Zarafshani

A high-performance, multi-frequency micro-controlled Electrical Impedance Mammography (EIM) excitation and phantom validation system

Asli Zarafshani

Preface

We all have experienced at least one relative or friend who died of cancer. I have completed this research to improve a biomedical imaging technique for detecting cancerous tissues in its early stages to increase the chances of diagnosis. It is worth noting that the cancer incidence rate has been significantly increased during the last decade. This increased rate requires more precise detection, diagnosis, and treatment procedures.

Cancer is found in so many organs in the body, such that each of them is named after the place that they started in the body; some of them are as follows:

Cervical Cancer	Cervical cancer	Oral cancer	Testicular cancer
Hodgkin lymphoma	Kidney cancer	Ovarian cancer	Uterine cancer
Laryngeal cancer	Leukaemias	Pancreatic cancer	Thyroid cancer
Liver cancer	Lung cancer	Prostate cancer	Vaginal cancer
Mesothelioma	Myeloma	Skin cancer	Vulvar cancer
Non-Hodgkin lymphoma	Oesophageal cancer	Stomach cancer	Breast Cancer

This research aims is to have an impact on improving a detection technique, it may be a very small help but I hope to save some people in the world. Since the treatment success rate is enhanced by detecting the cancer in its earliest stages this has a significant effect in preventing it from being distributed to other organs. Thus, detecting the cancer in its earliest stages, will lead to increased longevity of patients and decreased cancer re-occurrence. In fact, detecting cancer is quite a challenge in every patient's life. One type of prevalent screening of organs (i.e. Breast, prostate) is based on diagnosing cancers that exhibit changed cellular electrical properties, hence mapping the conductivity (or permittivity) of electrical currents in tissue and retained electrical charge permits assessment. In addition, this approach can reveal the difference between abnormal and normal tissue. It can be used to produce Electrical Impedance Tomography (EIT) images based on the impedance distribution and its variation in the human organs, it can be used to detect different types of cancers i.e. breast, brain and prostate. Each type of cancer needs a slightly different device and

instrument that is compatible with the organs shape and soft tissue accessibility to be able to detect cancer. We present here EIT as a medical imaging technique for breast cancer application. Within this research I have tried to illuminate the application of EIT for the clinical and physiological applications.

DEDICATION

This dissertation is dedicated to my parents and my wonderful wife, Hedieh Hashemi for their endless love, support and encouragement

Acknowledgments

The development of this dissertation was not possible without the emotional support of my family along with financial support from the University of Sussex as a teaching assistant in Engineering & Design department. I am also grateful to appreciate Professor Chris Chatwin, Dr. Thomas Bach and Dr. Wei Wang, my dissertation supervisors, for their guidance and support and all the facilities which they provided in their research group for me such as the Instrumentation Lab in the Sensatech Company and the Biomedical Lab at Sussex University.

The list of both direct and indirect contributions to this work is very long and the level of contribution of each one cannot be measured. In order to try to be fair in this very sincere acknowledgment, the names are listed alphabetically and I really apologise if your name is missing. It is quite difficult to remember all that happened in the last years just for a few minutes during my writing the acknowledgments for this thesis.

Ali, Arron, Ben, Borzooyeh, Chris, Carlos, David, Fan, Julian, Nan, Nevis, Nicolas, Mohammad, Philips, Robert, Tabassum, Tai, Tom, Quofeng, Wei, Xiaolin, Weida.

A major benefit that we had here in the biomedical research group at the University of Sussex was our opportunity for technical development along with validation experiments. These special opportunities facilitated EIT system development by working very closely with clinical practices. I had the chance to develop advanced essential performance features of EIT systems for further use in clinical settings for breast cancer detection.

List of Academic Publications:

Ali Zarafshani, Thomas Bach, Wei Wang and Chris Chatwin "Closed Loop conditioning a voltage source for EIT systems to compensate for effects of contact impedance and stray capacitance" preparing for IEEE Transactions on Biomedical Circuits and Systems.

Ali Zarafshani, Thomas Bach, and Chris Chatwin "A 3D Electronic Mesh phantom for planar structure EIT systems", (submitted).

Ali Zarafshani, Thomas Bach, and Chris Chatwin "Conditioning a current source for EIT systems to cancel unwanted capacitive effects using an OCCII-GIC", (submitted).

Ali Zarafshani, Tabassum R Qureshi, Thomas Bach, Chris Chatwin and Manuchehr Soleimani "A 3D Multi-frequency response electrical mesh phantom for validation of the planar structure EIT system performance", IEEE International Conference on Electro/Information Technology (EIT), 19-21 May, 2016, Grand Forks, North Dakota, USA, (accepted).

Ali Zarafshani, Thomas Bach, and Chris Chatwin "Using a planar EIT as a Structural Health Monitoring method to detect and evaluate the damage to CFRP composite used in aerospace structures", National Aerospace & Electronics Conference & Ohio Innovation Summit (NAECON-OIS), IEEE Aerospace and Electronic Systems Society, Dayton, Ohio, (submitted).

Ali Zarafshani, Tabassum R Qureshi, Thomas Bach, Chris Chatwin and Manuchehr Soleimani "An Electronic Mesh phantom for planar structure EIT systems", 16th International Conference on Electrical Bioimpedance (ICEBI) and 17th Conference on Biomedical Applications of Electrical Impedance Tomography (EIT), Presentation, 19-23 June 2016, Stockholm, Sweden, (accepted).

Ali Zarafshani, Thomas Bach, Wei Wang and Chris Chatwin "Conditioning a current source

using OCCII-GIC for EIT systems", Journal of Physics (IOP): Conference Series, EIT, 2015, at Switzerland.

Nevis Beqo, **Ali Zarafshani**, Tabassum R Qureshi, Chris Chatwin, Wei Wang "Converting EIT voxel based imaging and pixel based ultrasound imaging to standardised DICOM" XVth International Conference on Electrical Bio-Impedance (ICEBI) and XIVth Conference on Electrical Impedance Tomography (EIT), Poster Presentation, 22–25 April 2013, Heilbad Heiligenstadt, Germany.

Ali Zarafshani, Hedieh Hashemi, Nevis Beqo, Chris Chatwin, Wei Wang, Tabassum R Qureshi "Multi-frequency response mesh phantom for validation of EIT system performance" XVth International Conference on Electrical Bio-Impedance (ICEBI) and XIVth Conference on Electrical Impedance Tomography (EIT), Poster Presentation, 22–25 April 2013, Heilbad Heiligenstadt, Germany.

A Zarafshani, N Huber, N Béqo, B Tunstall, G Sze, C Chatwin and Wei Wang "A Flexible Low-Cost, High-Precision, Single Interface Electrical Impedance Tomography System for Breast Cancer Detection Using FPGA", Journal of Physics (IOP): Conference Series, EIT, USA

T R Qureshi, C R Chatwin, N Huber, **A Zarafshani**, B Tunstall and Wei Wang " Comparison of Howland and General Impedance Converter (GIC) circuit based current sources for bioimpedance measurements", Journal of Physics (IOP): Conference Series, EIT, USA

Nevis Béqo, Gerald Sze, Benjamin Tunstall, Guofeng Qiao, **Ali Zarafshani** and Wei Wang "A flexible and configurable hardware for the Combined EIM and Ultrasound device", Journal of Physics (IOP): Conference Series, EIT, USA

Abstract

The research concentrates on the design, development and calibration of a high performance Electrical Impedance Mammography (EIM) system for early detection of breast cancer at the macro and micro scale (at an early stage applicable for different breast sizes and shapes). The enhancement of the Electrical Impedance Tomography (EIT) system focuses on developing electrical and electronic instrumentations and improving the current source topologies to make them operate at multiple frequencies for the purpose of measuring permittivity and conductivity of different breast tissues. The calibration, assessment systems have employed current calibration in the EIT to evaluate the impedance distribution. This facilitates the acquisition of accurate impedance images to enable images of the internal structure of the breast to be constructed. A constraint on EIT systems is that the current injection system suffers from the effects of stray capacitance having a major impact on the hardware subsystem as the EIT is an ill-posed inverse problem which depends on the noise level in EIT measured data and regularization parameter in the reconstruction algorithm. This research aims are to prevent this problem by using a capacitance cancellation method based on a General Impedance Converter (GIC) implemented by operation of a second generation of current conveyor called OCCII-GIC and calibration methods to facilitate operation in the high frequency range. An EIT system based on a planar 85-electrode channel and using a Microcontroller unit (MCU) for addressing control between 85 electrodes and implementing calibration methods has been constructed. In EIT systems, assessment, validation of the performance and calibration of systematic errors in the electrical field generated inside of the interrogated volume is important. Evaluation of the EIT system will be assessed using a realistic electronic phantom (E-phantom). This enables the evaluation of the different conductivity values of the tissue, which has been created and evaluated based on the RSC circuit model for the different electrical conductivities and electrical impedivities in breast tissue.

Contents List

List of Figures:

List of Tables:

List of Acronyms:

2D: two-dimensional

3D: three-dimensional

ACT: Adaptive Current Tomography

ADC: analogue to digital converter

BCSP: Breast Cancer Screening Programme

BEM: Boundary Element Method

CCII: second generation operational current conveyor

CLK: Clock

CMRR: Common-mode rejection ratio

CT: Computed Tomography

DAC: Digital to analogue converter

DAS: Data Acquisition System

DCP: digital controlled potentiometer

Digital-pot: Digital potentiometer

DRV: Drive

ECG: electrocardiography

EEG: Electroencephalography

EIM: Electrical Impedance Mammography

EIT: Electrical Impedance Tomography

EMF: Electromagnetic field

EMI: Electromagnetic interference

E-phantom: Electronic Phantom

ESI: Electrical Source Imaging

FDA: Food and Drug Administration

FDM: Finite Difference Methods

FEM: Finite Element Method

f-MRI: functional MRI

FPGA: field-programmable gate array

GIC: General Impedance Converter

MCU: Micro Control Unit

MRE: Magnetic Resonance Elastography

MRI: Magnetic Resonance Imaging

MUX: multiplexer

MWT: Microwave Tomography

NHS: National Health Service

NIC: Negative-Impedance Converters

OC: operational current conveyor

Op amp: operational amplifier

PET: Positron Emission Tomography

PGA: Programmable gain amplifier

QA: Quality Assurance

REC: Receive

SNR: Signal-to-Noise Ratio

SPECT: Single Photon Emission Computed Tomography

TAT: Thermo Acoustic Tomography

UCL: University College London

X-ray: X-radiation

List of Symbols:

Hz: Hertz

F: Farad

H: Henries

Ω: Ohm

δ: Delta

Δ(Delta): Area

J: electric current flex

Freqs: Frequencies

ch: Channel

dB: decibel

A: Ampere

v: Volt

σ: Conductivity of medium

α: Gain of current in CCII

β: Gain of voltage in CCII

Φ(phi): Angle

Θ: Phase

Σ(Sigma):Sum

f: femto

p: Pico

n: nano

u: micro

m: milli

K: Kilo

M: Mega

∞: Infinity

+: Positive Polarity

-: Negative Polarity

˚: Degree

%: percentage

~: approximate

≠: Not equal

x,.,*: Multiplication (times)

<: less than

>: More then

X: reactance

C: Capacitor

R: Resistor

L: Inductor

Z: Impedance

G: Conductance

I: Current

V: Voltage

j: Imaginary

Y: admittance

ε: Permittivity

p-p: peak to peak

Δ(Θ):phase increment

Chapter 1 Breast Cancer and Early Detection Background

1.1. Overall aim of the research

In response to the need to increase the chances of detecting cancer at an early stage, which is directly related to survival of patients with respect to the increasing number of cancer cases, an electrical impedance mammography (EIM) system is presented. This system exploits opportunities to provide early stage detection of cancer using an alternative non-invasive biomedical imaging technique for screening of cancer in young, middle-aged and old people. By emphasizing non-invasive imaging techniques for clinical application in screening programmes, we have designed and developed a new electrical impedance tomography (EIT) system that operates at high frequencies from: 10 kHz up to 3MHz with low noise and high precision analogue circuits sufficient to inject current and measure the voltage needed to reconstruct impedance images. To assess the performance of the system an E-phantom was created to simulate the electrical properties of different tissue types, thus providing simulation and testing of the breast cancer using EIM. This research includes a specific target to design a new EIM system that will work effectively for clinical applications.

1.2. What purpose does this chapter serve?

This chapter describes the breast, breast anatomy, cancer stages and breast cancer incidence and gives a clinical introduction to breast cancer. This chapter describes the biomedical imaging modalities such as mammography, Computer Tomography (CT), ultrasound and Magnetic Resonance Imaging (MRI) that are usable in the area of breast cancer detection and the challenge of using Electrical Impedance Mammography (EIM) for early breast cancer detection.

1.3. Introduction

Tissue is made of millions of cells, which are constantly renewed and are replaced with younger cells. The meaning of cancer simply is defined when a single cell (abnormal cell) begins to multiply (overgrowth) out of control in a part of the body. As the cancer progresses, some cells may eventually break away and spread to other parts of the body, it is called metastasis cancer then tumours are formed through metastatic cancer cells (American Cancer Society 2015, Cancer Research UK 2015).

1.4. Breast Anatomy: stromal tissue and duct

The supporting cells and connective (glandular) tissue of the breast are called the stromal tissues. In case of the breast, various types of stromal cells are called stroma of the breast. Medical and anatomical scientists explain that the female breast consists of 6 to 10 major duct systems. When the breast becomes larger, it makes new internal structures, which are called lobules. These structures come together around the duct where the milk is produced during pregnancy and breastfeeding periods. Each duct contains numerous lobules, which consist of terminal acini and ductules (Kopans 1998). The adipose (a type of fat) tissue and supporting stroma surrounds these ducts and lobules forming the breast anatomy, shown in Figure 1. A group of lobules, forms lobes, each of the lobes is connected to the nipple by a duct. The milk ducts and lobules are growing during pregnancy. This process will lead to producing milk. The breast structure consists of the lobules and milk ducts will be changed and leave a few scuttle ducts in the breast after the cycle of milk producing terminates. There are

many different types of breast cancer. However, Ductal (milk ducts) and Lobules (milk-producing lobules) are the leading types. Lobule carcinoma begins in the lobes producing milk (milk-producing glands) and ductal carcinoma (tumour) begins and growths in the ducts that transfer the milk through the breast to the nipple as shown in Figure 2.

Some cancer cells will remain in milk ducts and lobules that are called non-invasive, but many become invasive and spread to other parts of the body. Although, the pathologist looks for the cancer cells under a microscope to identify the different appearances (generally physical appearances) as cancer cells have a unique appearance and the degree of difference between the cancer and normal cells is identifiable. However, cancer changes, physical and electrical cellular properties of cells. Therefore, there is a possible way to detect the cancer based on the different electrical properties of the cells.

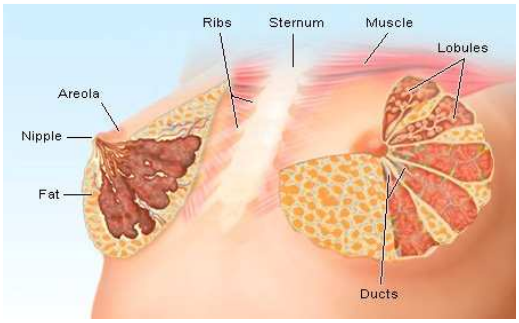

Figure 1 Anatomy of the Breast (MedicineNet 2010)

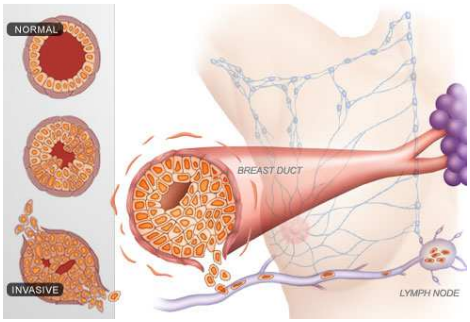

Figure 2 Ductal Carcinoma in situ (Movva 2013)

1.5. Breast Cancer stages

Cancer staging (staging classification system) is the way in which the extent of the spread of cancer will be determined as a clinical classification and assessment of results of treatment. There are various staging systems for cancer. The cancer stages range from the early form (stage–0) with the development of any abnormal cells (ductal carcinoma in situ), which are not invasive and can be cured with an almost 100% successful treatment. A localized (stage–1), tumour size is less than 2cm in diameter and the prognosis is very good around 72% of women with stage–1 breast cancer will have no recurrence of breast cancer for over 15 years and 99.1% of women

(aged 15–99 years) with stage–1 breast cancer have 5 years of survival (2002–2006). For the early locally advanced (stage–2), the breast tumour is 2cm or less in size, but cancer cells have already metastasized to other parts of the body such as lymph nodes or near the breastbone, or the cancer size is 2–5 cm or the cancer size is bigger than 5cm in diameter, but has not yet metastasized to other parts of the lymph nodes nor nearby breastbone and 87.6% of woman (aged 15–99 years) survive after 5 years (2002–2006) with treatment. The late locally advanced (stage–3) is the breast tumour size between 2 and 5cm with apparent spread or bigger than 5cm with no apparent metastasis, but there is a need to consider whether it is operable or inoperable (more difficult to completely remove with surgery), respectively, and the average survival rate is difficult to predict and depends on individual cases whether slow or fast growing and the response to treatment. However, in regard to breast cancer survival statistical reports, 55% of women (aged 15–99 years) survive after 5 years. Finally metastasized (stage–4), the cancer is metastasised to other parts of the body, i.e. the bones, liver or brain and unfortunately long term survival rate of women (aged 15–99 years) with this stage of breast cancer has a very low survival rate; around 14.7 % after 5 years (Breast Cancer UK and Breast Cancer (C50), Five-Year Relative Survival by Stage, Women Aged 15–99 Years, Former Anglia Cancer Network, 2002–2006)(Cancer Research UK 2014a). Successful treatment of breast cancer is highly dependent upon early detection and intervention.

1.6. Breast cancer overview

Breast, lung, prostate and bowel cancers are ranked the top four cancer incidences in the United Kingdom (2011), respectively. The breast 15.2%, lung 13.1%, prostate 12.6%, and bowel 12.5% (colorectum 8.3% and rectrum & rectosigmoid junction 4.3%) are 177,065 number of incidences of all malignant neoplasms (excl non-melanoma skin cancer), where the people population in 2011 is estimated to be 63,200,000. In fact, these four types of cancer made up 53.4% of all new cases in 2011 (Analysis by Ali Zarafshani based on Cancer Research UK, UK Cancer Incidence 2011, by Country Summary, January 2014)(Cancer Research UK 2014c). The commonest cancer incidence in 2012 especially in England for men were the prostate 25.9%, lung 13.6%

and colorectal 13.4% and for women breast 30.9%, lung 11.9% and colorectal 10.9% (Cancer Statistics Registrations, England, Series, MB1, No. 43, 2012) (Office for National Statistics (ONS) 19/6/2014). This shows that the common types of cancer (cancer diagnosed cases) among women and men in the UK are breast and prostate cancers, respectively, which is similar to the rest of the world. It is these two types of cancer that hold the top position among all races. In the UK, 50,285 people (cases) were diagnosed with breast cancer in 2011 and almost 350 men are diagnosed with breast cancer annually (UK Cancer Incidence and GLOBOCAN, 2008, Cancer Incidence and Mortality Worldwide, IARC) (Ferlay, Soerjomataram et al. 2014, Ferlay, Soerjomataram et al. 2015). Therefore, this incidence rate shows breast cancer is the commonest cancer in women and that is the reason why it is necessary to consider breast cancer so seriously.

1.7. The breast cancer incidence in women and the aged

The highest rate of breast cancer relating to age over a lifetime will be 1 case in 9 people. In the case of breast cancer, more women aged 60–64 years will be affected, 6,805 new cases per year between 2009–2011 (Breast Cancer (C50), Average Number of New Cases per Year and Age-Specific Incidence Rates, Females, UK, 2009–2011) (Cancer Research UK 2014b). The highest rate of breast cancer incidence by age for females is between 65–69 years worldwide (2012) (analysis by Ali Zarafshani (Ferlay, Soerjomataram et al. 2014)). Thus, the highest risk of breast cancer incidence occurs between 60 to 70 years old.

1.8. Early detection methods of breast cancer (protocol for a screening program)

For the purpose of earliest stage detection, the current strategy is to use screening programs related to different ages. Detecting cancer is normally done by mammogram, which is based on a type of X-ray screening. The other technologies which can be used for diagnosis besides a mammogram, such as digital mammography, computed tomography (CT) and ultrasound imaging, forming the basis

of UK NHSBSP, but at the moment ultrasound is just used for image guiding instead of using it for breast screening due to its limitations.

Mammography is generally recommended for three groups in the UK: 1st the people who have signs of masses (lump) infection, 2nd from 2011 the process of the breast screening with two\three screenings for woman in the 50–70 age range. All women will get their first screening by their 50th year, with two or three randomised extra screenings in the 50–70 age range. 3rd people with a family history of breast cancer (breast cancer history) (NHSBSP) are given specific attention. The American Cancer Society has used a similar protocol for a screening programme: 1st breast self-examination for women before 20s and starting 20s, 2nd clinical breast examination every 3 years for women in their 20s, 3rd clinical breast examination yearly for women aged 30s, 4th mammogram yearly for women over age 40 (National Breast and Cervical Cancer Early Detection Program, 2012).

1.9. Biomedical imaging modalities

There are many types of biomedical imaging modalities which apply different techniques. The most important quality factors for medical imaging modalities are based on invasive or non-invasive procedure, safety or minimum side effect of its use, the specification of tissues, distinguishability, ionization or non-ionization (radiation free), cost, rapid data collection, sensitivity, reliability and reproducibility, though possibility of long term monitoring is a factor for medical imaging devices that are used for observation studies i.e. lung injure, acute respiratory failure and other diseases.

Mammography, CT, MRI and Ultrasound imaging techniques are commonly used for detecting and monitoring of breast cancer at the different cancer stages. The X-ray and CT are generally used for screening programmes and MRI generally are utilized during the process of detection as well as used successfully in monitoring the treatment. Furthermore, ultrasound is a non-invasive and non-ionization imaging technique with a high spatial resolution. Since the ultrasound is a subjective technique and it is not based on the tissue electrical characteristics, hence it is more useful for establishing the physical geometry which adjunctively used with mammography

instead of a common techniques being used for screening programmes, particularly in breast cancer screening programme (BCSP)).

a. Mammography (X-radiation)

With the X-ray (X-radiation) method, the breast is squeezed using a dedicated mammography unit that consists of a pair of parallel compression plates (an X-ray on the bottom and a plastic plate on the top) and that reduces the thickness of the breast tissue. A diagnostic mammogram transmits low doses of X-rays (from centre to side) to one side of the breast with a detector on the other side of the breast. The thickness of the compressed breast must be reduced to reduce scattered radiation to increase the image quality. The enhancement of scatter reduces image quality and increases the required radiation dose, thus holding the breast is necessary. The breast images (mammograms) are produced by different attenuation of irradiance and from different angles of X-rays. The image of a 2D projection of X-ray is often difficult to interpret for breast cancer because it is focused in a particular area of abnormal tissue. However, the speed to practically take an image is fast and it is an objective technique. The important disadvantage of the X-ray technique is using ionizing radiation, which limits the total radiation dose that the body can tolerate. The doses of ionizing radiation to create a mammogram with low energy X-ray are around 30 kVp (a peak electron voltage, one electron voltage equal 1.602×10^{-19} Joules typically Molybdenum alpha radiation Mo-Kα normally same as using radiography of bones (50-150 kVp)) to examine the breast for detection of breast cancer where a mammogram has 0.4mSv (millisieverts) radiation dose (a person receives a radiation dose of 2.7mSv (in average) from natural sources in the UK). The result in Figure 3 shows the cancerous tissue absorbs X-rays and becomes white and opaque on the mammogram.

Figure 3 Normal (left) versus cancerous (right) mammogram, breast tissue appears white and opaque (Courtesy of the National Cancer institute 2015)

There are numerous variables that affect the performance of mammography for detecting breast cancer correctly, i.e. age and breast density (the amount of fatty tissue compared to glandular and fibrous tissues, and younger women naturally have higher breast density compared to older), hormone replacement therapy, image quality (resolution and movement), and experience of the radiologist (Penhoet, Petitti et al. 2005). The result of mammography until 2002 in the USA with a one year screening interval shows overall 71–96% has correctly determined cancer, but patients also required a biopsy. For a single mammogram, from 94 to 97% have correctly determined that a woman does not have cancer (with randomised trials), however, this requires further diagnostic evaluation, such as clinical examination or ultrasound (Humphrey, Helfand et al. 2002).

b. Computed Tomography (CT)

Computed Tomography (CT) was invented by G. N. Hounsfield in 1967, a British engineer who worked at a company in Middlesex, UK. The first prototype, was dedicated to imaging the brain and completed in 1971, it had a resolution of 80 x 80 pixels. The first commercial CT system (SIRETOM) developed by Siemens was launched in 1974. In the following years, CT rapidly emerged as a well-established diagnostic modality all over the world. CT is an X-ray machine in which the source and detectors are rotated together around the patient. The 2D and 3D reconstructed images use the Radon transform from a number of 1D projections at a number of different angles to achieve realistic soft-tissue data to produce volume data. It will cause a lot of difficulties in long time usage due to the radiation dose required for imaging organs (a CT scan of the chest has below 10mSv compared to a mammogram 0.4mSv). A number of studies have shown that the radiation does used in CT and mammography affect the body in the long term; leading to congenital anomalies in newborns from their mother who has been affected by X-rays and CT during pregnancy. This is why pregnant women are banned from being exposed to doses of X-ray and CT. Thus there is no

possibility of using X-ray mammography and CT during pregnancy (Ammari 2008, Penhoet, Petitti et al. 2005).

c. Magnetic resonance Imaging (MRI)

In contrast to X-ray, magnetic resonance imaging (MRI) is a non-ionizing 3D image technique (it requires around a 1000 of images of the breast from left-to-right, top-to-bottom, and front-to-back). The MRI signals will arise from the protons in body water and lipids when the patient is affected by the static magnetic field. The breast of the patient hangs into a depression and the scanning table (MRI scanner tube) is rotated into a tunnel-like scanning machine that surrounds a rounded magnet. This magnetic power is around 104 times higher than the earth's magnetic field. The proton becomes a small magnet when charged by the angular momentum. In fact, the protons precess around the direction of a large static magnetic field applied at the appropriate resonant frequency. There are two types of alignment of protons with their internal magnetic fields: in parallel or anti-parallel direction. By encoding the inducing voltages of a tuned detector coil into the magnetic field gradient where the protons process coherently, a linear variation will be produced in 3D in the magnetic field within the body. In fact, by using an inverse 2D Fourier transform, we can convert the signals to a spatial domain to create the image through the variation of phase and frequency of processing magnetisation. This is measured through a radio-frequency coil while the protons are linearly dependent upon their spatial location. A high spatial resolution image with the ability to change the data acquisition factors can be created based on the differential contrast between different tissues. Also, for the case of breast cancer, to improve the distinguishability of tissue properties a contrast agent (nonradioactive) can be given intravenously; which has the ability to improve the distinguishability of a tumour (Ammari 2008, Penhoet, Petitti et al. 2005).

The MRI has advantages over X-ray, which includes improved soft-tissue contrast and a high spatial resolution with higher sensitivity to detecting multi-centric ductal carcinoma than mammography, but it is less specific for detecting breast cancer compared to mammography (Hwang, Kinkel et al. 2003, Virnig, Shamliyan et al. 2009). Breast MRI is not approved by the FDA and NHS for routine breast screening and is

used to assess young breasts in high risk situations because the MRI is not able to precisely distinguish between abnormal (cancer) tissue and normal (noncancerous) breast tissue. MRI is also used for assessment of abnormalities indicated by other techniques (X-ray or ultrasound) or evaluating the spread of a tumour or effectiveness of treatment during or after treatment. MRI also requires further evaluation such as a biopsy (Schnall 2003). There are disadvantages, which include its high price (10 times more expensive than CT image technique and mammography) and the scan time, which is from 2-10 minutes and susceptible to patient motion. Moreover, if a contrast agent is given intravenously, the entire imaging session takes about one hour. Its most detrimental effect is an extremely low specificity image compared to other medical imaging techniques such as Electrical Impedance Tomography, which will be proposed to discriminate benign from malignant lesions.

d. Ultrasound imaging

Using ultrasound (sonography) for the diagnosis of cancer is based on a non-invasive, cheap and pain-free technique, which is beneficial since it is easily portable and is an inexpensive technique. It operationally works using high frequency sound waves over a range of 1 to 10 MHz via the backscattering of mechanical energy that comes from joining tissues or small structures within organs. The echoes produce an image (called a sonogram) only includes the physical properties (physical geometry) of the biological tissue. Ultrasound imaging produces a high spatial resolution without ionizing radiation (free radiation). The examination time for the case of breast cancer is around 10–20 minutes. In the case of breast cancer detection, ultrasound is usually utilized as an adjunct technology with mammography; it increases the accuracy of detection and provides guidance (Lee, Dershaw et al. 2010, Penhoet, Petitti et al. 2005). Its disadvantage is poor soft-tissue contrast and the most important weakness is the ultrasound image does not include the electrical data to determine the differences between the tissues, this makes certain organs difficult to image and just distinguishes between solid and fluid-filled tissues (cysts), this is why ultrasound is not a routine technology for breast cancer screening.

As I mentioned before in the breast anatomy section, some cancer cells will remain in milk ducts and lobules that are non-invasive, ultrasound is the most common technology for detection of ductal carcinoma when cancer cells (a mass) grows originally in the linings of the breast milk ducts invade surrounding tissue with speculated borders, but it is not much useful for the cancerous tissues that consist of calcium in the breast e.g. micro-calcifications which usually seen as linear micro-calcifications and linear orientation (Izumori, Takebe et al. 2010). However, at present ultrasound is recommended as an adjunct technology for young adults frequently as the breast tissue has a high density in this age group. It is worth noting that the ultrasound is an assistive procedure for cancer detection and is not a principal method instead of mammography, since the ultrasound shows the physical properties of the masses with an advantage of high spatial resolution image.

e. Microwave and radar imaging

The microwave tomography (MWT) is a non-invasive biomedical imaging technique which could be applied for detection, and diagnosis of breast and prostate cancers based on using electromagnetic waves in microwave frequency range. MWT generally operates between 300MHz up to 20GHZ to produce permittivity of subject. Microwave is a technique based on electrical and magnetic property distribution (Semenov 2009).

Considering the advantages of the MWT such as non-invasive, inexpensive and radiation free technique, some research groups are interested to utilize it in clinical studies as a biomedical imaging technique to detect breast cancer at an early stage (Bindu, Abraham et al. 2006, Fang, Meaney et al. 2004, Bond, Li et al. 2003, Fear, Li et al. 2002, Fhager, Hashemzadeh et al. 2006, Li, Meaney et al. 2003, Li, Hagness et al. 2003, Meaney, Fanning et al. 2000, Meaney, Fanning et al. 2007, Meaney, Fang et al. 2005, Miyakawa, Ishida et al. 2004, Poplack, Tosteson et al. 2007, Rubæk, Meaney et al. 2007). However, inhomogeneous and dispersive nature of the medium causes a long-time running and ill-conditioning imaging. Therefore, still many important improvements in hardware and image reconstruction are required. Here are some of the most common difficulties in microwave based on diffraction effects: 1)

impossibility of producing modulated, fine and narrow microwave beams with diameter less than the wavelength, 2) the restriction of the spatial resolution because of limitation in focus and 3) structure or signal interactions i.e. edge, wave effects and multiple scattering problems of the waves and creeping microwave breams.

In conclusion, it seems EIT and MWT have comparable advantages compare to X-ray, Ultrasound and MRI. Both have shown to be effective for relatively large tumours in a size of 0.5cm to 1cm because of spatial resolution. Therefore, it highly depends on the development of the system and improvements in regard to large scale clinical studies.

1.10. Challenges in using EIT instead of Mammography, MRI and Ultrasonic imaging techniques for early breast cancer detection

Overall, there are more than 15 biomedical imaging technologies i.e. Mammography (X-ray), CT (computed tomography), MRI (Magnetic Resonance Imaging), Ultrasound imaging, Microwave imaging, Elastic imaging, Optical tomography, SPECT (single photon emission computed tomography), PET (positron emission tomography), TAT (thermoacoustic tomography), Photoacoustic, ESI (electrical source imaging), EEG (electroencephalography), ECG (electrocardiography), and MRE (magnetic resonance elastography), which can be exploited for detection and diagnosis of different cancers, nevertheless only mammography (X-ray film and digital mammography), and CT have been approved for use in the breast screening programme in the USA by Food and Drug Administration (FDA) and in UK by the National Health Service (NHS). MRI and ultrasound are recommended as adjuncts to mammography, or for monitoring the response to the treatment process and image-guiding (Penhoet, Petitti et al. 2005). All efforts to detect breast cancer are trying to find a system to achieve the sort of data that can result in early detection for diagnosis of breast cancer. As the electrical properties of tissue are different when it changes from normal to abnormal tissue, Electrical Impedance Tomography (EIT) systems are recommended as it is capable of creating tissue condition data, which will be based on mapping the impedance of the tissue. Breast cancer screening using the EIT medical image technique is a more effective method since it can show cancers at an early

stage, though EIT provides the electrical specificity of tissues in a low-resolution image while the clinicians tend to use the high-resolution biomedical imaging techniques such as 128-slice CT, f-MRI, SPECT or 3D ultrasonic. However, the patients need to be assessed by a system operating on a different physical principle, i.e. non-ionizing radiation, and receive electrical characteristics, that electrical properties and response characteristics of cells and tissues seems to be a sufficient criterion for distinguishing cancerous tissues in screening programmes. EIT is the only biomedical imaging technique that can provide the images with these more useful features. In addition, EIT doesn't require a medical contrast mediums (contrast agents) though Ultrasound and MRI medical imaging techniques both require contrast agents. Therefore, EIT needs rapid improvement in order to achieve high-resolution images.

Mammography is a biomedical imaging technique that was founded around 40 years ago (FDA approval 1969). However, there are several side effects when using low energy X-ray in mammography compared to EIT, which is without any side effect and is a non-invasive technique. As the EIT technique injects very low currents around 0.5 to 2mA, there is no side effect from prolonged use for the monitoring of bedridden patients. However, as the EIT system is based on the impedance tomography system, it will be nonlinear, so there is no linear effect on measurements and electrical properties in relation to property changes. So it is an extremely ill-posed imaging technique.

The 2D EIT and CT images have similar mathematical functions when the desired image has been provided by acquiring data of the whole interior structure. Contrasting EIT with the MRI and CT techniques, which have high-resolutions, the EIT system uses diffusion of the current to create an impedivity distribution image with low-resolution. In contrast to MRI and electromagnetic, the EIT system is the only biomedical imaging technique that can produce an image using the distribution of electrical impedivity; EIT is a pain-free technology and produces inexpensive images. It has different applications and is a functional technique in contrast to other biomedical imaging techniques (Zou, Guo 2003, Brown 2003).

Mammography, MRI, and Ultrasonic imaging techniques have significantly improved the quality of the image in early detection of breast cancer. The image that is used for the early detections has the ability to diagnose accurately and renders precise and measured modes of treatment. The crucial factors that should be considered for different imaging techniques are as follows:

TABLE 1 COMPARISON OF PROPERTIES OF MAMMOGRAPHY, MRI, ULTRASONIC AND EIT

Features	Mammography	MRI	Ultrasonic	EIT
Cost of technique	Expensive	Expensive	Cheap	Cheap
Hazard attachments	Highest	High	No	No
Possibility of incessant uses (as long-term monitoring of physiological function is a common medical imaging technique in case of lung diseases)	No	No	Not useful	Yes
Capability of spectral of tissue specificities such electrical characterizations instead of physical features	No	Yes	No	Yes
Ionization radiation	Yes	No	No	No
Soft tissue contrast	Yes	Yes	No	Yes
High spatial resolution	Medium	High	Low	Low
Three dimensional capabilities	Yes	Yes	No	Yes
Susceptible to patient motion	Yes	No	Yes	No
Examining breast implant integrity	No	Yes	No	Yes
Invasive technique	Yes	Yes	No	No
Treatment efficiency	No	Yes	No	Yes

Table 1 shows the statistical information to emphasise why we need to focus more on EIT as an imaging technology, especially for detecting breast and other types of cancers. As a result, EIT has the opportunity to be a replacement for the breast cancer screening (as electrical impedance mammography EIM) as it is an inexpensive imaging technique and gives the possibility to detect and diagnose cancer at its different stages, different breast sizes and shapes and for high risk groups (such as family history and a genetic tendency). Moreover, there is some idea that EIT system will be useful in clinics as part of the normal clinical tools, for example clinical application of EIT for ICU patients. The EIT is also able to degrade the number of biopsies suggested to figure out or describe if a mass is cancerous. In regard to advantages and disadvantages, the aim is to use EIT as a replacement for mammography in breast cancer screening including adjunct method for detection and

monitoring treatment before and after therapy since FDA approval for clinical use in 1999 (U.S. Food And Drug Administration 2002).

The EIT has local resolution limitations; however, several researchers into EIT systems have made it an important subject in which research has become quite intensive rather than CT scanners, functional MRI (fMRI) methods, Single Photon Emission Computed Tomography (SPECT), and 3D ultrasound scanning.

The EIT system is highly preferred to the aforementioned diagnostic devices for the following reasons:

1) An EIT image describes electrical conductivity and impedivity distribution of biological tissues as a different type of data compared to other medical imaging techniques; it helps to detect breast cancer at the early stage applicable for different breast sizes and shapes.

2) The EIT system is useful in various applications such as distinguish cancerous from healthy breast tissue and as an adjunct method without causing any side-effect.

3) The EIT system is a pain-free and safe technology and will not place the patients' health at risk by exposure to ionizing radiation.

4) The EIT technique is a reasonable technique for screening programs as it is a less expensive technique compared to other available techniques.

5) Tissue characterizations (electrical parameters rather than simply physical information inside the body) are possible by making spectral impedance measurements.

With regard to the unique advantages of EIT as described above rather than other medical imaging techniques, the clinical application of EIT has been confirmed. EIT has been applied to: lung imaging, gastrointestinal system, as an accepted clinical imaging technique for clinical trials. One of the distinct features of EIT systems compared to other imaging technologies such as ultrasound, MRI and CT is the ability

to describe the dielectric properties of different tissues, which has been proved to work as a mammography imaging technique for detecting different cancer types in body regions like breast, cervical, skin and prostate. On the other hand, EIT still has challenges for clinical uses, as it is sensitive to errors introduced by data collection; affected by noise in frame measurements; weak sensitivity problem in areas; inaccurate electrode positioning; boundary shape problems which are mostly to do with the use and limitations of the hardware subsystem and inverse problem methods for image reconstruction. To solve some of these limitations, we are developing a new EIT system to overcome some of the hardware problems.

1.11. Conclusion

The new National Health Service Breast Screening Programme (NHSBSP) was established in 2012 in the UK. This national program invites all women aged between 47 and 73 for more precise screenings. These types of additional national efforts all try to detect breast cancer at the earliest possible stage. In the UK women are frequently referred for screening for breast cancer using X-rays, or breast Tomosynthesis mammography as the mammography equipment, (breast tomosynthesis mammography means taking multiple images of the entire breast in digital mammography instead of single image to avoid overlapping breast tissues. Because overlapping tissues can caused appear or beseem a breast cancer in the resulting image) (NHSBSP Equipment Report 1411, published in September 2014) (Baxter, Jones et al. 2014) and Magnetic Resonance Imaging (MRI), however, the masses will not be detected easily when they are small (less than 2cm). In fact, these screenings may not always detect early stage of cancer (cell changes). Cancer progression could be prevented by early detection and treatment, but then again the X-rays, Tomosynthesis, and MRI tests are not preferred in regard to their impacts. Nowadays, most breast cancers are detected by the screening programmes who report unusual changes through the Mammography (X-ray) screening programme. Mammography typically uses the mass characteristics and micro-calcifications for detection and this information seems insufficient for the early stages of breast cancer. The cost and side effects of screening programs are very important due to the scale of national

programs. In fact, this dissertation contains information about early detection of breast cancer by presenting a new EIT system with high-precision and improve-resolution. It would be a desirable system to use for the breast cancer screening programs and adjunct technology to other biomedical image techniques to increase the chance of a successful treatment.

1.12. Research achievement

A constraint on EIT systems is that the current injection system suffers from the effects of stray capacitance, which has a major impact on the hardware subsystem. The research has identified all the sources of stray capacitance and demonstrated how this limits high frequency performance.

The research has identified schemes to compensate for stray capacitance to facilitate high frequency operation of the EIT system.

The research has addressed the stray capacitance problem by using a capacitance cancellation method based on the General Impedance Converter (GIC) implemented by the operation of a second generation current conveyor called OCCII-GIC and calibration methods to facilitate operation in the high frequency range. In addition the new EIT system developed based on an auto-calibration method using a MCU and cascading topology in order to reduce on/off switch capacitance of the drive multiplexers that utilized to share the excitation system between different electrodes.

An E-phantom to assess the performance of the EIT system such as SNR and modelling accuracy of the system has also been created and evaluated. In addition the RSC circuit model of the breast tissues (the intra- and extra-cellular and membrane capacitance of the breast tissue) have been instated in the E-phantom in order to simulate the frequency dependent targets in the homogenous conductivity medium and the measured tissue impedances compared with Cole-Cole theoretical impedance measurements. Finally, we reconstructed the image to evaluate the image reconstruction algorithms.

1.13. Dissertation flow

As we described early, the first chapter presents the general knowledge about the cancer and especially breast cancer at the early detection stage, using different biomedical imaging techniques. Chapter 2 provides a literature review and feasibility study of the key hardware and instrumentation required for the EIT system. Chapters 3 and 4 describe the hardware of the new EIT system (AZ1 EIT system) in detail, focussing on the conditioning of the current injection system. The improved Howland current source as well as a current conveyor current source combined with the stray capacitance cancellation method to eliminate the effect of multiplexers in the system. Chapter 4 describes a feasibility study of using an MCU control system and software platform for implementing control all on a single platform. Chapter 5 and 6 focuses on the assessment and function of a high-performance E-phantom to assess the new current source combinations for the EIT system with the simulation and experimental results and impedance image reconstructions based on the RSC circuit model of different conductivities and impedivities. Chapter 7 provides a general discussion and conclusion plus suggestions for future works.

Chapter 2 Literature Review

2.1. Introduction

In general based on Ohm's law (V=IR), the resistance (R) (reciprocal of electrical conductance G) of an object can be determined if the current (I) passes through the object and the potential (V) difference across the object are known. Subsequently, electrical impedance (Z) is derived from the amplitude of resistance when there is a ratio of phases (θ) between the voltage and current in AC circuits ($|Z|\angle\theta$). Indeed, the electrical impedance is not purely a real resistance (R) value and is affected by the reactance (X), thus, (Z=R+jX). Furthermore, the effects of capacitors and inductors associated with intra and extra cellular properties in the case of biological objects will cause negative or positive phase shifts between current and voltage. Impedance has a direct cause-and-effect relation to the alteration of the current flows into an object. In fact, the impedance is the impeded or restricted current flow. The inverse of impedance is called admittance Y, which is admitting the current flow. Based on linear conditions for a unique tissue-specific cell, the cell impedance is the inverse of the cell admittance (Z=1/Y). If the distinction between the impedance and admittance is not relevant, the more generic term will be defined as immittance. Permittivity (ε) describes the subject's ability to transmit the electric field that is generated per unit charge in the medium. Practically the permittivity is a measure of the ability to permit

the storage of electrical energy in the medium. In regard to the above concepts Electrical Impedance Tomography (EIT), in biomedical engineering, is a medical imaging technique that maps the permittivity distribution inside the volume of a subject under test or a biological tissue sample, by injecting current or applying a voltage to the tissue and collecting voltages or currents on the subject surface (Zarafshani, Huber et al. 2010). EIT systems use impedance data for imaging biological tissues using the change of impedance brought about by disease states.

2.2. Historical review of EIT technology

The impedance imaging systems are known by different names as Resistance or Impedance Imaging (RI/II), Electrical Resistance Tomography (ERT), Applied Potential Tomography (APT), and Electrical Impedance Tomography (EIT) for biomedical image modalities (Brown 2003). It is recommended in terms of breast cancer screening programmes to use the Electrical Impedance Mammography (EIM) and in case of multi-frequency EIT is called Electrical Impedance Spectroscopy (EIS).

EIT as a medical imaging technique that was firstly established by Henderson and Webster (Henderson, Webster 1978). In the early 1980's Barber and Brown began to construct an EIT system (Barber, Brown 1984, Barber, Brown et al. 1984). At this time EIT was represented as a new biomedical imaging technique for various applications, i.e. gastric emptying, brain function monitoring, lung and cardiac function evaluation and screening and diagnosis of different cancers (e.g. Breast, prostate, skin, and cervical cancers and brain tumour).

Brown and Seagar were the first scientists to manufacture a fully operational EIT system in 1987 called Sheffield Mark I (Brown, Seagar 1987); as a consequence a new major research field was initiated in medical imaging by Barber and Brown's efforts(Barber, Brown 1984, Barber, Brown et al. 1984). The first EIT systems used a maximum of 5 kHz frequency and an efficient back projection algorithm (Brown, Seagar 1987). However, the resulting images had low-resolution. This algorithm had been derived from CT imaging technology, which has been generalised from the integral transform over straight lines to be called the Radon transform method. The

Radon transform produces an image from scattering data related to the cross-sectional area of an object. The inverse result of a tomography area will be produced from the scattering data, which means the inversed Radon transform creates the original density (intensity function); this is called image reconstruction (IR) (Barber, Brown et al. 1984). Based on this method, there were major problems in unavailability of any alternative to remove or filter the good data from the bad during the investigation, making its use not feasible for all types of targets. Furthermore, it has had no capability to be applied sequentially for different values of current and voltage related to measurements (Yorkey, Webster et al. 1987). This means that the Sheffield reconstruction algorithm had innate restrictions related to its use in comparison to iterative approximation methods, e.g. finite element method (FEM), finite difference method (FDM) and boundary element method (BEM) that can generate results more efficiently(Teschner, Imhoff 2011).

Following Sheffield Mark I, the Rensselaer Polytechnic Institute group presented an imaging method using the conductivity distribution (Gisser, Isaacson et al. 1988). The method that the Rensselaer group had presented, to obtain the conductivity distribution, had been based on current perturbation, which utilized an adaptive current pattern tomography system (ACT) (sometimes called dynamic electrical impedance tomography), which is produced by the current perturbation (Choi, Isaacson et al. 2003). However, a high-quality background conductivity is needed to achieve a highly accurate image (Choi, Isaacson et al. 2003, Holder 2005).

a. Review of EIT technology in other research groups

Rensselaer and Sheffield's groups were the first two groups that worked on primary image techniques, while the other research teams subsequently developed the hardware and software subsystems of electrical impedance methods. The histories of EIM, EIS, and EIT instruments are quite different in the case of capability. Overall, more than 10 research teams have developed an EIT machine. The following list indicates the major teams developing an efficient and effective implementation of the EIT machine:

I. Dartmouth college group
II. Kyung Hee University group
III. Oxford Brookes group
IV. Rensselaer Polytechnic Institute group
V. Sheffield group
VI. University College London group
VII. Duke University group
VIII. Moscow research group

TABLE 2 HISTORICAL REVIEW OF EIT TECHNIQUES IN DIFFERENT RESEARCH TEAMS

Research group/Drive name	Drive / Measurement Protocol	No of electrodes serial/parallel	Speed (frames per second / measurements per second)	Resolution Electrode Topology	Bandwidth No. of frequencies	SNR (dB)
Dartmouth group(Bayford 2006, Hartov, Mazzarese et al. 2000)	Two-terminal measurement Current/Voltage source	32 electrodes/64 ch parallel	30/30	16 bits Ring	10 kHz–10 MHz 30freqs	100
KHU Mk2 (Oh, Wi et al. 2011)	Four-terminal Current source	Any number of channels between 8-64 ch parallel	2/100	12 bits Ring	10 Hz–500 kHz 7 freqs	75-85
Oxford Brookes group /OXBACT5 (Bayford 2006)	2 & 4-terminal/16 current source 64 voltage measurements	Current and volt semi-parallel	25/25	16 bit Ring	26 kHz–56 kHz Single Freq	n/a
Rensselaer group ACT4 (Holder 2005, Ross 2003a)	Two-terminal 72 Voltage/Current sources	Ch 1.1 parallel	20	16 bits Planar	500 Hz–1 MHz 8 Freqs	90
Sheffield group, Mk3.5 (Wilson, Milnes et al. 2001)	Four-electrode Current source	8 electrodes semi-parallel	25/25	12 bits Ring	2kHz–1.6 MHz 30 Freqs	40
UCH Mk2.5 (Fabrizi, McEwan et al. 2009, McEwan, Romsauerova et al. 2006, McEwan, Cusick et al. 2007)	Four-electrode Current source	32/64 electrodes Serial	0.12–1/33	12 bits Ring and EEG applicator Head-shaped	20 Hz–1.6 MHz 30 Freqs.	40
Duke EIT (Ybarra, Liu et al. 2007)	Four-electrode Voltage source	128 electrodes Serial and parallel	120s screening process	23bits Funnel-shaped	Low frequency	High

Sussex group (former Rev.)	Four-electrode Current source	85electrodes Serial and parallel	20/20	14 bits Planar	1kHz-500 kHz (Current Source) 10 Freqs	60

Table 2 shows a recent review of EIT machines in other research groups. Although, there are several limitations in the technology, still several research groups are continuing to investigate the EIT efficacy.

b. Historical review of EIT techniques in Sussex research team

The Sussex group has had the motivation to improve the sensitivity and to create enhanced Electrical Impedance Mammography (EIM) systems focussing on hardware and software elements during all phases of research and clinical trials. The Sussex research group has established versions of the Electrical Impedance Tomography (EIT) system. EIT systems in the Sussex research group have been designed for breast cancer detection for clinical uses continuously generating cross-sectional images of the breast. There are several EIT machines using from 4 to 64 electrodes in the ring topology with more than 1% accuracy by using multi-frequencies (Wang, Tunstall et al. 1998). Overall, the existing records from previous publications show the historical background of EIT systems in the Sussex research group in detail. Table 3 summarises key points of the latest EIT development from 2008 to 2012.

TABLE 3 HISTORICAL REVIEW OF EIT AND EIM TECHNIQUES IN SUSSEX RESEARCH GROUP

Characteristic Points	**Ver3b system in 2008**	**Ver4 system in 2012**
Frequency points: Semi or Multi-frequency	Multi-frequency	Multi-frequency
Number of electrodes	85 electrodes	85 electrodes
Electrode topology: Ring or Planar	Planar electrodes	Planar electrodes
Type of applying source	Current Source	Current Source
Source Bandwidth	Up to 500 kHz	Up to 500 kHz
Speed of Data Acquisition System (frame/s)	>20 frame/s (DAS)	>25 frame/s (DAS)
Method of electrical impedance imaging	Dynamic image	Dynamic image
Signal-to-noise ratio(SNR):	SNR: 40dB	SNR: 50dB
Value of Accuracy of DAS:1%	Accuracy: > 1%	Accuracy: > 1 %
Speed of Image reconstruction	1frame/s	1frame/s

The Sussex EIT system has performed as a bioimpedance measurement technique. The earlier version of Sussex EIT systems for clinical proposes was built using an electrode plate containing 85 electrodes in a planar topology area that are

designed to be driven by a single current source technique. Based on personal experiences working with Ver3b and Ver4 systems, the most concerning limitations are as follows: limitation in bandwidth of the system, accuracy and SNR, image reconstruction resolution and low-sensitivity, speed of addressing control in regard to the acquisition time (speed of the system).

These kinds of limitations are quite common in the design of EIT systems. For instance, regarding speed, we incorporated an external board as an address board, which had been used to control the switching logic based on logic gate components. For this reason, the acquisition time has been increased, causing problems with electrolysis bubbles on the electrodes. (Huber, Béqo et al. 2010). The speed of data acquisition is an issue and the control system is designed to minimise the acquisition time.

c. Historical review of commercial EIT technology

The first commercial EIT machine was created by Hellinge and Hahn in the 1990s it was called the GOE MF II that was made by Maltron International, which was based on the Sheffield Mark I. This system was mainly evaluated by using it on regional lung function sections (Maltron International 2012). Maltron International presented a Sheffield Mark 3.5 image technology in 2000 that represented the first EIT in daily clinical practice (Maltron International 2012).

Siemens medical systems launched a system in 2000, which was not tomographic calling it Transcan TS2000 for breast imaging by employing a 2D rectangular array of electrodes using a set of measurements from a large electrode plate (TransScan Tscan-2000 2000). In 1999, the FDA approved the EIT technology as part of the clinical tools as an adjunct for mammography or to reduce the usage of biopsies (U.S. Food And Drug Administration 2002).

In the first decades of the 21st century Drager Medical GmbH also developed PulmoVista 500 as a clinical tool, which was used in intensive care in order to monitor the function of the lungs and the respiratory system (Teschner, Imhoff 2011).

After 25 years of EIT system development, the Russian Academy of Science in Moscow and SIM technika presented the MEIK III machine that was trialled in the Russia research centre and the clinical hospital of Yaroslavi. Spetspribor, it was a system represented by SIM technika in the 2007 version of the MEIK V system for daily clinical practice of breast cancer assessment (SIM technika 2008).

2.3. Key components of the EIT system

Typically, an EIT system consists of the following parts: (I) excitation system, (II) signal measurement system or data acquisition system (DAS), (III) Phase-sensitive demodulation system, and (IV) image reconstruction algorithm (Brown 2003). The excitation system consists of a current flow pattern that is produced by different source methods (such as current or voltage sources), is applied to two or more electrodes on the body surface. In order to have a high precision system, it should be able to pass the maximum known amount of the applied signals through the object (here a part of the body e.g. breast). The signal measurement system consists of voltmeters or ammeters, which are used to measure the resulting signals of the electric field appearing within the body.

An EIT system necessarily implements some functions in analogue electronics while as many as possible are implemented digitally. The first two parts (excitation and measurement systems) are analogue. A phase sensitive demodulation system consists of demodulators, which are utilized to extract both the real and imaginary parts of the measured signals; this can be done either in hardware or software. Afterwards, the extracted signals are passed to an image reconstruction algorithm to construct the image of the object under observation. The EIT images are provided at multi-frequency in case of having low-spatial resolution by using the generalised inverse problem or a finite element method (FEM) of the organ to construct the impedivity (could be permittivity) and conductivity images. However, these have different effects; by using the inverse method, an image with different permittivity and conductivity will be generated, and it is needed to create accurate mesh elements of the organ to review and to place the exact position of the electrodes.

Bioelectrical impedance is the basis of the EIT system that is the reciprocal of electrical admittance. The EIT system is based on different impedances that come out of different tissue types where there are extreme differences between the impedance of organs, and related to various frequencies as well.

In order to flow the current through a conductive medium, the current flows between two electrodes, these electrodes are called source and sink electrodes. The circuitous routes have negligible current flow. There are several methods that have been developed for measuring impedance. However, the topology of the four-electrode method introduced by Schwan, is a standard and the best method for bioimpedance measurement especially for the EIT system (Schwan 1963). According to the Schwan's explanation, two of the electrodes will measure the electrical impedance Z (reciprocal of electrical admittance Y) of the subject (e.g. Tissue) while the other two have injected the current into the object as shown in Figure 4. For the case of EIT, a constant current is injected to evaluate the impedance or admittance of an object over a frequency range. The maximum possible range of frequencies for the EIT system to be designed for most of the biological objects is around a few megahertz because of hardware limitations. However, at low frequencies, the electrode impedances are extremely high, impeding a constant injection current from being injected into a subject at frequencies below a few hundred hertz (Brown 2003). In addition, systematic errors will be produced from the effects of parasitic capacitances and inductances that infiltrate at high-speed measurement for a high-frequency system. Indeed, the frequencies for EIT systems should be considered from 10 kHz to a few megahertz. The resulting system not only makes less electrode impedance problems and transient change issues, but also reduces the risk of nerve stimulation in which a small harmless alternating current is injected into a subject.

Briefly, the behaviour of the current that flows to the tissue would be different at low and high frequencies. At low frequency (<1 kHz), the current that flows to the tissue impeded by cell membrane which particularly acts as an isolating layer. Hence, the current at very low frequency moves via intersection between cells and the measured impedance would be the value of the extra-cellular layer. On the other

hand, at high frequency, the capacitance of the membrane will be shorted and intra-cellular start to effect in the impedance measurement value as well as extra-cellular. Therefore we are considering significant differences between tissue properties at a narrow (low to high) frequency bandwidth. Although the value of the impedance that will be measured also depends on morphology of the tissue at the cellular level that means the ratio of the number of cell per unit divided in medium (what space are exists between cells in a tissue).

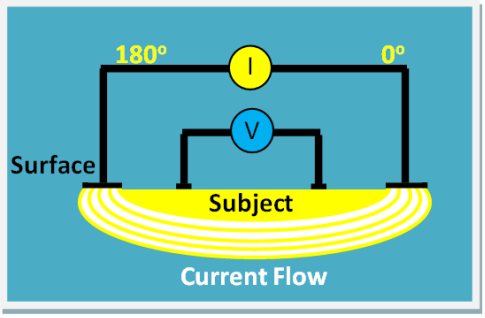

Figure 4 principle of pick-up the potential difference measurement with a four-electrode array (Martinsen, Grimnes 2008)

Overall, the two different sources are employed in practical EIT imaging systems used in clinical applications and diagnosis pathological:

(I) One technique using the bioelectrical impedance is measuring the potential response of the current injection excitation system when the electrodes are connected to the surface of the object for the impedance distribution calculation. To implement the technique, a known and constant (or a variable) value of alternating current is applied to a set of electrodes (between two or more electrodes) to create a current pattern and the resulting voltages are measured with other electrodes. Overall, it is required to have a high output impedance by using a large number of precision components to tune the current injections over a wide range of frequencies. However, the system is influenced by variations in load impedance as well as parasitic capacitance where the system becomes complex and time-consuming; calibration is needed to avoid this effect.

(II) The other technique is applying voltage on the electrodes and measuring the output current variation, there are advantages over current injection such as using a precision voltage source, high accuracy, and stability resulting in wide bandwidth compared to current injection. However, unknown contact impedance of electrodes will be the main issue in this technique.

Therefore, the key components of our EIT system includes a signal generator, a data acquisition system (DAS) and an image reconstruction system. There is a plug-in board (main board) which allows measurement of a set of transfer impedance measurements as analogue signals. This board is the key element in the system to cover the current injection switching between different channels. It is connected through a DAS with a cycle of processes from the signal generator, voltmeter, and control system in order to reconstruct the image. The signals are filtered and calibrated so that multi-frequencies and multi-channel circuits can have maximized bandwidth.

a. Sussex EIT Ver4 (former version) system

The Sussex EIT Ver4 (former version) system uses a quadrature (four-electrode) method for impedance detection (Xiaolin Zhang, Wei Wang et al. 2014). The EIT Ver4 system does not include any on-board calibration method to calibrate the current injection and voltage measurement. The ADC and DAC are based on the NI (National Instrument) PXI chassis. Also, the system has used a separate address control board. The Sussex EIT system is attached to a plane of 85 electrodes (as the electrode mesh of 85 electrodes shown in Figure 5) in which circular electrodes measure the electronic potential difference of all parts of the subjects, with thought of flowing in a half rice-seed shaped volume as shown in Figure 4 for the case of a planar structure. The principle of EIT is that hundreds of impedance measurements that pick-up the potential difference from a subject will create a higher resolution image when each measurement obtains the impedance of a half rice seed shaped volume of tissue produced by the distribution of current flow over a mesh of 85 electrodes, as shown in Figure 5.

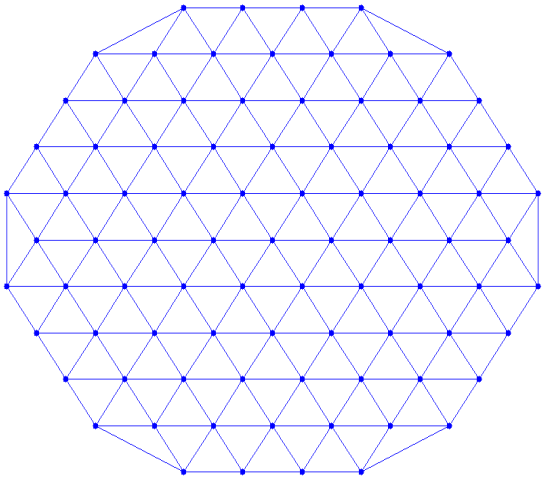

Figure 5 a coarse mesh of 85 electrodes with circular electrode plate

The Sussex EIT Ver4 is based on a single current source using an enhanced Howland current source which is shared between 85 electrodes using 8 multiplexer (MUX) ICs. The system specification is shown in Table 4 as the following:

TABLE 4 CURRENT SOURCE SPECIFICATION OF SUSSEX EIT VER4

Item	Feature	Specification
1	Amplitude of Current	0.5mA, 1mA
2	Operating Multi-Frequency	1kHz – 500 kHz
3	SNR	50 dB
4	Calibration method	Circuit test
5	Resistance Load	1k-2kΩ
6	Stray Capacitance (per each channel injection)	Most is caused by MUX and buffer op-amps (per multiplexer channel) C_{OFF}=11 pF, C_{ON}=18.5pF in total: 11pF*8ICs+8.5pF (per ch)=94.5pF (Data Sheet-AD8114 2005a)
7	Output Impedance	500 kΩ @ 100kHz and less then at 500 kHz
8	Accuracy	60dB

2.4. Technical challenge of EIT system

The goal is to improve impedance imaging technology, especially the performance of the EIT system for diagnosis of breast cancer in relation to the different densities of tissues, which vary depending on age, in general, premenopausal women have denser breasts than postmenopausal women, (breast density means the amount of breast and connective tissue i.e. fibrous and glandular tissues is large when compared to fat tissue). The deficit of the current EIT system that should be addressed first is the difficulty of achieving multi frequency electrical hardware. There are other

limitations or challenges such as spatial resolution, speed, accuracy improvement and decreasing sensitivity. The use of a current source is among the techniques mainly used for producing a current map (when injecting current) into a medium, by measuring electrical properties that are related to the density of various tissues, from the effect of current flowing between two electrodes and its measurement. Therefore, it is difficult to create a high-performance EIT system using an operational frequency range up to a few megahertz with high accuracy and stability.

In EIT systems, high precision circuitry is essentially necessary to resolve the ill-posed problem in image reconstruction, where a small change of surface current leads to massive changes in the spatial distribution of permittivity inside of the body (Bragos, Blanes et al. 1995).

The imaging resolution depends on number of electrodes because only a limited number of current injections and voltage measurements is obtainable. For example in ring topology with 16 electrodes, we are able to have 15 injection channels and 120 potential measurements (N (N-1)/2) (Brown 2003). Moreover, it depends with mesh density i.e. size of the mesh, number of nodes and elements, amount of data and number of frequency points. In addition, the image reconstruction software need to improve by number of sufficient factors such as uniform amplitude response, small and uniform position error, small ringing artefacts, uniform resolution (Adler, Grychtol et al. 2015, Holder 2005) .

Building a source with the greatest possible precision is urgently important for EIT technologies. This source can either be a constant current source so that each electrode chosen has a certain AC constant current injected into it, or the source can be a voltage source putting a specified voltage on each electrode.

Typically any two electrodes fixed to the target volume are driven 180 degrees out of phase and any two electrodes fixed to the target volume have their voltage difference signal measured with a difference amplifier and synchronous demodulation referenced to the source oscillator. The errors will be larger in using an applied voltage method compared to using an injected current method that is measuring the current

for modelling the permittivity because of the inability to account for the case where the contact impedance of an electrode is high.

2.5. Outline of proposed research targets

The proposed target of this research is the investigation and implementation of the new EIM system, which is based on the improvement of existing EIT systems applied in breast cancer screening/detection, presented as a new mammography method. So progress seems difficult without defining the targets more clearly as in the following:

a. Feasibility study of key hardware elements of the EIM system for improvement of the system sensitivity, the system performance and efficiency.

b. To study and to design the high-performance Cole-Cole based electronic mesh phantom in order to improve the system sensitivity, reliability and reproducibility by validating and assessing the performance of the EIT system.

Identification of EIT system features helps to find the direction of what should be achieved regarding improving sensitivity and image resolution. In regard to the Sussex EIT Ver4 (former version) and its weaknesses, I design a new EIT system. This new EIT system is called AZ1 EIT system to investigate the high-performance of different current sources of the EIT for improvement of the bandwidth as well as calibration methods to improve resolution.

a. Proposed Targets 1: Feasibility study of key hardware elements of EIM system for improvement of the system sensitivity

As it was mentioned before, the EIT systems can be implemented by injecting current to receive a voltage. Therefore, a possible topology would be creating a system based on two different current sources on a single platform with the choice of a stray capacitance cancellation method as a multi-source structure. This multi-source structure is the key element to determine high efficiency in highly sensitive EIT

systems. For the multi-frequency system, the single channel signal, and multi-signal measurement would be calibrated to achieve the maximum bandwidth and SNR measurement in the presence of minimized noise.

1. The feasibility study of current source implementation

The excitation system when based on the current source is limited by system bandwidth due to the effects of output and stray capacitances. The most important factor in producing a constant output current is the source impedance of the current source, which is frequency dependent. A good current source having a high output impedance will be affected negligibly by the unknown contact impedance. The source impedance is ideally infinite, but due to the presence of unwanted capacitances, the source (or internal) impedance is limited across a wide band. The current sources that have been commonly recommended in EIT systems are based on the improved Howland current source (as a voltage-based structure) and current conveyor current source (as a current-based structure). The improved Howland current source is among the methods that traditionally have been used for current injection. The improved Howland current source has limited output impedance which is consistent across a wide bandwidth. The source impedance of a current source reduces in the presence of unwanted capacitances at higher frequencies. When these unwanted capacitances (output and stray capacitances) are cancelled, a higher output impedance of a current source can be achieved. (Qureshi, Chatwin et al. 2010).

In order to do this, a general impedance converter (GIC) was placed in parallel with an improved Howland circuit as a common solution (Antoniou 1969). However, the common GIC (i.e. Antoniou 1969) which is composed of two op-amps and five passive components does not have an ideal result when combined with the current sources. For this reason, a novel method has been created to cancel the stray capacitance of the design. This method has been created by utilizing an operational second generation current conveyor (OCCII) combination acting as a GIC in place with current sources when producing an inductance in parallel (as an RLC circuit). It is worth noting that this technique is a novel method in EIT systems and this method is named

here as an OCCII-GIC. In order to reduce the output capacitance of the system, different GIC designs were tested, and then output impedance and bandwidth performance were evaluated. Results show that high output impedance can be achieved over a limited bandwidth. This configuration makes the current source very complex, which requires high precision and additional complex trimming circuits. We use tuning techniques to achieve a system with high output impedance at higher frequencies.

Chapter 3 presents a multi frequency OCCII-GIC circuit to cancel the unwanted capacitance in an EIT system. We test the OCCII-GIC circuit with different current source methods such as voltage-based and current-based structures (i.e. Improved Howland current source and current conveyor current source). The simulation and experimental results of the EIT system show it should be useable at frequencies above 3MHz.

2. Fast switching channel and control system

The main aim of this research is the integration of two schemes: the wide bandwidth and fast multiplexer (MUX) for excitation and DASs. Each of them is individually effective in achieving the required design specification when DAS uses digital techniques, and different excitation signals combined with the advantages of high stability and low noise. The most recent single-source designs are based on a switching function using DRV and REC multiplexers. A microcontroller unit (MCU) is usually used for controlling systems in order to achieve a high-speed and a high precision system. The MCU also has the task of communication between the system interface and channel modules. It additionally uses an automatic procedure for calibrating the system and image reconstruction algorithms, which are attached, as a micro-controlled structure. These advances in technology bring improvements in performance, such as wide bandwidth, high speed and high precision when they are applied to an EIT system. For instance, the aim is to design the fast multiplexer for the EIT over a model reference adaptive structure in order to boost the performance, especially in image reconstruction speed. It will be ideally a combination of the entire system via the focus in analogue varying channels for 85 electrodes. It is required to

use MUXs in case of controlling shifts (changes) between each source channel. The MUXs also are used to select the channel (measuring electrodes) in the acquisition system. The switching channels are a key factor for system speed as they affect the speed of the acquisition system. Long capture times mean that there is more likelihood of patient movement that may cause further artefacts in the EIM capture. As a demonstration of the architecture to achieve fast prototyping only one channel in the system will be selected (or changed) in the EIM capture.

b. Proposed Target 2: To study and to design a high performance Cole-Cole based electronic mesh phantom for improvement of system sensitivity, reliability and reproducibility

Assessment and validation of the EIT system performance and calibration of systematic errors in the electrical field generated inside of the interrogated volume is paramount. System instabilities can be caused by the EIM design and must be characterized before and during the clinical trials. Evaluation of the EIT system used in the clinical study can be based on a realistic electronic phantom (E-phantom). This research describes an electronic mesh phantom based on the electrode configuration and mesh structure of the planar Sussex EIM system. The phantom has the capacity to model the cellular electrical properties that are operative within a circular homogeneous medium. The design is optimized to assess the planar topology of the internal impedance distribution. This includes the effect of the complex impedance model of tissues using a distributed circuit, exploiting look-up tables of the extracellular resistance R, resistance of intracellular tissue S, and the membrane capacitance properties C (RSC circuit model). The system employs the information on the electrical properties of biological tissues to achieve the Cole-Cole dispersion data. The study will present a dynamic phantom to assess the performance of the EIT system to simulate *in vivo* conditions. The mesh phantom has the capability to generalize the RSC circuit models between 85 electrodes. It is possible to use different RSC values at six different locations each in a one slice; consisting of 123 combinations (current injection) with the capability to generalize the model using a hexagonal topology in the planar structure that is measured at multiple frequencies. This mesh phantom

provides predictable, stable, and reproducible signals with the capability of using digital-potentiometers in place of R and S resistances in the RSC model that is formed between 2 electrodes for the dynamic model. This mesh phantom is also capable of producing localized conductivity perturbations between each arbitrary channel in the electrode placement planar phantom topology by measuring all combinations, which are used in the image reconstruction. The phantom is especially designed for the planar 85-electrode EIT structure and can validate system performance of measurements consisting of SNR, accuracy, and modelling system accuracy. The preliminary results have demonstrated that the novel electronic phantom can be very effective as a clinical prototype for QA assessment and future certification. The purpose of this phantom is system validation and performance testing during all phases of the clinical trials: pre-trial, during the trial and future clinical derivatives. The new phantom will also be a useful research tool for EIT researchers, as altering the location and distribution of the impedivity is readily achieved.

2.6. Summary

The aim of this research is the early detection of breast cancer through using an EIM system. The EIM system will diagnose whether or not a lump or mass in the breast is benign or malignant. EIT is a very practical tool as an alternative to mammography or as an adjunct technique with other medical imaging techniques.

Another crucial factor is that despite 35 years of historical research; EIT systems still have not found a place in clinical settings. The reason is that the dielectric properties of tissue present a very slight change with changed tissue characteristics, resulting in voltage changes of less than 200uV in the planar electrodes. The use of EIT at high frequencies has been limited by hardware and software difficulties. These are the most important challenges which must be addressed before an EIT system can be used for screening programmes. The previous EIT systems had significant problems, however, the introduction of fast computers results in a reduction in preparation time and memory size problems. The other limitation considered for EIT systems is that various electrode applications and software tools can identify the relevant parameters which are not covered by generally applicable parameters in historical EIT systems.

2.7. Achievements

The literature review will mainly include the following topics:

- The historical review of EIT techniques in existing research groups and commercial purposes
- Review of Sussex EIM systems
- The technical challenges for EIT technology
- Reliability, reproducibility and sensitivity of the EIM system through advance research in the application of assessments and validation methods.

Chapter 3 conditioning an improved Howland topology using operational conveyor (OC) based on GIC (OCCII-GIC) for EIT systems

3.1. Introduction

For reconstructing the permittivity or conductivity of an image, it is required to employ a current or voltage source and the DAS to measure different potentials at multi-frequency points (about 5-10 frequency points). In principal, the impedance is the ratio between voltages and currents, and this ratio could be between voltage measurements and current injections or current measurements while applying voltages, which are called, transfer impedance measurements (Brown 2003).

Indeed, on the subject of injecting current, in order to achieve a high precision system, it is important that the current injection circuits have a high output impedance over the required frequency bandwidth. This will deliver a high-performance system with improved spatial resolution at high frequency, while the electrical properties of biological tissues changes over a frequency range. The change in electrical properties of a small section of tissue can be observed (or measured) at high frequencies. These changes can provide significant information about the structure and composition of

the tissue. Tissue electrical properties depend upon their important resistive and capacitive characteristics, which assume values that are dependent upon the permittivity ε, which quantifies the tissue's ability to permit storage of electric energy; so these high-frequency measurements are vital for intra- and extra-cellular impedance imaging.

The aim of this study is to use the EIT system as a biomedical imaging technique, which is effective in the early detection of breast cancer. This research begins with the theoretical description of current source topologies and proposes a current conveyor in application of Gyrator to eliminate the current source limitations and its development followed by simulation and experimental results, which are presented at the end.

3.2. General overview of the current source

The most recent techniques for the clinical and physiological applications of EIT systems are based on applying a known value of low amplitude current (between 0.1mA to 2mA) that is injected into the subject at different frequencies and measuring the resulting potentials at different frequencies (around 10kHz to a few megahertz) in order to produce an impedance image of the tissue. In regard to the advantages of the current source topologies i.e. predictability of constant current with low noise, are commonly employed in EIT systems as is utilized by Kyung Hee (IIRC); Oxford Brookes (OXBACT5); Rensselaer (ACT4); Sheffield (Mk3.5); UCL (Mk2.5&1b) and also the Leicester group (Mk3) (Oh, Wi et al. 2011, Holder 2005, Bayford 2006, Isaacson, Mueller et al. 2003, Brown 2003).

The sources are the key modules in the impedance measurement systems. The sources operate by injecting current or applying voltage. The key factor in EIT system assessment consists of SNR and accuracy, which are directly affected by the output impedance of the current source when measuring the voltage between two points of the tissue. Figure 6 shows the ideal current source circuit.

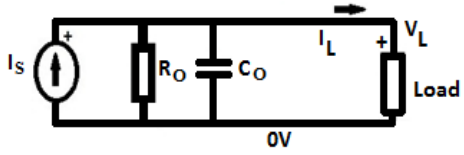

Figure 6 Ideal current source circuit

In reality, the output impedance of the current source will not be infinite and the current source is affected by output capacitance effects generated by the current source circuitry, extra capacitance that exists in electrical components in the output signal path such as multiplexers, capacitances on the printed circuit board (PCB) copper tracks carrying the output signal to other copper areas and the load capacitance. These capacitances in parallel with the load resistance are shown in Figure 7, represented by the output capacitance of the source, C_O, stray capacitance, C_{STRAY} and load capacitance, C_L. They can significantly reduce the output impedance amplitude of the current source circuit and introduce phase shifts at high frequencies. In the remainder of this dissertation C_O and C_{STRAY} will be lumped together as C_{STRAY}.

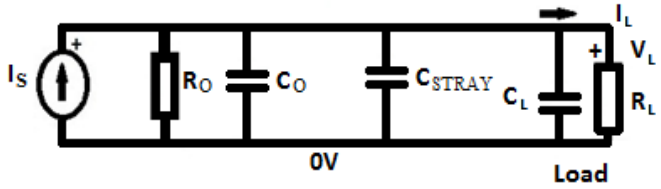

Figure 7 Real current source circuit with stray capacitances

Thus, a current source for use in an EIT system needs to be able to produce a stable, constant current at low and high frequencies with different loads. This means it needs to have a high output impedance and constant Transconductance into the load across the frequency range used.

Various electrical configurations are used to implement the current sources used in bioelectrical impedance devices; their function and performance can be considered to be the most important part of the system. Each has advantages and disadvantages regarding its topology. The most popular current sources that are employed in bioimpedance systems are: Howland current source, improved Howland current source, general impedance converter source, mirror current source, mirror

modification Howland current source, Wien Bridge circuit, Wien Bridge circuit with voltage to current converter circuit (V/I) and current conveyor current source (CC current source).

Stray capacitance is the key issue affecting the output impedance of the current source. It reduces the useful frequency bandwidth of the entire system. In this chapter, we consider two major structures of current source topology. These are voltage and current-based structures. The voltage structure consists of a voltage source V_{IN} and operational voltage amplifier generating a constant current into various loads. An example is a Howland current pump. The current-based structures produce an output current based on active components such as Operational Transconductance Amplifiers (OTA) and Current Conveyors (CC). In this chapter, the improved Howland current source and the current conveyor current source will be described more thoroughly and used as the two main current injection topologies for bioimpedance measurement systems.

3.3. Improved Howland current source

Prof Bradford Howland at MIT developed the basic Howland current source around 1962. It was published in 1964 by D.H. Sheingold (Sheingold 1964, Pease 2008). The Howland current source is an excellent circuit that gives a current in either direction or alternating (AC or DC) current source that can have a high output impedance and wide bandwidth range (Pease 2008). Regarding the output capability that does not normally swing very close to the rail, the “Improved” Howland source consisting of 5 resistors in which the R_4 Howland source is divided into R_{4a} and R_{4b} (see Figure 8), and the output node of the current source is connected between these two resistors.

One of the most significant advantages of the improved Howland current source compared to other sources is its ability to work at higher frequencies and its reduction of the common-mode voltage and loading effects. Thus the commonly used current source is based on the improved Howland circuit. The improved Howland

current source functions as a voltage controlled current source (VCCS) circuit. Its schematic is shown in Figure 8.

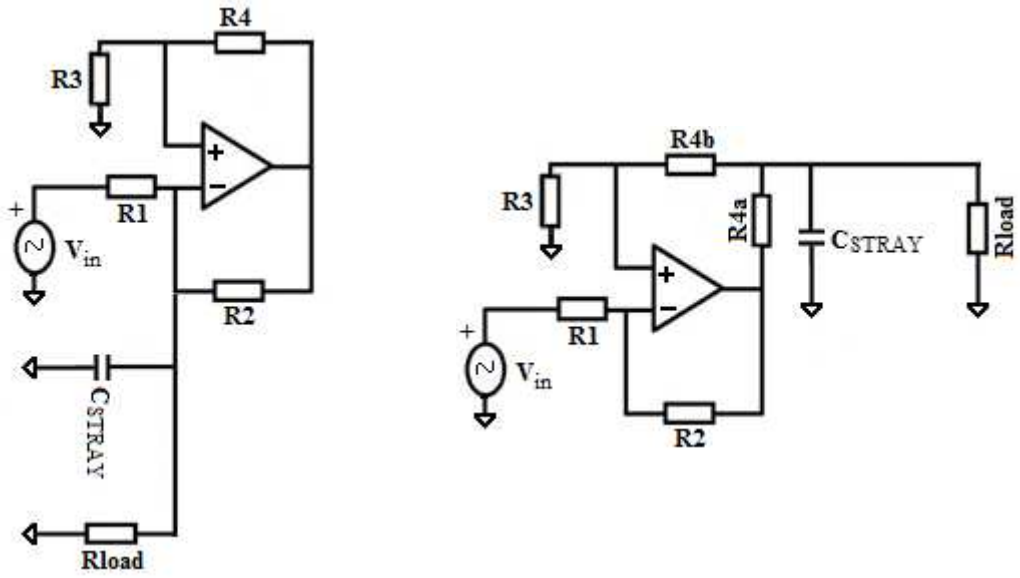

(a) (b)

Figure 8 (a) the Howland pump (R1/R2=R3/R4) and (b) the improved Howland current source

The output resistance of the improved Howland current source circuit is calculated using the following equation:

$$R_O = \frac{R_1 R_{4b}(R_3 + R_{4a})}{R_2 R_3 - R_1(R_{4a} + R_{4b})} \quad (1)$$

where $Z_0 = R_O \parallel C_O$

Rearranging by dividing numerator and denominator by R_2:

$$R_O = \frac{\frac{R_1}{R_2} \cdot R_{4b} \cdot (R_3 + R_{4a})}{R_3 - \frac{R_1}{R_2} \cdot (R_{4a} + R_{4b})} \quad (2)$$

After that dividing the result by $R_{4a}+R_{4b}$ we get:

$$R_O = \frac{\frac{R_1}{R_2} \cdot \frac{R_{4b} \cdot (R_3 + R_{4a})}{(R_{4a} + R_{4b})}}{\frac{R_3}{(R_{4a} + R_{4b})} - \frac{R_1}{R_2}} \quad (3)$$

The maximum output impedance would not be achieved if there is a tolerance between any resistor R_1, R_2, R_{4a} and R_{4b} and two times of R_3. For example, if R_1, R_2, R_{4a} and R_{4b} are equal to 1kΩ and R_3 is equal to 2kΩ, equation (4) will be obtained as:

$$R_O = \frac{1k * 1k(2k + 1k)}{(1k * 2k) - 1k * (1k + 1k)} = \infty \quad (4)$$

Thus by inspection, we see that the denominator in this equation becomes zero and R_O become infinite when the ratio of R_1 / R_2 is equal to R_3 / (R_{4a}+R_{4b}). For example, if we chose the special case where R_1 equals R_2 then R_3 must also equal (R_{4a}+R_{4b}) to get the maximum output resistance. However, resistors are available with different tolerances from common suppliers with banding B, C, D, F, G, J, K and M with a tolerance of 0.1% to 20%. If a 1kΩ resistor was Band K 10% for example, it could be expected to be between 9kΩ and 1.1kΩ. Thus we can see that the tolerance of the resistors can cause alteration in the output impedance of the current source (Pease 2008).

However, in practice, non-idealities from the op-amp limitations, resistor tolerances and the presence of stray capacitance in the design have the result of reducing the output resistance and increasing the output capacitance and accordingly output impedance of the current source (Webster 1990, Cook, Saulnier et al. 1994, Muñoz, Berga et al. 2005). A high precision EIT system requires a frequency bandwidth up to 3 MHz to increase the spatial resolution of the permittivity image.

Instability of the transfer impedance measurements is caused by circuit problems and field problems. The current source with a low impedance output is a part of the circuit problems as a category of hardware systematic errors, thus for a given stable current source, it is important to reduce systematic errors with effective hardware design.

Primarily, the current source in EIT systems will investigate ways to achieve the highest possible value of output impedance suitable to implement in the high-frequency range around a few megahertz.

In practice the effective output capacitance of the current source and the parasitic capacitances create a total grounded capacitance that makes it impractical to produce an EIT system operating at high frequency. Thus, for utilizing the improved Howland current source at high frequency we recommend using a stray capacitance cancellation method of producing the inductance in parallel (Holder 2005, Ross, Saulnier et al. 2003b, Oh, Lee et al. 2007).

3.4. Current-mode current source

As mentioned previously, current sources suitable for EIT systems for breast cancer detection need to produce high output impedance Z_{OUT}, ideally infinity over the frequency range of 10 kHz to a few megahertz. In reality the output impedance of the current source is finite; if it is more than a few mega-ohms (MΩ), it is commonly acceptable. One of the most common techniques to make a current generator is the current mirror technique, which can produce a constant current with high output impedance at high frequency based on using a Current Conveyor (CC) or Operational Transconductance Amplifier (OTA) as utilized by many research groups (Bragos, Rosell et al. 1994, Casas, Rosell et al. 1996, Yerworth, Bayford et al. 2002, Seoane, Bragós et al. 2008). This type of current source model is based on current-mode structure, when the output current is produced by an active component.

In this section, we present a current conveyor as a current-sense based on VCCS. A current conveyor is based on an active component, thus, it will be more stable and suitable for integrated implementation.

a. Second-generation current conveyor (CCII)

The current conveyor is an open-loop current-mode amplifier with low and fixed current gain. The second-generation current conveyor (CCII) is a flexible and versatile building block (Sedra, Smith 1970, Sedra, Roberts 1990). The CCII is capable of conveying current with very different impedance levels and is used in high-frequency applications for which it has significant advantages (Sedra, Roberts 1990, Eloranta 2004). The current conveyor simplifies circuit design and can be implemented

as an operational amplifier with higher voltage gain, which is not limited by the conventional voltage feedback operational amplifier having a standard gain bandwidth (Sedra, Smith 1970, Eloranta 2004). The CCIIs are used as a current feedback operational amplifier (Robinson 2008), If a voltage is applied to the high impedance non-inverting input (Y), it is expected that the same voltage appears on the low impedance inverting input (X), which means $V_X=V_Y$, while the current applied to the inverting input X node is conveyed by mirrors to the Transimpedance output node (TZ), $I_{TZ}=I_X$. Based on the circuit shown in Figure 9 and Figure 10, TZ and Y are high impedance and X is low impedance, since the current in non-inverting node Y is ideally equal to zero, $I_Y=0$.

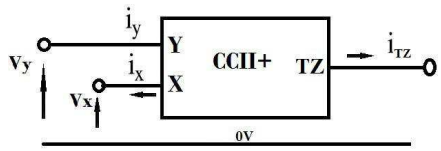

Figure 9 Symbol of CCII+

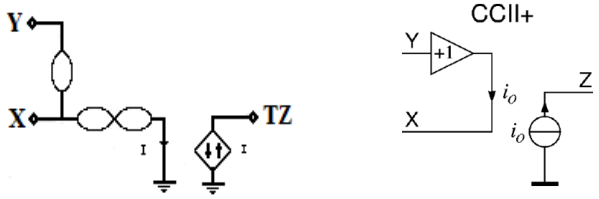

(a) (b)

Figure 10 (a) Current models of CCII and (b) simplified current follower in CCII+

The matrix of an ideal current conveyor is given by:

$$\begin{pmatrix} I_Y \\ V_X \\ I_{TZ} \end{pmatrix} = \begin{pmatrix} 0 & 0 & 0 \\ 1 & 0 & 0 \\ 0 & \pm 1 & 0 \end{pmatrix} \begin{pmatrix} V_Y \\ I_X \\ V_{TZ} \end{pmatrix} \quad 5$$

where the characteristic functions are given by,

$$V_X = V_Y, I_Y = 0 \text{ and } I_Z = \pm I_X$$

Figure 11 shows a simplified schematic of the available current conveyor module. The transistor schematic of the current conveyor shows the differences between the simple conventional voltage feedback op amp and current conveyor.

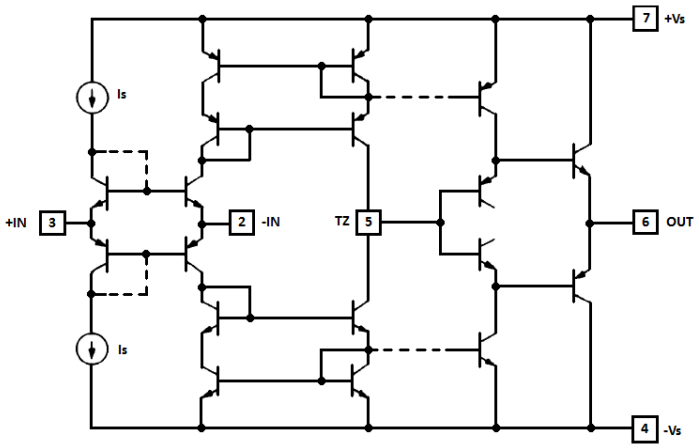

Figure 11 Simplified schematic of a current conveyor (Data Sheet-AD844S 2009)

The advantage of the CCII is its ability to control the output resistance of the TZ node, thus encouraging a large quality factor. The other advantage of using the CCII is that it provides a linear response over a wide bandwidth when compared to op amp based circuits (Khan, Zaidi 2003, Maundy, Gift et al. 2007).

However, in an actual implementation, the voltage at X node (V_X) does not equal that at Y node (V_Y) and the current at X node does not equal that at TZ node. So we must use the following matrix of a non-ideal current conveyor:

$$\begin{pmatrix} I_Y \\ V_X \\ I_{TZ} \end{pmatrix} = \begin{pmatrix} 0 & 0 & 0 \\ \beta & 0 & 0 \\ 0 & \pm\alpha & 0 \end{pmatrix} \cdot \begin{pmatrix} V_Y \\ I_X \\ V_{TZ} \end{pmatrix} \qquad 6$$

where the characteristic functions are given by,

$$V_X = \beta V_Y, \quad I_Y = 0 \text{ and } I_Z = \pm\alpha I_X$$

In non-ideal behaviours the error forms are accounted for by the coefficients of β and α. These coefficients are the voltage and current tracking errors of the current conveyor (Biolek 1995, Shaktour, Biolek 2008).

In regard to CCII behaviour Figure 12 shows the schematic of a current source based on a current conveyor, the TZ node generates the output current with high impedance, when the X (input node) is connected to ground through a resistor (R_X), the output current will be calculated as:

$$I_X = \frac{V_{in}}{R_X} = I_{TZ} \qquad 7$$

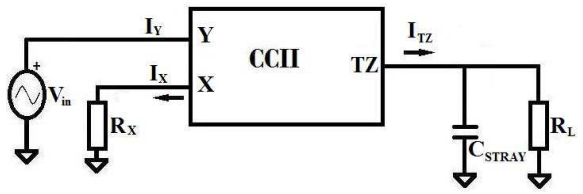

Figure 12 Current Conveyor Current Source (Bragos, Rosell et al. 1994)

Therefore, the current conveyors are presented as a current-mode device in the application of the EIT source. In the current conveyor current source structure based on the typical characteristics of CCII, the voltage at the non-inverting input (Y node) will transfer to the X node with a low offset voltage (β). The inverting input (X node) is the common emitter node of a complementary pair of the grounded base stages. It acts as a current summing node.

In reality with regard to the specification of the module, the input resistance exists at about tens of ohms. Thus, the current that is applied to the inverting input would be delivered to a complementary pair of unity gain current mirrors, which delivers the same current to the output node of TZ, that means $I_{TZ}=\alpha\ I_X$ when the full output voltage is generated.

For a given stable current source with stray capacitance, firstly it is important to reduce systematic errors with an effective hardware design such as possible solutions to reduce the effect of the resistor tolerance problem. Secondly, it needs techniques to reduce the effect of stray capacitance in an EIT system such as considering only the real part of the load voltages, which overcomes the sensitivity resulting from the stray capacitance (when considering only the load as a resistance)

that only produces the conductivity (or resistivity) image of the tissue, or which we explore herein, we can use a method of capacitance cancellation to reduce the effective capacitance to comply with the required output impedance.

3.5. Current source performance with general impedance converter (GIC)

The GIC can be used in many applications such as programmable impedance in the synthesis of a filter design, oscillator design, analogue phase shifters and cancellation of parasitic elements (Muñoz, Berga et al. 2005). These use combinations of passive impedances, operational amplifiers, Transconductance amplifiers and current conveyor to synthesize programmable impedances (Sedra, Brackett 1978, Bowron, Stephenson 1979, Franco 2014, Muñoz, Berga et al. 2005, Ferri, Guerrini et al. 2007, Qureshi, Chatwin et al. 2010).

The implementation of the current source in EIT systems at high frequency is well known. The associated effective output capacitance of the current source and parasitic capacitances of multiplexers and coaxial cables in the total system makes it impractical to produce an EIT system operating at high frequency in terms of its bandwidth. The advent of the GIC in parallel with the current source has provided a way to reduce the stray capacitance effect at high frequency (Oh, Lee et al. 2007, Holder 2005). It creates an RLC circuit with an LC resonant condition for high-frequency application of EIT systems. The LC resonance occurs when both inductive and total capacitive reactants are equal in value at a particular frequency. An ideal GIC would be used to cancel the effects of both stray and output capacitances of the current source through a compensating inductance realized by the GIC component.

Type A: Current source performance with GIC based on operational voltage amplifier and passive components

An inductance synthesized by using a GIC structure in parallel with the current source (Qureshi, Chatwin et al. 2010, Wang, Brien et al. 2007a) is improved by incorporating the tuning system; this maximizes output impedance and eliminates the

stray capacitance. The proposed GIC utilized in ACT4 and KHU Mark1 EIT systems used five passive elements and two op amps to provide a grounded inductance circuit (Ross, Saulnier et al. 2003b, Oh, Lee et al. 2007). Figure 13 shows the GIC in its original format combined with an improved Howland current source.

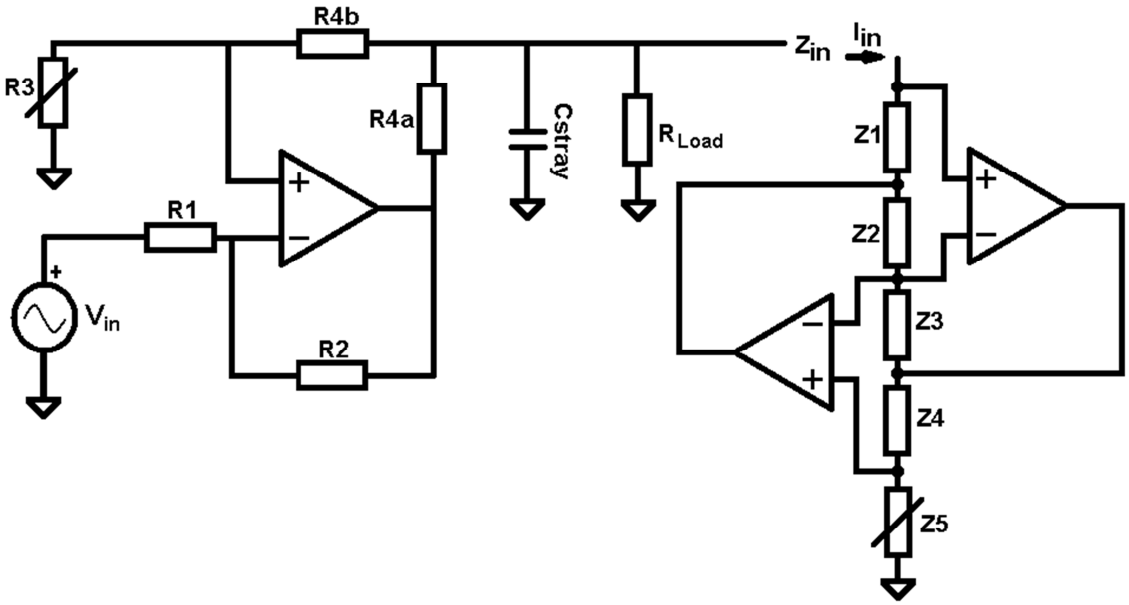

Figure 13 An improved Howland current source combined with GIC structure based on two op amps and five passive elements (Antoniou 1969, Wang, Brien et al. 2007a, Ross, Saulnier et al. 2003b, Oh, Lee et al. 2007, Qureshi, Chatwin et al. 2010)

The GIC is fed with input impedance Z_{IN}, which supplies an input current I_{IN}. The input impedance, admitting an ideal op amp, is given by:

$$Z_{in} = \frac{V}{I} = \frac{Z_1 Z_3 Z_5}{Z_2 Z_4} = j\omega \frac{R_1 R_3 C_4 R_5}{R_2} = sL \qquad 8$$

where $Z_1=R_1$, $Z_2=R_2$, $Z_3=R_3$, $Z_4=\frac{1}{j\omega C_4}$ and $Z_5=R_5$

This suggests that in an ideal stage, the imaginary part of the parallel impedance combination is set to zero at the LC resonant frequency ω; thus, the tuning circuit resonant frequency is given by:

$$f = \frac{1}{2\pi\sqrt{LC}} \quad 9$$

An ideal GIC would be used to cancel the effects of both stray and output capacitances of the current source through a compensating inductance realised by the GIC component. On the other hand, in practice, non-idealities of the GIC caused by op amps with passive components also produce a negative grounded resistance ($-R_G$) in parallel with the entire current source output resistance, as shown in Figure 14. It appears that a pure inductance without a negative resistance ($-R_G$) condition is impossible. Therefore, a negative resistance is generated in parallel with the output resistance, which is a problem for the equivalent output resistance of the EIT current source.

It is necessary for the output resistance and the negative resistance to being balanced in the current source to obtain the maximum output impedance (Holder 2005).

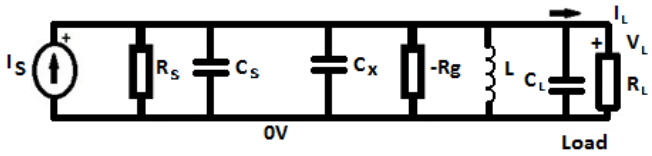

Figure 14 the equivalent current source circuit with stray capacitance and GIC behaviours

The disadvantage of an inductance with a negative resistance in this form of GIC results in an unpredictable variation. This interferes with the output impedance of the circuit (Holder 2005, Oh, Lee et al. 2007). A maximum stable frequency bandwidth of about 500 kHz has been reported by McEwan, Ross and Oh et al. (Oh, Lee et al. 2007, McEwan, Cusick et al. 2007, Ross 2003a).

In practice, adjustment of the current source combined with GIC, is necessary to achieve maximum output resistance of the improved Howland current source by replacing a digital-potentiometer (digital-pot) for resistor R_3 in the improved Howland circuit (as indicated in Figure 13). Afterward, adjustment of the GIC is made for different frequencies by replacing resistors R_1, R_2, R_3 and R_5 with digital-pots in the GIC

and capacitances for Z_4=C_4 to obtain as high as possible an output impedance of entire current source topology and by minimizing output capacitance of the current source as well (McEwan, Cusick et al. 2007, Oh, Lee et al. 2007, Ross, Saulnier et al. 2003b). This method cancels the stray capacitance, therefore maximizing the output impedance of the system.

In order to improve the performance of current sources, Ross (Ross, Saulnier et al. 2003b) based his work on the theoretical phase, simulating the improved Howland current source and GIC structure to produce a variable grounded inductor with the ability to adjust within the frequency range from 100Hz to 1MHz and achieve an output impedance in excess of 2GΩ within the desired frequency range. This means the GIC structure would need to be tuneable as much as possible to obtain this high output impedance, effectively producing a variable grounded inductor cancelling the stray capacitances, although this has not been implemented above a 100kHz frequency. Also, using a digital-pot naturally produced parallel grounded capacitors in high and low pins and a wiper with a variable resistor directly reduces the entire current source output impedance.

The research by Oh et al. (Oh, Lee et al. 2007) has embedded six GIC structures, identical to those in the last reference, assigned to different frequency ranges in order to achieve the same effect at six different frequencies by switching between the different GICs and balancing the equivalent output resistor. However, the implemented results show it is extremely difficult to achieve an output impedance exceeding 1MΩ at frequencies above 100 kHz. This system generally operates satisfactorily within the frequency range of 10 Hz to 500 kHz which is less than <1 MΩ output impedance. This design, used as part of its calibration system, two digital-pots (as shown in Figure 13); one is utilized in place of R_3, which is located in the improved Howland current source to trim out the resistor tolerances in the improved Howland source and the other is employed in GIC (Z_5) to trim out the resistor tolerances in the GIC, it is adjustable over the frequency range (adjustable in minimum steps of ΔR=40Ω and 8Ω) to achieve maximum output impedance, generally improving system performance.

The advantages of using six GICs, as reported by Lee Oh (Oh, Lee et al. 2007), must be set against the high component count, instability with composite waveforms as well as the complex circuitry caused by op amps, passive components and capacitance effects. In a practical implementation, it may be necessary to use more than six GICs, each tuned to a very narrow frequency range. This may prove impractical when faced with a large stray capacitance. In order to avoid instability of the current source system, it is necessary to reduce the resistor tolerance of the current source by replacing low tolerance resistors (e.g. 0.01% tolerance) and redesign the circuit board to reduce its stray capacitance or develop a better method of cancelling this capacitance. On the other hand, to use this method for frequencies above 500 kHz it is required to assume that an op amp can provide a maximum output impedance for the source with infinite bandwidth, this is not feasible in practice.

To the best of the authors' knowledge, there has not been any practical system using inductance to cancel the effect of capacitances of the current source above the 500 kHz range with acceptable output impedance for the EIT systems. The objective is to optimise the current source by maximizing output resistance R_O and minimizing output capacitance C_O. However, the output resistance of current source R_O resulting from both negative resistance $-R_G$ (produced by the GIC) and output resistance of current source R_S may be unmanageable by using a GIC based on an operational voltage amplifier and passive components.

Type B: Current source performance with GIC based on active components

There are active network synthesisers in the practical design (e.g. current integrator, current differentiator, voltage amplifier, voltage-to-current converter, current amplifier, frequency dependent negative resistance, and grounded/floating inductors) employing various active devices (e.g. CCII) and passive elements in their functions (or applications) (Sedra, Smith 1970, Higashimura 1987, Khan, Zaidi 2003, Maundy, Gift et al. 2007, De Marcellis, Ferri 2011). The CCII in the GIC form is used to provide an inductance without any matching constraint, using minimum grounded

passive components; this cannot be implemented with general GICs using two voltage op amps and five passive components (Biolek 1995, Shaktour, Biolek 2008).

We aim to present a new GIC technique for cancellation of the parasitic elements in EIT current sources operating in the frequency range from 10 kHz to few a megahertz.

GICs based on CCII, consist of negative active circuit elements, whereas general GICs consist of negative passive impedance transformations based on op amps and some passive elements from which it is impossible to obtain a high output impedance at high frequency range (Biolek 1995, Shaktour, Biolek 2008). The CCIIs are used for the GIC due to their attractive inductive behaviour, which is dependent on the impedance structure of the output current of the CCII for capacitance compensation (Khan, Zaidi 2003, Khan, Bimal et al. 2002).

i. The proposed circuit topology

The stray capacitances should be removed from a current source; otherwise the effect of it can be cancelled with an inductor producer based upon a GIC. The proposed combination of current conveyors as a GIC circuit is shown in Figure 15 (Khan, Zaidi 2003, Maundy, Gift et al. 2007, Gift 2004, Abuelma'Atti 2000, Abuelma'atti, Tasadduq 1999, Prakobnoppakao, Chipipop et al. 2002).

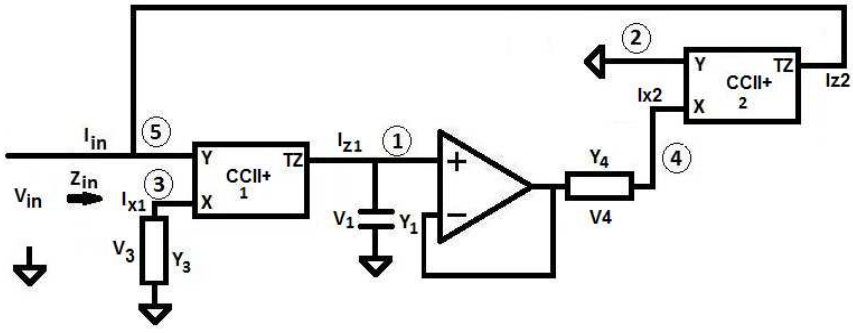

Figure 15 A schematic of the proposed grounded inductor using two stages of CCIIs

The corresponding Signal Flow Graph (SFG) of two operational conveyors with three passive components, creating a GIC based on CCII is shown in Figure 16.

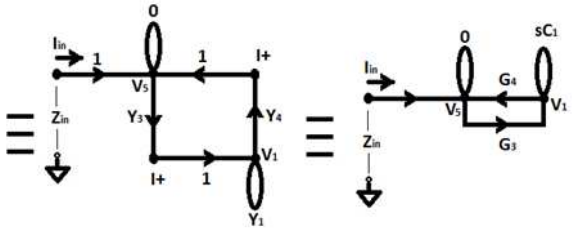

(a) (b)

Figure 16 (a) Shows a Signal Flow Graph (SFG) and (b).shows its simplified SFG (Biolek 1995)

In regard to the behaviour of the total circuit above, we need to find what current is taken from the input if a certain voltage is applied to the input and thus what is the impedance of the input.

1) In the first stage if a voltage (V_{IN}) is applied to the terminal non-inverting input Y (node 5), an equal potential (voltage) will appear at the input terminal inverting input X (node 3) i.e. $V_{IN}=V_3$. Thus the current, I_{X1}, through the admittance Y_3 is determined by the voltage V_3 across it and as this equals V_{IN} thus $I_{X1}=V_{IN}\times Y_3$. (The components used to implement the first stage CCII+ have high input impedance at the Y input; thus, the input current of the first CCII is approximately equal to zero , $I_{Y5}=0$). The current at node I_{X3} (node 3) will be mirrored to output terminal TZ (node 1) thus $I_{Z1}=I_{X1}$ and $I_{Z1}= V_{IN}\times Y_3$. If output terminal TZ drives the admittance Y_1 then the voltage V_1 across Y_1 is $V_1=\frac{I_{Z1}}{Y_1}=\frac{V_{IN}\times Y_3}{Y_1}$.
2) The next stage is a voltage amplifier with unity gains thus its output voltage $V_4=V_1=\frac{I_{Z1}}{Y_1}=\frac{V_{IN}\times Y_3}{Y_1}$.
3) In the last CCII+ stage any current into the input terminal X is negatively mirrored at the output of the stage. If a voltage is applied to terminal non-inverting input Y (node 2), an equal potential (voltage) will appear at the input terminal inverting input X (node 4). Thus the voltage across Y_4 is $V_4=V_1$. Therefore if V_{Y2} is connected to 0V then 0V appears at node 4 ($V_{X2}=0$) and the current I_{X2} through Y_4 is

$I_{X2}=-V_4\times Y_4=-V_1\times Y_4=-\frac{V_{IN}\times Y_3}{Y_1}\times Y_4$. Thus the current $I_{Z2}=I_{X2}=-V_4\times Y_4=-\frac{V_{IN}\times Y_3\times Y_4}{Y_1}$.

This output is connected to the input, so this is our required value. Therefore we can write if V_{IN} is applied to the input the sink current is: $I_{IN}=-I_{X2}=-I_{Z2}=\frac{V_{IN}\times Y_3\times Y_4}{Y_1}$ (the output of the OCCII-2 is connected to the non-inverting input of the OCCII-1).

This means the impedance Z_{IN} shown at the input is:

$$Z_{IN}=\frac{V_{IN}}{I_{IN}}=\frac{V_{IN}}{-I_{Z2}}=\frac{V_{IN}}{\frac{V_{IN}\times Y_3\times Y_4}{Y_1}}=\frac{Y_1}{Y_3\times Y_4} \quad 10$$

In order to make this circuit acts as an inductor we have replaced the passive admittances with resistances (R_3 and R_4) and capacitor, C_1, as follows:

$$Y_3=G_3=\frac{1}{R_3}, Y_1=sC_1 \text{and } Y_4=G_4=\frac{1}{R_4} \quad 11$$

Then the input impedance, using s=jω (i.e. ω= 2π x frequency) becomes

$$Z_{IN}=sC_1\times R_3\times R_4 \quad 12$$

Therefore, the input impedance acts as an inductor, Z_{IN}= sL, thus Z_{IN} acts like an inductor where $sL=sC_1\times R_3\times R_4$.

After simplifying the SFG as indicated in Figure 16 (b), the equation for input impedance is obtained; if we consider Y_3 and Y_4 as conductance and Y_1 as a capacitance, therefore the impedance functions for the non-ideal cases of the grounded inductor circuit are based on 12 and the tracking errors are given by:

$$Z_{in}=\frac{V_{in}}{I_{in}}=\frac{Y_1}{(\alpha_1\alpha_2\beta_1\beta_2)Y_3Y_4}=\frac{sC_1R_3R_4}{\alpha_1\alpha_2\beta_1\beta_2}=sL_{eq} \quad 13$$

where α_1, α_2 and β_1, β_2 are the current and voltage tracking errors of CCII-1 and CCII-2, respectively.

ii. Operational Conveyor

The combination of an op amp with the CCII produces the OCCII. The OCCII increases the accuracy compared to a CCII. The additional op amp is connected in a negative feedback loop in the CCII to form the OCCII circuit; this reduces the transfer function error in conveying the current.

The circuit symbol as demonstrated in the Figure 17 shows the combination of the op amp and CCII+ producing the OCCII (Gift 2004). This new arrangement offers significant improvement in the accuracy of the CCII. In the circuit used, both of the inputs of the CCII will be located within the negative feedback of the op amp, this design will be beneficial in reducing the effect of the input inverting resistance of R_X (X is a low impedance input). This composition of an op amp and CCII will enhance the circuit performance addressing the transfer function error.

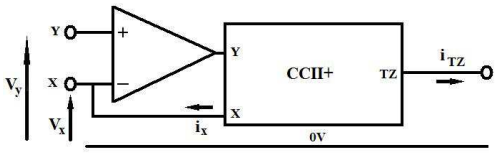

Figure 17 schematic of an operational conveyor (OCCII+) model (Black-box) that is a combination of an op amp and a CCII

iii. Multi-frequency current source with OCCII-GIC

A multi-frequency current source using the stray capacitance cancellation method is developed by utilizing digital-pots to operate as variable resistors to produce the variable inductor corresponding to a different frequency point. The GIC based on OCCII, here is called OCCII-GIC structure. The circuit topology was chosen to be a method to cancel the stray capacitance in the multi-frequency system; Figure 18 shows the schematic of a grounded inductor based on the OCCII, where the conductance Y_3 and Y_4 are variable resistors.

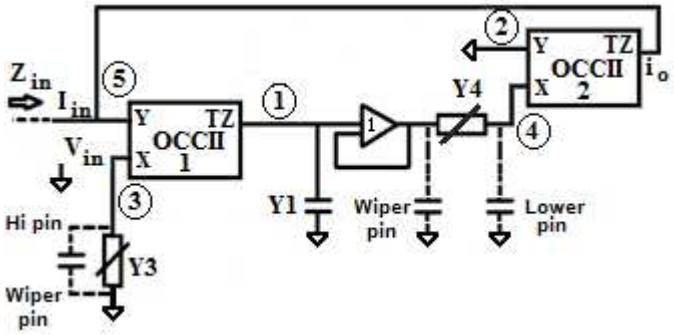

Figure 18 An improved schematic of an OCCII-GIC as a grounded inductor

There are limitations to produce a pure inductance in the multi-frequency system because of using digital-pots; each digital-pot (resistor replacement) naturally comes with grounded capacitance at both ends and parallel capacitance at the wiper.

When using digital-pots in place of Y_3 and Y_4, the capacitances of the terminals of the digital-pots need to be taken into consideration. Typical values of a digital potentiometer are 10pF at the outer terminals and 25pF at the wiper terminal. The circuit above uses variable resistors (potentiometers), so we use only the wiper terminal and one outer terminal. Ideally the wiper terminal having more capacitance is connected so that it is a capacitance that has more effect. For Y_3 this is obviously with the lower terminal connected to the node 3 (X terminal) and wiper terminal is grounded. Y_4 should have its lower terminal connected to the node 4 as this is a node that is not moving in voltage. This leaves the wiper terminal of Y_4 connected to the follower amplifier 1 output. This results in an oscillation problem as 25pF will then be directly connected to the output. If so a small resistor, 5 to 10 Ohms needs to be put in series so that the amplifier does not drive the 25pF directly.

The following equations are computed to consider the action of the OCCII-GIC circuit caused by the digital-pots, as the digital-pot swings from 1 to the full-scale value to operate in multi-frequency systems, as shown in Figure 19.

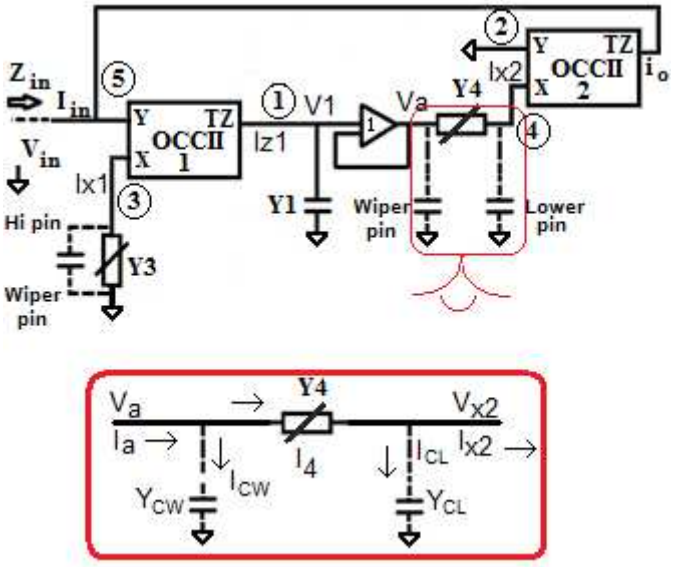

Figure 19 An improved schematic of an OCCII-GIC as a grounded inductor when it shows a network of Y_4

Thus, $I_a=I_4+I_{CW}$ and $I_4=I_{CL}+I_{X2}$ or $(I_{X2}=I_4-I_{CL})$, so, we can write:

$$I_a = (V_a - V_{X2}) \times Y_4 + V_a \times Y_{CW} \quad (14)$$

$$I_{X2} = (V_{X2} - V_a) \times Y_4 - Y_{CL} \times V_{X2} \quad (15)$$

The input voltage at the node (a) is equal to V_1 (i.e. $V_a=V_1$) so, we can also write:

$$I_4 = V_1 \times (Y_4 + Y_{CW}) - V_{X2} \times Y_4 \quad (16)$$

$$-I_{X2} = V_1 \times Y_4 - V_{X2} \times (Y_4 - Y_{CL}) \quad (17)$$

and, using these equations we can compute:

$$\begin{bmatrix} I_4 \\ -I_{X2} \end{bmatrix} = \begin{bmatrix} Y_4 + Y_{CW} & -Y_4 \\ Y_4 & -Y_4 + Y_{CL} \end{bmatrix} \cdot \begin{bmatrix} V_1 \\ V_{X2} \end{bmatrix} \quad (18)$$

The current at the inverting node of second OCCII is equal to:

$$I_{X2} = I_{Z2} = -I_{IN} \quad (19)$$

The input voltage at the node V_3 is measured by:

$$V_1 = \frac{I_{z1}}{Y_1} = \frac{V_3 \times Y_3}{Y_1} \Rightarrow V_3 = \frac{V_1 \times Y_1}{Y_3} \quad (20)$$

Therefore, the value of Y_{IN} will be calculated as follows, then rearranging by 20, we find:

$$Y_{IN} = \frac{I_{IN}}{V_{IN}} = \frac{-I_{Z2}}{V_3} = \frac{V_1 \cdot Y_4 - V_{X2} \cdot Y_4 + V_{X2} \cdot Y_{CL}}{V_3} = \frac{\frac{V_3 \cdot Y_3}{Y_1} \cdot Y_4}{V_3} - \frac{V_{X2} \cdot Y_4}{V_3} + \frac{V_{X2} \cdot Y_{CL}}{V_3} \quad (21)$$

Rearranging, we find that:

$$= \frac{Y_3 \times Y_4}{Y_1} - \frac{V_{X2} Y_4}{\frac{V_1 \times Y_1}{Y_3}} + \frac{V_{X2} Y_{CL}}{\frac{V_1 \times Y_1}{Y_3}}$$
$$= \frac{Y_3 \times Y_4}{Y_1} - \frac{V_{X2} \times Y_4 \times Y_3}{V_1 \times Y_1} + \frac{V_{X2} \times Y_{CL} \times Y_3}{V_1 \times Y_1} \quad (22)$$
$$= \frac{Y_3 \times Y_4}{Y_1}(1 - \frac{V_{X2}}{V_1}) + \frac{V_{X2} \times Y_{CL} \times Y_3}{V_1 \times Y_1}$$

The admittance of Y_{CL} and Y_1 and Y_3 and Y_4 is:

$$Y_{CL} = sC_{CL}, Y_1 = sC_1, Y_3 = G_3 + sC_3 \text{ or } Z_3 = \frac{R_3}{1 + sC_3R_3}, Y_4 = G_4 \quad (23)$$

So we compute:

$$Y_{IN} = \frac{Y_3 \times Y_4}{Y_1}(1 - \frac{V_{X2}}{V_1}) + \frac{V_{X2} \times Y_{CL} \times Y_3}{V_1 \times Y_1}$$
$$= \frac{(G_3 + sC_3) \times G_4}{sC_1}(1 - \frac{V_{X2}}{V_1}) + \frac{V_{X2}}{V_1} \times \frac{sC_{CL}}{sC_1} \times (G_3 + sC_3) \quad (24)$$
$$= \overbrace{\frac{G_3 \times G_4}{sC_1}}^{L_{eq}}(1 - \frac{V_{X2}}{V_1}) + \overbrace{\frac{C_3}{C_1}(1 - \frac{V_{X2}}{V_1}) \times G_4 + \frac{V_{X2}}{V_1} \times \frac{C_{CL}}{C_1} \times G_3}^{G} + \overbrace{\frac{V_{X2}}{V_1} \times \frac{C_{CL}}{C_1} sC_3}^{C}$$

Since node 2 is grounded, ideally the V_{Y2} is equal to 0, then V_{X2} is also equal to zero, so we can calculated Y_{IN} as follows:

$$Y_{IN} = \overbrace{\frac{G_3 \times G_4}{sC_1}}^{L_{eq}}\left(1-\overbrace{\frac{V_{X2}}{V_1}}^{0}\right)+\overbrace{\frac{C_3}{C_1}\left(1-\overbrace{\frac{V_{X2}}{V_1}}^{0}\right)\times G_4}^{G}+\overbrace{\overbrace{\frac{V_{X2}}{V_1}}^{0}\times\frac{C_{CL}}{C_1}\times G_3}^{0}\overbrace{\frac{V_{X2}}{V_1}}^{0}\times\frac{C_{CL}}{C_1}sC_3 \quad (25)$$

Although, in reality the buffer and OCCII has also R_{Buffer}, C_{Buffer}, C_{TZ}, C_Y, R_{TZ}, R_X, R_Y and R_{OUT} based on the following figures.

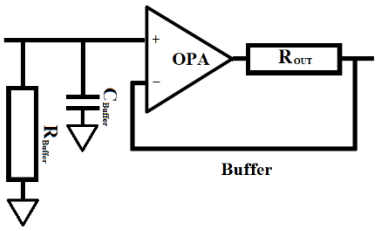

Figure 20 parasitic impedances involving with the buffer op amp

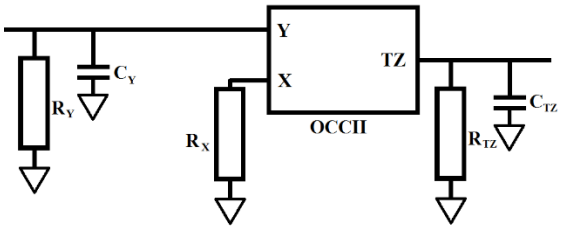

Figure 21 parasitic impedances involving with the current conveyor

Therefore, based on the Figure 20 and Figure 21, it produces a new schematic and the new equivalent admittance of Y_1, Y_3 and Y_4:

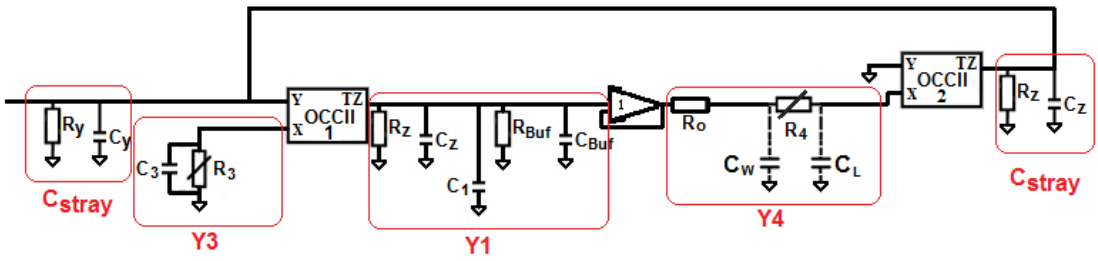

Figure 22 real schematic of the capacitance cancellation circuit

The input resistance of the X node of CCII+ would be equal to 50Ω (Data Sheet-AD844S 2009) by using the extra op amp producing OCCII+ the R_X would be equal to zero. The C_{Z1} would be parallel with C_1 so the total admittance would be equal to $Y_1 = sC_1+sC_{Z1}+sC_{BUF}+G_{Z1}+G_{Buf}$, $Y_3 = sC_3+G_3$ and $Y_4 = Y_4+G_O$. Then the C_{Z2} (4.5pF) and C_{Y1} (2pF) would be in parallel with the stray capacitance of the whole current source

circuit, therefore it would be added to $C_{Y1}+C_{Z2}+C_{STRAY}$, and R_{Y1} || R_{Z2} || R_S as shown in Figure 22.

The RLC parallel circuit is implemented when an OCCII-GIC parallels with the output of a current source circuit.

In addition, it seems the C_3 (the grounded capacitance of the first digital-pot at the high pin) parallel with R_3 in Y_3 (as shown in Figure 22) results in a phase advance in the first stage (OCCII-1) and the C_{WIPER} and C_L(produced by the second digital-pot) makes a phase delay in the second stage (OCCII-2).

3.6. Current source design

i. Resistors

In the design of a current source with high output impedance, a higher priority is given to the balance between resistors to achieve full precision output. Resistors with a tolerance of 1% achieving an output impedance maximum of around 250kΩ at low frequency. Therefore, for the case of the EIT system, a high resistor matches (especially necessary in the improved Howland source) with precision tolerance of ±0.01%, TCR ±5ppm/˚C (Stackpole Electronics, Inc. Precision Thin Film Chip Resistor) (Data Sheet-Resistive Product 2015), is recommended to achieve maximum output impedance at high frequency.

ii. Operational amplifier

Since we need to get the maximum output impedance in a current source, the common-mode rejection ratio (CMRR) of the op amp needs to be optimised, e.g. an op amp with a CMRR of 60dB results in an output impedance of less than 1MΩ. In addition, the non-linearity of the CMRR curve in an op amp results in a disadvantage in that it will not produce a flat output impedance curve (non-linear result). In reality, the non-linearity of the amplifier CMRR is increased in bipolar and CMOS amplifiers

compared to FET amplifiers. Thus, we recommend amplifiers with a FET input instead of CMOS or bipolar input.

In the case of the current source, we selected OPA656 (Texas Instruments) (Data Sheet-OPA656 2008), which is built with a JFET input stage to offer an ultra-high dynamic range amplifier with high precision performance. Typical characteristics show that the OPA656 has a high input impedance and low bias current provided to support the ultra-low 7nV/Hz input voltage noise to achieve a very low integrated noise over a wide bandwidth of 500MHz. OPA656 has a high input impedance of $10^{12}||2.8pF$ in common-mode and in differential-mode $10^{12}||0.7pF$. It has excellent THD distortion performance of -80dBc at 10MHz with excellent differential-gain and differential-phase of 0.02% and 0.05°, respectively (Data Sheet-OPA656 2008). The OPA656 is the best op amp that we could find in the market for our application in regard to its typical characteristics (Data Sheet-OPA656 2008, DATA SHEET-OPA657 2008b).

iii. Current conveyor module

We selected an AD844S (ANALOG DEVICES' module) for current feedback with a high-speed monolithic op amp (a Transimpedance op amp). The AD844S combines wide bandwidth and very fast large signal response with a settling time of 100ns to 0.1% and essentially independent gain. The AD844S combines low distortion, low noise and low drift. It shows excellent differential gain and differential phase of 0.03% and 0.15° with an input capacitance of 2pF and input resistor for inverting input equal to 50Ω and non-inverting input of 10MΩ; all typical characteristics make it suitable as a current conveyor module with high bandwidths (Data Sheet-AD844S 2009).

Based on the functional behaviour of the current conveyors, the voltage input of the Y node will be followed by the X node (voltage output node) with a low offset voltage, since this device is built by laser trimming where the offset voltage is reduced (only a few tens of microvolts). The ideal current conveyor should have a zero input resistance, although in reality the input resistance is around 50Ω. Thus, the current that is applied to the inverting input would be delivered to a complementary pair of

unity gain current mirrors, which deliver the same current to the output node (an internal node of outputs pin5, TZ output); in realty $I_{TZ}=\alpha. I_X$ when the full output voltage is generated (Data Sheet-AD844S 2009).

The real module also will buffer the unity gain complementary voltage that it uses to drive the low impedance loads with typical characteristics. This module can deliver up to ±50mA into a 50Ω load with low distortion with regard to voltage ripple. Figure 23 shows the internal structure and parameters of the current conveyor of AD844S (Bruun, Olesen 1992, Data Sheet-X9C102 1996).

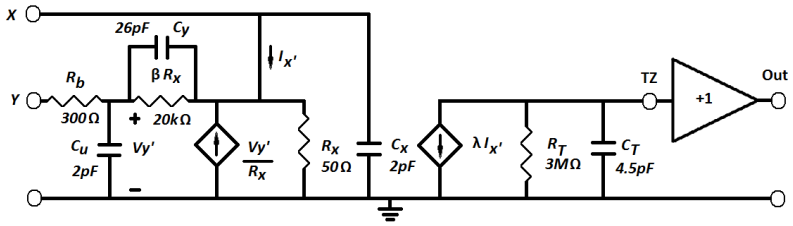

Figure 23 Internal structure of AD844, the equivalent schematic is showing that the input capacitances = 2pF, input inverting resistance (X)= 50Ω, non-inverting input resistance (Y) =10MΩ, Transcapacitance =4.5pF and Transresistance =3MΩ (Data Sheet-AD844S 2009, Bruun, Olesen 1992)

iv. Potentiometer network

The multi-frequency current source is delivered by using a digitally controlled potentiometer (DCP) XICOR of X9C102 that is employed in the OCCII-GIC circuit (Data Sheet-X9C102 1996). The multi-frequency current source will be obtained via control lines of the DCP. The schematic circuit of the DCP of XICOR of X9C102 is depicted in Figure 24(a) with 10pF at both ends and 25pF at the wiper (Data Sheet-X9C102 1996).

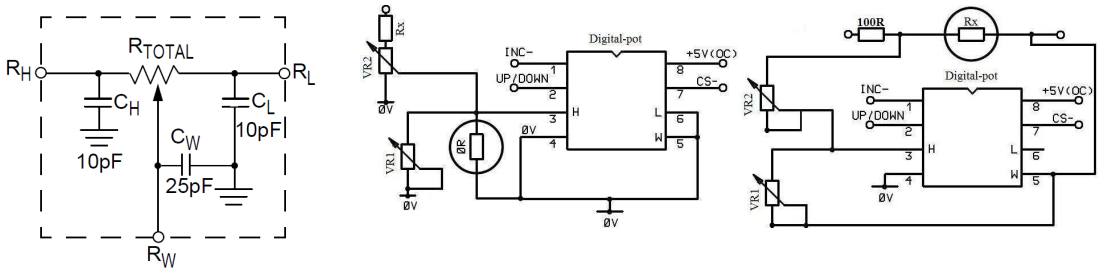

Figure 24 the left diagram (a) shows the DCP schematic circuit (Data Sheet-X9C102 1996) and

the center diagram (b) shows the Trim-pot and digital-pot network as an equivalent circuit for a grounded resistor and the right diagram (c) shows the floating resistor

The DCP includes 99 resistive elements that can be changed in 100 steps (for example 1kΩ/99=10.1010Ω in each step) where it is in parallel/series with trim pots of 1kΩ resistors; so the variable resistor can be changed by ΔR=0.9 Ω. We selected trim pots of BOURNS 3269W-102 with 12 turns with a rotational time of 200 cycles (Data Sheet-3269W 2011). Figure 24(b) shows an equivalent grounded resistor network. An equivalent resistor network for a grounded resistor is utilized when three parallel variable resistors consist of two trim-pots (VR_1 and VR_2) and a digital-pot. A 0R is used when the digital-pot needs to be bypassed. In the case of a floating resistor (Figure 24c), the equivalent variable resistor is created by a combination of a digital-pots paralleled with a trim-pot in series with another trim-pot (Data Sheet-X9C102 1996).

v. Circuit board

In this research, we have studied the OCCII-GIC as a means of capacitance cancellation combined with two types of current sources: (i) the improved Howland current source that is voltage sensing based and (ii) the current conveyor current source that is current sensing based. The combination of current sources with OCCII-GIC is a feasible way to build a suitable multi-frequency current source working at frequencies up to 3MHz for EIT application. We have built a single EIT circuit board with 6 layers with a finished board thickness of 1.76mm consisting of the improved Howland current source and the current conveyor combined with the OCCII-GICs. Figure 25 shows the bottom and top sides of the circuit board. The EIT board consists of an MCU (Data Sheet-PIC18F87K90 2010) for switching control and a DAS shared between 85 electrodes.

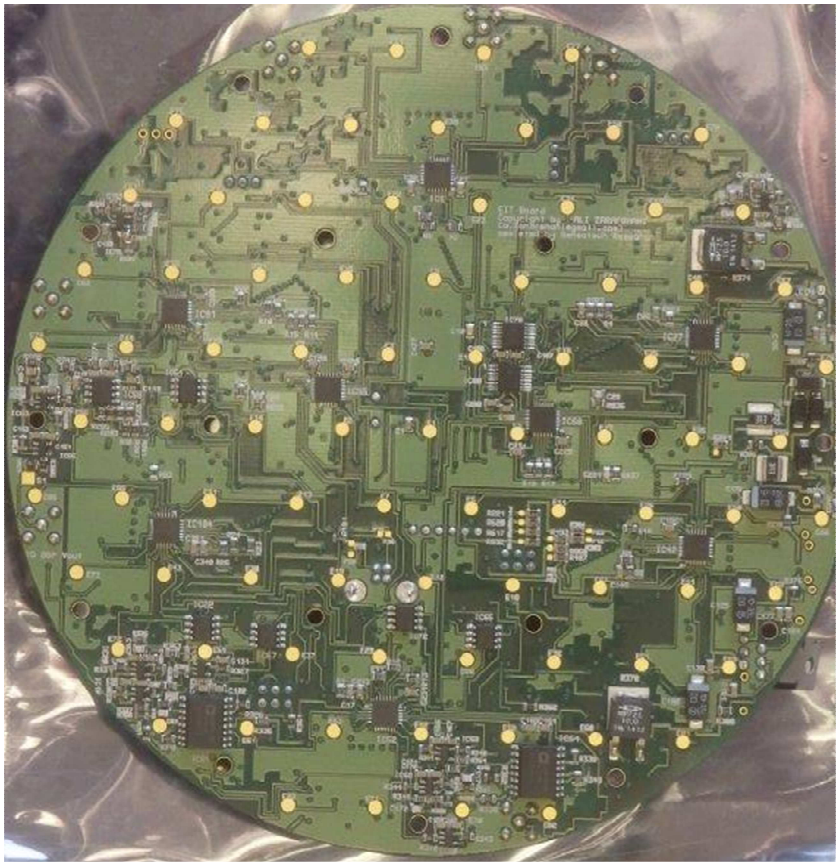

(a)

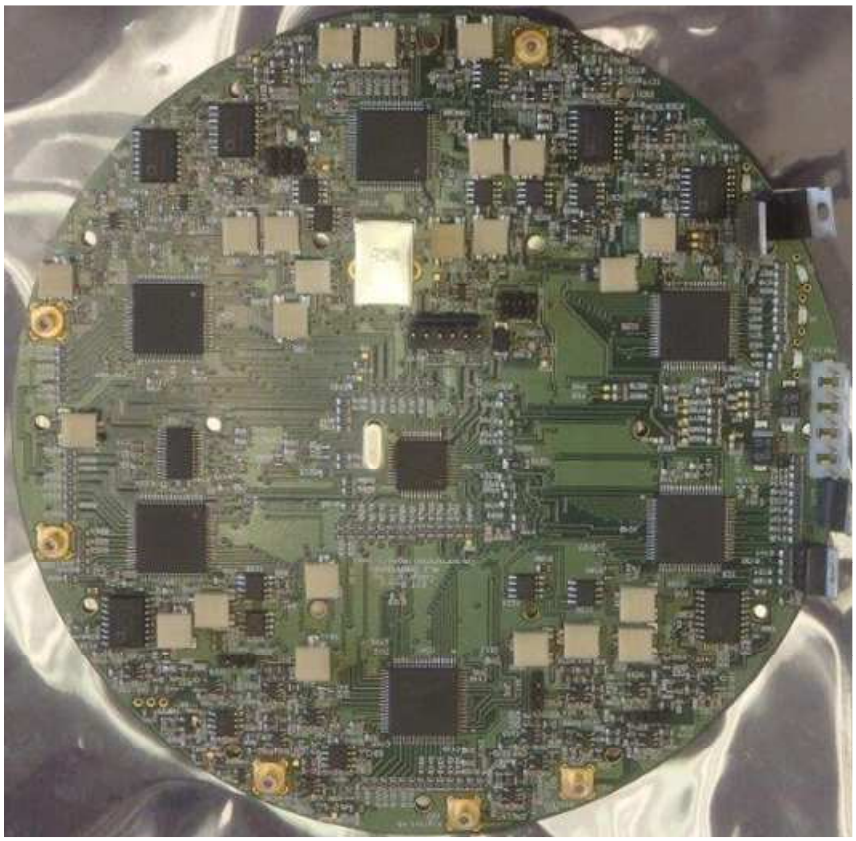

(b)

Figure 25 the AZ1 EIT circuit board includes the improved Howland and current conveyor current sources combined with OCCII-GIC, (a) the top and (b) bottom figures show the bottom and the top sides of AZ1 EIT board consisting of a planar 85-electrode plate and its drive and receive multiplexers

Chapter 4 Investigating and designing of software and hardware for the AZ1 EIT system

4.1. System overview

Generally, biomedical imaging technologies are implemented in hardware and software subsystems that are usually developed together. Software based components are implemented via several functional blocks. Access to hardware is based on the availability of control software functional blocks. Employing programmable logic to implement and control the hardware will be described in this chapter delivering low cost, control flexibility, high precision and high-speed as their advantage. Using programmable logic for the EIT application for control, signal generation, address control, communication via high-speed data convertors (such as digital to analogue convertor (DAC) and analogue to digital convertor (ADC)) is developed. Despite the EIT application approach (i.e. repeated measurements), the major issues are the restriction of the availability of supporting tools and complex algorithms as they are not able to generate fast and unique net-lists through hardware description language structures in a simple manner. However, the numerous benefits presented by modifiable hardware control are effective excitation of the target. The EIT application employs embedded systems having software modules as the main processing elements. This chapter investigates strategies and methodologies for the design and implementation of the EIT subsystem control based on a Microcontroller unit (MCU) for control and calibration of the hardware. It also provides a direction for

future work to investigate the feasibility of using an FPGA to improve the performance abilities of the EIT system signal generation and demodulation.

4.2. Microcontroller Unit (MCU)

The specification and architecture of an MCU driven EIT system is introduced in this section. The MCU is used to control the EIT system as follows:

1. The EIT switching logic system at the highest possible speed to minimize acquisition time
2. Control and switch between EIT sources used to switch between different input signal sources at different frequencies
3. Control and variable EIT measurement system gain
4. Calibration and evaluation of the EIT system

4.3. MCU design

The framework of the control system of the AZ1 EIT includes address control, which is required to select the different input signal sources, select the different DCPs and control the different DCP steps and increment values for the purpose of implementing the multi-frequency system to improve measurement accuracy. The selective electrode combinations based on the current injection input channels and the measurement output channels are controlled by a program addressing control unit communication with multiplexers. The PIC18 (Programmable Interface Controller), a family of 65K90 manufactured by (Microchip Technology Inc.) is used to carry out EIT control tasks. Table 5 shows the highlights of the microcontroller functionality that are selected. The PIC18F65K90 has 53 inputs/outputs signals that are used as an addressing control unit in the AZ1 EIT system.

The PIC sends and receives the data via the receive (RX) and transfer (TX) lines when connecting the PIC to the computer by a USB port through a serial UART. We selected an FT232RL (Future Technology Devices International-FTDI chip) as a USB to serial UART interface of the RS485 that is utilized to transfer the data from/to the PIC to the interface software (Data Sheet-FT232R 2010). Thus, the platform software is

directly connected to the interface connection of the MCU for monitoring and transferring the commands.

The compiler tools are based on the MPLAB C Compiler for the PIC18 MCUs (C18) for compiling/performing different control commands (Data Sheet-PIC18F87K90 2010).

TABLE 5 SPECIAL MICROCONTROLLER FEATURES

Device	Flash Program Memory (Bytes)	SRAM Data Memory (Bytes)	EEPROM (Bytes)	I/O	LCD Pixels	8/16-Bit Timers	CCP/ ECCP	SPI	I²C	EUSART	12-Bit A/D (Channels)	Comparators	CTMU	RTCC
PIC18F65K90	32K	2K	1K	53	132	4/4	5/3	Y	Y	2	16	3	Y	Y

4.4. Clock (CLK) System

The Clock (CLK) system of the MCU is based on an external 20MHz quartz crystal to provide a stable clock signal as illustrated in Figure 26. The circuit in Figure 26 is connected to the input and output pins of the MCU.

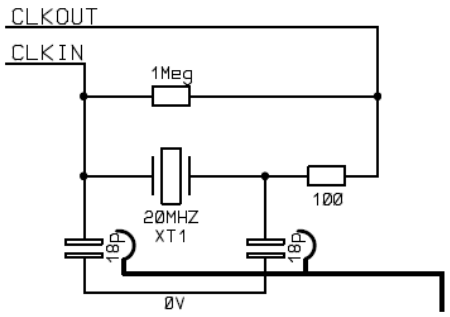

Figure 26 The external CLK system with a Quartz crystal of XT1=20MHz where the two capacitors (18pF) have to be adjusted to stabilise the frequency for transmit and receive

The common part of the hardware subsystem of the AZ1 EIT consists of investigation of channel-selecting MUXs, programmable gain of the voltage measurement structure, calibration of the measurement subsystem and power supply design as well as investigating the PCB design as we will describe in the following.

The AZ1 EIT structure is made up of the two different sources (an improved Howland current source within the OCCII-GIC circuit and a current conveyor current

source within the OCCII-GIC circuit) as well as a measuring subsystem consists of a programmable gain amplifier and a set of multiplexers as the DRV and the REC MUXs.

4.5. Addressing Control Unit

There are two arrangements of the source and the data acquisition topologies in the multi-channel EIT systems (I) multi-source and multi-channel signal measurement structure where a single source and a signal measurement structure are embedded by an individual electrode. (II) Single-source/ measurement or partially parallel (semi-parallel: a group of the paralleled single-source/measurement) is used to implement a multi-channel structure. A multiplexer structure is allocated to the single source and the single measurement to different electrodes; it provides the multiplexed structure for the multi-channel system.

The EIT system conducted over a channel connection that is generally subjected to environmental factors that can adversely impact measurements via parasitic capacitance.

Each arrangement has certain advantages and disadvantages. The primary disadvantage of the multiplexer-based approach is that there is on-resistor and grounded capacitance during on/off switches; therefore, the value of stray capacitance of the system is increased. The disadvantage of the multi-source is that it needs a complex calibration method to use in the individual sources and signal measurements requiring a validation process of differently affected data in regard to different characteristic errors in the modules to achieve an equal result with the same accuracy for all the channels. In regard to component count, the best way would be using a multiplexer-based system, but it requires a method to reduce the effect of the capacitance caused by the multiplexers. In the case of the AZ1 EIT system with a four-electrode structure, two input signal sources are utilized to connect to two electrodes, one with 0 degree phase shift and the other with 180 degrees phase difference. Therefore, it will provide a matrix of 2 to 85 analogue channel multiplexers that require low on and off capacitances.

Multiplexers generally consist of a number of analogue switch channels called switch arrays or switch matrix. Each analogue switch consists of on and off capacitors (C_{ON}, C_{OFF}), when the switch is opened the grounded off-capacitors will be involved in the input lines. When the switch becomes a closed channel the grounded on-capacitor and the on-resistor between these two on and off capacitances will be involved in the signal line of that channel as shown in Figure 27.

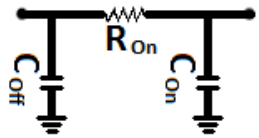

Figure 27 Multiplexer switch model

There are two current source lines which are 180 degrees out of phase to make a current mirror structure when it is fed to the 85 electrodes. Thus, the switching array is required to cover 2*85 channels. As mentioned in the literature review the Sussex Mk4 EIT system used a multiplexer structure with one stage DRV MUXs as 8 drive multiplexers are built in parallel and the off-capacitance of the 85 channels affects each single source signal as well as one stage of the REC MUXs, which consists of 8 receive multiplexers, which connect to a single measurement system.

To solve the issue of off-capacitance effects in DRV MUXs, we built the multiplexer structure of the AZ1 EIT using two-stages of the DRV MUXs where it has been broken into parallel elements of the input of the 8 DRV MUXs. This will be achieved by cascading the drive MUXs that share the different source topologies between different electrodes. The outcome of cascade multiplexer topology focuses on some modified key elements to improve system performance in regard to reduce the on/off capacitances of multiplexers that affect a single channel consequently achieving a low parasitic capacitance allowing an EIT system to operate over a wide high frequency bandwidth.

i. Drive Multiplexers (DRV MUXs)

The AZ1 EIT consists of an 85-electrode plate and different source topologies, so it needs to connect the different sources to the 85 electrodes individually. Thus, the

optimal solution would be to use a combination of series and parallel multiplexers to achieve the minimum stray capacitance effects.

As a first stage, we selected the ADG1211 (Analog Devices) of iCMOS Quad SPST switches and ADG2128 (Analog Devices) of CMOS 8 × 12 unbuffered analogue switch array which can be configured, through the I^2C-compatible interface as the second stage to build a cascade drive multiplexer (DRV MUXs) model (Data Sheet-ADG2128 2012b, Data Sheet-ADG1211 2012a). Figure 28 and Figure 29 shows the functional block diagram of two stages of multiplexers that we have chosen as the DRV MUX (Data Sheet-ADG1211 2012a, Data Sheet-ADG2128 2012b).

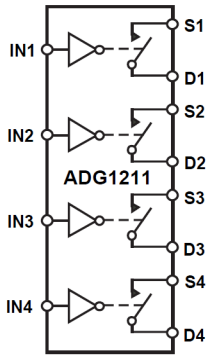

Figure 28 Function Block Diagram of the ADG1211

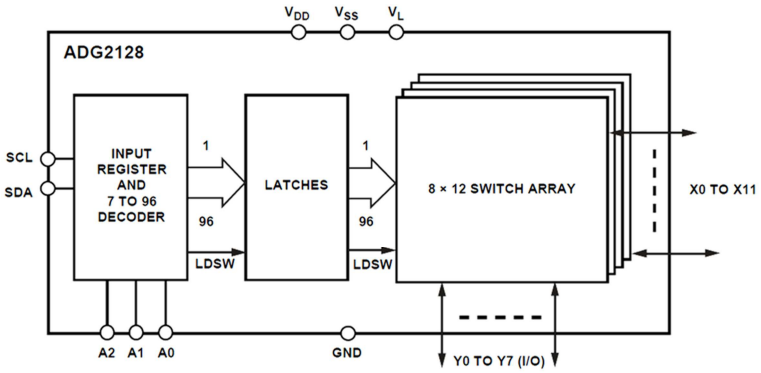

Figure 29 Function Block Diagram of the ADG2128

An ADG2128 has a switch array of 8 columns by 12 rows, for a total of 96 switch channels. The ADG2128 is fully flexible so that it connects any number of inputs to any output lines when it is addressed (Data Sheet-ADG2128 2012b). In the case of the 85-electrode plate, by utilizing an ADG2128, two input signals (source signals with 180 degrees phase difference) are connected individually to 12 different output lines (i.e. Electrodes). Thus, we employed eight modules to produce a maximum array of 8*12=96 output lines; therefore, we connected the 85 output lines (of the 96 output lines) to the 85-electrode plate and the rest of 96-85=11 output lines are used for calibration purposes. Therefore, each module of the ADG2128 uses one calibration line (the total of 8 modules of ADG2128 are used). So, it has reserved 8 output lines here and three output lines are connected to the measurement subsystem for its calibration process.

Figure 30 shows the switching schematic of one input to 12 outputs in an ADG2128 module. In this case, 12 output lines of the ADG2128 can be connected to an input (here it is connected to a source). We connected 11 electrodes to 11 output lines with one output line reserved for the calibration process. The address control of the ADG2128 is carried out via an I^2C interface. This component is operated from dual ±5V supplies. Regarding the data sheet, the ADG2128 has the dynamic characteristics of capacitance, when the switch is off and on; the capacitances are 6pF and 9.5pF respectively. Thus, the input capacitance of the switch is 6pF, which is connected to the input channel and the output capacitance of a switch equals 3.5pF (9.5pF-6pF) which is added when the switch is turned on.

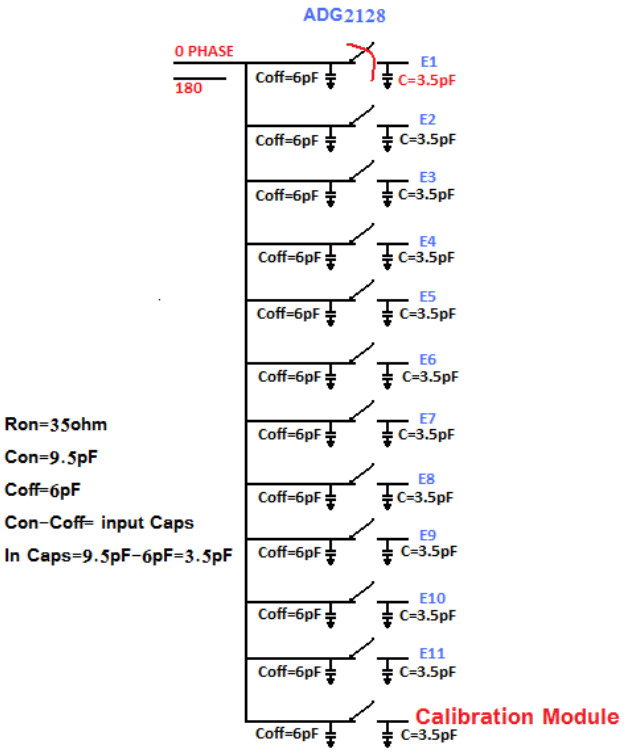

Figure 30 Switch Schematic of the ADG2128 with on/off switch capacitances

The 85-electrode plate needs to employ 8 components of the ADG2128 in parallel. Thus, a source line will be involved with the input capacitance of 6pF (C_{OFF}) * 8 (modules of ADG2128s) = 48pF plus 3.5pF (C_{ON}) =51. 5pF (C_{ON} where only one switch is turned on). That is the reason why some other research groups recommended using multi-sources so as to avoid these capacitance effects in the system.

Thus, we propose a cascade structural design in order to reduce the off/on capacitance at the output node by breaking the parallel structure. The architecture of this design is fully addressable with high-speed channel processing. Channel selection speed is similar to the parallel one stage multiplexer. We proposed to insert one stage of a 1*4-channel analogue multiplexer with a minimum on/off capacitance, and each fed to two ICs of ADG2128s. Figure 31 shows the cascading method that is proposed for DRV MUX topology to reduce the capacitance effect of ADG2128s. We recommend utilizing ADG1211, which exits 4 separate switches with on and off-capacitance of 2.6 and 0.9pF (type) respectively. That means each input source will have the effect of 0.9pF and when the input source is connected to the common input channel it will be 4*0.9pF=3.6pF plus 1.7pF when the switch is turned on (Data Sheet-ADG1211 2012a).

The cascading method will reduce the capacitance of the DRV MUX because we selected ADG1211 with the off-capacitance of 3.6pF plus 1.7pF when each channel is turned on for the first stage. Then, we selected ADG2128 with the off-capacitance of 6pF plus 3.5pF when each channel is turned on for the second stage. A total capacitance of 20.8pF in comparison to 51.5pF shows the cascade method would be a useful approach in EIT systems for multi-source and multi-channels based on the multiplexer structure. Moreover, multiplexers also produce an on-resistor between each of the input and output lines, as R_{ON} is equal to 120 Ω (type) in the case of the ADG1211 and R_{ON} is equal to 35 Ω (type) in the case of ADG2128. Thus, the effects of on-resistors need to be considered. The existence of on-resistors in the EIT system has a detrimental effect on the output voltage. Thus, it is required to apply calibration techniques to calculate these effects.

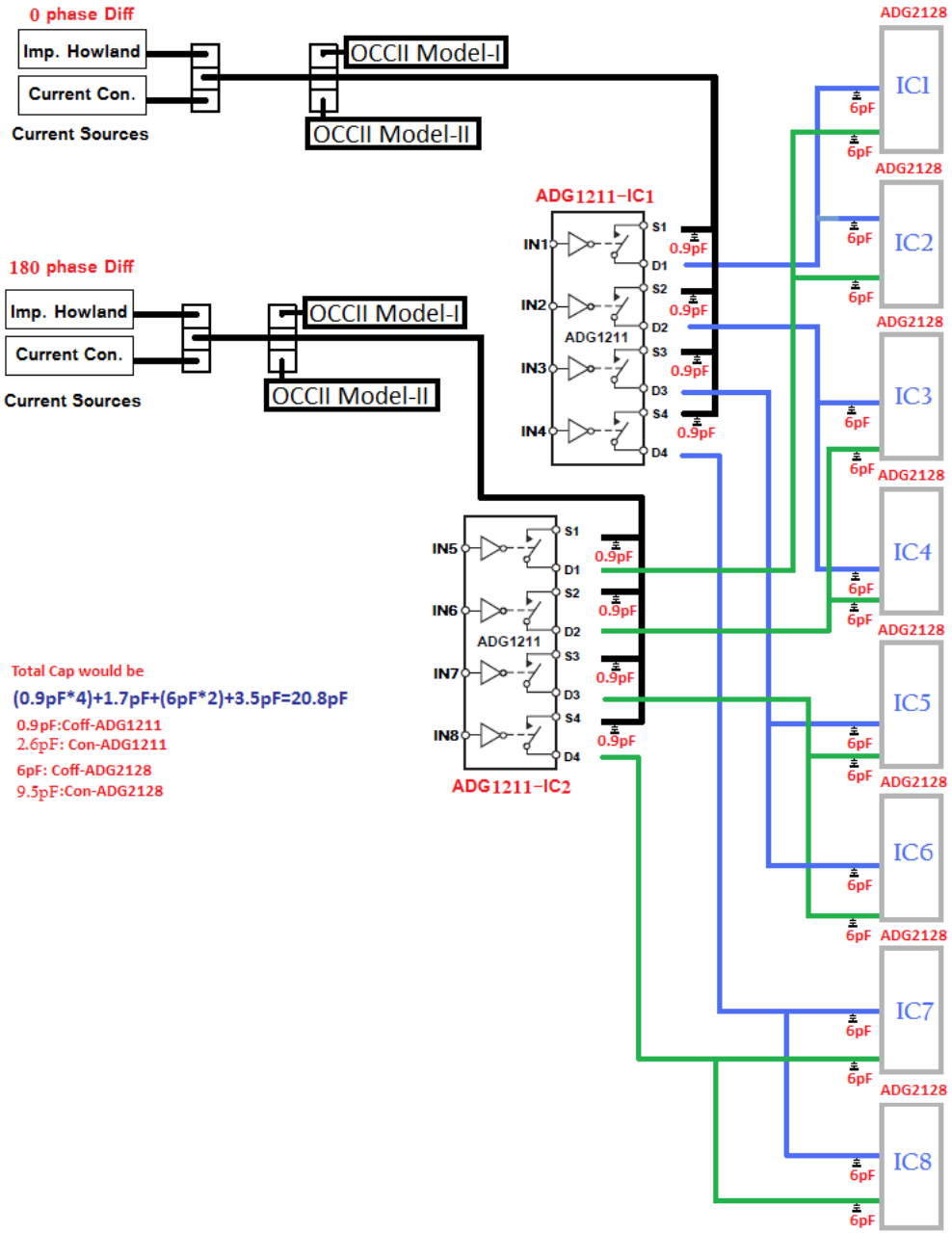

Figure 31 Cascading method for the drive multiplexer (DRV MUXs) with the switch on/off capacitances. It consists of 2-modules of the ADG1211s as the first stage and 8-modules of the ADG2128s as the second stage.

ii. Receive Multiplexers (REC MUXs)

We choose ADV3205 (Analog Devices) for the receiving multiplexers (REC MUXs) that connect the electrodes to a single-ended differential amplifier to measure the output voltage. Figure 32 shows the functional block diagram of the REC MUX which is based on an analogue cross-point switch 16*16; high-speed no blocking switch array, with parallel programming of the switch array within the buffer inputs

and output amplifiers. It offers a -3dB signal bandwidth of 60MHz and channel switch times of less than < 60ns with 0.1% settling (Data Sheet-ADV3205 2011).

By using this module as a REC MUX, it is permitted to connect multiple output channels to a single-ended differential device without loading the output bus by disabling other module outputs. We have also used a reset pin to disable all the outputs to measure the CMRR ratio of the differential amplifier of the measurement subsystem as part of calibration scheme. There is an extra shielding surrounding all inputs and outputs, with a differential gain of 0.1% and differential phase of 0.1 degrees that only with 0.1dB flatness out at 10MHz. The channel switching control consists of a parallel control, which allows updating a single output without reprogramming the entire module (Data Sheet-ADV3205 2011).

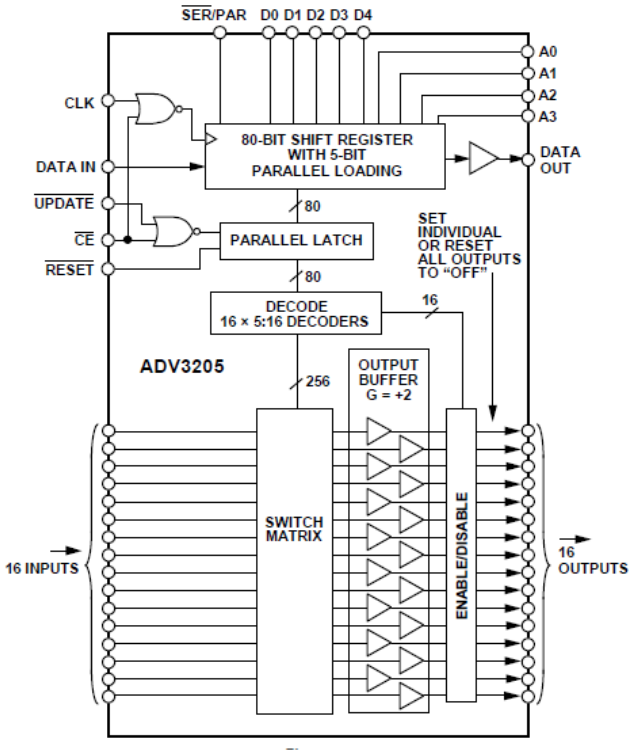

Figure 32 Block diagram of the ADV3205

An ADV3205 has an input capacitance of the switch equal to 4pF. This will be involved in each channel it is quite low and an excellent value to be used in EIT systems for the voltage measurements comparing to other modules that deal with stray capacitance. The input resistance of any channel that is connected to the output is equal to 50 MΩ.

4.6. Measurement subsystem and programmable gain amplifier (PGA)

A differential receiver amplifier is used to physically form a high-speed, high accuracy variable gain instrument amplifier. A differential to signal-ended amplifier AD8130 (Analog Devices) with very high CMRR at high frequency is utilized. This is used for converting the differential signal to a single-ended signal. An AD8130 module has user adjustable gain to use as a programmable gain for amplifying the gain of the output signal. The gain is set by the ratio of two resistor values of R_G and R_F ($1+R_F/R_G$) (Data Sheet-AD8130 2005b). The AD8130 module has a very high input impedance for both inputs and we will measure the CMRR ratio at different frequencies, regardless of the gain setting. A schematic of the differential voltage amplifier is given in Figure 33. It has a high distortion performance with low distortion of $1V_{P-P}$ around 75dBc worst harmonic in second harmonic distortion to -80dBc at third harmonic distortion at 10MHz.

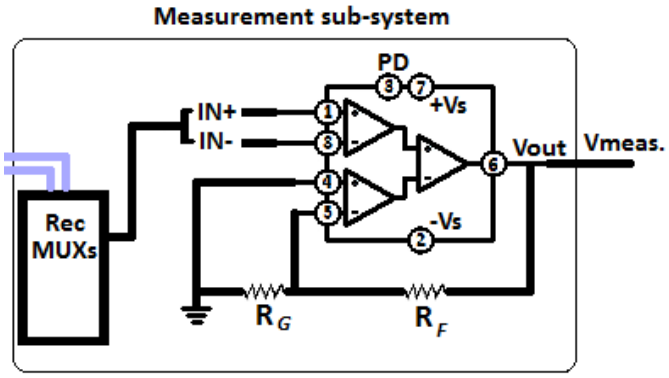

Figure 33 Differential voltage amplifier schematic of the AD8130 with the gain of $1+R_F/R_G$.

The programmable gain amplifier provides, by using the control lines of the DCP that are employed by a differential amplifier to create a different gains for the output voltage. The DCP consists of a resistor array, wiper switches, a control section and non-volatile memory (Data Sheet-X9C102 1996). Figure 34 shows the architecture of the DCP of XICOR of X9C103 that is combined with a differential voltage amplifier to build a PGA (Data Sheet-X9C102 1996).

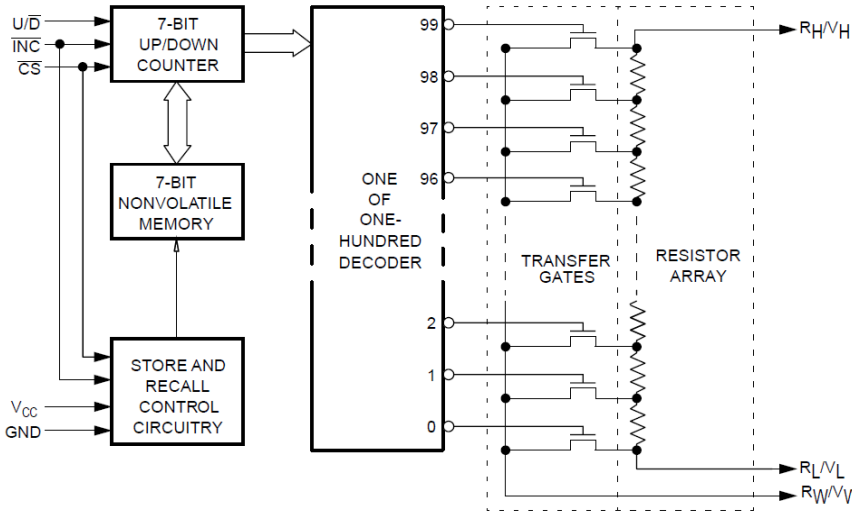

Figure 34 Schematic Diagram of the DCP of X9C103

Finally, the voltage measurement transfers to two filters and a noise isolator then sends to an ADC. The overall circuit will have a minimal effect. We also used filters for the output signal before connecting to the ADC.

In most applications it is desirable to get the ADC readings quickly. The circuit sequentially selects electrodes by controlling the DRV and REC MUJXs (channel-selecting multiplexers). AZ1 EIT uses a four-electrode measurement method, with 123 drive electrode combinations per frame, the latency is equal to the sum of all the internal delays and external delays per electrode combination × the number of combinations per frame, which is equal to 1416 measurement combinations.

The switching of the two stages of drive MUXs is done very fast in tens of microseconds and has little effect on speed, but there are other delays necessary that slow down this ADC acquisition process due to the need for filters in the demodulation of the signal.

Synchronous demodulation can be used to determine the amount of the in phase, 0 degree, signal and the out phase 180 degree signal. This requires two analogue or switching multipliers and two filters followed by buffer amplifiers for each signal to be demodulated. The synchronous demodulator essentially does a full wave rectification and the filter removes the ripple. For each frequency used ideally different values of resistors and capacitors are chosen to remove the ripple. For 12 bit

accuracy this ripple should be less than 5V/4096=1.22mV/division. Obviously smaller capacitors will remove the ripple to this point at higher frequencies. Typically only resistors and capacitors are used in the filter. Either an active or passive filter can be constructed with the buffer amplifier.

Every time a different signal is presented to the input of this circuit the capacitors in the filter must charge or discharge to a different value. This can be seen in the output of the buffer amplifier ramping up or down to a final value. This will take some time, so it will always be necessary to have a significant delay time before the ADC is used.

Thus practically, we wrote software that allows us to set the delay time after setting up the MUXs, before we are taking an A to D measurement. We used a filter in the demodulators that speeds up the process by a factor of 10 by switching in resistors 10 times smaller for 0.5ms to speed up the charging process and make the output closer to the final value faster. These are then switched out so a filter is in place to ideally remove ripple. After a 0.5ms wait the ADC reading is taken. Practically, this means using a 100 KHz measurement frequency in similar circuits they are able to take a single ADC measurement in 1ms to 12bit accuracy.

Ideally, we would use a different filter when we are measuring at a certain frequency so that a frame done at a high frequency can use a faster filter to eliminate the ripple and the filter capacitors can also charge up faster. Practically at 1MHz, we would probably be able to take a single ADC measurement in 0.1ms. This would take 1416ms per frame.

The purpose of the next section is to explain the system architecture, its measurement process, and the related calibration performance in detail. The ultimate aim is to design an EIT system with a stable measurement and source in a single interface that works at multi-frequency. The next section addresses the calibration method used for high precision EIT's measurement data.

4.7. Calibration process for a multi-channel and multi-frequency AZ1 EIT system

In EIT systems, high precision circuitry is essentially necessary to overcome the ill-posed problems in the reconstruction of an image, where a small change of current or voltage on the surface or measurement subsystem leads to massive changes in the spatial distribution of complex conductivity and permittivity images of the body. The current injection method requires a high output impedance since the current is injected for various loads over a wide frequency range. It cannot be created without using both a calibration and a function trimming circuit to get high output impedance while leading to a complex circuit, this problem was described with regard to the current source in chapter 3.

In our topology, an external signal generator produces the desired input voltage (V_{SOURCE}) passing through the two op amps (one non-inverting voltage follower and one with an inverting amplifier) to create the desired voltage with 180 degrees out of phase. These input voltages drive current sources to inject the current into the load. During this process, the voltage will be measured across the load simultaneously. Thus, the current flows through the load (I_{LOAD}) in proportion to the voltage measurement (V_{MEAS}), therefore it can be measured by knowing the value of the current load (V_{MEAS}/I_{LOAD}). Therefore, measuring the voltage across the load results in the load impedance, considering the fact that in the ideal case, the value of the current that flows through the load is equal to the voltage measured from the load divided by the current (thus Z=V/I).

The combination of AD8130 and DCP are influential for converting differential signals to a single-ended signal with extremely high CMRR and a high-speed instrument, which includes the programmable gain amplifier, when the programmable line is controlled by a PIC.

Measuring the value of the voltage of the biological load with the greatest possible precision is extremely important for EIT technologies. In an EIT system, the source can be a contact current, so that each electrode chosen has a certain AC

constant current injecting into the subject. Typically, any two electrodes fixed to the target volume are driven 180 degrees out of phase, and any two electrodes fixed to the target volume have their voltage difference signal measured with a difference amplifier and synchronous demodulation referenced to the source oscillator. One of the most common parts of EIT technology is signal calibration, which is used for electrode arrays, image reconstruction algorithms, and DAS, as part of the measurement system. The measurement data needs to be adjusted based on the calibration results, as the AZ1 EIT system is based on a single source that shares a voltmeter and source between the electrodes by employing drive and receive multiplexer structures (DRV and REC MUXs).

Based on the AZ1 EIT design, it requires a calibration method when measuring high precision voltage signals. This calibration method will consider the effect of the drive multiplexers on the injecting side as well as the receive multiplexers effect in the measuring side when using the dummy load. In addition, it is necessary to use a very well-built calibration method that employs the application of 123 injection channels in different locations of an 85 electrode area when reconstructing an image using 1416 measurement combinations.

Figure 35 indicates the block diagram of the AZ1 EIT system with the 85 electrodes and two stage multiplexers, one set on the driving side (DRV MUXs) and the other set on the receiving side (REC MUXs). Each electrode is connected to a channel of the driving and receiving multiplexer stages. Two applied sources that are within 0 and 180 degrees out of phase are connected to the inputs of drive multiplexers. It is worth noting that Figure 35 shows only 0 degrees phase and the 180 degrees phase will be exactly the same as this branch.

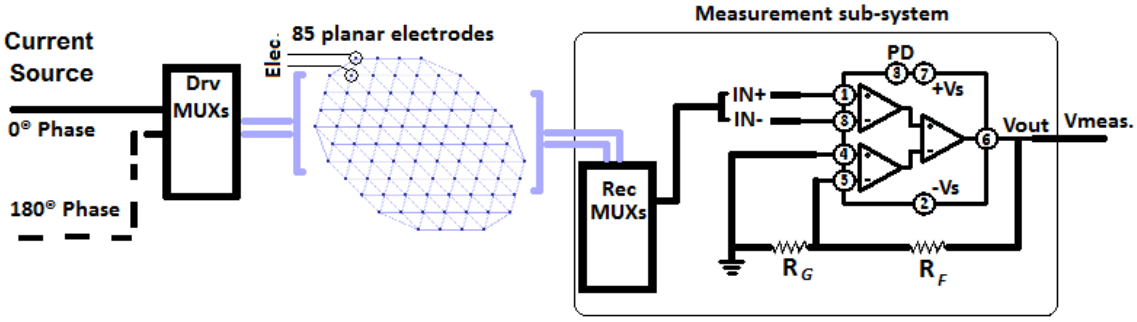

Figure 35 The block diagram of the EIT system with the 85 electrodes, measurement subsystem, drive multiplexers (DRV MUXs) and receive multiplexers (REC MUXs).

In the first stage of the calibration process, the current source is directly connected to the drive multiplexer with the effect of a known dummy load and electrode. In the second stage, it considers the effect of two different dummy loads and electrodes for calibration of the differential amplifier in the measurement subsystem when fully calibrating the system properties. On top of that, it uses an electronic mesh phantom that will be discussed in detail in the next chapter, to fully assess the performance of the EIT system such as series resistance and inductance of electrodes in the EIT system.

Figure 36 indicates the overview of the current design with an ability of parallel data acquisition when injecting a current and measuring a data frame of the voltage.

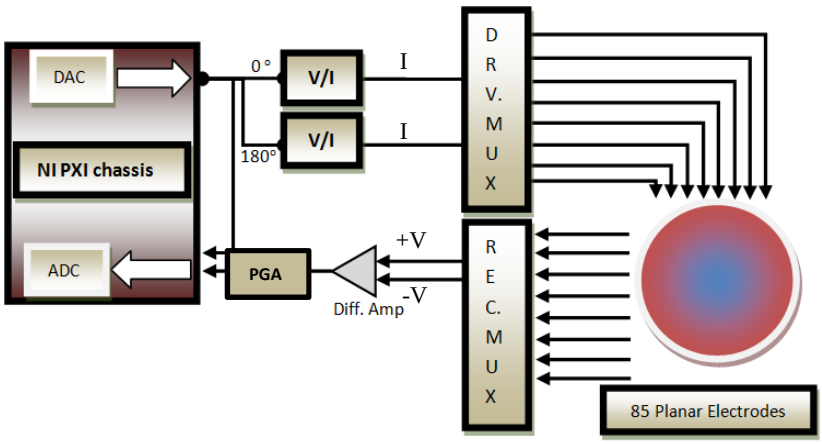

Figure 36 Overview of AZ1 EIT system

a. Measurement subsystem calibration process

In the design of the EIT system based on different current sources in a single platform required to have a voltage measurement instrument that is capable of measuring the biological load data through both current source topologies. A sequence of calibration tasks will be described below collecting high precision data.

Afterwards, image reconstruction software and a control system will use the calibration features to find the exact voltages; resulting in an EIT image.

Calibration of the measurement subsystem is the first step of the hardware calibration process. A differential amplifier is used to measure the voltage across the load. Therefore, the first stage of the calibration method is dealing with a unity gain differential amplifier that is measuring the load voltage (V_{LOAD}) when delivering a known current to the load (I_{LOAD}) through the different electrodes. For this reason, the two input voltages of the differential amplifier (called V_{IN}^{+} and V_{IN}^{-}) are attached to the different calibration arrangement to get the actual gain of the differential amplifier.

Ideally, V_{OUT} is equal to the difference between V_{IN}^{+} and V_{IN}^{-}, however, in reality, if the voltage is applied to the inverting (V_{IN}^{-}) and non-inverting (V_{IN}^{+}) inputs, the gain (A) related to the input voltages will exist. Since, in the ideal case it can be assumed that the $V_{OUT} = V_{IN}^{+} - V_{IN}^{-}$ and the gain is equal to unity-gain (A=1). But in reality, the output voltage of the unity-gain differential amplifier (V_{OUT}) can be calculated by the following equation (Saulnier, Ross et al. 2006):

$$V_{OUT} = A_{DM} \times V_{DM} + A_{CM} \times V_{CM} \qquad 26$$

The gain of the common-mode of the differential amplifier inputs is represented by A_{CM} and the gain of the differential-mode of the differential inputs is represented by A_{DM}. An accurate value of the output voltage will be calculated by knowing the value of the A_{CM} and A_{DM} of the differential amplifier (Saulnier, Ross et al. 2006). The output voltage calibration process for the differential amplifier consists of the following steps:

1. Computing common-mode gain of the differential voltage amplifier (A_{CM})
2. Calculating differential-mode gain of the differential voltage amplifier (A_{DM})

1. Common-mode gain of the differential voltage amplifier of the measurement subsystem (A_{CM})

Typically, the common-mode gain in the real differential amplifier observed is small, but non-zero gain. However, we need to calculate this gain in regard to

designation of multiplexers in the system and the quality of the circuit design. To calculate the gain of the common-mode (A_{CM}), it is required to apply an equal voltage to both inputs of the differential amplifier ($V_{IN}^{+} = V_{IN}^{-}$). Thus, the measured output voltage would be the voltage of the common-mode (V_{CM}). To find the common-mode voltage the following equation must be evaluated:

$$V_{CM} = A_{CM}\left(\frac{V_{IN}^{+} + V_{IN}^{-}}{2}\right) \qquad 27$$

We present a desired schematic to determine the A_{CM} of the measurement subsystem by configuring the DRV and REC MUXs switches and employing a calibration line that drives both inputs of the differential amplifier equally. Thus, the two inputs of differential amplifier would be fed with the equal input voltage when they are connected to the same input signal of the REC MUXs.

Figure 37 shows a circuit schematic that measured the gain of common-mode of the measurement subsystem when all switches of the DRV and REV MUXs have been arranged for this purpose to collect the two equal voltages V_{IN}^{+} and V_{IN}^{-}. The calibration line L1 is designed to connect directly the DRV MUX to REC MUX through a known dummy resistor (e.g. 100R) then this voltage line is directly connected to two inputs (IN^{+} and IN^{-}) of the differential amplifier.

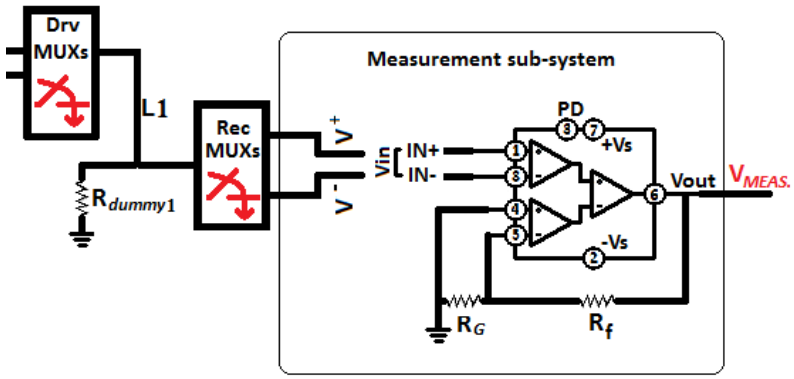

Figure 37 the arrangement schematic of the multiplexer switches for calibration of the measurement subsystem by measuring the common-mode voltage

The above schematic through switching in DRV and REC MUXs prepares the appropriate common-mode voltage from the equation **27** combination of V_{IN}^{+} and V_{IN}^{-}

'where in the common-mode schematic the two inputs drive the equal voltage ($V_{IN}^{+} = V_{IN}^{-}$), so that the gain of the common-mode would be:

$$A_{CM} = \frac{V_{OUT}}{V_{IN}^{+}} = \frac{V_{OUT}}{V_{IN}^{-}} \quad 28$$

2. *Differential-mode gain of differential amplifier of measurement subsystem (A_{DM})*

The requirement for calculating the differential-mode gain of the differential amplifier is applying two different input voltages and measuring the difference between these voltages. Two calibration lines of L_3 and L_4 designed when the L_3 and L_4 are carrying the different voltage through two different dummy resistors R_{DUMMY1} and R_{DUMMY2}, respectively, then drives to the REC MUXs. We also arranged the switches of the DRV and REC MUXs to apply two different input voltages to V_{IN}^{+} and V_{IN}^{-}. Therefore, two different input voltages are applied and the differential-mode voltage V_{DM} can be measured. Figure 38 shows the schematic diagram of the calibration arrangement to measure the V_{DM} then calculate the A_{DM}.

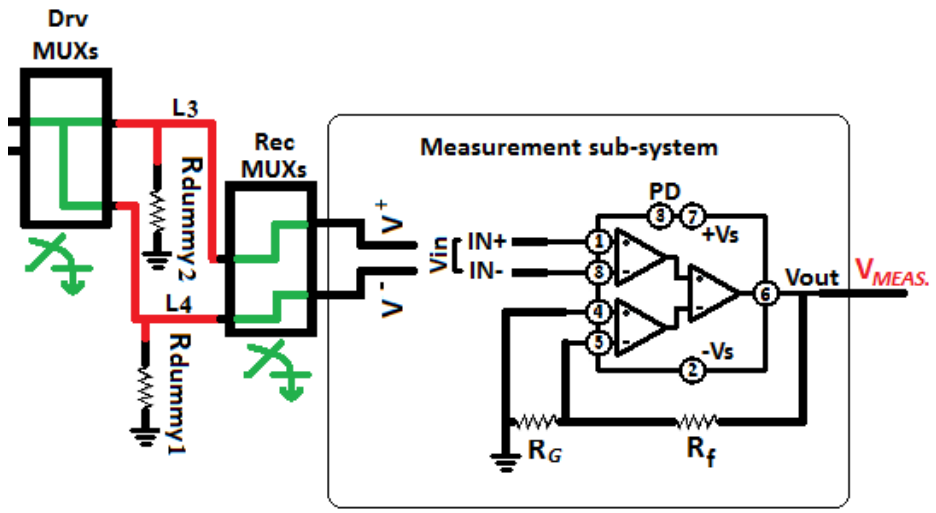

Figure 38 the arrangement schematic of the multiplexer switches for calibration of the measurement subsystem by measuring the differential-mode voltage

The output voltage at the differential-mode (V_{DM}) is related to the differential-mode inputs V_{IN}^{+} and $V_{IN}^{-}$and the gain of differential-mode (A_{DM}), therefore, we can write:

$$V_{DM} = V_{IN}^{+} - V_{IN}^{-} \quad 29$$

In the case of differential-mode, the V_{MEAS} is equal to:

$$V_{OUT} = A_{DM} \times V_{DM} \quad 30$$

By substituting the above equation into equation 26, we can write:

$$A_{DM} = \frac{V_{OUT} - (A_{CM} \times V_{CM})}{V_{DM}} \quad 31$$

The common-mode rejection ratio (CMRR) of the differential amplifier can be computed by using the results of equation 28 and 31. Therefore, it is used to calibrate the CMRR of the measurement subsystem.

$$CMRR_{MEAS} = 10 \log_{10} \frac{|A_{DM}|^2}{|A_{CM}|^2} \text{ dB} \quad 32$$

This calibration process is continued until all input channels of the DRV and REC MUXs were measured, while it has attached to the planar 85-electrode plate as a second stage of the calibration procedure to compute the current value that is dropped by the shunt impedance of the electrodes. We have used the calibration method of the droop as explained by Cook and Saulnier, which is based on two trans-impedance measurements (Cook, Saulnier et al. 1994). We will also evaluate and assess the performance of the full EIT system based on an electronic mesh phantom in detail in the next chapter.

4.8. Power supply subsystem

The level of current and voltage of analogue electronic equipment is highly sensitive to the noise of the power ripple. Thus, obtaining a high precision system is extremely dependent on the power supply conditions. To provide exact power supply ripple to all analogue components such as op amps and MUXs, we separated all parts of the power supplies in the AZ1 EIT system. For example, an op amp output voltage is equal to input voltage $\times$ gain, if it is greater than the power supply given to the op

amp (V_{CC} or V_{dd}), then the op amp goes into saturation. In general, the system will produce different results depending on the power supply.

There are four levels of power supply ±5V and ±15V. Each power supply level is individually designed for each subsystem package to avoid perturbation in the power supply of other equipment. In addition, each power supply component is separated from other components. The linear power supply rates exceed the peak current demands of the analogue components in AZ1 by more than 10%. Figure 39 shows the output voltages for each part of the system that are fed. A voltage regulator is required to produce the individual and fixed voltage level of ±5V and ±15V for each power supply line. Using a couple of decoupling capacitors on each component and individual power supply planes result in minimization of the voltage ripple and it acts as a filter to avoid the noise at high frequencies. The efficiency of the power supplies and the total power of the supplies result in significant heat production. Heat dissipation is achieved by cooling heat-sets for each linear power supply package. To prevent the noise travelling through the power lines reduction resistors and filter modules are utilized. In addition to improved power supply decoupling, if high-frequency energy is generated on the chip because it will leak into the power supply planes, hence, ferrite beads have been used to block the high-frequency energy coming back through the supply lines. Electromagnetic Interference (EMI) suppression is also used to reduce the effect of the power supply. Significant design effort has been used to create a high precision power supply for the AZ1 EIT system. Figure 39 shows the circuit diagram of the power supply for the AZ1 EIT system.

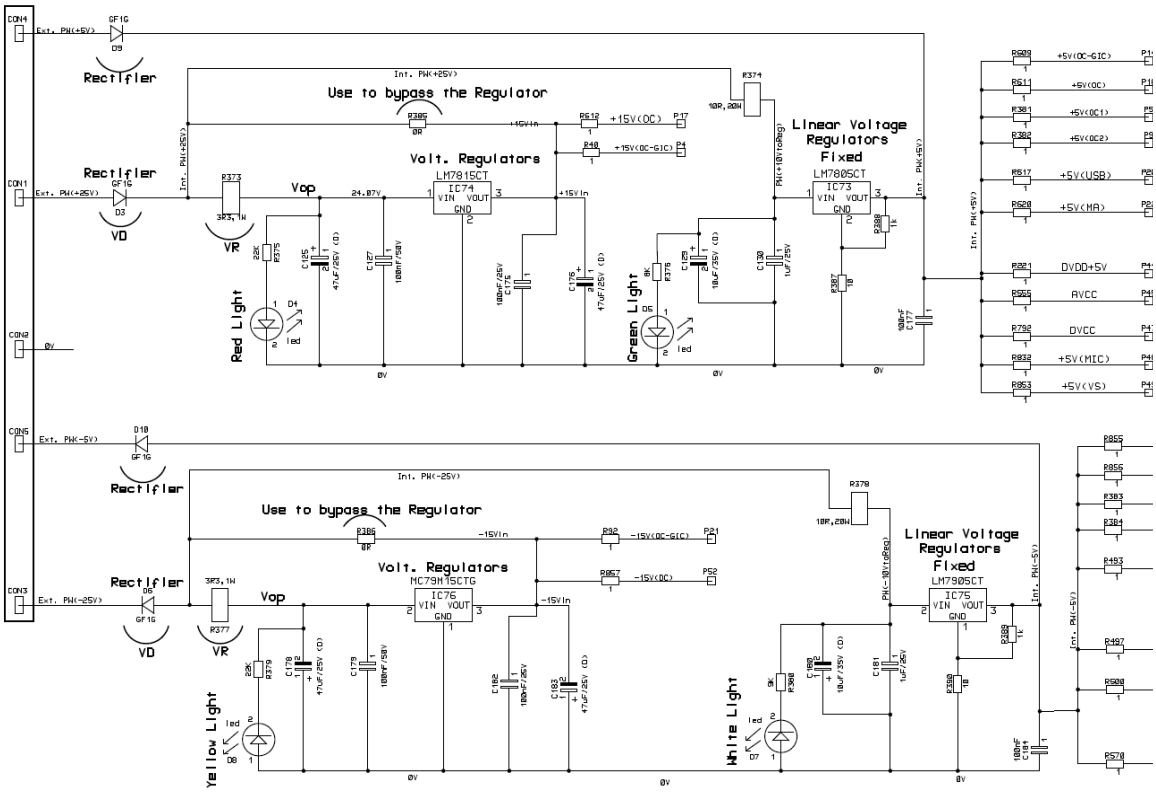

Figure 39 The power supply schematic

External power supply voltage provides V_{IN}=±25V. As was mentioned before, there are four linear voltage regulators of fixed output voltage to supply the output voltage levels ±15V and ±5V. These regulatory modules take a variable input voltage between 23V to 35V to maintain a constant, stable output voltage of the nominal value equal to ±15V. Also, two regulators are used with the variable input voltage between 10V to 35V to maintain a constant (fixed) and a stable output voltage of nominal value equal to ±5V. It is worth noting that before connecting the input voltage in order to adjust voltage, it is useful to apply the external power supply to rectifiers for DC power supplies and a steady constant DC current. This is why we selected a rectifier for each power line (GF1A, Vishay Semiconductors). The voltage drops across the rectifier are represented by V_D equal 0.6V (Vishay 2013). Although the regulators can work with an input voltage of 35V as far as the temperature coefficient and the drop voltage across the regulator that are concerned, it is better to reduce this voltage close to the output voltage of the regulator. Therefore, we employed the drop resistors 3R3, 20R with 1, and 20W respectively for the 15V and 5V lines. We also selected LM78M15CT [+15V] (FAIRCHILD SEMICONDUCTOR), MC79M15CTG [-15V] (ON SEMICONDUCTOR), LM7805CT [+5V] (STMICROELECTRONICS) and LM7905CT [-

5V] (FAIRCHILD SEMICONDUCTOR) regulators with the package of TO-220-3 in the power supply circuit.

Lets assume V_{IN} = ±25V with a total current of 100mA. So, the voltage across input resistor would be equal to V_R: I_{OP}*R= 100mA * 3.3Ω= 0.33mV then the voltage across rectifier reduced by V_D (rectifier) = 0.6V. In the above schematic V_{IN}-V_R-V_D=V_{OP}, we selected LM78M15CT that will take: +25V-0.6V-0.33V=24.07V input voltage to regulate with the maximum current output of 500mA and fixed output voltage of +15V. A similar calculation is made for ±5V.

Table 6 shows the power supply current for each module. AZ1 consists of different source topologies for the EIT application, such as different types of current source with OCCII-GIC. It is worth noting that AZ1 will work only with one active source to measure a frame of data. So, the total supply current would be a maximum of the highest quiescent of supply current plus the common parts such as measurement subsystem and multiplexer sections.

TABLE 6 QUIESCENT OF POWER SUPPLY CURRENT FOR EACH MODULE

		Quiescent of Supply Current			
		Min	**Max**	**Condition**	**Power supply rail**
OPA656		11.1mA	16.3mA		±5V
AD8130		9mA	10.6mA		±5V
ADG2128		20uA	Low quiescent current		±5V
ADG1211		220uA	380uA		±15V
ADV3205	**AV_{CC}**	45mA	50mA	Output enable No load	+5V
		31mA	35mA	Output disable	+5V
	AV_{EE}	45mA	50mA	Output enable No load	-5V
		31mA	35mA	Output disable	-5V
	DV_{CC}	8mA	13mA	No load	+5V
DCP (X9C102)		3mA		Active	+5V
		500µA		Standby	+5V
AD844		6.5mA		7.5mA	±15V

Figure 40 shows the different parts of the power supply. The EIT system consists of independent topology sources with common parts of the acquisition and measurement systems. Practically, only one type of source is active (active-mode) and all other sources are stationary-mode. Thus, we considered the total quiescent supply

current for each source technique plus a common part which includes data acquisition system with PGA and multiplexers of the DRV and REC stages.

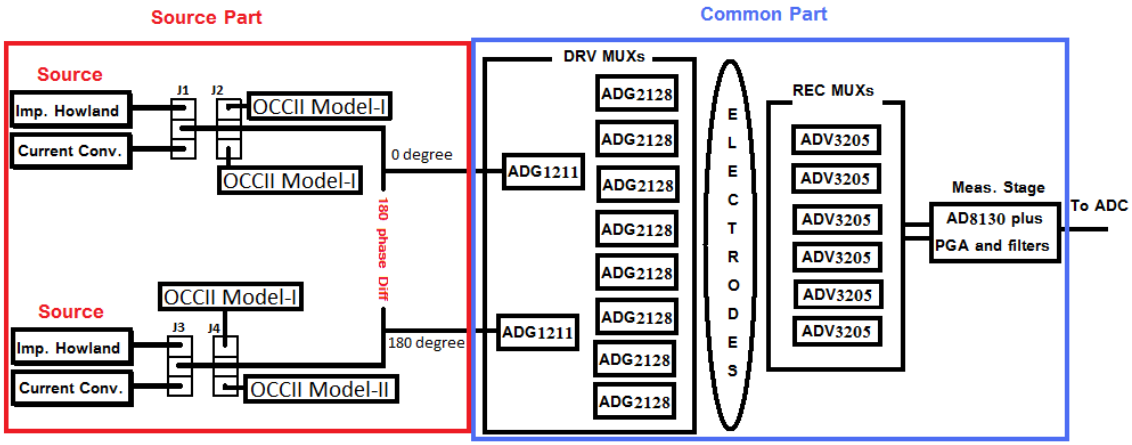

Figure 40 Supply Part Schematic consists of different sources and Common parts

The designed power supply has a separate power line for each section. Therefore, the power lines of ±15V or ±5V branch to the different parts of the system. Figure 40 shows the schematic of the power supply system. As a result Table 7 obtains the total quiescent supply current for each section through calculation of the quiescent supply current of each module as shown in the Table 6. Appendix-A shows how to do the detail calculation of maximum total current of power supply.

TABLE 7 QUIESCENT OF SUPPLY CURRENT FOR EACH SECTION OF EIM SYSTEM

Subsystem	Quiescent of Supply Current			
Rail level	+5V	-5V	+15V	-15V
Improved Howland + OCCII-GIC-I	189.8mA	179.3mA	30mA	30mA
Improved Howland + OCCII-GIC-II	104.8mA	104.8mA	15mA	15mA
Current Conveyor Source + OCCII-GIC	81.5mA	81.5mA	15mA	15mA
Common mode	251.22mA	235.22mA	720uA	720uA
Total	627.32mA	520.82mA	60.72mA	60.72mA
Total +20%	752.78mA	624.98mA	72.86mA	72.86mA
Selected Regulator Output Current	1000mA	1000mA	100mA	100mA

4.9. Board layout of op amps

For the high frequency system, it is also necessary to consider board layout parasitics by minimizing the parasitic capacitance to any AC ground, minimizing the distance between any components, short direct tracks, and power supply pins to high frequency decoupling capacitors.

The parasitic capacitive load is one of the most difficult and very common problems in an op amp. As OPA656 is a high speed and high open-loop gain amplifier, it is very sensitive to reduced stability and closed-loop response peaking. A parasitic capacitance in the output pin will mitigate against the stability, so it needs to consider the open-loop output resistance. The parasitic capacitance introduces an extra pole in the signal path, causing a reduction in the phase margin. The most important factors when there is parasitic capacitance are frequency response flatness, pulse response fidelity, and distortion. A solution would be to use an isolation resistor to isolate the feedback loop from the capacitive load. An isolation resistor could be placed between the capacitive load and the output pin of the amplifier since a zero pole would be added to loop response at the higher frequency. So, it will increase the phase margin, improving stability and stopping the oscillation of op amps. Thus, series resistors (around 100Ω) should be placed as close as possible in the output line of op amps. The best choice of this resistor will result in good frequency response at load and achieve a maximum flat frequency response.

The other consideration in the board layout is the effect of other layers that act as a capacitance load on the output pin. For this reason, a boundary line is added to the output pin to cancel the capacitance caused by the copper filling between the board layers (in order to avoid the capacitive load). Figure 41 shows an example of boundary lines that are surrounded by an output track of an op amp. This boundary line technique avoids production of capacitance from other layer effects to the input and output pins of op amps.

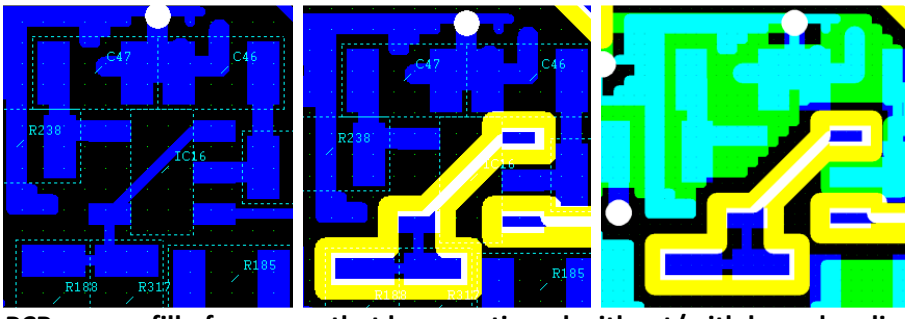

Figure 41 PCB copper fill of op amps that has mentioned without/with boundary lines

The parasitic capacitive loads cause a reduction in the performance of op amps. Therefore, it is necessary to avoid the long tracking and unmatched cabling as they exceed the parasitic capacitance value.

In addition, ferrite beads and decoupling capacitors of 100nF have been used. Figure 41 shows the location of C46 and C47 are exactly as close as possible to the module (i.e. Op amp) and the ferrite beads, inputs/outputs to reduce tracks. Regarding the complexity of circuit design we were not able to add the decoupling capacitors and the ferrite beads on the other side of the board.

4.10. EIT board PCB description

PCB design is the most important part of the design of the EIT system and great care has been taken with this, otherwise it will cause oscillation or give crosstalk between ICs, components and copper tracks.

It is necessary to add (around) 100R resistors to all op amp outputs near output pins to keep the output from driving the capacitance of the line directly. Therefore, the output lines are not loaded with an extra capacitance. However, there is a lot of capacitance between power layers. It required us to make short lines between power supply lines to decoupling capacitors. It also needs to use the top most layer vertical signal lines in contrast with the bottom layer when it is used, the signal lines are horizontal to reduce oscillation and crosstalk in the PCB. Assign three different layers of the ground, positive voltage (+V) and negative voltage (–V) when first using copper lines between two points, then using copper filling, the capacitance coupling between layers will be large (or good enough). In addition, we need to avoid putting vias under ICs. Overall a lot of techniques were used to minimise the stray capacitance and to avoid interaction (crosstalk, influence of noise) during PCB design.

I have created PCBs using XL Designer PCB creator from Seetrax PCB CAD software. The EIT board was restricted to 6 copper layers with a finished board thickness of 1.76mm. Table 8 shows the size of the thickness of PrePreg, core and layer assignments and layer assembly order.

TABLE 8 SIZE OF THICKNESS OF 6 COPPER LAYERS WITH LAYER ASSIGNMENTS OF EIT BOARD

Layer Name	Copper	Thickness
Copper Layer 1 (Top-Signals)	**1.00 Oz**	**0.035mm**
PrePreg		**0.295mm**
Copper Layer 2 (Ground 0V)	**1.00 Oz**	**0.035mm**
Core (c/c)		**0.300mm**
Copper Layer 3 (Power +)	**1.00 Oz**	**0.035mm**
PrePreg		**0.360mm**
Copper Layer 4 (Power -)	**1.00 Oz**	**0.035mm**
Core (c/c)		**0.300mm**
Copper Layer 5 (Signals)	**1.00 Oz**	**0.035mm**
PrePreg		**0.295mm**
Copper Layer 6 (Bottom-Signals)	**1.00 Oz**	**0.035mm**

Figure 42 and Figure 43 show the Top and Bottom layers of the AZ1 EIT board in software layout design with outlines of each component and its copper filled.

After finishing the design of PCBs, eventually, it was used to generate the Gerber files. Then, it was sent to GC-Prevue version free (22.4.6) tools as PCB Gerber viewer, for looking through and viewing what the PCB maker will actually make, where the most important design is the copper layers. There is another way outside PCB creator software to view layers and information properties, layer alignment, and aperture and drilling tables to inspect for mistakes, it does not show in PCB creator software, before sending for fabrication and assembly.

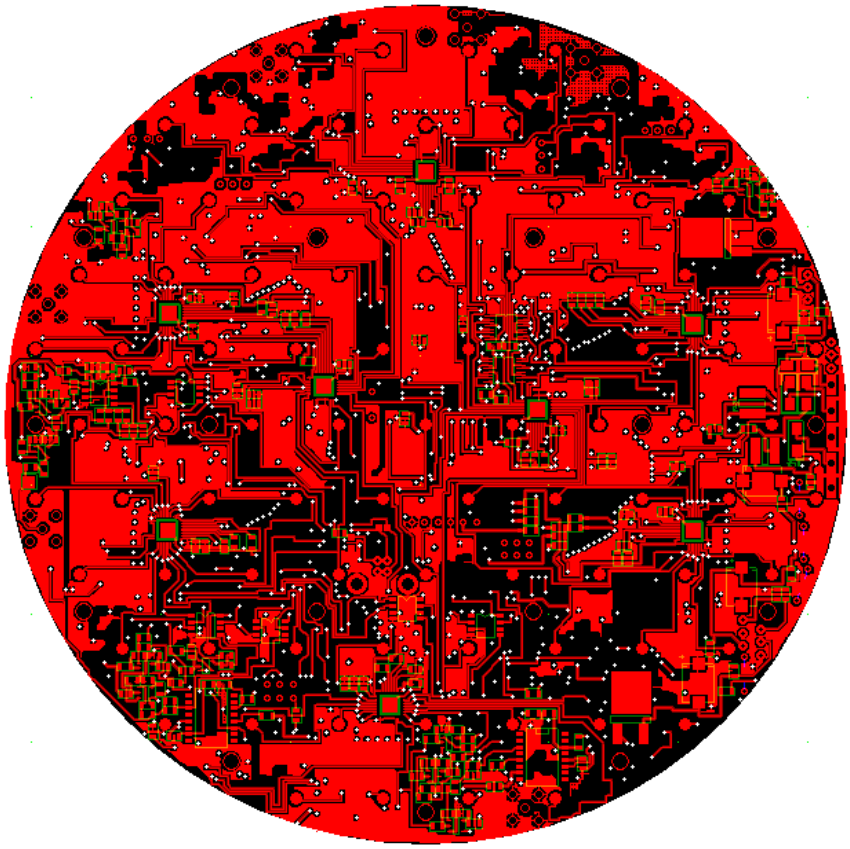

Figure 42 the Top layer of the AZ1 EIT board in software layout

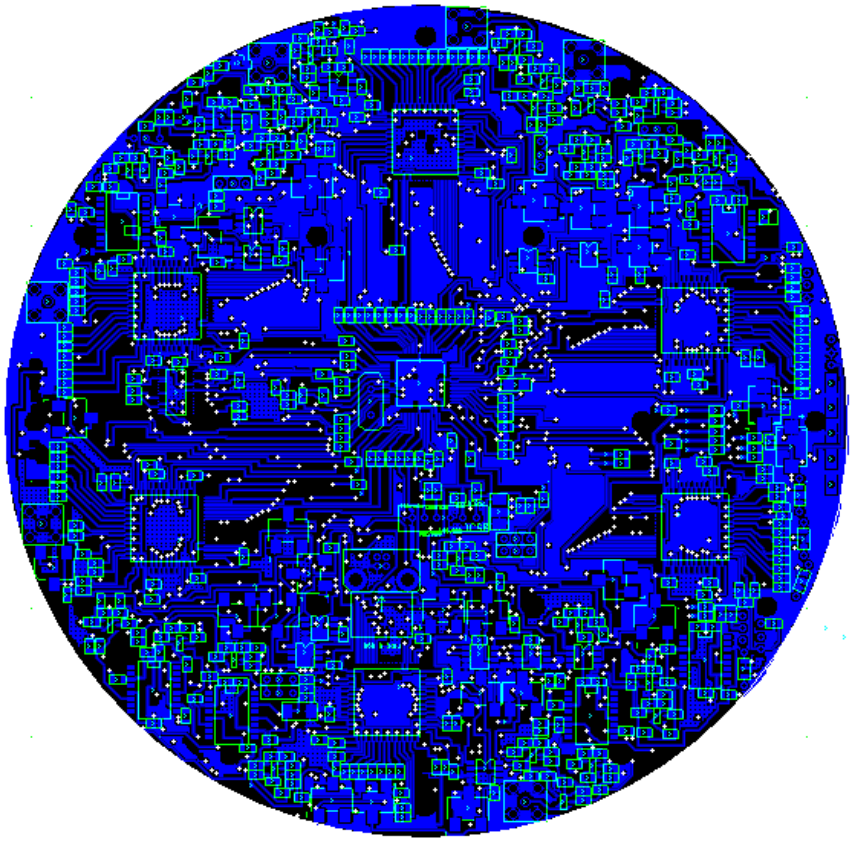

Figure 43 the Bottom layer of the AZ1 EIT board in software layout

4.11. Control interface

We developed the interface software to control and auto/manually address selection of the electrodes for calibration purposes. The first display from of the interface software establishes a connection between the interface software and the external MCU through the USB communications port to the asynchronous serial data transfer interface of RS485. Appendix-B shows the software port usage for all analogue and digital signals in the MCU.

Figure 44 shows the communication settings such as port number, baud rate, bit size and speed. The feedback driven from the interface will confirm that there is an established connection between interface software and PIC for transferring/receiving data.

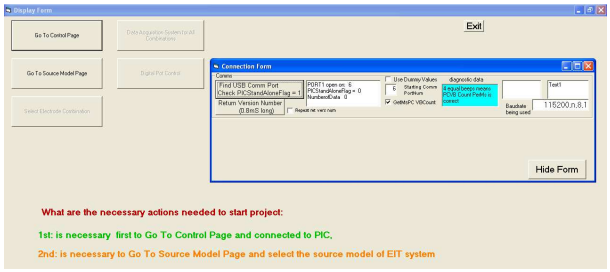

Figure 44 connection setting as a first step of communication between PIC and control system

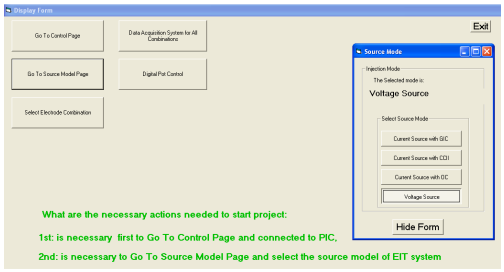

Figure 45 Source mode (selection between different type of injection mode for EIT system)

Three types of sources have been defined in the AZ1 EIT system. However, only one source topology will be active in the system during the experiment. Therefore, there is a source mode selection form to choose between different types of sources. Figure 45 shows the source selection mode as the second action of the interface software.

One of the main purposes of the control system of the specific AZ1 EIT is based on selecting the different combinations of drive and receive electrodes. There are 1416 rows of electrode combinations to produce an image in the planar 85-electrode plate of the AZ1 EIT system. Figure 46 shows the interface software that allows transferring the selected drive and receive channel automatically and manually to the

MCU. For the calibration process, an electrode combination could be selected individually in arbitrary form by choosing the drive and receive channel.

We sequentially measure the voltage of all 1416 combinations, one by one when selecting each corresponding drive and measurement channel through the interface software in order to transfer these voltage measurements to the image reconstruction software to produce a 3D image as shown in Figure 47, the data acquisition system.

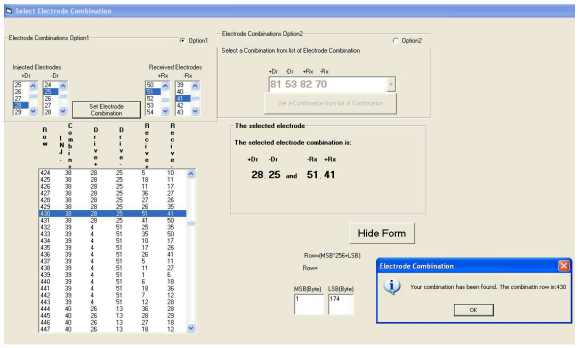

Figure 46 Select combination system

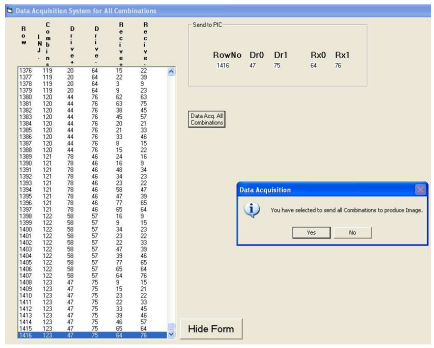

Figure 47 Data Acquisition System for all combinations

DCPs are utilized for different calibration and functional purposes, i.e., PGA, maximize the output impedance of the improved Howland and current conveyor current source circuits with the OCCII-GIC circuit to operate at multiple-frequencies. The positions of the resistor wiper elements are individually controlled by the component select (CS), the Up/Down mode (U/D) and number of the increment gain (INC) input pins. The position of the resistor wiper can be stored in non-volatile memory and then can be recalled when the component is powered up. Figure 48 shows the Digital-pot form for selecting and controlling each DCP.

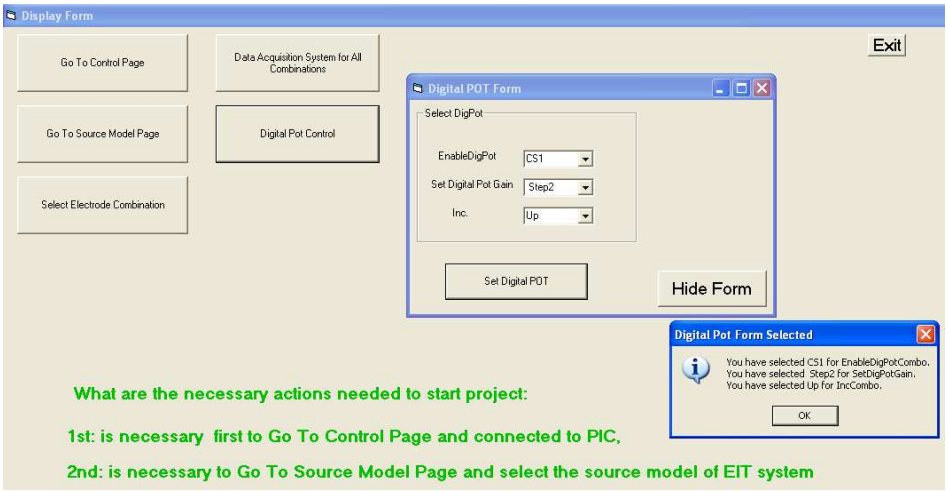

Figure 48 Digital-pot selection mode, e.g. CS1 (DCP1) is selected with tap point represents 10.10Ω and a gain of 2, so the equal resistance would be 20.20Ω.

Chapter 5 Investigate and Design of High Performance Cole-Cole based E-phantom for EIM System Sensitivity Study and System Performance

5.1. What purpose does this chapter serve?

Assessment and validation of the AZ1 EIT system (the new Sussex EIT system) performance and calibration of systematic errors in the electrical field generated inside of the interrogated volume is an important requirement. System instabilities can be caused by the EIT design and must be characterized before and during the clinical trials. Evaluation of the AZ1 EIT system used in the clinical study can be based on a realistic electronic phantom (E-phantom). This chapter describes a mesh phantom based on the electrode configuration and mesh structures of the image reconstruction. The phantom has the capability of modelling the cellular electrical properties that are operative within a circular homogeneous medium. The design is optimized to assess the planar topology of the internal impedance distribution. This includes the effect of the complex impedance model of tissues using a distributed circuit, exploiting look-up tables of the extra-cellular resistance R, resistance of intra-cellular tissue S and the membrane capacitance properties C (RSC circuit model). The

system employs the information from the electrical properties of biological tissues to implement the Cole-Cole dispersion model. The research will present a dynamic mesh phantom to assess the performance of the EIT system to simulate *in vivo* conditions. The mesh phantom has the capability to generalize the RSC models between 85 electrodes. It is possible to use different RSC values at 6 common locations; consisting of 123 current injection combinations with the capability to generalize the model using a hexagonal topology in the planar structure that is measured at multiple frequencies. This mesh phantom provides predictable, stable, and reproducible signals with the capability of using digitally controlled potentiometers (DCPs) in place of resistance R in the RSC circuit models that is formed between 2 electrodes for the dynamic model. This mesh phantom is capable of producing localized conductivity perturbations between each arbitrary channel in the electrode placement planar phantom topology by measuring all 1416 combinations that are to be used in the image reconstruction. The phantom is especially designed for the Sussex EIM system to validate system performance of measurements consisting of SNR, and modelling system accuracy.

5.2. Introduction

In bioelectric systems, impedance (Z) is defined as the complex relation between the voltage and current (Z=V/I) in an AC circuit. EIT systems are able to distinguish cancerous abnormal tissue from normal tissue using their different impedance properties and to find the impedance distribution of the target (Sree, Ng et al. 2011).

Essentially, the permittivity is a measure of the ability to permit the storage of electrical energy in the medium. Electrical Impedance Tomography (EIT), in biomedical engineering, is a medical imaging technique that maps the conductivity or permittivity distribution inside a biological tissue sample or the volume of a subject under test, by injecting current or applying a voltage to the tissue and collecting voltages or currents at the subject surface (Holder 2005, Brown 2003). EIT systems use impedance data for imaging biological tissues using the change of impedance brought about by disease states (Brown 2003).

A lot of effort has been made to increase the measurement accuracy and spatial resolution of EIT systems for detecting breast cancer in its earliest stage (Hartov, Mazzarese et al. 2000, Wtorek, Stelter et al. 1999, Osterman, Kerner et al. 2000, Cherepenin, Karpov et al. 2001, Goharian, Soleimani et al. 2008, Ybarra, Liu et al. 2007). The EIT technique is one of the most effective modalities that could be used for detection or screening breast cancer. That means, EIT systems are able to distinguish cancerous abnormal tissue from normal tissue using its different impedance properties and to find the impedance distribution of the target (Zou, Guo 2003).

The Sussex EIT system connects an array of electrodes to the target using a medium having its own and homogeneous conductivity distribution. It then chooses two electrodes and injects in-phase and 180 degrees out of-phase constant currents and chooses two other electrodes and measures the differential voltage between them (Zou, Guo 2003). It does this for different injecting and receiving electrode pairs collecting the data into an array and then uses a mathematical inverse algorithm to find the impedance distribution that could have given such data.

It is necessary to use a very accurate constant current delivery system and measurement system to ensure that impedance differences are not affected by systematic errors in the electrical field generated inside of the interrogated volume (Wan, Negishi et al. 2013, Hahn, Just et al. 2008, Schneider, Kleffel et al. 2000). In order to meet a high specification in delivery and measurement, improve throughput and performance of the system, a calibration phantom has been designed and built that connects known impedances to the electrode array. This calibration system can also apply impedance differences that imitate those of abnormal tissue. Although, there is no standardization at the device level of the EIT system, all calibration procedures are aimed at achieving high performance through the designed instrument architecture. However, calibration and validation of the measurement results are evaluated using a phantom to assess the performance. This phantom is used both for calibration and validation of the measurement results and to assess the performance of both the hardware (HW) and image reconstruction (IR) algorithms in parallel.

The Sussex EIT system is used to deliver *in vivo* image reconstruction from impedance measurements. The mesh phantom is utilized to assess the EIT system and optimise its performance in identification and categorization of abnormal cell properties with a focus on cancer data.

There are two phantom types to assess an EIT system: physical and electronic phantoms. The physical phantom that is used for EIT systems typically is composed of a conductive saline solution or gel medium with objects embedded in this medium. The medium and object have different impedances which permit the EIT system to detect changes of impedance and image them (Gagnon, Cousineau et al. 2010).

The electronic phantom (E-phantom) is used to assess the system characteristics of the EIT system such as: current or voltage delivered, internal stray impedance and effects of the impedance of the medium on the measurements. These results can then be used to optimise the electronic circuitry and components relevant to the impedance measurements to improve the performance of the system.

In general the mesh phantoms are designed to assess the performance of the EIT system by providing reconfigurable conductivity distributions. Using a mesh phantom can reduce the difficulty of calibration and validation of the design as it is relatively simple and quick to use (Gagnon, Hartinger et al. 2008, Hahn, Just et al. 2008).

In this chapter, we will describe the mesh phantom that has been used to assess and validate the Sussex EIT system. The phantom is utilized to simulate the interaction of the EIT system with a breast immersed in a saline liquid. This liquid makes the electrical connection between the electrodes and the breast surface. The phantom imitates the bioelectrical impedance generated in the breast when a low amplitude sinusoidal current flows through the EIT electrodes. In compliance with IEC60601-1, the general standard for medical equipment and medical systems the maximum amount of injection current into the body must be limited to 10mA for frequencies above 100 kHz. The voltage measurements are converted to an impedance image of the simulated breast by solving the finite element modelling

solution with a measurement strategy using the combined RSC model of the electrical properties of different tissues. This phantom is useful for studying dielectric relaxations and polarizations that are generated in the tissue.

5.3. Phantom Concepts

The concept of the phantom here is to use a non-biological device to simulate a biological medium. This E-phantom is capable of simulating biological items such as pieces of carcinoma, fat, and stroma tissues in a saline based solution. A saline conductivity of 0.5mS/cm has been used as the homogeneous medium in order to give a low impedance connection from sensor electrodes to the breast target.

This study uses an electrical mesh phantom, in contrast to the use of a physical phantom, to mimic an electrical impedance distribution of biological objects for comparison of different methods to improve the mathematical inverse and EIT hardware and for validation of the impedance inverse image found.

Physical phantoms composed of a conductive medium of saline solution with insulator, agar or vegetable have common problematic issues of: short life, inflexibility, instability and uncontrollable physical characteristics (Bera 2014).

In order to correctly model the impedance distribution between electrodes, it is vital to make the model E-phantom mimic the impedance of the medium and the impedance of the biological tissues of a physical phantom or a real breast. This E-phantom, with its repeatability and stability advantages, can be used to study the electrical properties (conductivity σ and permittivity ε_r) of cancerous and healthy tissue over a wide spectrum of frequencies. The advantages of an E-phantom compared with the physical phantom are: improved quality, reproducibility, predictability and stability of signals. Then a standard calibration method can be used to periodically verify the continued validity and accuracy of the EIT system (Yasin, Böhm et al. 2011).

The Sussex 3D EIT system is especially designed for breast cancer detection

application for different breast sizes and shapes. It is fitted in a bed with the patient assessed whilst in a prone position, as shown in Figure 49. An 85 electrode plate, with a distance of 17mm between any two electrodes is shown in Figure 50; it is located at the bottom of a tank so that the breast is immersed in a saline solution. The electrode plate is moved up or down to accommodate different sizes of breast where we can find the perfect position to maximise the number of electrodes covering the breast. The vertical cylinder saline tank has dimension of 180mm (d) × 50mm (h) with insulated cylindrical side walls. It should be seen as a Phase1 feasibility prototype to discover practically, which are the most important parameters needed for a more sophisticated design. For simplicity the phantom uses only resistors in most of its construction. The resistor values are chosen to model, in the first instance, only saline water with a depth of 10mm in the tank. The side walls and bottom of the tank are considered to be good insulators. Changes in the depth of the liquid in the tank are not taken into consideration (though the saline solution is going to move). Impedance changes, under software control over a USB link, can be introduced in sections, by switching-in different resistors and capacitors, to model the reactive characteristics of normal and cancerous tissue. This Phase1 phantom is not designed to model a complete breast in the tank.

Figure 49 Measurement tank 180 mm dia. (right side inside) the clinical bed (left side), open top surface, 5mm thick acrylic walls and 85 electrodes at the bottom

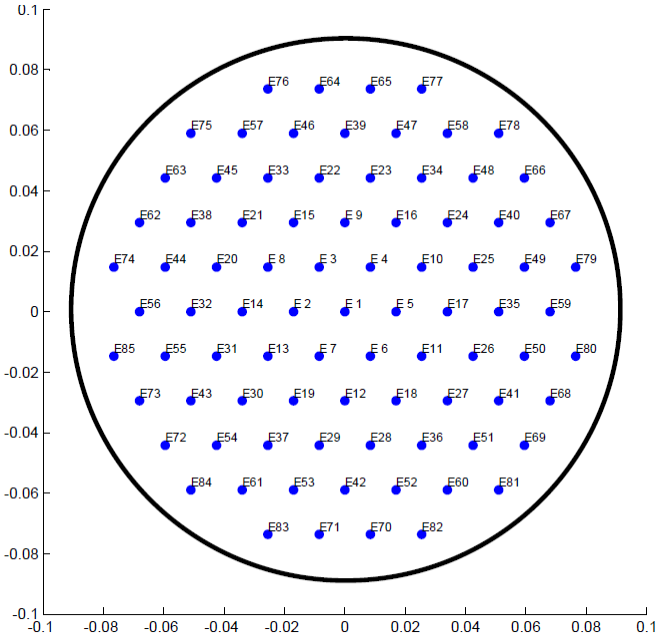

Figure 50 Planar electrodes with circular electrode plate

A 3D conductivity distribution model of the tank can be created by dividing the tank into 5 layers (Sze 2012) as shown in Figure 51 and considering the tank with a 50mm depth of liquid. The present E-phantom uses one layer (layer 1). This layer is the one attached to the electrodes. This layer will have the highest electric fields with high sensitivity induced in it from the driven electrodes.

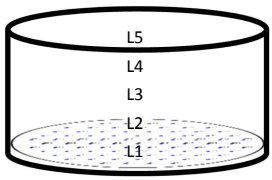

Figure 51 3D meshes created by dividing the 50mm depth of liquid into 5 layers 180mm (diameter d) * 50mm (h). The E-phantom only shows the layer 1 with 10mm liquid depth

Figure 52 shows a 2D mesh with triangular elements and a 3D mesh with tetrahedral elements. One of the limitations of the present resistive E-phantom is that this phantom is a 2D structure of resistors not a 3D one. This is also a limitation of the image reconstruction algorithm. It only considers layer 1 (L1) for the model and takes away effects of layer 2 to 5 from consideration in the design.

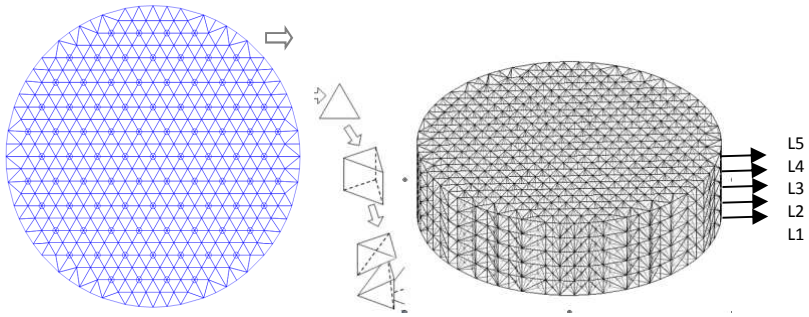

Figure 52 The 2D mesh with triangular elements and 3D mesh with tetrahedral elements

5.4. Phantom Design Considerations

A number of properties were taken into consideration during the design of the phantom. This section presents a description of a suitable design for the electrical mesh phantom, which provides the main characteristics relevant to the assessment process. In the following some of the new electrical mesh phantom's spatial and constituent design features are described, the Cole-Cole dispersion effect has been incorporated into the phantom.

a. Design Considerations

The characteristics of the design are as follows:

1. An issue arises from the use of a planar array over a circular topology having a non-equivalent element at the boundary compared to the interior (inner) elements of the planar array.
2. An issue arises from the use of the Cole-Cole model required to emulate local impedance perturbations at different frequencies.
3. An issue that arises from the use of a planar topology giving a difference in the measurement impedances at the boundary. In fact, the electrodes of the drive pairs are at the same distances relative to each other, so, it is expected that the breast, due to its positioning, will not completely cover all the electrodes when immersed in a saline solution in the device; hence presenting the device with varying measurements across the planar electrode plate. A set of measurement impedances are used as initial potentials of pure impedance saline at the first data collection stage. Many electrode

measurements will be at the same potentials, since they will only measure the purely resistive saline at the first stage. Since during the measurement process, there is no boundary line adjustment between the electrodes that are fully covered by the breast or not, when the breast is inserted into the device, there will be significantly different potentials between electrodes that are not covered and others that may be fully covered by the breast.

b. Mesh Phantom principles

It is worth noting that this mesh phantom design is not limited to this topology and number of electrodes. It can be expanded to phantoms with different shape and size of planar and even ring electrodes through minor modifications. In the Sussex EIT system, it was desirable to design a phantom based on 85 electrodes in a planar topology. The principles are defined in the following bullet points:

1. A 2D circular continuous homogeneous medium.
2. The driving signals are required to be a single source, comprising frequency and amplitude in the range that is realistic for the EIT application that is compatible with *in vivo* conditions.
3. The Cole-Cole dispersion data can be extracted.
4. The performance of the EIT system can be evaluated for the *in vivo* environment.
5. Ability to change the impedance at different locations. This means the capability to provide predictable localized impedance changes i.e. by resistance and reactance changes at a key mesh element.
6. The capability to utilize the RSC models between two electrode channels. It will be considered in 6 places; each RSC model is directly fitted into a segment of the planar electrode area since the measurement volume can be divided into 6 planar segments.
7. Results and effects of capacitance properties of the tissues will be considered in regard to tissue dispersion.

It is worth noting that the phantom is especially designed for the planar model. This has been implemented in the laboratory with an 85-electrode, multi-channel and multi-frequency EIM system that employs a 4-electrode method in which the design is rooted in applying two electrodes with constant out of phase currents, over available output frequencies, whilst the other two non-invasive electrodes are used to measure the developed potential difference concurrently. This is repeated for all injection and measurement combinations. The voltage measurements at the first stage are amalgamated with a 2D image reconstruction algorithm to provide the impedance image. Figure 50 shows the mesh phantom including 85 electrodes, where the electrodes are located at the vertices of the triangles within the circular electrode plate.

5.5. Phantom model

Our goal is to design an electronic resistive mesh phantom by using the finite element method (FEM) in a planar structure to model a conductively homogenous saline solution. The nodes in an element and location of electrodes used in the FEM method are matched with the mesh used in the image reconstruction software.

The nodes in an element, and location of electrodes used in the FEM method are matched with the resistive mesh phantom designed. The image reconstruction software used to examine system performance uses the same mesh and a finer mesh.

a. Methodology

Most of the research in the design of E-phantoms has focused on its application to the ring topology found in some EIT systems (Griffiths 1995, Griffiths 1988, Hahn, Beer et al. 2000, Gagnon, Sigmen et al. 2009, Gagnon, Cousineau et al. 2010). The context in which these works were reported shows that an E-phantom was useful in assessing calibrating and validating the function of different EIT systems. Similarly an E-phantom design is used to assess and validate the function of the Sussex EIT system.

In order to design a mesh phantom for a planar electrode array with a

homogeneous conductivity distribution, an algorithm based on the correlation between FEM and the electrode array has been applied to solve for the electrical conductivity field by registering all FEM element matrixes into the 2D system of electrical circuits. This work extends to designing an electronic mesh phantom that simulates the existence of small impedance differences (such as the capacitive effect of different tissues) immersed within a homogeneous medium over a planar topology.

b. Finite Element Method

Numerical methods that are important in the computational solution for physical applications are the finite element method (FEM), the finite difference method (FDM) and the boundary element method (BEM).

FEM is the most powerful and famous mathematical numerical technique derived from variation methods for solving partial differential equations (PDE) by finding approximate solutions to boundary value problems. It uses the discretization domain process over the entire domain of the continuous conductive medium Ω. It works by dividing the domain into small sub-domains called finite elements. It then solves the differential equations for each finite element and gathers all elements using compatibility and equilibrium conditions for the entire domain.

For EIT, the continuous conductive medium can be described by the Maxwell equations as follows:

$$\nabla.(\sigma(\nabla V) = 0 \text{ in } \Omega \qquad 33$$

This governs the electrical potential V inside the domain Ω with the electrical conductivity σ. In EIT, to simulate the stimulus/response process (I/V), we have a boundary condition given by:

$$\sigma.\frac{\partial V}{\partial n} = \bar{J} \text{ on the boundary } \partial\Omega \qquad 34$$

where $\bar{J}$ is the normal component of electric current flux. So, for the EIT system, if the

injected current J for every node is known, Maxwell's equations (Neumann boundary conditions) can be solved if the conductivity distribution of σ could be pre-defined, which means V can be found. Then the voltage distribution V_n (voltage at each node) can be calculated by solving the Dirichlet problem (with Dirichlet boundary $V|_{\partial\Omega} = V_n$). In this case, we use the FEM to pre-define the conductivity distribution. Variational methods, which are similar to FEM in that the governing equations (here Maxwell's equations) in matrix form on a continuous conductivity medium can be evaluated. The geometry of electrodes and nodes present in the FEM is preserved in the physical phantom made up of resistors. In order to make it easy to calculate the value of the resistors the following procedure is used: (i), the FEM is used to calculate the conductivity of each element in the matrix; (ii), these conductivity elements are then replaced by resistors with the same conductance.

The Sussex EIT system has 85 electrodes. The phantom is also designed to have 85 electrodes over a planar topology. We have employed a mesh of homogenous conductivity medium as shown in Figure 53. The FEM can offer a smaller discretization error by using triangular elements compared to FDM, which typically uses rectangular elements, which is a more complex implementation. Increasing the number of elements, realized by increasing the number of nodes in a domain gives a better model of the characteristics of the medium. In order to simplify the construction of the physical phantom it was built only with resistors. For this reason, we did not model the permittivity characteristics for the homogeneous medium using the FEM and include reactance effects. Our phantom is thus expected to show increased errors, with respect to the characteristics of the medium, at high frequencies.

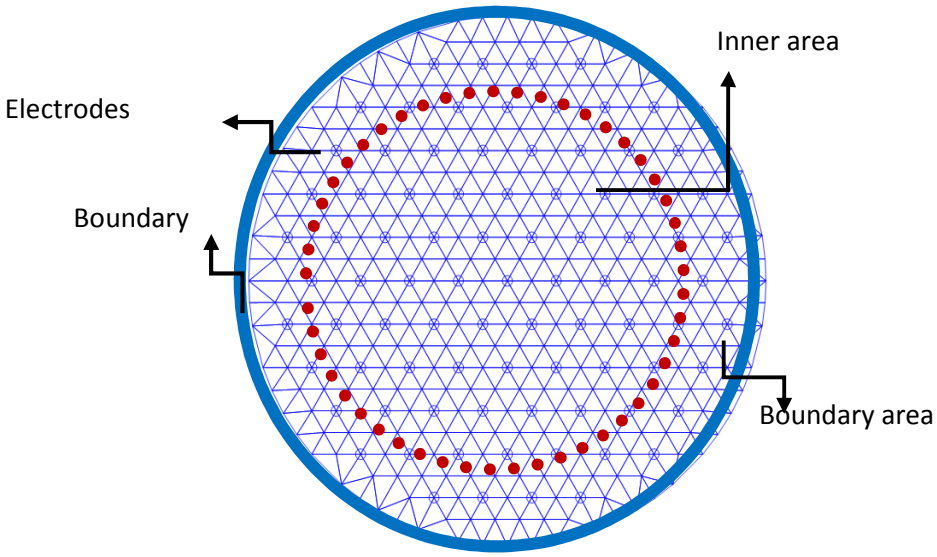

Figure 53 Electrodes and 2D mesh used in image reconstruction

Figure 53 shows a red-dotted line to separate the boundary and inner areas. This red-dotted line indicates the approximate separation between the high/low sensitivity areas. In planar topology, the sensitivity increases from the boundary to the inner area. Furthermore, it is difficult to detect an object when it is near to the boundary of the tank, in contrast to the ring topology in which the sensitivity decreases from the boundary to the inner area.

Based on FEM with linear interpolation, we will find the matrix of the conductivity, potential and current vectors. In order to find these matrices, first, we need to find the elementary matrix of conductance, potential and current vectors. In the next step, the global matrices will be produced by combining these elementary matrices together.

We have created a resistive mesh phantom using the same numbers of elements with the same coordinates as the nodes used in the FEM model, so we have the same accuracy with which to show an object.

We created this resistive phantom by placing a resistor at each edge of the triangular mesh used in the FEM. The values are based upon the FEM admittance results. We will improve the possibility of getting an accurate mesh phantom based on

this method.

In order to simplify the application of this method, we introduce a Sample Mesh Circuit (SMC) as shown in Figure 54. In this SMC, the local admittance area, the location of the electrodes and nodes can be used to produce the admittance matrices and then the voltage and current vectors.

A triangular element consists of three nodes located at the vertices of the triangle. This SMC consists of four elements defined by three nodes; in total it has six dedicated nodes. The value of admittance between each two nodes is represented by $Y^{e}_{n,m}$, since this is a region between three electrodes (see Figure 54), in total 6 nodes that consist of 9 admittances $Y_{(1,2)}$,$Y_{(1,3)}$,$Y_{(2,3)}$,$Y_{(2,4)}$,$Y_{(2,5)}$,$Y_{(4,5)}$,$Y_{(3,5)}$,$Y_{(5,6)}$,$Y_{(3,6)}$. Thus, the FEM method determines the distribution of admittance between three electrodes that have been formed by four elements.

A triangular element has been labelled to be identified. Then, identifying three nodes formed at the vertices of each element. This provides an array of elements with the node identification, where the j and k-coordinates of nodes are connected with regard to the location of the associated element.

In this regard, the symbol of n(i,e) is obtained, the location of the i^{th} node in the e^{th} element.

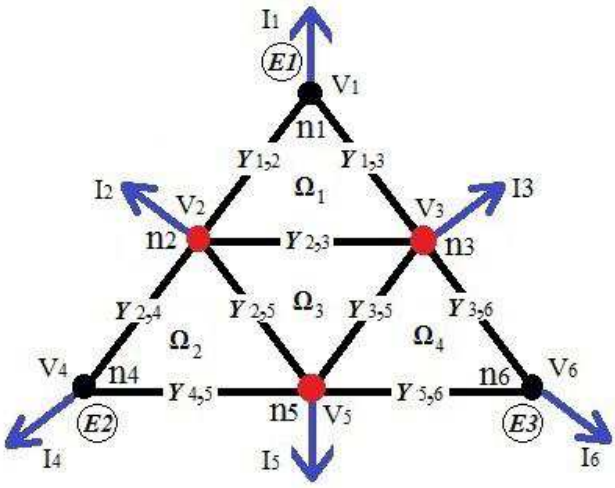

Figure 54 The sample mesh circuit composed of six nodes (n_1, n_2...n_6) and nine admittances $Y_{(n,m)}$, where V_n denotes the electrical potential at the n^{th} node, I_n denotes the current vector at the n^{th} node

c. FEM method process on network phantom

The numerical solutions of the master element in regard to SMC of Figure 54 can be found by the FEM method as shown in the following steps:

1. The numeration is assigned to produce n(i, e) for each element and node. The array n(i, e) can be numbered from node (1,2,3) of each element as declared in Table 9:

TABLE 9 THE NUMERATION NODE AND ELEMENT

e	n (1, e)	n (2, e)	n (3, e)
1	n_3	n_1	n_2
2	n_5	n_2	n_4
3	n_3	n_2	n_5
4	n_6	n_3	n_5

the numeration is assigned to produce the n (i, e) in which *i* is the node number and e the element number where n (1, e) right location, n (2, e) top location, n (3, e) left location (counter clockwise ↺)

Thus the Laplace equation:

$$\nabla.\sigma.\nabla U = 0 \quad (35)$$

$$\mathfrak{F}(U) = \frac{1}{2}\sigma \int_{\Omega} \nabla U.\nabla U d\Omega \quad (36)$$

where $\nabla U = U_i.\nabla \alpha_i$ thus

$$\mathfrak{F}(U) = \frac{1}{2}\sigma U_i \int \nabla \alpha_i \nabla \alpha_j d\Omega \, U_j = \frac{1}{2} U^T Y_{ij} U \quad (37)$$

where $U = a + bx + cy \Longrightarrow \begin{Bmatrix} U_1 \\ U_2 \\ U_3 \end{Bmatrix} = \frac{1}{4\Delta}\begin{bmatrix} 1 & x_1 & y_1 \\ 1 & x_2 & y_2 \\ 1 & x_3 & y_3 \end{bmatrix}\begin{bmatrix} a \\ b \\ c \end{bmatrix}$ then

$$U = [1 \quad x \quad y]\begin{bmatrix} 1 & x_1 & y_1 \\ 1 & x_2 & y_2 \\ 1 & x_3 & y_3 \end{bmatrix}\begin{bmatrix} U_1 \\ U_2 \\ U_3 \end{bmatrix}$$

Therefore $U = \sum_{i=1}^{3} U_i \,.\, \alpha_i(x, y)$

For each triangle element, the interpolation function of admittance Y^e is obtained from the specified point (n_i, i=1,2,3) $n_1(x_1,y_1)$, $n_2(x_2,y_2)$, $n_3(x_3,y_3)$ to produce the constant coefficients of a_i^e, b_i^e, c_i^e that are enforced by the numeration of n(i,e) as follows:

$$a_1^e = x_2^e y_3^e - y_2^e x_3^e \,, \quad a_2^e = x_3^e y_1^e - y_3^e x_1^e \,, \quad a_3^e = x_1^e y_2^e - y_1^e x_2^e \qquad 38$$

$$b_1^e = y_2^e - y_3^e \,, \quad b_2^e = y_3^e - y_1^e \,, \quad b_3^e = y_1^e - y_2^e \qquad 39$$

$$c_1^e = x_3^e - x_2^e \,, \quad c_2^e = x_1^e - x_3^e \,, \quad c_3^e = x_2^e - x_1^e \qquad 40$$

The element number is identified by the e^{th} element, where i=1, 2, 3 are the 3-nodes of the triangular element. The coordinate of the node n(i,e) is located by (x_i, y_i).

2. Apply boundary conditions for solving Δ^e (the area of the e^{th} element of the 2D triangular mesh), defined by the following equation:

$$\Delta^e = \frac{1}{2}\det\begin{vmatrix} 1 & x_1^e & y_1^e \\ 1 & x_2^e & y_2^e \\ 1 & x_3^e & y_3^e \end{vmatrix} = \frac{1}{2}(b_1^e c_2^e - b_2^e c_1^e) \qquad 41$$

The electrical potential function of the e^{th} element is approximated as follows, if linear triangular elements are used:

$$V^e(x,y) = (a^e + b^e x + c^e y) \qquad 42$$

where the value of $V^e(x,y)$ is for nodes residing in Ω^e of e^{th} element. Thus, for the

three nodes n=1, 2, 3, we have:

$$V^e(x,y)=\sum_{n=1}^{3}N_n^e(x,y)\,V_n^e \tag{43}$$

So, N^e is the interpolation function and obtained by:

$$N_n^e(x,y)=\frac{1}{2\Delta^e}(a_n^e+b_n^e x+c_n^e y) \tag{44}$$

where x, y are the coordinates of the n^{th} node, n =1, 2, 3 are the node numbers and e=1, 2, 3, 4 are the element numbers for the SMC as shown in Figure 54.

3. The admittance components of e^{th} element in matrix form Y^e is given where by the admittance between n and n+1 node is $Y_{n,m}^e$:

$$Y_{n,m}^e=Y_{m,n}^e=\frac{\sigma(b_n b_m+c_n c_m)}{4\Delta^e} \tag{45}$$

Thus for each element of 3 nodes:

$$Y_{1,1}^e=\frac{\sigma((b_1)^2+(c_1)^2)}{4\Delta^e}$$

$$Y_{2,2}^e=\frac{\sigma((b_2)^2+(c_2)^2)}{4\Delta^e}$$

$$Y_{3,3}^e=\frac{\sigma((b_3)^2+(c_3)^2)}{4\Delta^e}$$

$$Y_{1,3}^e=Y_{3,1}^e=\frac{\sigma(b_1b_3+c_1c_3)}{4\Delta^e}$$

$$Y_{3,2}^e=Y_{2,3}^e=\frac{\sigma(b_2b_3+c_2c_3)}{4\Delta^e}$$

$$Y_{1,2}^e=Y_{2,1}^e=\frac{\sigma(b_1b_2+c_1c_2)}{4\Delta^e} \tag{46}$$

The admittance matrix of the e[th] element is given by:

$$Y_{n,m}^{e}=\begin{bmatrix} Y_{1,1}^{e} & Y_{1,2}^{e} & Y_{1,3}^{e} \\ Y_{2,1}^{e} & Y_{2,2}^{e} & Y_{2,3}^{e} \\ Y_{3,1}^{e} & Y_{3,2}^{e} & Y_{3,3}^{e} \end{bmatrix}_{3*3} \quad (47)$$

Thus for the SMC with four elements (*e1:3,1,2; e2:5,2,4; e3:3,2,5; e4:6,3,5*):

$$Y_{n,m}^{1}=\begin{bmatrix} Y_{3,3}^{1} & Y_{3,1}^{1} & Y_{3,2}^{1} \\ Y_{1,3}^{1} & Y_{1,1}^{1} & Y_{1,2}^{1} \\ Y_{2,3}^{1} & Y_{2,1}^{1} & Y_{2,2}^{1} \end{bmatrix}_{3*3}, Y_{n,m}^{2}=\begin{bmatrix} Y_{5,5}^{2} & Y_{5,2}^{2} & Y_{5,4}^{2} \\ Y_{2,5}^{2} & Y_{2,2}^{2} & Y_{2,4}^{2} \\ Y_{4,5}^{2} & Y_{4,2}^{2} & Y_{4,4}^{2} \end{bmatrix}_{3*3}$$
$$Y_{n,m}^{3}=\begin{bmatrix} Y_{3,3}^{3} & Y_{3,2}^{3} & Y_{3,5}^{3} \\ Y_{2,3}^{3} & Y_{2,2}^{3} & Y_{2,5}^{3} \\ Y_{5,3}^{3} & Y_{5,2}^{3} & Y_{5,5}^{3} \end{bmatrix}_{3*3}, Y_{n,m}^{4}=\begin{bmatrix} Y_{6,6}^{4} & Y_{6,3}^{4} & Y_{6,5}^{4} \\ Y_{3,6}^{4} & Y_{3,3}^{4} & Y_{3,5}^{4} \\ Y_{5,6}^{4} & Y_{5,3}^{4} & Y_{5,5}^{4} \end{bmatrix}_{3*3} \quad (48)$$

The elementary matrix of the e[th] element is given by:

$$V_{n}^{e}=\begin{bmatrix} V_{1}^{e} \\ V_{2}^{e} \\ V_{3}^{e} \end{bmatrix}_{3*1} \text{ and } I_{n}^{e}=\begin{bmatrix} I_{1}^{e} \\ I_{2}^{e} \\ I_{3}^{e} \end{bmatrix}_{3*1} \quad (49)$$

where V^{e} represents the electrical potential and I^{e} current vector of e[th] triangle element. Thus we obtain:

$$I_{n}^{1}=\begin{bmatrix} I_{3}^{1} \\ I_{1}^{1} \\ I_{2}^{1} \end{bmatrix}_{3*1}, I_{n}^{2}=\begin{bmatrix} I_{5}^{2} \\ I_{2}^{2} \\ I_{4}^{2} \end{bmatrix}_{3*1}, I_{n}^{1}=\begin{bmatrix} I_{3}^{3} \\ I_{2}^{3} \\ I_{5}^{3} \end{bmatrix}_{3*1}, I_{n}^{2}=\begin{bmatrix} I_{6}^{4} \\ I_{3}^{4} \\ I_{5}^{4} \end{bmatrix}_{3*1} \quad (50)$$

4. By combining of Y_{i}^{e} for e: 1, 2, 3, and 4 and i=1, 2 ...6 with regard to the SMC Figure 54, the global matrix Y will be produced with the respect to the element of the element matrix of each sub-domain.

The global matrix Y generates a matrix of Y_{6*6} that will be produced through the

matrix of 4 elements and 6 nodes (e.g. we look for $Y_{1,1}$ in all element matrixes and placed location of that with the corresponding element number in the global matrix as this is $Y^1_{2,2}$). We obtain Y_{SMC} from $Y^e_{n,m}$ where e=1, 2, 3 and 4:

$$Y_{SMC}=\begin{bmatrix} Y^1_{2,2} & Y^1_{2,3} & Y^1_{2,1} & 0 & 0 & 0 \\ Y^1_{3,2} & Y^1_{3,3}+Y^2_{2,2}+Y^3_{2,2} & Y^3_{2,1}+Y^1_{3,1} & Y^2_{2,3} & Y^2_{2,1}+Y^3_{2,3} & 0 \\ Y^1_{1,2} & Y^1_{1,3}+Y^3_{1,2} & Y^1_{1,1}+Y^3_{1,1}+Y^4_{2,2} & 0 & Y^3_{1,3}+Y^4_{2,3} & Y^4_{2,1} \\ 0 & Y^2_{3,2} & 0 & Y^2_{3,3} & Y^2_{3,1} & 0 \\ 0 & Y^2_{1,2}+Y^3_{3,2} & Y^3_{3,1}+Y^4_{3,2} & Y^2_{1,3} & Y^3_{3,3}+Y^2_{1,1}+Y^4_{3,3} & Y^4_{3,1} \\ 0 & 0 & Y^4_{1,2} & 0 & Y^4_{1,3} & Y^4_{1,1} \end{bmatrix}_{6*6} \quad (51)$$

5. We need to solve Y.V=I formulation to produce an admittance matrix for the conductive medium. These values will be used for the electrical circuit mesh, where,

6. I is assembled from:

$$I_{SMC}=\begin{bmatrix} I^e_1 \\ I^e_2 \\ I^e_3 \\ I^e_4 \\ I^e_5 \\ I^e_6 \end{bmatrix}_{6*1}=\begin{bmatrix} I^1_2 \\ I^1_3+I^2_2+I^3_2 \\ I^1_1+I^3_1+I^4_2 \\ I^2_3 \\ I^2_1+I^3_3+I^4_3 \\ I^4_1 \end{bmatrix}_{6*1} \quad (52)$$

Therefore, we have produced the Y and I matrixes from corresponding elemental matrixes. Thus, by using the FEM method and knowing δF(V)=0 and equation (51), we obtain:

$$[Y][V]=[I] \quad (53)$$

7. From the global admittance matrix Y(n,m), we can extract each conductance G(n,m) value creating.

8. The resistance values R(n,m) between n^{th} and m^{th} nodes of the mesh phantom can be evaluated from the inverse of the conductance value of G(n,m) for each edge. This is a resistor network equivalent to an FEM model.

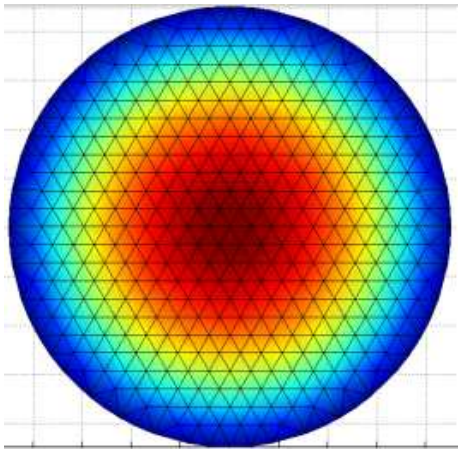

Figure 55 The image is made by the inverse created from the FEM method of the planar electrode plate

The electrical conductivity of the medium is symbolized by σ, (the electrical conductivity of the medium used for saline solution is assumed $\sigma = 0.5\mathrm{mS/cm}$).

The global matrix of the SMC obtained in equation (51) was based on solving Y.V=I formula and utilizing the FEM method. We used the same method to find the conductivity distribution and build a global matrix of resistors for the phantom. The global matrix $[Y]_{421\times421}$ is assembled from $[Y^e]$ with 421 nodes of 780 elements using the designation n(i,e) where n is the node number for (i=1, 2, 3,…, 421) and (x,y) is the coordinate of each node in the phantom element as the image is made by the inverse created from the FEM method shown in Figure 55. We number these elements from right node to top node, from the top node to left node and left node to right node in a counter anticlockwise direction and e is the element number of each sub domain (e=1, 2, 3,..., 780). We use this global admittance matrix to create a resistive mesh as illustrated in Figure 56 with the resistance value of each edge.

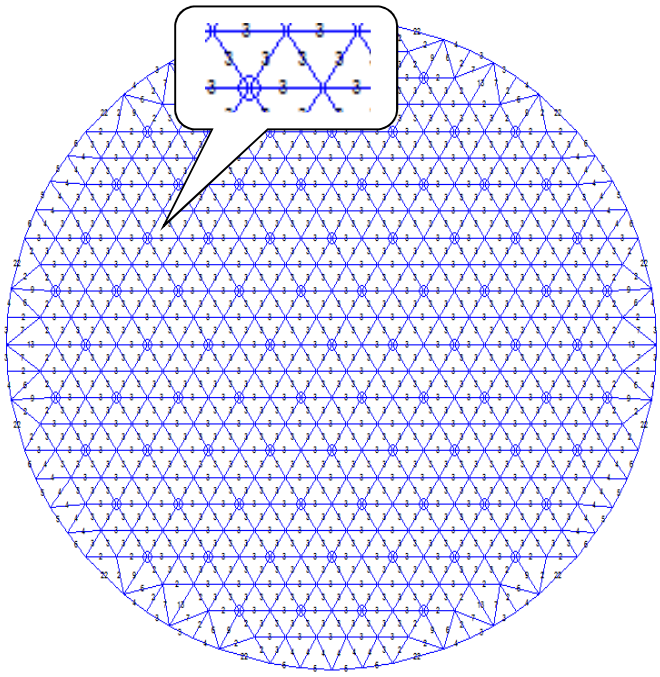

Figure 56 The Mesh phantom consisting of 780 elements and 421 nodes and 1200 resistors. The resistance values were found for the edges of the triangle mesh

By solving the $Y.V=I$ formulation we obtain the characteristics for a circular homogeneous conductive medium. The medium is discretised into 780 elements by using 421 nodes with 1200 edges. Each edge of a triangular element corresponds to a resistor. Table 10 shows the ideal (nominal) values determined from the FEM and the real parallel resistance values used. The resistors used had a 0.1% tolerance with the temperature coefficient: ± 25ppm/°C and power rating: 250mW.

TABLE 10 THE RESISTANCE VALUE

R Name	Quantity	Ideal (Nominal) value of R (Ω)	Real(Equivalent) value: $R_X \| \| R_Y = R_{EQ}$ (Ω)		
			R_X	**R_Y**	**R_{EQ}**
1	12	1153.05	1k3	10k2	1153.04
2	12	1263.45	1k27	243k	1263.39
3	960	2000.05	-	-	2000
4	12	1381.13	1k4	102k	1381.04
5	12	1385.01	1k4	130k	1385.08
6	12	1396.47	1k4	549k	1396.43
7	12	1414.43	1k43	130k	1414.44
8	6	1652.57	1k69	75k	1652.75
9	12	1726.57	1k78	57k6	1726.64

10	12	1846.72	2k49	7k15	1846.83
11	12	1860.88	1k87	383k	1860.91
12	12	2273.74	2k8	12k1	2273.82
13	12	2322.92	3k57	6k65	2322.94
14	12	2500.25	-	-	2500
15	12	2538.90	2k61	93k1	2538.82
16	12	2990.58	3k01	464k	2990.59
17	12	3392.48	3k4	1.54M (1%)	3392.51
18	12	3642.79	3k65	1.87M (1%)	3642.88
19	12	4277.55	4k53	76k8	4277.68
20	12	5019.27	8k06	13k3	5018.63
21	6	7592.66	8k25	95k	7592.70
22	12	12479.49	13k7	140k	12478.85

Nominal and real resistor values for the E-phantom resistors numbers as shown in Figure 56

d. Measurement sequence

Consideration of certain factors is required when you are preparing to collect data, find the inverse and construct an image. The quality of the inverse image is directly dependant on the number of measurement combinations, i.e. data points (Metherall, Barber et al. 1996, Brown 2003). One approach to improve the resolution is to increase the number of electrode sources and thus increase the number of independent measurement combinations. The Sussex EIT system consists of 85 electrodes and achieves 1416 independent measurement combinations based on 123 current injection combinations. The image that is constructed using this large number of measurement combinations could mean this system should have the ability to make clearer images.(Sze 2012, Wang, Wang et al. 2007b).

Our device achieves its measurement combinations for the planar electrode plate by using a hexagonal structure based on a 4-electrode method (there are two electrodes used as receivers for each channel injection and two electrodes used to inject a constant current). The constant current injector electrodes are located at the vertices of the hexagonal measurement shape. Figure 57 shows the measurement sequence of the planar EIT system for one hexagon shape.

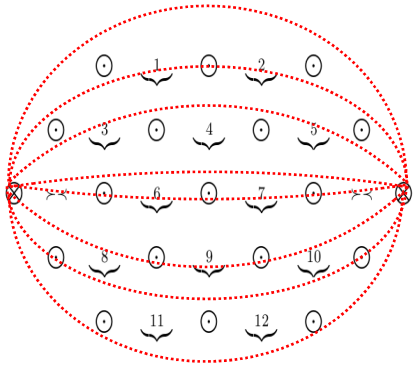

Figure 57 The hexagon combination table consists of 19 electrodes [⊙, ⊗]. The current injection electrodes are denoted by [⊗] and the voltage measurement electrodes are denoted by [⊙]. The hexagon 19 electrodes mesh is capable of giving 12 measurement combinations and denoted by $\underbrace{1-12}_{\text{Measurements}}$

The hexagonal measurement structure is an experimental result that shows that a suitable drive pattern for the planar electrode plate is a hexagon combination with the 19 electrodes forming 3 injection channels by using a 120 degree rotation around the x axis for each pair of electrode injections as shown in Figure 58. The drive electrodes (e.g. in Figure 58 the hexagon corners are e_1-e_{19}, e_8-e_{12} and e_3-e_{17} are drive electrodes) are always at a constant distance apart in any direction whereas the differential voltages (potential of 19 electrodes in 3D spatial) are measured between any two electrodes. This process is continued for all electrodes.

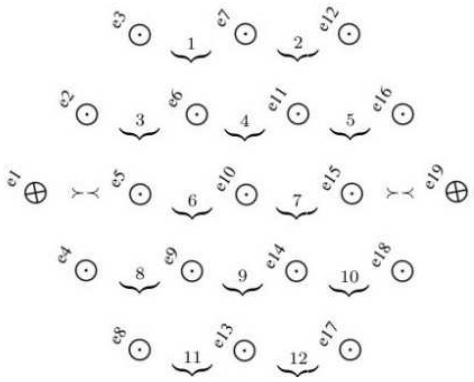

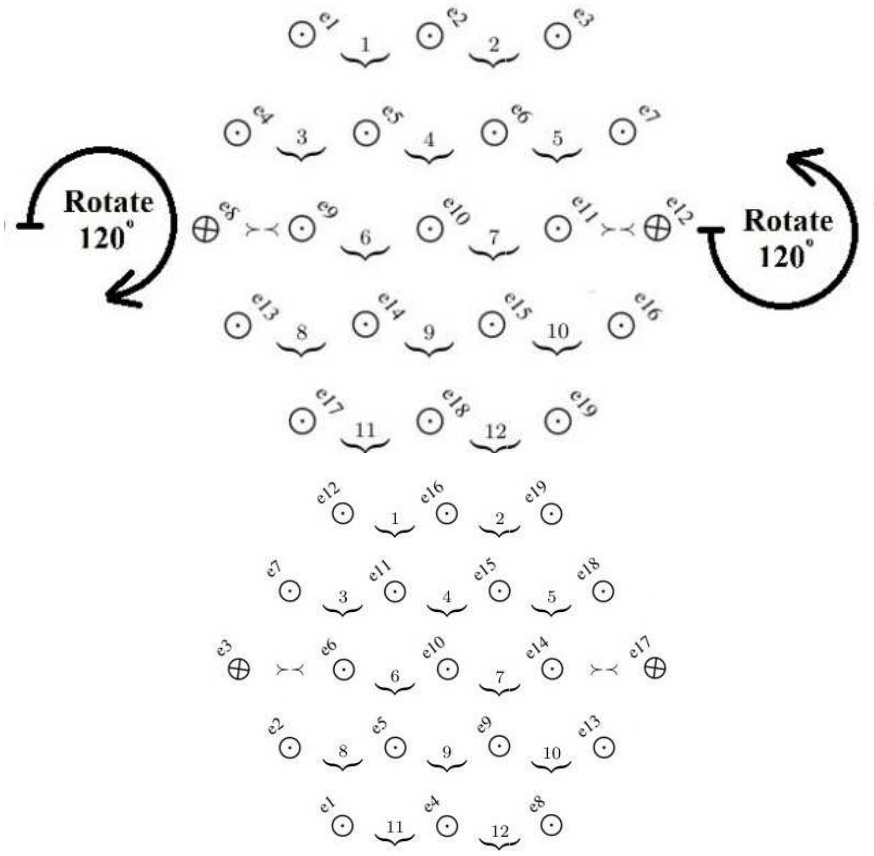

Figure 58 Measurement sequence used to acquire the EIT planar topology; e_n denotes electrode number n=1, 2... 85

In the measurement for each choice of two injection electrodes located in the inner area, there are 12 measurement combinations. If the injection electrodes are in the boundary area the hexagon pattern shown in Figure 57 cannot be shaped. In this case 9 to 12 measurement combinations will be used depending on the injection electrode locations.

It is worth noting that the Sussex EIT system has a dynamic range of the voltage measurement frames as shown in Figure 59. This plot presented 12 voltage measurements for a uniform conductivity medium with the 3D model is for a homogenous distribution of saline with 0.5mS/cm conductivity and 1mAp-p current injection. That's why the image obtained from the data of the phantom representing a uniform case with variation across is as shown in Figure 61, this method helps us to know the position of the error.

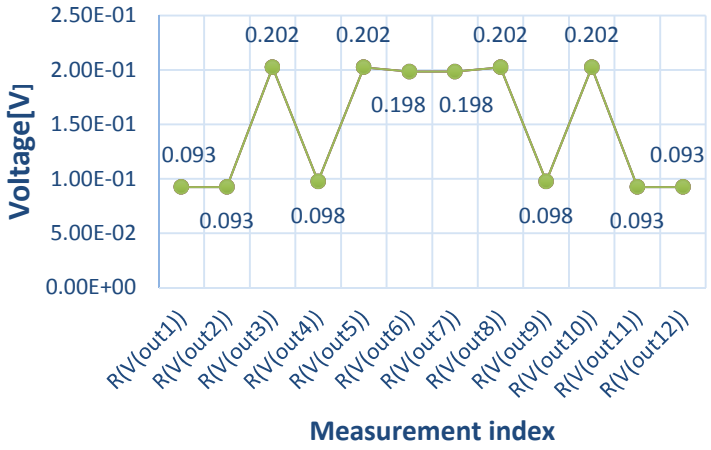

Figure 59 shows the 12 real voltage measurements of a current injection (current injection combination: 61, 62 and 63 measurement index: 691-702, 703-714 and 715-726, respectively) of a hexagon combination table consists of 19 electrodes. The Sussex EIT has a dynamic range of the voltage measurement frames.

5.6. Modelling the Resistive Phantom in OrCAD

As a next step, a simulation analysis process of the EIT system is used to validate the phantom that has been designed. The simulation mesh phantom used with OrCAD PSpice is shown in the schematic in Figure 60. This simulation design uses the same system of resistors as used in the resistor mesh used in the phantom.

Figure 60 shows a schematic view of the E-phantom design using the OrCAD PSpice simulation. The E-phantom simulation uses 85 electrodes based on triangular structures with hexagonal measurement combinations. Resistors and electrodes are simulated using models available in OrCAD. The schematic circuit uses the resistor values as shown in Table 10. The simulation allows us to examine the non-ideal behaviour of the source, model the noise of the system caused by the tolerance of the resistors used and so provide a worst case analysis and by varying the values in certain areas of the phantom simulate the variation of conductivities in different portions of the phantom. The E-phantom simulation has been tested with the test scheme that would be used in an EIT system.

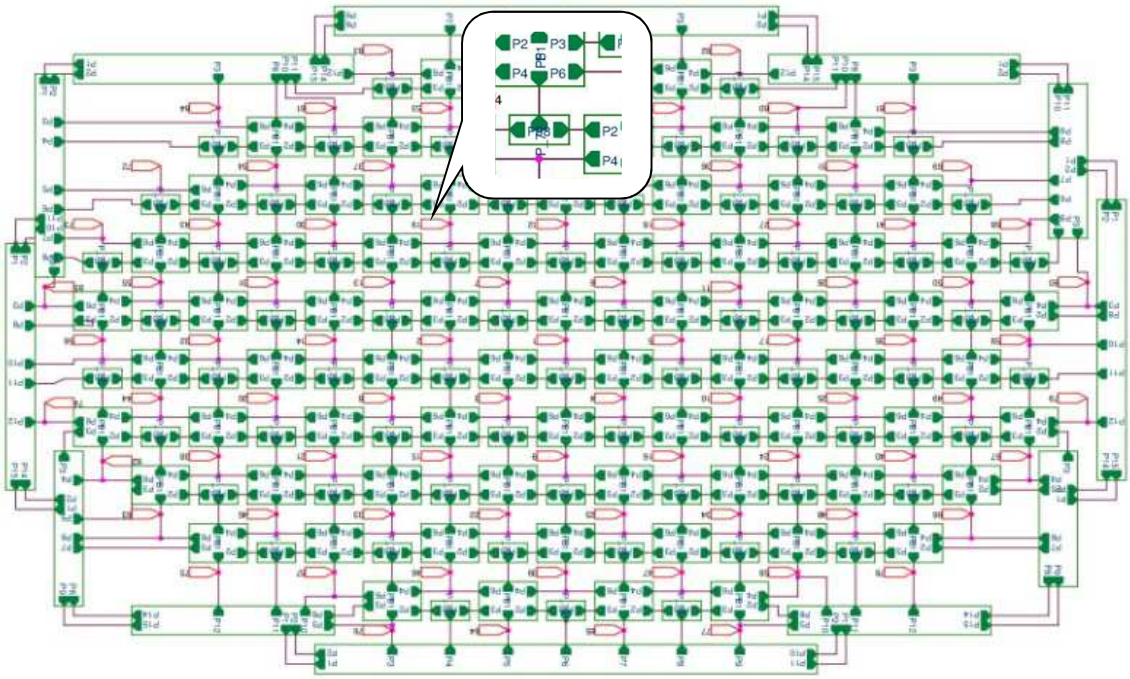

Figure 60 The schematic of the Mesh phantom

The simulation system is established to generate and measured data (acquire data) using the measurement sequence illustrated in Figure 58, which is the same as used in the actual EIT system, where each pair in opposite corners of the hexagon forms an injection channel pair.

The measurement results are fed to the image back projection reconstruction algorithm to produce a conductance image for the homogenous conductive medium. In this regard, the image of the conductivity has been produced by image reconstruction software as shown in Figure 61 with 123 injections and 1416 measurements. This image is assumed to be ideal back projection data obtained from the dynamic measurement.

In reality, resistors are not ideal, but have a very small series lead inductance and have a parallel capacitance of around 0.3pF. We have ignored these effects in our system.

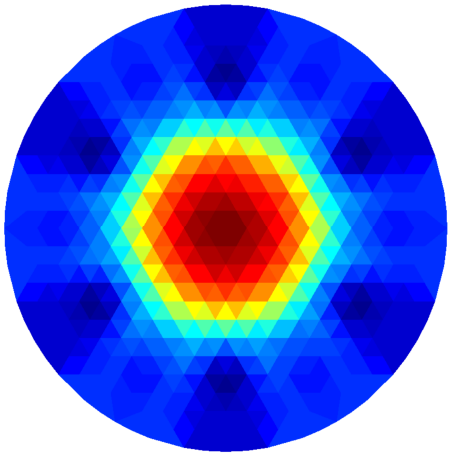

Figure 61 the image is made by the inverse created from OrCAD simulated results of 1416 measurements simulating a homogenous medium.

The image acquisition of the E-phantom is based on the acquisition of 123 data frames, each consisting of a maximum of 12 measurements a result is shown in the simulation shown in Figure 61. In order to attempt to produce an accurate simulation model for the physical homogeneous conductive medium, standard resistors are used in parallel to optimise their equivalent value being close to the FEM calculated value. This image is assumed to be back projection data.

In addition, the resistors used have temperature coefficients of approximately ± 25ppm/°C and manufacturing tolerances of 0.1%. In order to consider this tolerance we have used Monte Carlo analysis in OrCAD PSpice simulation. The Monte Carlo analysis allows examination of the effects on the performance of the E-phantom when the resistor values are varied within the band of their tolerance. We have used the Monte Carlo analysis with 100 runs, with the Gaussian distribution and with 17366 as the random seed number to achieve the average theoretical signals as shows in Figure 62.

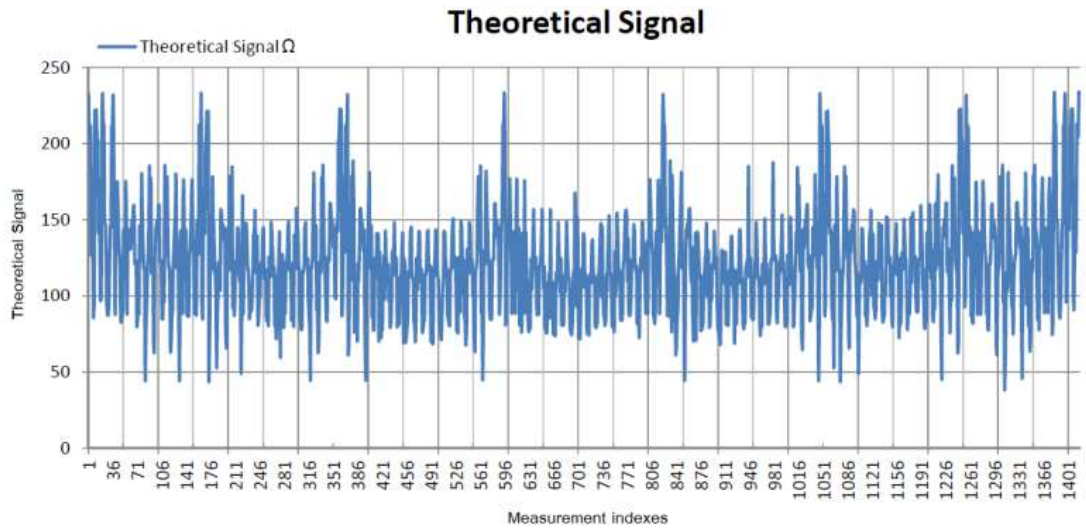

Figure 62 The average theoretical signals (Ω)

This work extends to designing an E-Phantom that simulates the existence of small impedance differences (such as the capacitive effect of different tissues) immersed within a homogeneous medium over a planar topology. A number of properties were taken into consideration during the design of the phantom based on the phantom's spatial characteristics relevant to the assessment process. We used the Sussex EIT planar topology, to give a difference in the measurement impedances, the electrodes of the drive pairs are at the same distances relative to each other (always three electrodes between each two electrode injections in the high current flow direction), but presenting the device with varying measurements across the planar electrode plate in one measurement combination, it is called a dynamic measurement system. Hence, a set of measurement impedances is used as initial potentials of pure impedance saline at the first data collection stage in order to assess the system. Although, in multi-frequency systems, there is no need to have a set of data from a homogeneous medium as a reference data set and we can use a set of data at one frequency point as a reference data set (Fitzgerald, Thomas et al. 1997).

5.7. RSC model

The Cole-Cole impedance model is utilized to describe characteristics of the electrochemical properties of biological tissue with frequency dependent (Cole, Cole 1941, Cole, Cole 1942). The model is created by using three electrical components of R,

S and C. R and S being resistors (extra- and intra-cellular resistances), C being a capacitor (membrane capacitance). From the experimental tissue values extracellular media is purely resistive, where the resistor R dominates the effect mainly at low frequency (zero frequency) since all currents flow through the extracellular resistance. Resistor S and capacitor C come into effect at high frequency (infinite frequency) when the current that flows through the capacitance of the cell membrane produces an isolating layer for intra-cellular resistance. Hereafter in this research this model will be referred to as the RSC model. The phantom is able to incorporate RSC models between electrodes to simulate tissue. Figure 63 shows the RSC circuit model that is used in the E-phantom.

In this case, a set of constant current sources applied in a homogeneous conductive medium with conductivity of σ. In principle, it is sufficient to solve equation (33) in the homogenous media, for the sample tissue to obtain the frequency dependent of tissue. Thus, including the frequency dependent of electrical parameters such as frequency dependent of conductivity σ_ω enables the model to capture all range of physical phenomena. Thus, we obtain:

$$\nabla.\sigma_\omega.\nabla U=0 \qquad 54$$

Then solving this equation as it is a frequency dependent in homogeneous media. The impedivity data (or dispersion data) extracted from injection currents and voltage measurements in the EIT system and compared with the impedance results that are determined using the Cole-Cole equation when the RSC models are placed between electrodes to simulate the impedance of different tissues at different frequency points. Thus the impedivity data produces frequency dependent electrical properties. To validate these results, we have also simulated the electrical properties of tissues by using a RSC model and measuring the complex impedance between two electrode points in our OrCAD simulation similar to compared with the actual EIT measurement data.

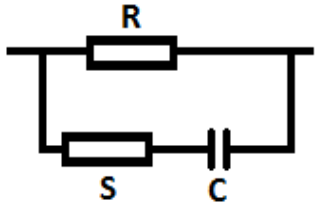

Figure 63 Equivalent electrical circuit model for Cole-Cole equation

The Cole-Cole equation for the Figure 63 is:

$$Z = R_{\infty} + \frac{(R_0 - R_{\infty})}{1 + (\frac{jf}{F_r})^{(1-\alpha)}} \quad 55$$

where R_{∞} represents the tissue resistance as the frequency approaches infinity and R_0 represents the tissue resistance as the frequency approaches zero (for direct current), F_r corresponds to the relaxation frequency and α symbolizes the relaxation time. In the RSC model, the extracellular resistance R is equal to R_0 in the Cole-Cole equation and the resistance of the intracellular tissue is called S, where paralleling R with S (R||S) results in the high frequency resistor R_{∞}.

Considering Carcinoma, Fat and Stroma tissues in a cube shape with the dimensions of 10mmW×10mmD×10mmH, with a uniform flow of electric current then the electrical resistance is defined by the following equation:

$$R = \rho \frac{L}{A} \quad 56$$

where ρ, L and A are resistivity, length and cross section area of tissues, respectively. The relaxation frequency of tissues is defined by:

$$F_r = \frac{1}{2\pi C(R+S)} \quad 57$$

The electrical properties of Carcinoma, Fat and Stroma are produced by introducing the RSC circuit model into the E-phantom. Table 11 shows three different

tissues that we have selected to use in the E-phantom (Wang, Tang et al. 2001, Qiao, Wang et al. 2007, Jossinet 1998).

TABLE 11 THE COLE-COLE PARAMETERS OF THE DIFFERENT TISSUES

Tissue	R(Ω)	S(Ω)	C(F)	F_r	α
Carcinoma	3.89	0.99	6.83E-8	477kHz	0.54
Fat	23.9	69.69	7.87E-9	216kHz	0.43
Stroma	13.62	28.8	8.37E-9	448kHz	0.49

The different electrical properties of the Carcinoma, Fat and Stroma tissue of the breast that is cubic and has the dimensions of 10mm *10mm*10mm

We are using the RSC models in 6 places; each is inserted as a target individually inside one of the segments. Figure 64 shows the RSC model locations that are introduced into the E-phantom.

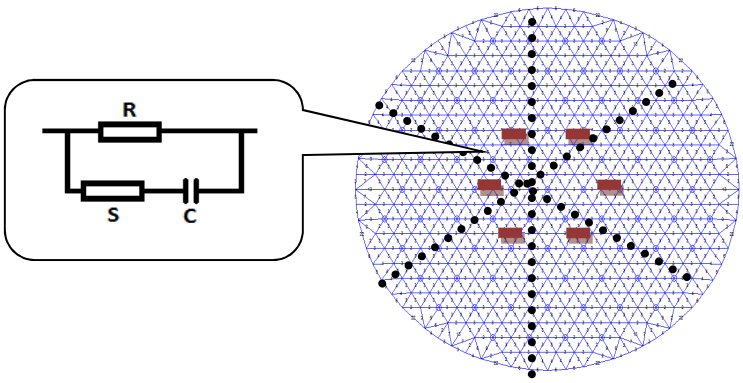

Figure 64 The RSC location inside of each segment as an object. The object has been placed on layer 1 (bottom layer) with high conductivity distribution layer.

5.8. PCB Phantom board

The FEM is programmed in MATLAB based on the same framework of elements that are exploited in the reconstruction algorithm. This program generates a mesh phantom based on a global admittance matrix. The E-phantom PCB was built based on the FEM design that has been explained in a previous section. Figure 65 and Figure 66 show the top and bottom layers of the E-phantom PCB designed for the schematic of Figure 64. The PCB is fabricated on a circular board with an 83mm radius fitted with 85 electrodes.

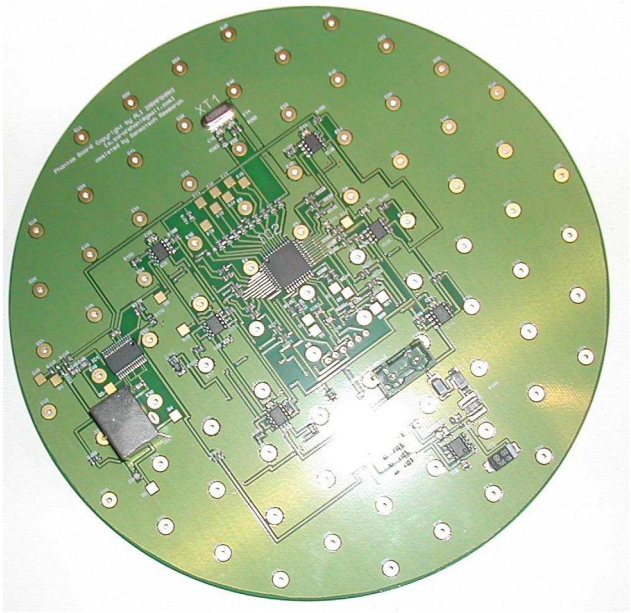

Figure 65 top layer of Mesh Phantom PCB

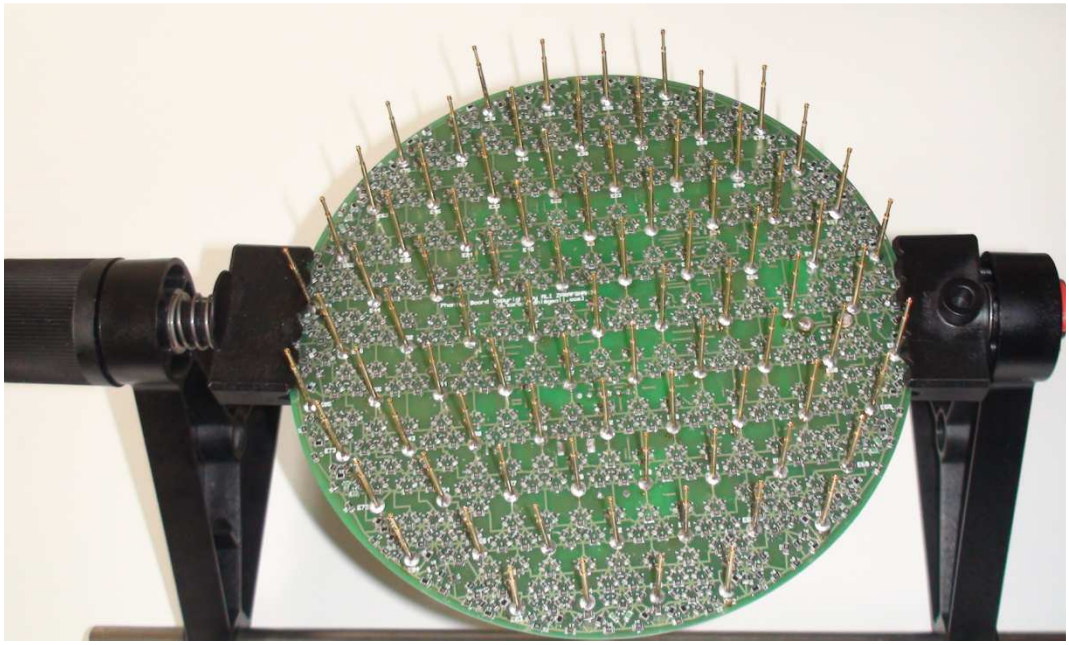

Figure 66 bottom layer of Mesh Phantom PCB

This PCB is fitted with the 1200 resistors as mentioned in Table 10 with resistors of 0.01% to ±0.05% tolerance and temperature coefficient of ±25ppm/˚C. For 456 resistors, each two resistors are matched to an equivalent resistor ($R_{EQ}=R_X||R_Y$) with a tolerance target of ±0.2%. Each pair of selected resistors has been manually measured to ensure that the parallel combination is within the ±0.1% tolerance of the nominal value.

The E-phantom connects to the EIT electrodes by means of 85 spring-loaded, stainless steel electrodes with gold plated tips. The tip style is a 6-points crown with a higher set middle point. Its internal resistance is less than 20mΩ (INGUN GKS-100 224 130A 2000E) as shown in Figure 67. The electrodes are inserted to a small depth (~2mm) into the electrode plate. The electrodes are exactly the same as the electrodes used in the real EIT system (DATA SHEET-INGUN 2004).

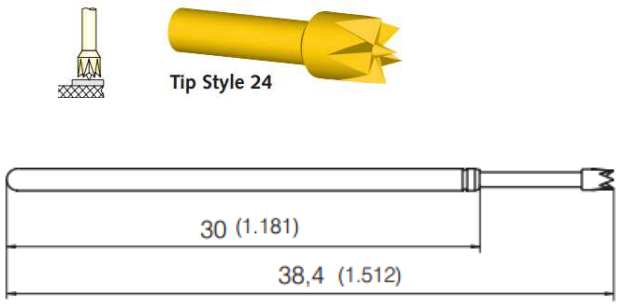

Figure 67 Electrode style and dimensions, Tip style 24 which has 6-point Crown with higher set middle point (DATA SHEET-INGUN 2004)

We have not taken into consideration the size and shape of the electrodes in the FEM use to find the resistors of the E-phantom and we have ignored the complex impedance behaviour of the INGUN electrodes used to connect the EIT board electrode nodes to the E-phantom electrodes. The INGUN GKS-100 electrodes have very low contact resistance ≤2mΩ so they should have little effect.

We have utilized six DCPs (digital potentiometers X9C10x, Xicor Inc.) in order to produce different resistivities in the phantom. The E-phantom has been divided into six segments where this variable resistivity can be applied. We can change the resistivity of each segment of the planar electrode plate by using the variable resistor (DCP) located between two nodes in each segment. This scheme allows us to employ the DCP modules to produce localized conductivity perturbations in the phantom i.e. the simulated medium, which can be easily implemented and controlled.

Chapter 6 Simulation and experimental results for the current source with stray capacitance cancellation method and using E-phantom for assessment and validation of the AZ1 EIT system

6.1. Introduction

In this chapter simulation and experimental results are presented for a capacitance cancellation system to address its use in the AZ1 EIT system using two types of current sources: *i)* the voltage-based (improved Howland) and *ii)* current-based (current conveyor) current source structures.

The simulation and experimental results for each of the current source structures are presented to address a clearly specified system design and operational issues (mainly the cancellation of capacitance effects).

We also used a phantom composed of resistors and microprocessor controllable switchable passive components to evaluate the ability of the AZ1 EIT system to distinguish significant system objects such as cancerous parts of the target volume.

As previously mentioned, the Sussex EIT system is based on a four-electrode technique; where two electrodes that are driven 180 degrees out of phase inject with a fixed current through multiplexers to the subject (two current branches are utilized) and the other two electrodes are used to measure the voltage. This is repeated at

multiple-frequencies and each current branch switched between 85 electrodes. The target volume is contained in a cylindrical container with the electrodes on the bottom surface.

In chapter 4, I have shown that the use of two different multiplexers in series, called a cascading configuration, for the direction of the current from a current source to an electrode gives the lowest total switch capacitance $C_{ON/OFF}$ = 20.8pF, in each injection channel. These capacitances are paralleled by additional stray capacitance of the measurement system (i.e. $C_{TOTAL} = C_{ON/OFF} + C_{STRAY}$). Two OCCII-GICs are used for the two 180 degrees out of phase current branches to cancel these unwanted capacitances.

A simulation model was constructed of the current source used and the chosen capacitance cancellation system in order to determine the best component values and circuit architecture needed.

Experimentally in order to show the performance of the current sources and chosen capacitance cancellation system, we have attached a variable load and used an oscilloscope probe to measure the output voltage (i.e. injection current value = V_{OUT}/R_{LOAD}). The probe caused some effects. Table 12 shows the characteristics of the probe used to calculate the output current ratio of the sources by measuring the output voltage of the attached dummy load when showing the actual results on the oscilloscope.

TABLE 12 PROBE CHARACTERISTICS

Type	Attenuation	Bandwidth	Comp. Range	System Input Resistance	Typical Input Cap.	Input RMS
Tektronix P6109B*	10X	100 MHz	15pF to 35pF	10MΩ	13pF	300V RMS CATII

*With instruction manual (070-7849-06)

We added input capacitance of the probe to the simulation model. We eliminated the EIT source by a simulation model of the current source when attached

to a load and a stray capacitance as follows: $C_{STRAY}=C_{PROBE} + C_{ON/OFF} + C_{SOURCE} + C_{STRAY\text{-}of\text{-}the\ PCB}$.

The simulation circuits (schematic captures) used Cadence OrCAD Capture release 16.2.0 and simulation models using PSpice A/D 16.2.0, with a spice Macro-Model of the AD844 Rev. A and OPA656 Rev. A with the simulated resistors had a tolerance of 0.01% paralleled with a capacitance of 0.3pF estimated to be that of a SMD resistor on an FR4 PCB board with standard size pads (that generally is created on a circuit board across a resistor).

We used a function generator able to produce a sine wave signal with a variable amplitude operating over a frequency range of 10 kHz up to 5MHz and a digital scope with a SNR of 80dB (as has been tested and has the required accuracy for our measurement procedure).

We used the channel settings in the scope as follows: the probe attenuation 10:1 with ratio 1:1, input impedance of the probe 1MΩ, with a bandwidth of the scope connector equal to 35MHz, and bandwidth of the probe equal 60MHz.

Since one of the advanced measurement techniques is specifying circuit behaviour. We compared the simulation and experimental results using the following steps:

Step 1) Showing the simulation result of each source without attaching the OCCII-GIC circuit in order to approximate the output capacitance for the source as an expected experimental result.

6.2. Output Capacitance of the Current Source

As a first step in understanding the current source behaviour we measured the output impedance of the current sources in simulation. Hence, I simulated the improved Howland current source and current conveyor current source and measured the simulated output capacitance and resistance of these sources and compared them with a perfect current source (ideal source) available in the Cadence OrCAD simulator.

The measurement was done by experimentally adjusting PSpice using the capacitance and/or resistance until the curves (as the frequency was swept) of the simulated current sources graphically matched those of an ideal current source with additional parallel resistance and capacitance. The schematic diagrams used are shown in Figure 68.

Figure 68 (a) compares an ideal current source and an improved Howland current source with an attached load of 10kΩ. Figure 68 (b) shows a current conveyor current source when it is compared with an ideal current source.

I experimentally and graphically measured the output voltages of the two sources and compared them with the ideal current source in order to estimate the output capacitance of each source. Figure 69 (a) and (b) illustrate the result of the estimated output capacitance by adjusting the capacitance (C_S) in parallel with the perfect current source until the curves with changing frequency meet that of the tested current source.

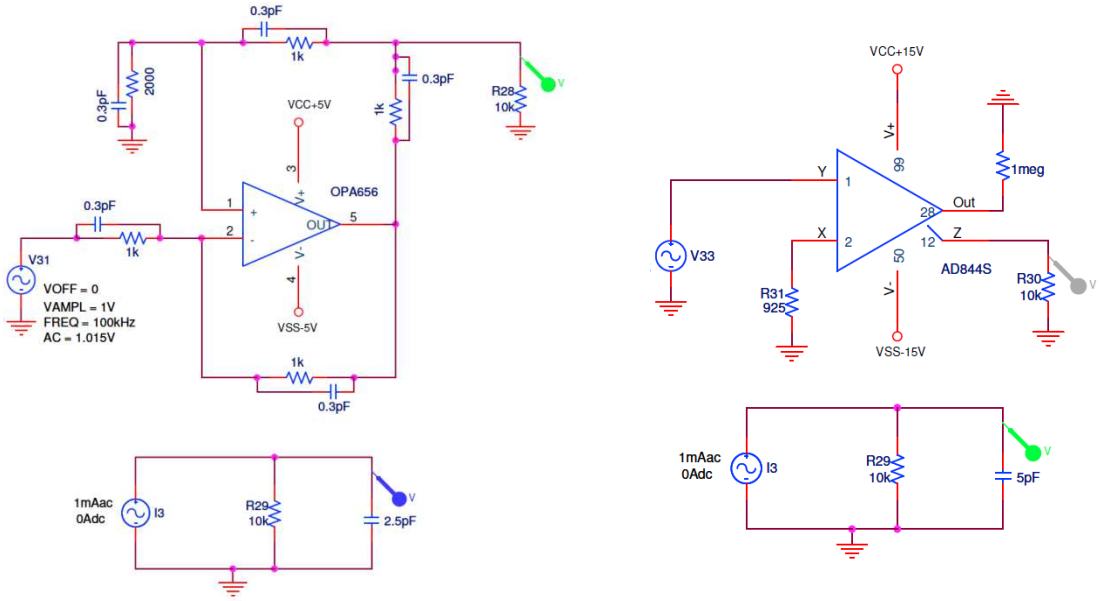

(a) (b)

Figure 68 shows two schematic diagrams (a) and (b) that compare the perfect current source with (a) improved Howland current source and (b) current conveyor current source to measure the output capacitance of each of the sources when attached a 10kΩ load.

We found the output capacitance of the C_S = 2.5pF and 5pF, respectively for the improved Howland and current conveyor current sources based on the simulation results as shown in Figure 69.

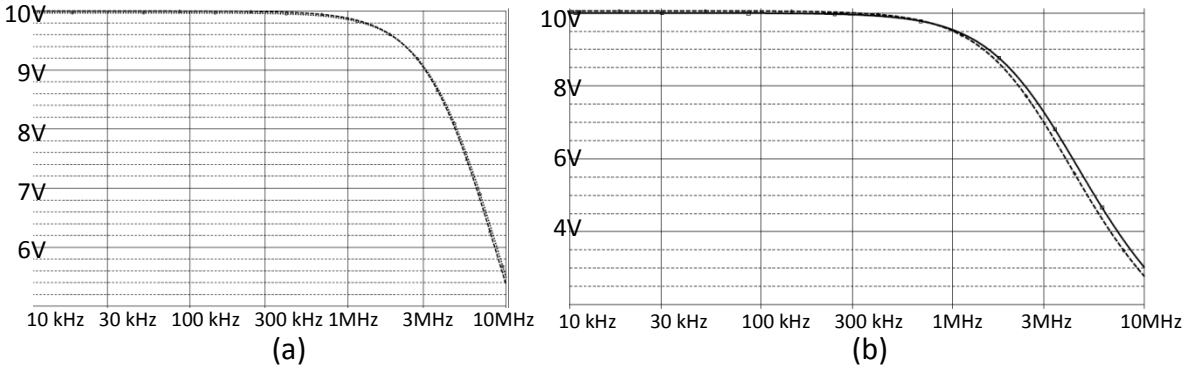

Figure 69 shows the simulation result of the schematic capture of the current sources (dotted-line) compared with perfect current source (line) to measure and confirm the source capacitance of each source, C_s=2.5pF (left graph shows the improved Howland source) and C_s=5pF (right graph shows current conveyor current source).

We wondered what changes we could make by altering R_S and C_S. We found a few improvements in the current sources by adding resistors and capacitors as shown in the new schematics in appendix-C.

Step 2) Simulating two sources with the effect of capacitances (i.e. source, stray and probe capacitances). These results show the measurement output voltages that we expect to measure in the experimental curves.

Here, we simulated two sources with an extra dummy capacitance (as stray capacitance plus source capacitance) when a load is attached. We then compared it with the input signal (as a reference signal) and output signal without the effect of any capacitance, as shown in Figure 70. This simulation is based on the actual probe characteristics (as shown in Table 12) and source capacitances that we expected based on the previous test.

In regard to above results, the source capacitance of the improved Howland and current conveyor current source are equal to 2.5pF and 5pF respectively. Then, the probe capacitance is added to these capacitances. Thus, in the case of the

improved Howland current source this capacitance is equal to 2.5pF as a source capacitance and 13pF as a probe capacitance (type) which in total is equal to 15.5pF and in the case of the current conveyor current source it is equal to 18pF.

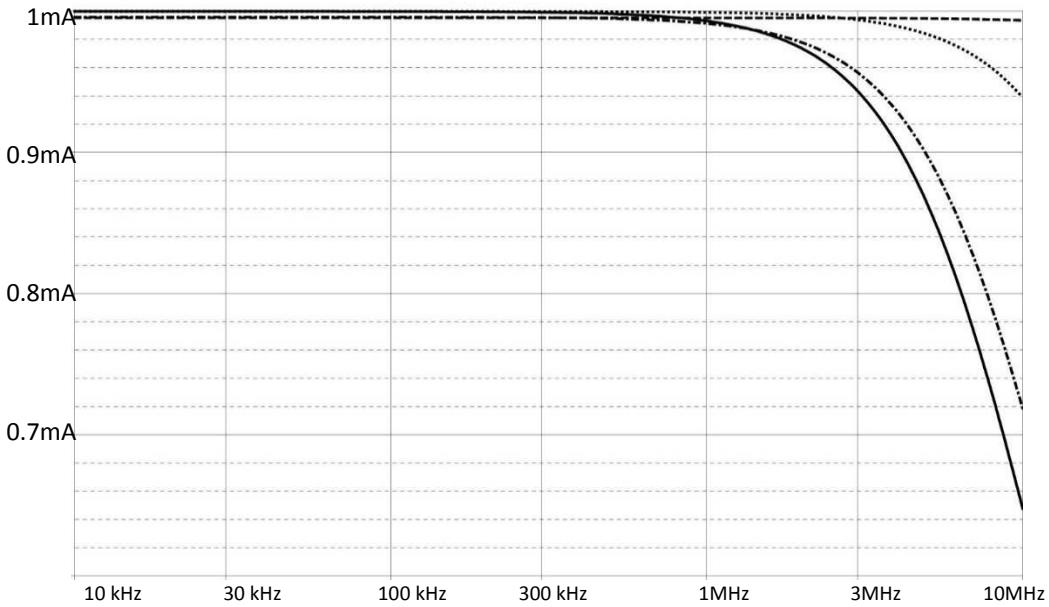

Figure 70 shows three output currents of the different current sources, dashed curve (-----) shows output current of the improved Howland current source without stray capacitance effects and a 1kΩ load, dotted curve (…….) shows the output signal of the current conveyor current source without stray capacitance effects when it attached to a 1kΩ load. These curves only show the effect of source capacitance (C_S). Dotted and dashed curve (._._.) shows the output signal of the improved Howland and lined curve (____) shows current conveyor current sources with the effect of the probe and source capacitances, which consists of a source capacitance of (i.e. 2.5pF or 5pF) plus probe capacitance of 13pF (type) which expected equal to C_X=15.5pF and 18pF.

6.3. The current source with stray capacitance

The expected parasitic capacitance of the current source is equal to C_{PROBE} + $C_{ON/OFF\text{-}DRV\text{-}MUXs}$ + C_{SOURCE}. Thus the expected parasitic capacitance is equal to 13pF (probe input capacitance) + 20.8pF (DRV MUXs) + 2.5pF (improved Howland current source) = 36.3pF and in the case of the current conveyor current source 13pF (probe input capacitance) + 20.8pF (DRV MUXs) + 5pF (improved Howland current source) = 38.8pF. We illustrated the effect of these capacitances for each of the sources. Figure 71 shows the expected results for these current sources with expected stray

capacitances (i.e. C_X=36.3pF and 38.8pF) when it attached a load of 1kΩ (thus if output voltage signal measured from a 1kΩ load is equal to 1^{Vp-p} this means the current source injects 1mA into the attached load, $1^{V}/1^{k\Omega}=1^{mA}$). So, these simulation results show the expected experimental result for improved Howland current source and current conveyor current source, therefore the total stray capacitance affecting our measurement results is equal to 36.3pF and 38.8pF.

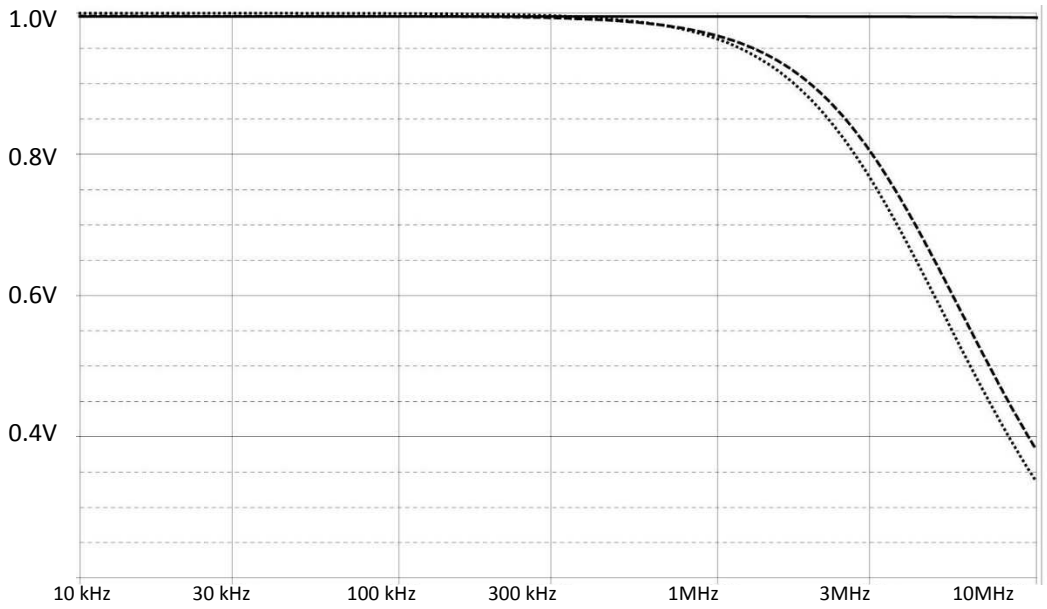

Figure 71 shows the simulation results of different between the input (—) and output signals of the improved Howland and current conveyor current sources with a load of 1kΩ (e.g. $1^{V}/1^{k\Omega}=1^{mA}$) when the input signal is 1^{V} and the output signal is affected by a parasitic capacitance equal to 36.3pF (---) and 38.8pF (….) respectively for these two sources.

Step 3) Comparing the result of the experimental test coming from the actual circuit board and the expected results such as parasitic capacitance measured from the schematic captures. I measured the output signals by using the oscilloscope and took snapshots to show these results as experimental results.

6.4. Experimental output signal of the current sources

First, I needed to calibrate the function generator and oscilloscope including the probes by making a close loop when connecting directly the function generator to the oscilloscope via the probes and measuring the same value of the amplitude that is set on the function generator and make sure that probes are accurate as much as

possible, in our case we measured by a difference less than 1mV. The next step is calculating the SNR of the two devices. We calculated the SNR of the oscilloscope by connecting the $0^{Vp\text{-}p}$ and $2^{Vp\text{-}p}$ amplitude over different frequency ranges and using the following equation:

$$\mathrm{SNR} = 20\log\left(\frac{\mathrm{V_{signal}}}{\mathrm{V_{noise}}}\right) = \frac{2_V}{200_{uV}} = 80dB \quad (58)$$

I found a SNR of 80dB is obtainable in the frequency range of 10 kHz to 5 MHz, based on several experimental results. Thus, the experimental time domain analysis measurement results of the current sources with a dummy load for a sweep frequency starting at 100 kHz and stopped at 1MHz frequency with steps of 100 kHz and a sweep frequency starting at 1MHz which stopped at 5MHz with steps of 500 kHz were used. The amplitude of the input signal was set for a sine waveform of 0.5^{V} or $1^{Vp\text{-}p}$ to achieve $1^{mAp\text{-}p}$ output current signal when attached a load of 1kΩ (i.e. the amplitude of the input signal equal to 0.5^{V} thus $1^{Vp\text{-}p}/1^{k\Omega}=1^{mAp\text{-}p}$).

I then measured the output signals for these two different scenarios:

Test-I the current sources effects with all parasitic capacitance (such as source, probe, PCB, and component parasitic capacitances) apart from the on/off capacitance of the drive multiplexers and electrode capacitances. Then we measured the load voltage of a dummy load (1kΩ with 10% tolerances [here is 918Ω]).

Test-II connecting total stray capacitances and combining with the OCCII-GIC circuits as a stray capacitance cancellation method and measuring the voltage of two different dummy loads when placing the probes at the electrodes.

Test-I

The following test expects to achieve similar results when the output current of the current source is affected by the source capacitance, probe capacitance when a load (1kΩ with a tolerance of 10%) is attached. In this test, we attached a resistor of R_{LOAD}=918Ω by placing the probe to measure a load voltage with the room

temperature (25^{o}C). By the load voltage and knowing the load resistor value, thus we were able to calculate the value of the current.

Figure 72 shows the test configuration of a function generator, current source, oscilloscope and probes. We used a t-connector to able to directly connect the input signal to the scope to compare the reference signal and measurement output signal.

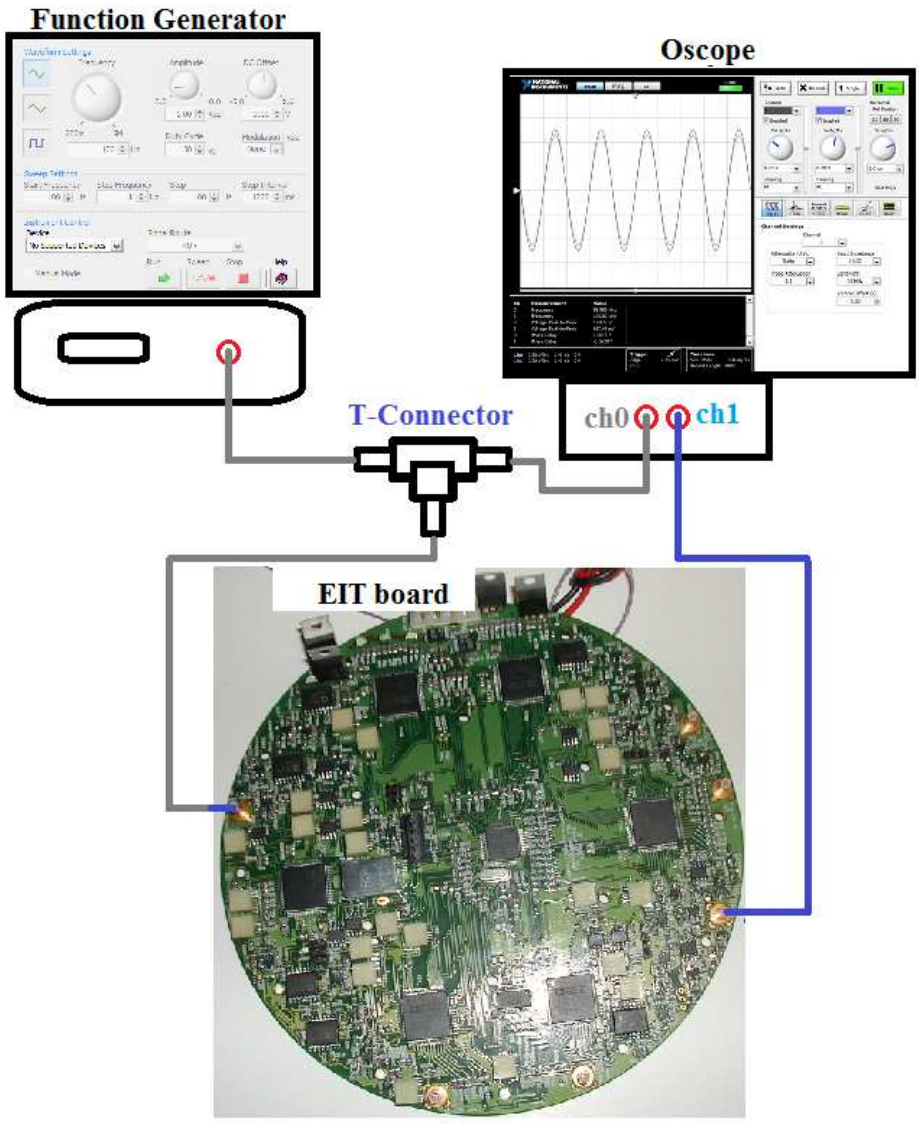

Figure 72 Test schematic configuration

Figure 73 shows snapshots from the oscilloscope when the function generator produces a sine wave of 1$^{Vp\text{-}p}$ (Amplitude = 500mV) at different frequency points to confirm the input signal on the signal generator and output signal of the improved Howland current source (x10) on the scope as the test schematic shows in Figure 72.

The current source is affected by the stray capacitance of the probe, and source. Although we adjusted resistor R_3 in the improved Howland to achieve a maximum output impedance for this frequency range and it should be 0^o phase delay between the reference signal and output signal but it is not because of stray capacitance. Appendix-D shows the result of the current conveyor current source with the same test structure with an 813.6Ω load resistor.

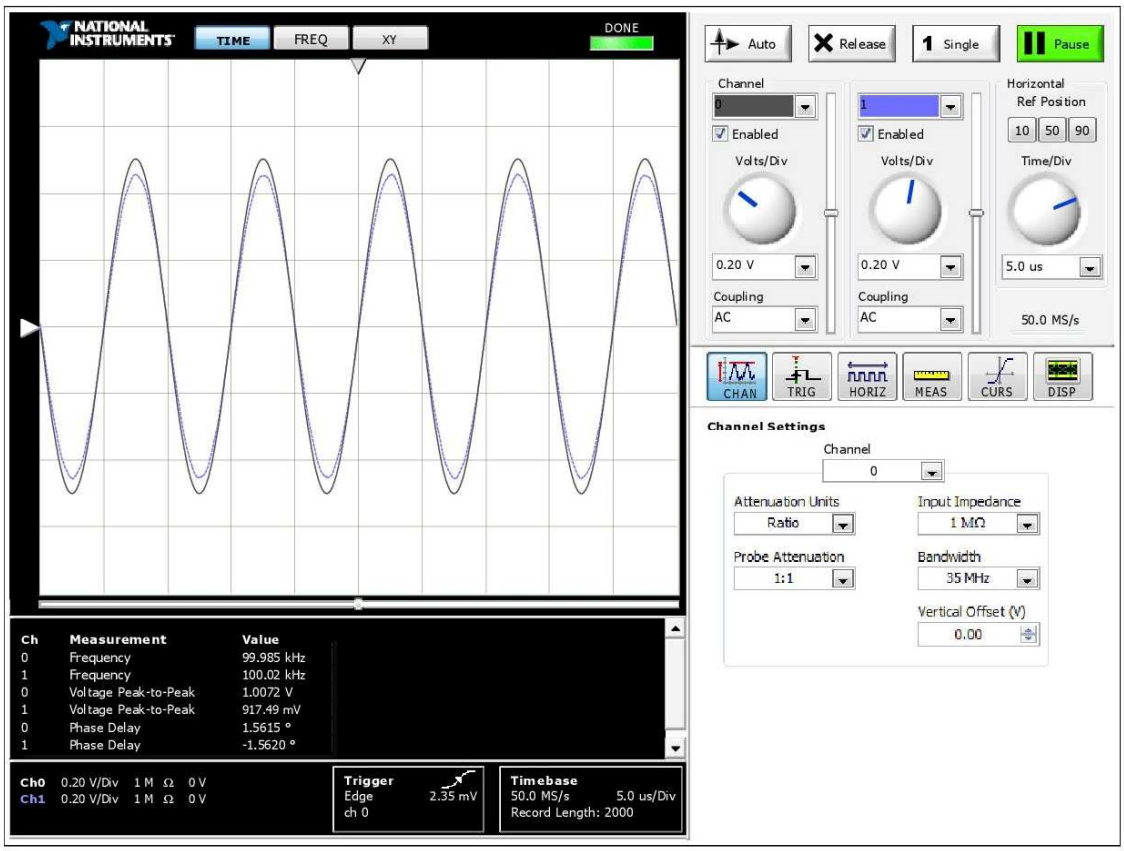

Amplitude=500mV, F=100kHz, phase different=0^o between input signal and output current, probe (x10), R_{LOAD}=918Ω (1kΩ, 10% tolerance) phase delay = 1.561^o, Ch: 0.5v/div and probe 1MΩ, Trigger 0V and Time base of 10MS/s (5us/Div)

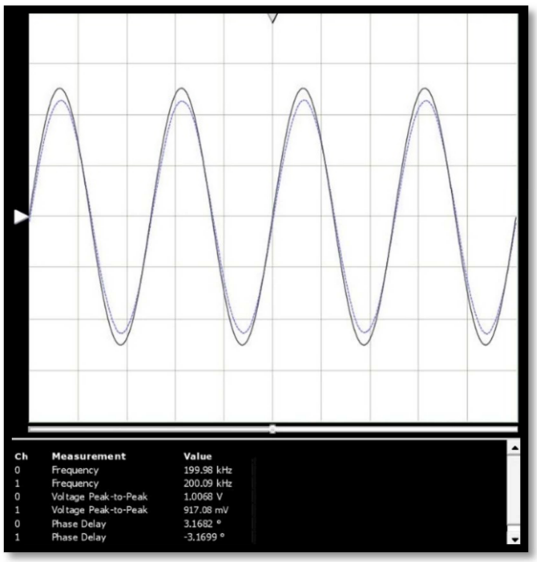

F= 200kHz, R_L=918Ω, V_L=917^{mVp-p}, Phase delay with input signal +3^o

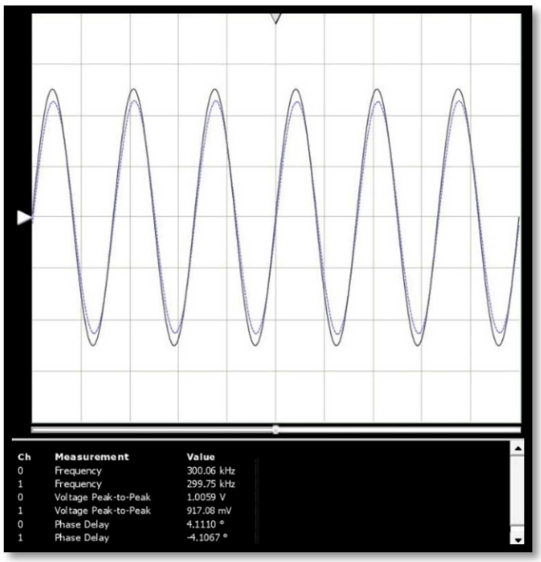

F= 300kHz, R_L=918Ω, V_L=917^{mVp-p}, Phase delay with input signal +4^o

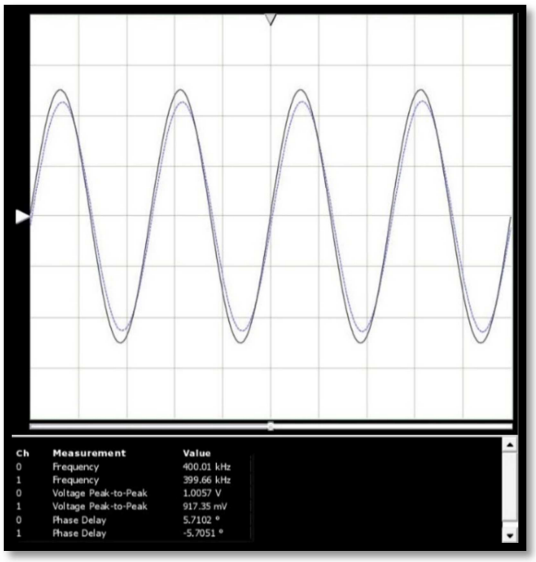

F= 400kHz, R_L=918Ω, V_L=917^{mVp-p}, Phase delay with input signal +5^o

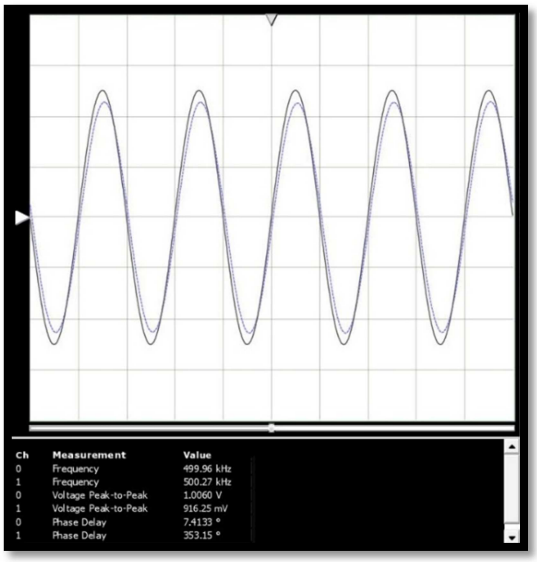

F= 500kHz, R_L=918Ω, V_L=916^{mVp-p}, Phase delay with input signal +7^o

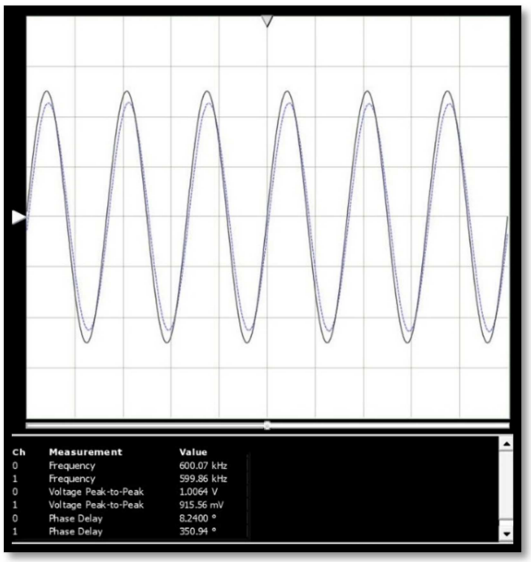

F= 600kHz, R_L=918Ω, V_L=915^{mVp-p}, Phase delay with input signal +8^o

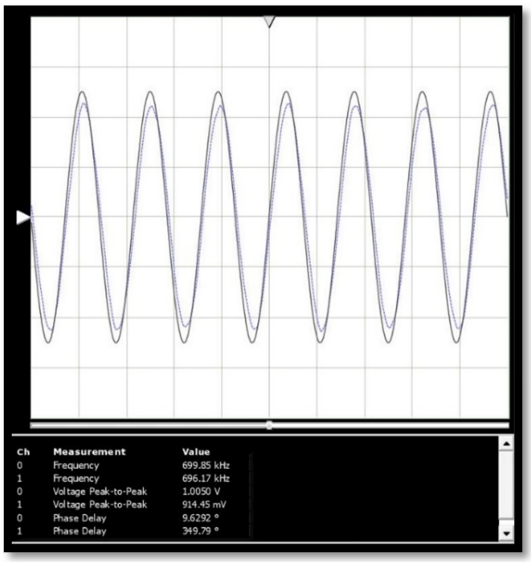

F= 700kHz, R_L=918Ω, V_L=914^{mVp-p}, Phase delay with input signal +9^o

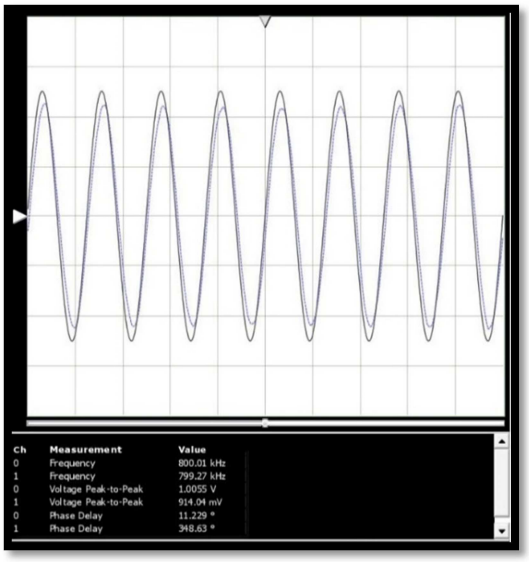

F= 800kHz, R_L=918Ω, V_L=914^{mVp-p}, Phase delay with input signal +11^o

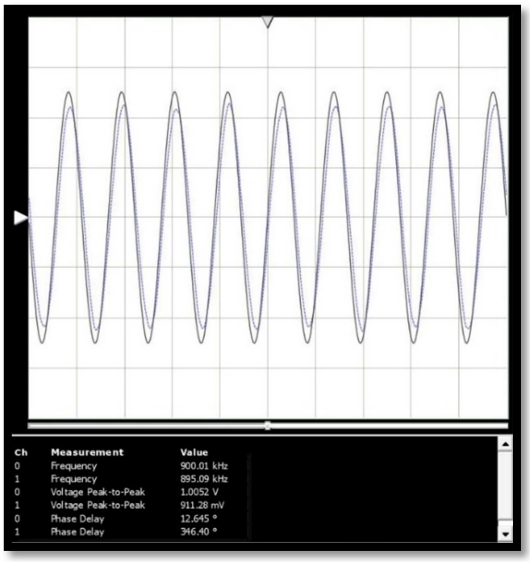

F= 900kHz, R_L=918Ω, V_L=911^{mVp-p}, Phase delay with input signal +12^o

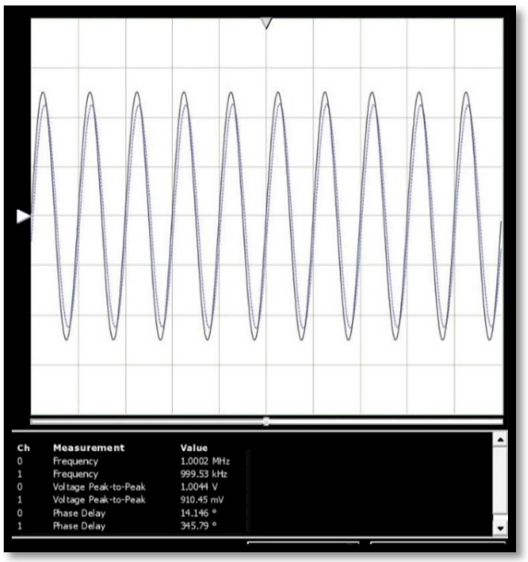

F= 1MHz, R_L=918Ω, V_L=910^{mVp-p}, Phase delay with input signal +14^{o}

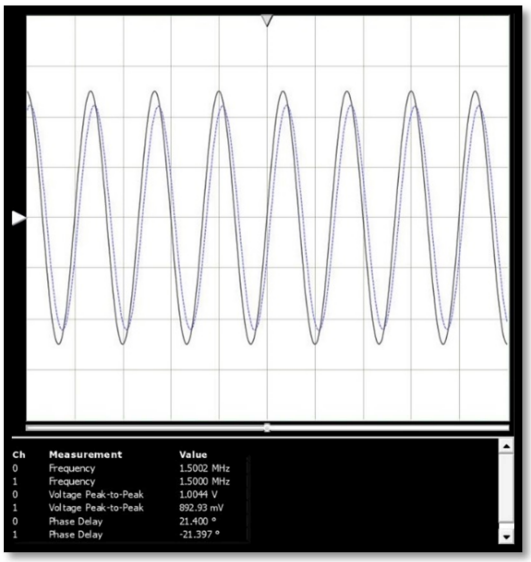

F= 1.5MHz, R_L=918Ω, V_L=892^{mVp-p}, Phase delay with input signal +21^{o}

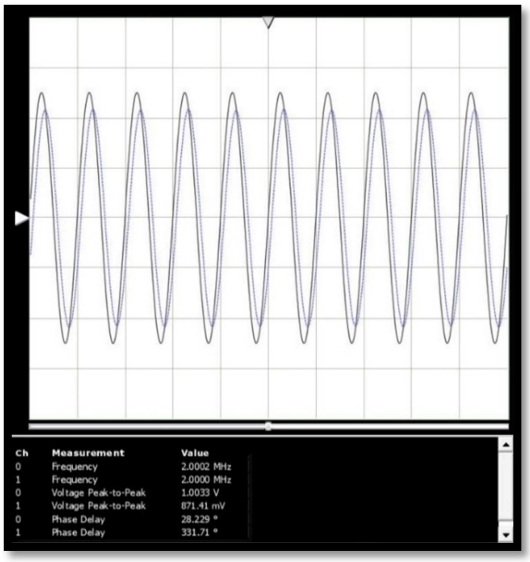

F= 2MHz, R_L=918Ω, V_L=871^{mVp-p}, Phase delay with input signal +28^{o}

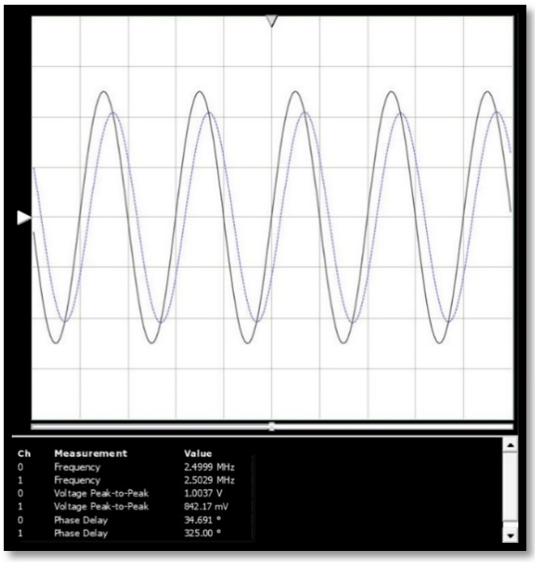

F= 2.5MHz, R_L=918Ω, V_L=842^{mVp-p}, Phase delay with input signal +34^{o}

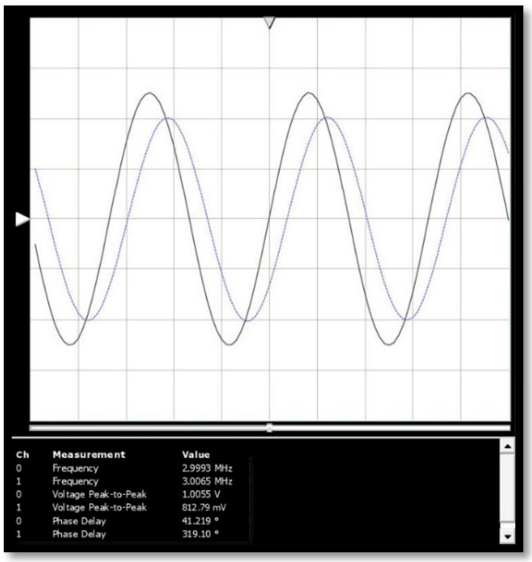

F= 3MHz, R_L=918Ω, V_L=812^{mVp-p}, Phase delay with input signal +41^{o}

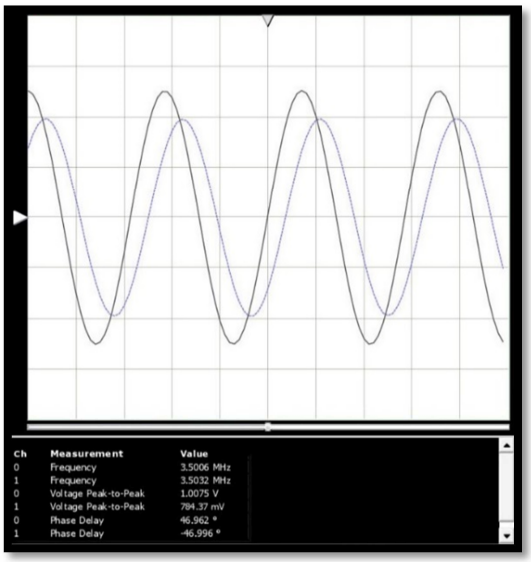

F= 3.5MHz, R_L=918Ω, V_L=784^{mVp-p}, Phase delay with input signal +46^{o}

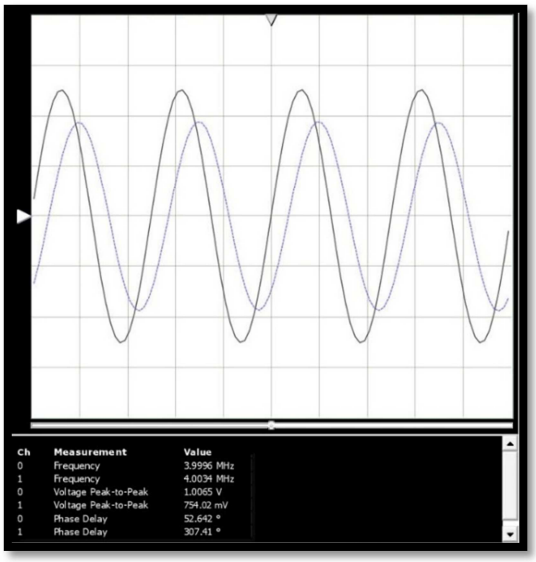

F= 4MHz, R_L=918Ω, V_L=754^{mVp-p}, Phase delay with input signal +52^{o}

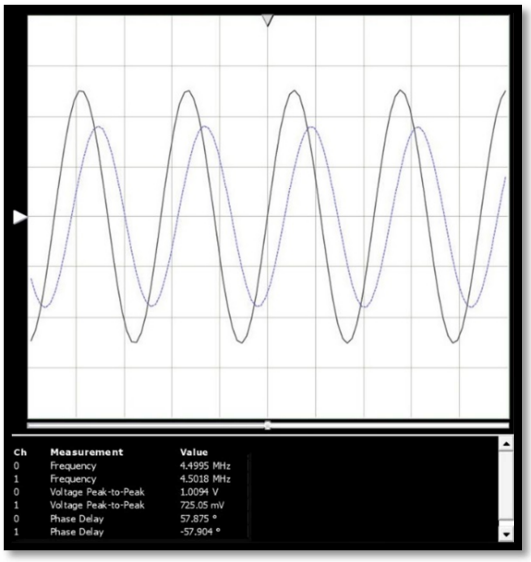

F= 4.5MHz, R_L=918Ω, V_L=725^{mVp-p}, Phase delay with input signal +57^{o}

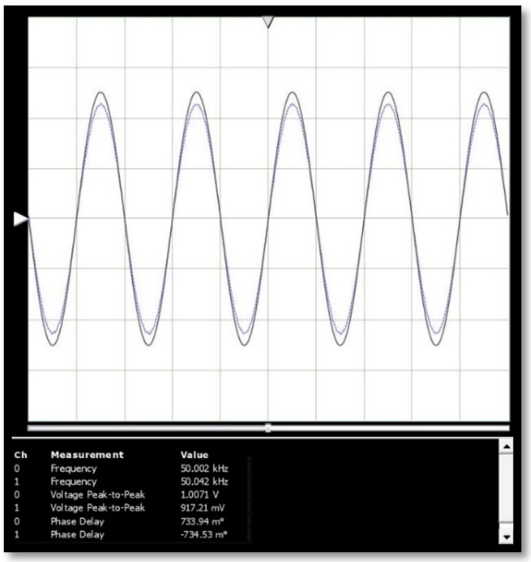

F= 50kHz, R_L=918Ω, V_L=917^{mVp-p}, Phase delay with input signal +0^o

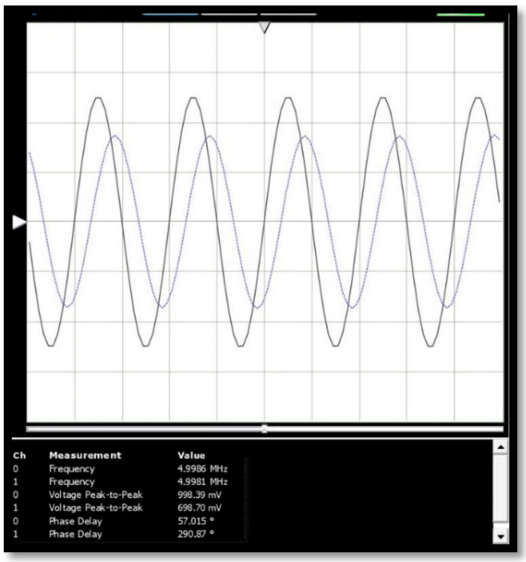

F= 5MHz, R_L=918Ω, V_L=698^{mVp-p}, Phase delay with input signal +57^o

Figure 73 shows snapshots of the oscilloscope at different frequencies with fixed load (R_{LOAD}=918Ω) that shows the input signal of the signal generator (amplitude of the input sine wave set 1^{Vp-p}) and output signal of the current source on the scope when connecting to an improved Howland current source for sweeping the frequency from 100kHz to 1MHz in steps of 100kHz and for 1MHz to 5MHz with steps of 500kHz step.

The reference signal is compared with the output voltage curves as the experimental results are presented in Figure 73. We measured the output voltage of the improved Howland current source when it is attached to a 1kΩ load (actual value is equal to 918Ω). These curves were obtained using actual electronic components, probe and other unwanted source capacitances. As we measured the SNR of the function generator with measurement probes, it is around 60-70dB. The above curves were measured over an operating frequency of 50 kHz to 5MHz and show a drop in output voltage (V_{OUT}=R_{LOAD} * I_{OUT}) when a fixed load resistor is attached. These current drops are affected by the presence of stray capacitance in the EIT circuits. We measured these curves to compare with the simulation results as we expected the total stray capacitance of the system. The last two curves show a compression between the beginning (50 kHz) and ended (5MHz) frequency points in the AZ1 EIT system. We also measured the phase changes between the input signal and output

signals and achieved a phase delay of 0^{o} at 50 kHz to 60^{o} at 5MHz with a current $998^{uAp\text{-}p}$ to $760^{uAp\text{-}p}$.

Although, we achieved a phase shift between these two signals during these tests, as we expected, based on the simulation results, the range of output voltage would be $918^{mVp\text{-}p}$ at 50 kHz dropped to $698^{mVp\text{-}p}$ at 5MHz with a related phase shift.

Figure 74 shows the measurement result of the improved Howland current source for the different frequency points without OCCII-GIC circuit.

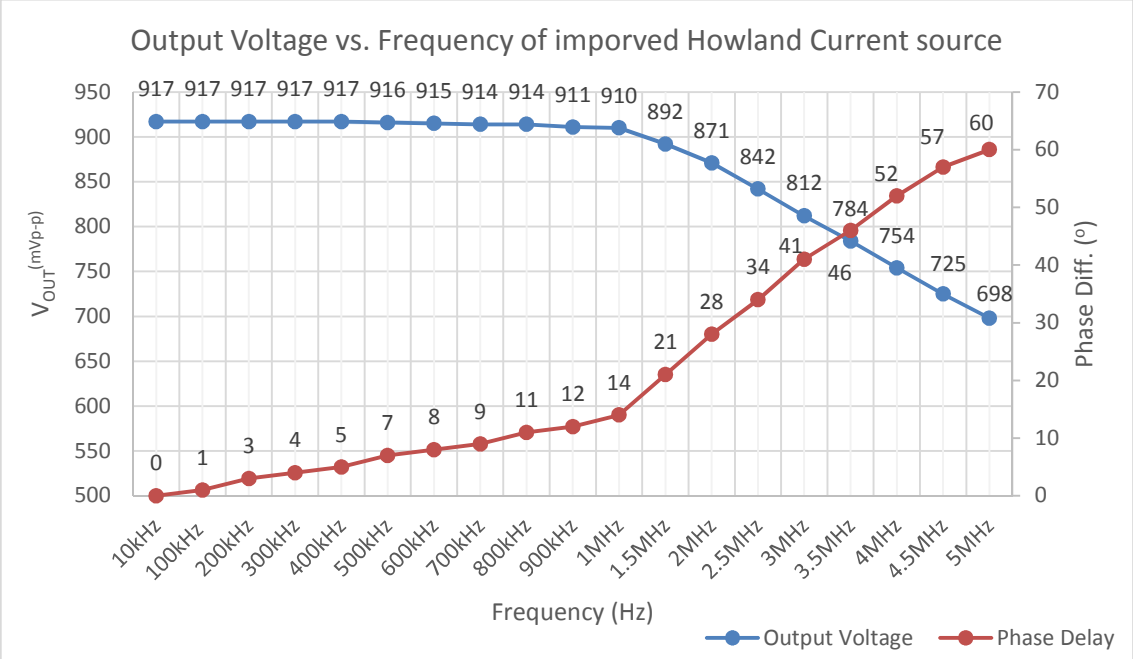

Figure 74 the output voltage and phase delay compared to reference input signal at different frequency points for the improved Howland current source with capacitance effects from the probe and source, the value of output current realized from $I_{OUT}=V_{OUT}(mv)/R_{LOAD}(\Omega)$, the load resistors are equal to 1kΩ (918Ω 5% tolerance)

The output current and phase delay curves of the current conveyor current source are shown in Figure 75 when the current conveyor current source is compared with the reference input signal with 180^{o} out of phase. A load resistor is attached to the current conveyor current source to measure the output voltage signal from the load. This current conveyor branch has a 180 degrees phase difference with the reference (input) signal. The actual load resistor is equal to R_{LOAD}= 813.6Ω and the reference signal is a sine wave signal with amplitude of 0.5^{V} ($1^{Vp\text{-}p}$). We measured

output voltage of the current conveyor current source with the α and β tracking errors. Ideally the output voltage would be equal to $813.6^{mVp\text{-}p}$ if the gain is equal to 1. However, in regard to the current and voltage tracking errors, we measured $767^{mVp\text{-}p}$ at 100 kHz and dropped to $497^{mVp\text{-}p}$ at 5MHz. We also measured a phase shift between these two signals during these tests. As we expected based on the simulation results the range of output current would be $938^{uAp\text{-}p}$ at 10 kHz dropped to around $660^{uAp\text{-}p}$ at 5MHz with a phase shift. We also expected to measure the output voltage equal to $767^{mVp\text{-}p}$ based on the simulation results with the C_{STRAY} equal to 33.8pF at 10 KHz to around 500mVp-p at 5MHz (includes the tracking errors of the current and voltage. Thus the gain would equal to 0.942, thus $\frac{V_{IN}}{R_x}\times gain=\frac{1^{Vp\text{-}p}}{1^{k\Omega}}\times 0.942=942^{uAp\text{-}p}$ then the output current would be equal $I_{OUT}=\frac{V_{OUT}}{R_{LOAD}}=\frac{767^{mVp\text{-}p}}{813.6\Omega}=942^{uAp\text{-}p}$. Appendix-D shows the experimental results of these tests.

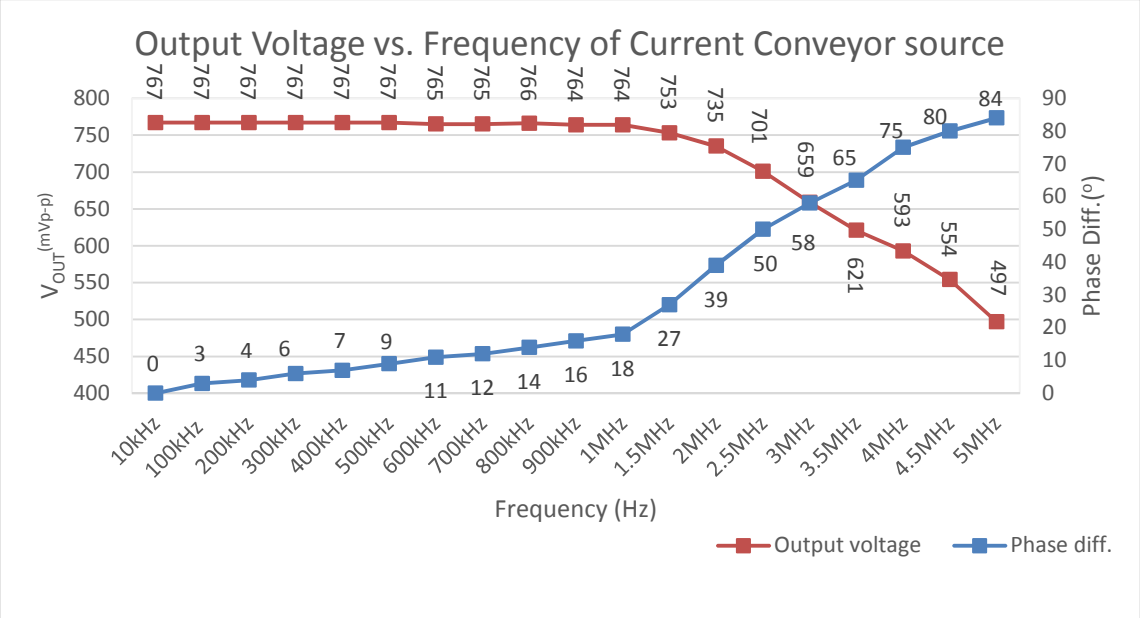

Figure 75 the output voltage and phase delay compared to reference input signal at different frequency points for the current conveyor current source with the source and probe capacitances, the value of output current realized from $I_{OUT}=V_{OUT}(mv)/R_{LOAD}(\Omega)$, the load resistors are equal to 800Ω (813.6Ω 5% tolerance), with tracking errors of the current conveyor current source.

By comparing the simulation results (Figure 71) and experimental results (Figure 74 and Figure 75) we confirm almost the same value of parasitic capacitance that we

expected for two current source types in the EIT system. Now we are using a cancellation method to remove the stray capacitance. As we mentioned in previous chapters we presented the OCCII-GIC circuit as a capacitance cancellation method.

Test-II

The next step in the test procedure, simulating the current sources with the parasitic capacitances (such as on/off capacitance of the DRV MUXs and source capacitance) and using the OCCII-GIC circuit to cancel the capacitance effects in the current source circuits. We illustrated the simulation and experimental results in this section for the different frequency points from 1MHz to 5MHz, with 1mA peak to peak output current as it connected to a load attached to electrodes and measured the voltage by using a probe with x10 at these electrodes. We measured the output voltage (mVp-p), when using a digital-pot in place of Y_4. Moreover, a digital-pot in place of Y_3 also can be set at the fixed values for all these frequencies points. However, during the simulation we have considered capacitances as expected caused by using two digital-pots.

6.5. Simulation of the current sources for the EIT system

We consider the effect of digital-pots capacitance on the circuit board for the floating and grounded resistors. We found that the best arrangement for the digital-pot in order to obtain the minimum effect from pin capacitances when using the digital-pots in different forms (floating and grounded resistors) would as follows:

In the case of the grounded resistor (Y_3 in OCCII-GIC circuit), the equivalent (variable) resistor is paralleled by a grounded capacitance of C_H=10pF with the wiper and low pin terminals grounded thus $Y_3=R_3+C_H$.

In the case of a floating resistor (Y_4 in OCCII-GIC circuit), the equivalent (variable) resistor is connected with the grounded C_{WIPER}=25pF and C_H=10pF at both ends when the low pin terminal is floated.

In reality, the digital-pot (DCP of X9C10X) with 100 steps combined with a trim-pot network achieves the minimum variable (ΔR) resistor with the smallest capacitance effect. The current source simulations were run for different loads with a variable load of R_{VAR} (load) from 1kΩ up to 5kΩ.

6.5.1. The simulation of Improved Howland current source combined with OCCII-GIC

A combination schematic of the improved Howland current source with OCCII-GIC topology is shown in Figure 76. In practice, each op amp (OPA656) has an input capacitance of the differential of 0.7pF and common mode of 2.8pF (typical value) (Data Sheet-OPA656 2008).

To simulate the same behaviour of the circuit as practice, when each op amp (OPA656) in practice has an input impedance of the differential of 0.7pF||10^{12}Ω and common mode of 2.8pF||10^{12}Ω, therefore, we considered these input impedances when simulating this type of source. To achieve the maximum output impedance, it requires tuning of the current source on both sides of the circuit (0 and 180 signal branches) together. It also needs to consider the current source gain and Transconductance gain with common-mode input impedance and the CMRR of the amplifier.

In practice, we need to follow the tuning process, step by step so that the tuning of the output resistor is achieved (a tune resistor of the R_3 inside the Improved Howland circuit and tune resistor of R_3 or R_4 in OCCII-GIC). This obtains the maximum output impedance corresponding to the stray capacitance of the circuit design for each frequency point.

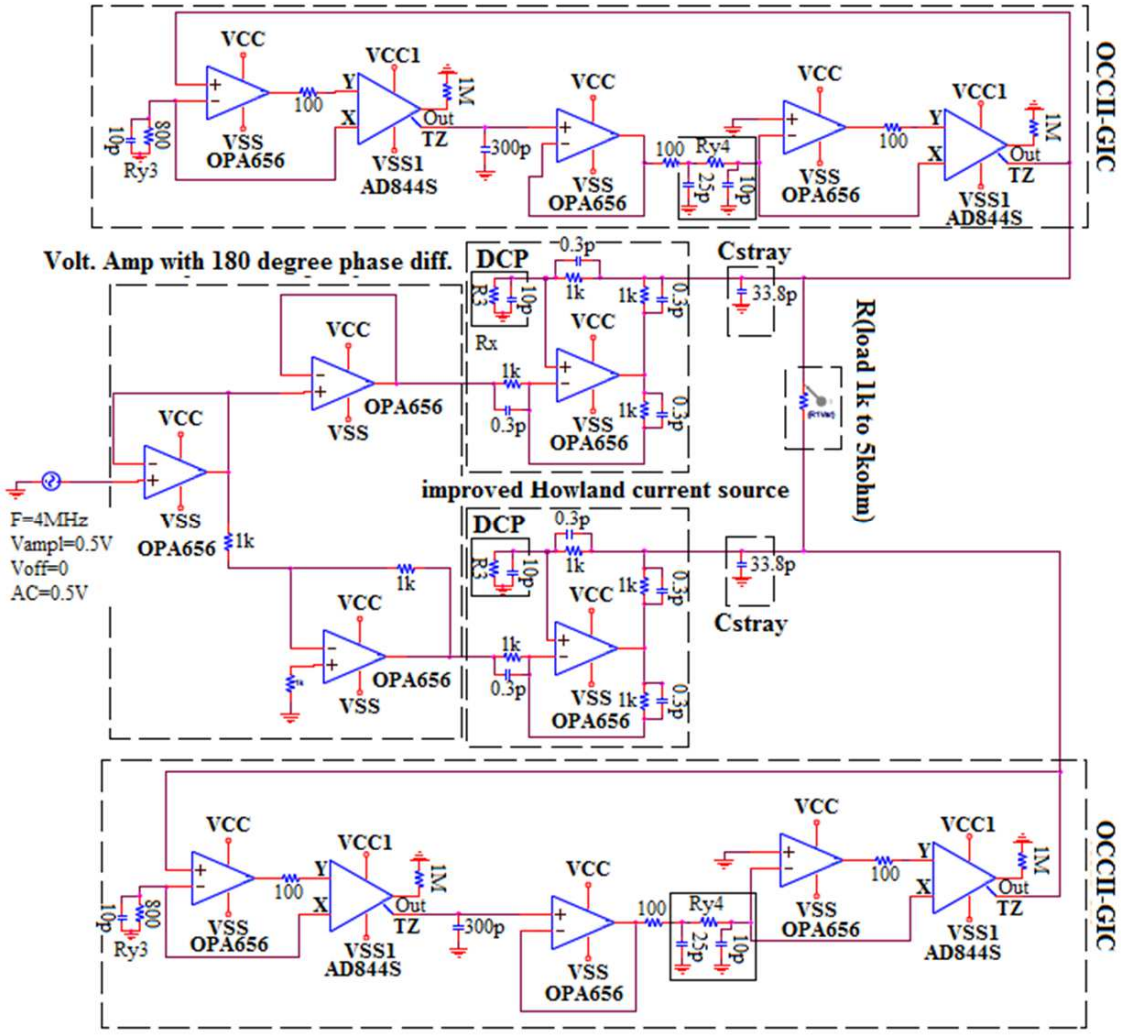

Figure 76 Simulation a schematic of the mirrored improved Howland current source with OCCII-GIC combination

The process is: first adjust the digital-pot inside the OCCII-GIC for the particular frequency point as in the simulation phase, we incremented from 100Ω to 5kΩ, in 10 logarithmic steps per decade then as a second step obtained the maximum output impedance using the digital-pot inside the improved Howland circuit as shown in Figure 77.

The AC sweep results of the multi-frequency system are obtained. Figure 77 shows the sweeping frequency range up to 7MHz.

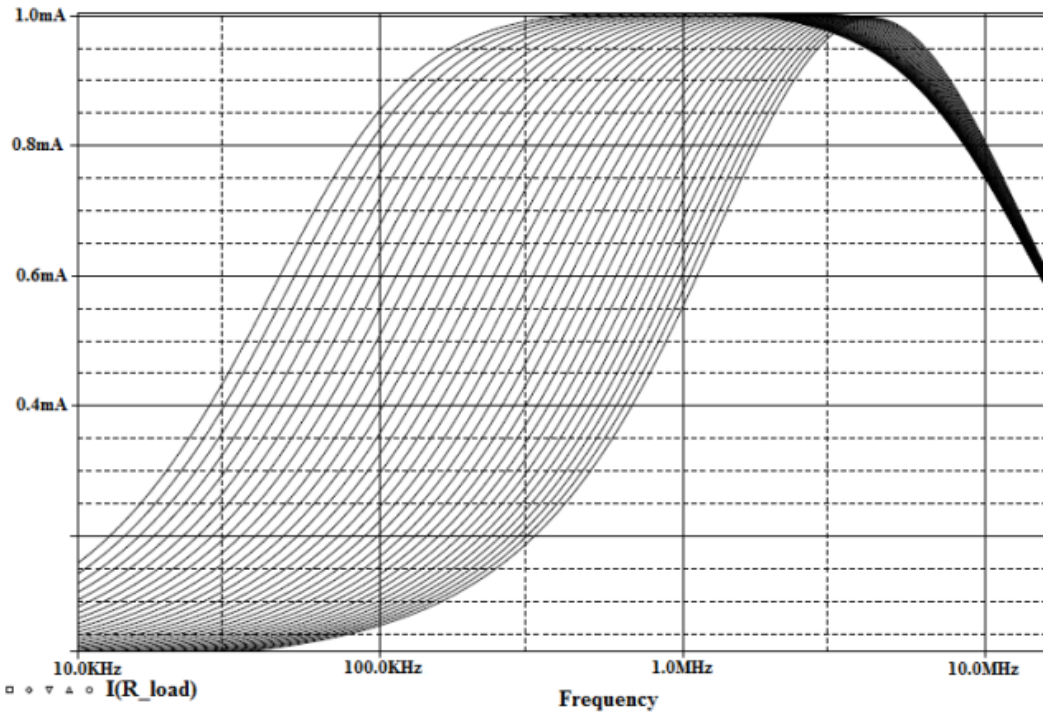

Figure 77 The simulation graph shows a multi-frequency AC sweep output of the OCCII-GIC and improved Howland current source. Digital-pot Y_4 (100Ω to 5kΩ, increment in 10 logarithmic steps per decade)

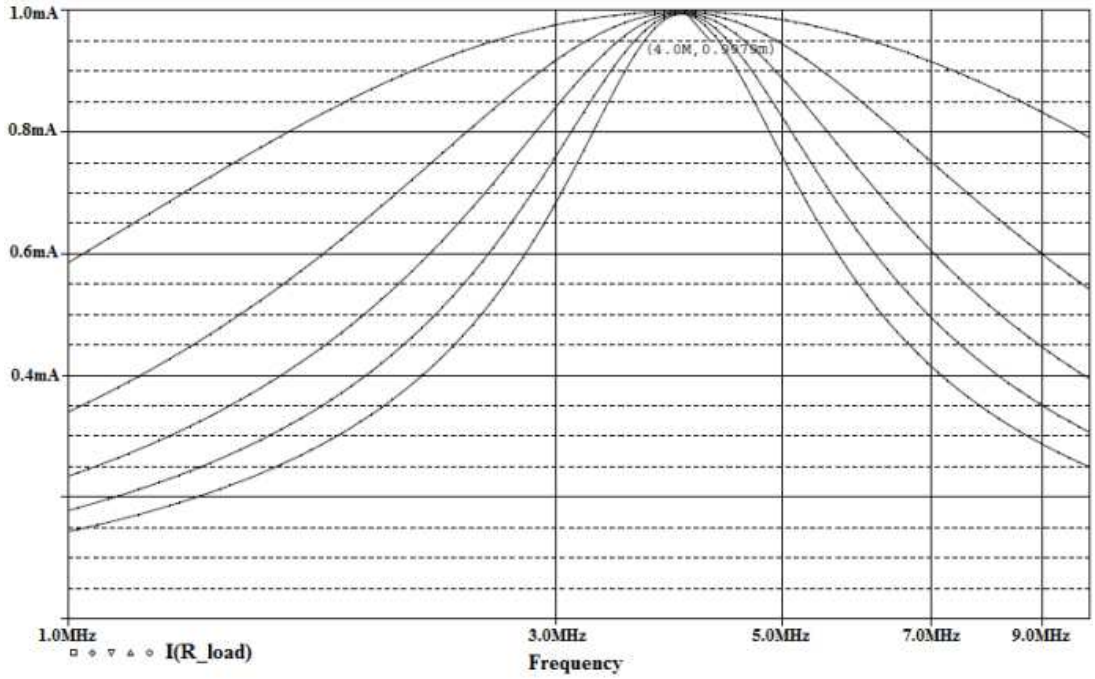

Figure 78 The simulation graph shows the AC sweep output at a frequency of 4MHz as an example frequency point with different loads from 1kΩ to 5kΩ [wide to narrow curve].

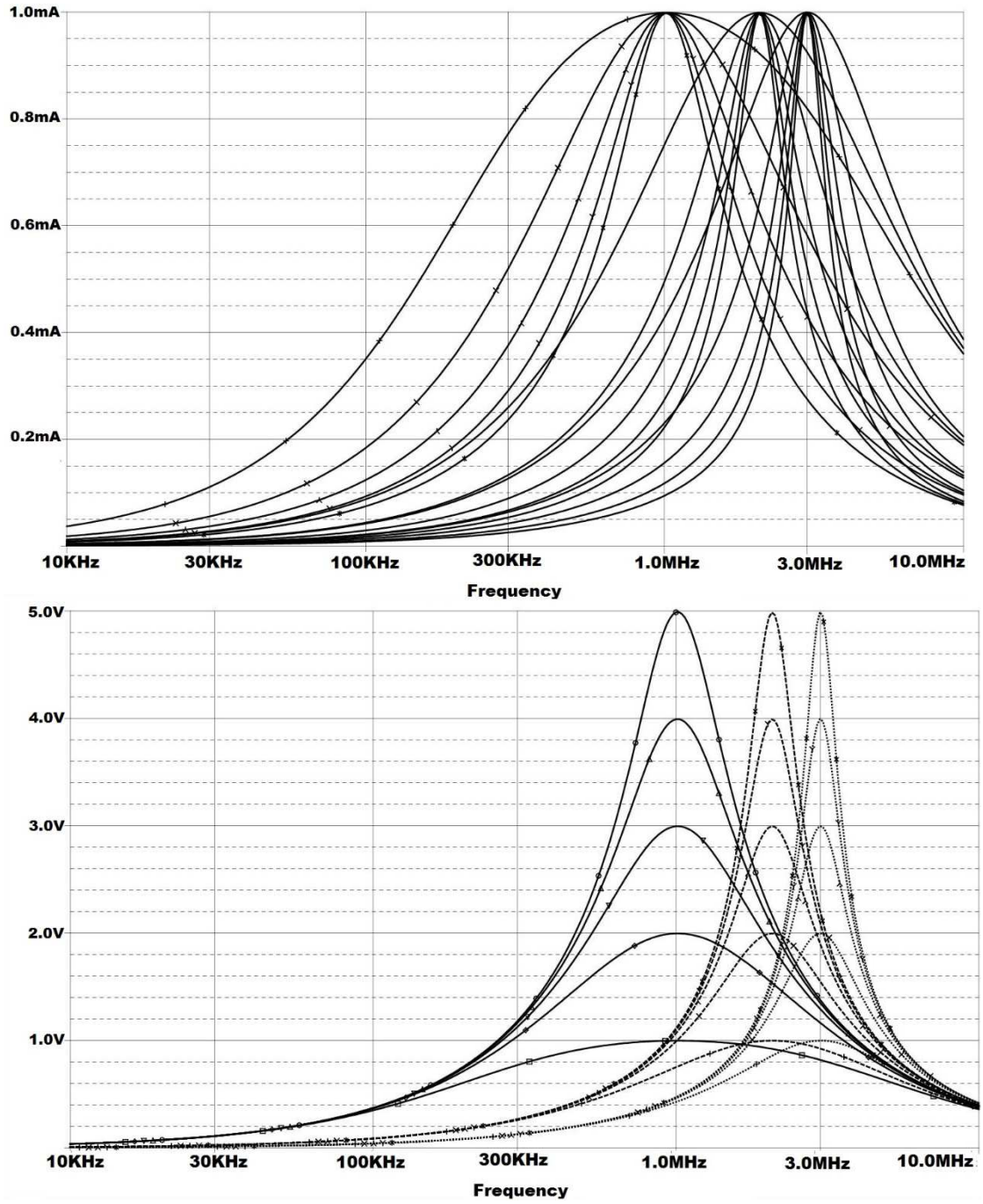

Figure 79 The simulation graph shows the AC sweep output at three different sample frequency points (1MHz, 2MHz, 3MHz); the top graph shows the output currents (1mA) for different loads from 1kΩ to 5kΩ, wide to narrow curve and the bottom graph shows the output voltage (1VAC to 5VAC) for different loads.

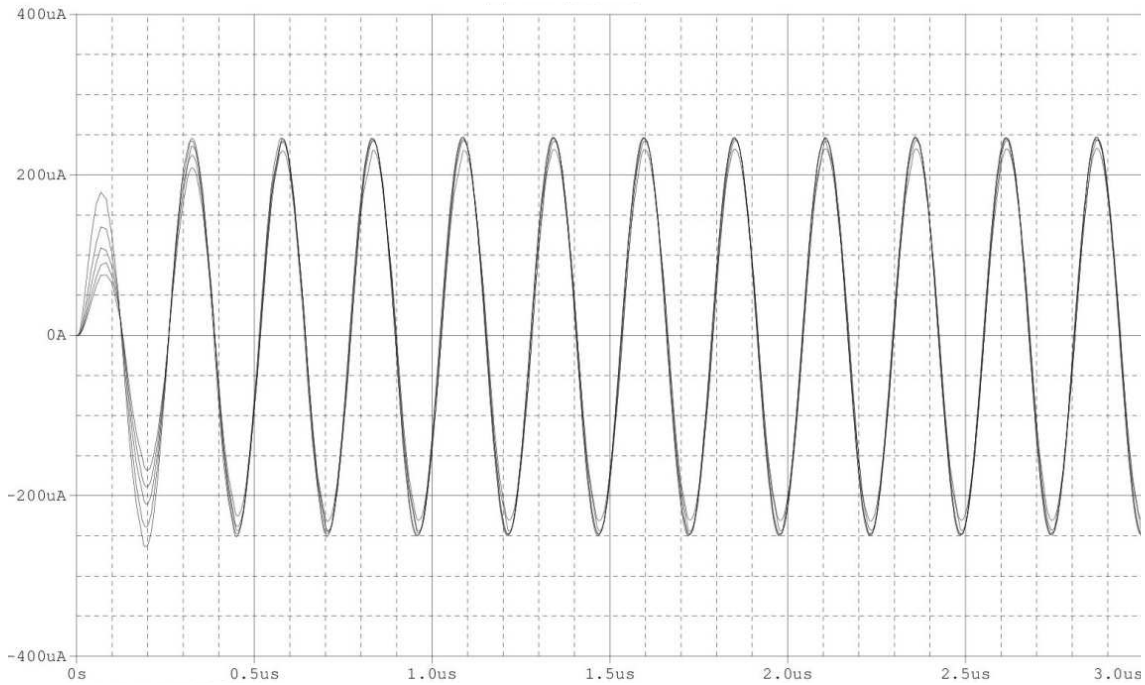

Figure 80 the time domain (transient) output current analysis of the improved Howland current source combined with OCCII-GIC circuit at the single frequency sample (3.927MHz) for the variable load 1kΩ to 5kΩ with 0.5mA peak to peak.

The AC sweep and time domain analysis (Transient) results (see Figure 78 and Figure 80) show the possibility of the stray capacitance cancellation method combined with the improved Howland current source for the high-frequency EIT systems (at the single frequency sample of 3.927MHz, as shown in Figure 78). The AC sweep frequency graph shows the resulting output current with the frequency increment of 200 kHz between 1MHz to 7MHz (see Figure 77). As a result, the multi-frequency EIT system gives good performance due to the digital-pot inside the OCCII-GIC, which reduces capacitance effects. Although we found that the output capacitance will not be fully removed and causes the appearance of a phase shift in the output current signal (see Figure 80). The AC sweep output graph at three different sample frequency points (1MHz, 2MHz, 3MHz); and the output currents of (1mA) for different loads from 1kΩ to 5kΩ, wide to narrow curve with the output voltage graphs (1VAC to 5VAC) for different loads shown in Figure 79.

6.5.2. The simulation of current conveyor current source combined with OCCII-GIC

The second source structure that was simulated is the current mirror current conveyor circuit based on the current-mode structure used in the four-electrode topology of the EIT system when it is combined with OCCII-GIC to cancel the stray capacitance as represented in Figure 81. It is worth noting that the same conditions apply to this circuit as mentioned before such as: load and stray capacitance values.

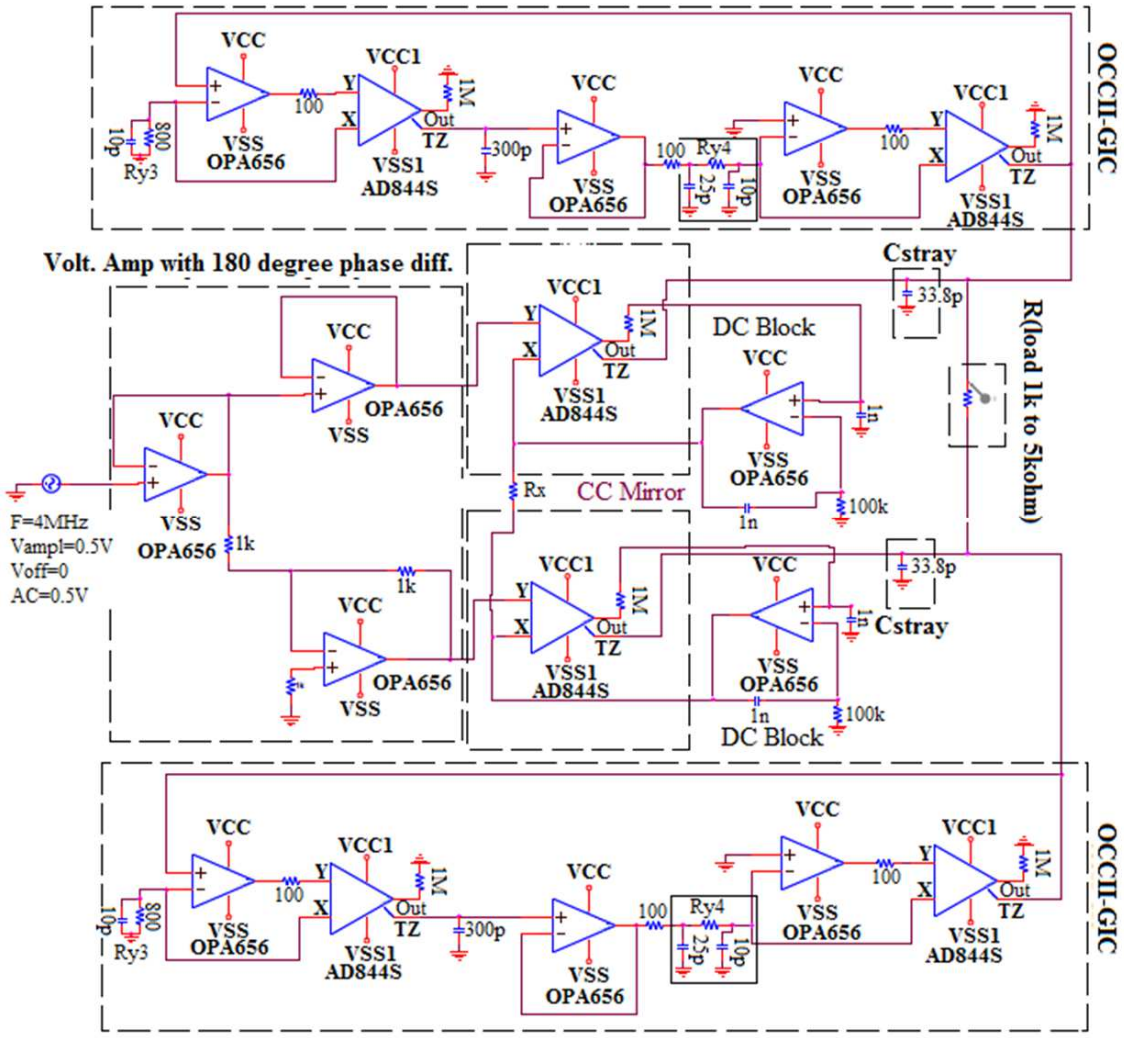

Figure 81 Current conveyor source by utilizing the OCCII-GIC

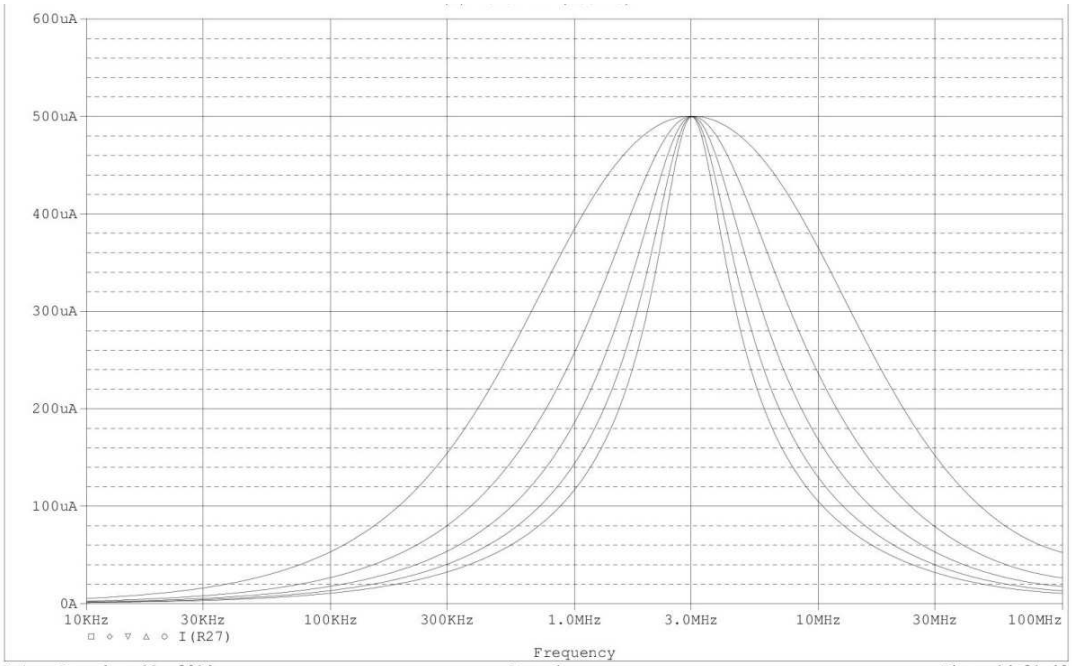

Figure 82 the simulation results from the AC Sweep/Noise results of current mirror current conveyor source with OCCII-GIC with the load parametric sweep from 1kΩ to 5kΩ at 3MHz frequency (as an example frequency point), with 1mA peak to peak output current.

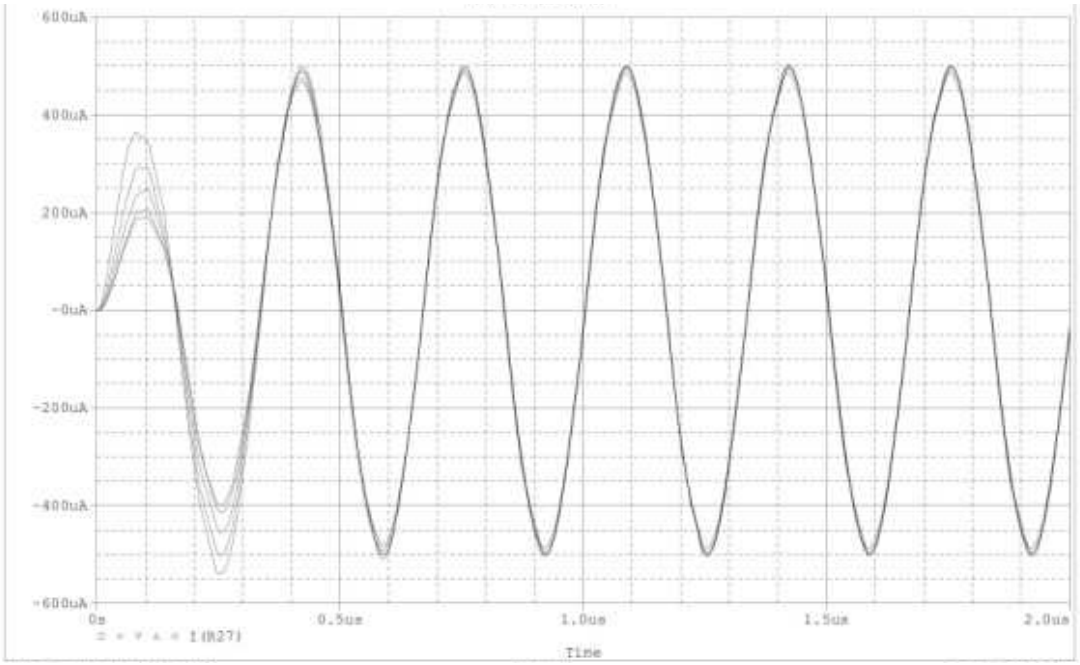

Figure 83 the simulation shows the time domain (Transient) analysis results of current mirror current conveyor source with OCCII-GIC with the load parametric sweep from 1kΩ to 5kΩ at 3MHz frequency (as an example frequency point), with 1mA peak to peak output current.

Based on the simulation results at high frequency (illustrated in Figure 82 and Figure 83), the current mirror current conveyor combined with the OCCII-GIC is also

recommended for use in the EIT system. Both branches of the current mirror have the same reference current; thus, there is no need to adjust the Transconductance resistor. It is necessary to adjust the OCCII-GIC corresponding to the stray capacitance in each branch for a frequency point, as shown an example frequency point 3MHz in Figure 82. The large output impedance would be achieved by considering the above adjustment. We also recommend using DC blocking capacitance to prevent the outputs going into saturation initiated by the interaction between two DC feedback circuits. In regard to the DC block, if we want to use the current conveyor as a single current source with the OCCII-GIC, it needs the DC current to flow through the DC feedback loop to the X terminal. This means measuring the actual DC voltage at the Z node and applying a correction to the input of X. This reduces part of the effect of stray capacitances in the circuit by connecting the output buffer of the current conveyor to the input X terminal (Bragos, Rosell et al. 1994).

In fact, AD844S includes two output signals: one is used as the output with unity gain current, and the same current is delivered to a buffer providing the load driving power for low impedance loads (Data Sheet-AD844S 2009). Hence, it would be useful to utilize for the DC feedback loop with low loop distortion.

We simulated the system when we removed and added the $C_{WIPER\text{-}pin}$=25pF in place of Y_4 in the OCCII-GIC circuit and we found that the $C_{WIPER\text{-}pin}$ does not appear to have any negative effects on the output impedance of the circuit. Therefore, it would be a good solution to use the digital-pot in place of Y_4 when the wiper pin with higher capacitance (25pF) connected to the buffer and the high pin with lower capacitance (10pF) connected to the 2nd current conveyor component (OCCII-2).

6.5.3. Used the OCCII-GIC circuit to cancel the stray capacitance

Table 13 shows component values of OCCII-GIC circuit such as R_3, R_4 and C_1 with the stray capacitance of C_{STRAY}=33.8pf as we expected. The stray capacitance calculated by comparing the output voltage with the dummy capacitance that has been measured in simulation. The expected capacitance includes the input capacitance of the probe C_{PROBE}=13pF plus the on/off capacitance of the DRV multiplexers

$C_{ON/OFF}$=20.8pF (in cascade arrangement). The value of C_1 and R_3 are fixed, and are simply used a digital-pot as a variable resistor in place of R_4 and it has changed by control lines through MCU.

TABLE 13 VALUES OF COMPONENTS USED IN OCCII-GIC CIRCUITS FOR DIFFERENT FREQUENCY POINTS (1MHZ TO 3MHZ) TO CANCEL THE STRAY CAPACITANCE

Frequency	C_1(pF)	R_3(Ω)	R_4(Ω)	$C_{EXPECTED-STRAY}$(pF)
1 MHz	300pF	963Ω	2595Ω	33.8pF
1.25MHz	300pF	963Ω	1660Ω	33.8pF
1.5MHz	300pF	963Ω	1153Ω	33.8pF
1.75MHz	300pF	963Ω	847Ω	33.8pF
2MHz	300pF	963Ω	648.4Ω	33.8pF
2.5MHz	300pF	963Ω	415.2Ω	33.8pF
3MHz	300pF	963Ω	288.25Ω	33.8pF

The value of the digital-pot Y_3, dummy capacitance (simulating the stray capacitance of EIT system) and Y_1 are fixed and only the value of the digital-pot Y_4 is changed from the full size to low during frequency change.

Figure 84 shows the snapshot of the oscilloscope to confirm the performance of the capacitance cancellation method in the current sources by comparing the reference input signal with the output voltage signal. The signal produced by the signal generator set with an amplitude of 0.5V (1^{Vp-p}) at probe channel 0 (——) with x1 connected directly to the reference signal compared with the output signal of channel 1 (----) with x10 measured the output signal of current source for two different grounded load resistors. We used two different loads and connected to two current sources with 180 degree phase difference. Each output signal was compared with the reference input signal when cancelled the stray capacitance of the system using OCCII-GIC circuits. Figure 84 shows the results that we have achieved during these tests.

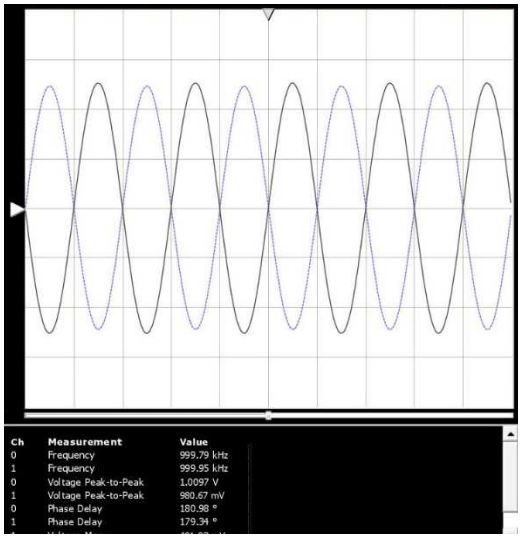

F= 1MHz, R_{LOAD}=980Ω, V_{OUT}=980.67^{mVp-p}, phase delay of 98m^{o} between output and reference signals.

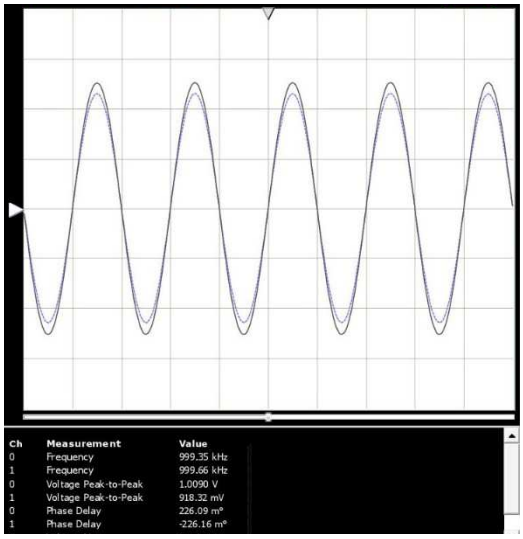

F= 1MHz, R_{LOAD}=918Ω, V_{OUT}=918.32^{mVp-p}, phase delay of 226m^{o} between output and reference signals.

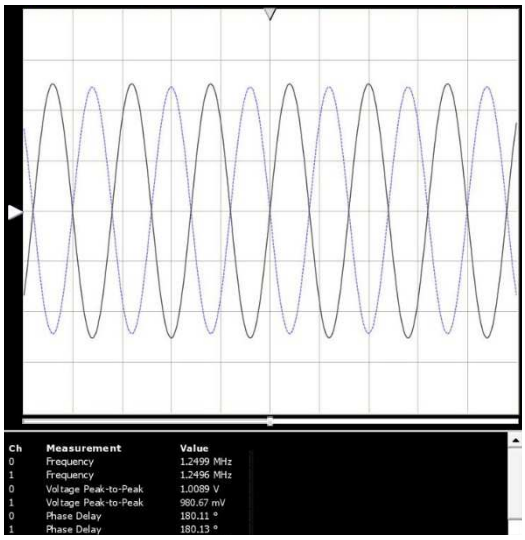

F= 1.25MHz, R_{LOAD}=980Ω, V_{OUT}=980.67^{mVp-p}, phase delay of 110m^{o} between output and reference signals.

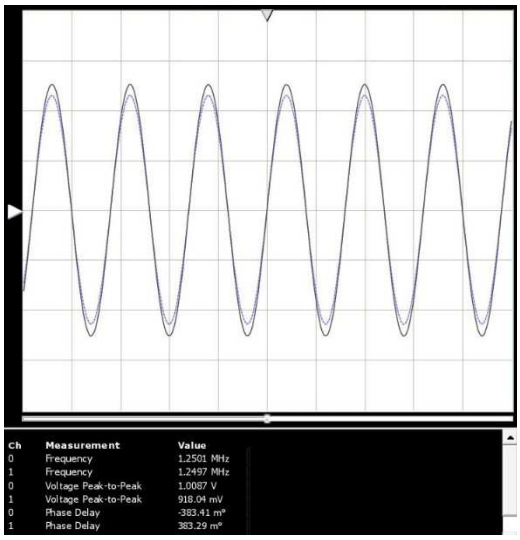

F= 1.25MHz, R_{LOAD}=918Ω, V_{OUT}=918.04^{mVp-p}, phase delay of 383m^{o} between output and reference signals.

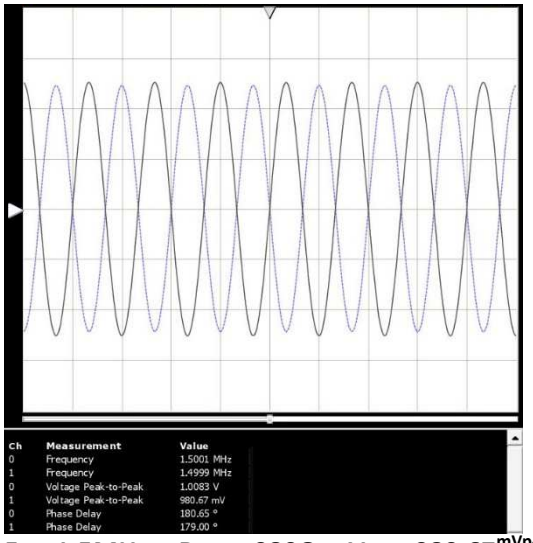

F= 1.5MHz, R_{LOAD}=980Ω, V_{OUT}=980.67^{mVp-p}, phase delay of 650m^{o} between input signal 1^{Vp-p} and measured output voltage.

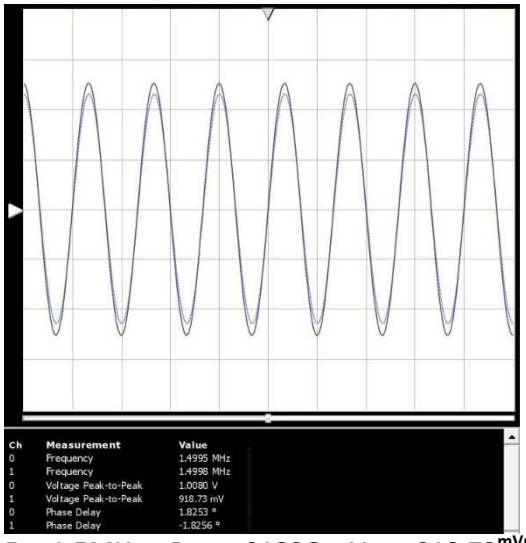

F= 1.5MHz, R_{LOAD}=9180Ω, V_{OUT}=918.73^{mVp-p}, phase delay of 1.825^{o} between output and reference signals.

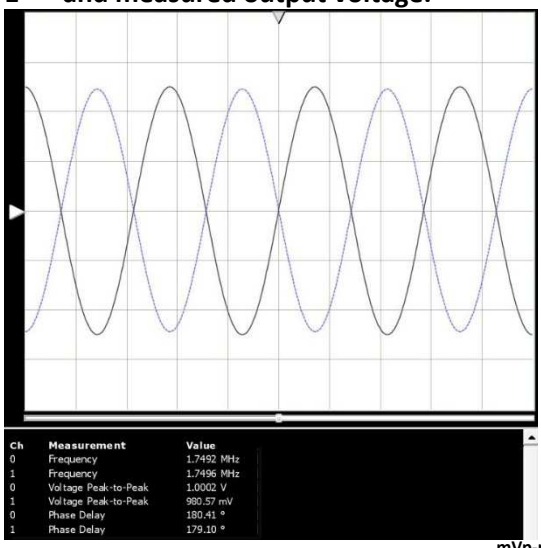

F= 1.75MHz, R_{LOAD}=980Ω, V_{OUT}=980.57^{mVp-p}, phase delay of 410m^{o} between input signal 1^{Vp-p} and measured output voltage.

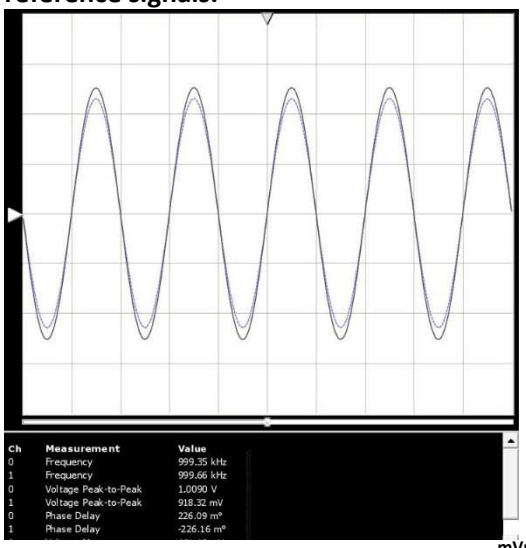

F= 1.75MHz, R_{LOAD}=918Ω, V_{OUT}=918.32^{mVp-p}, phase delay of 226m^{o} between input signal 1^{Vp-p} and measured output voltage.

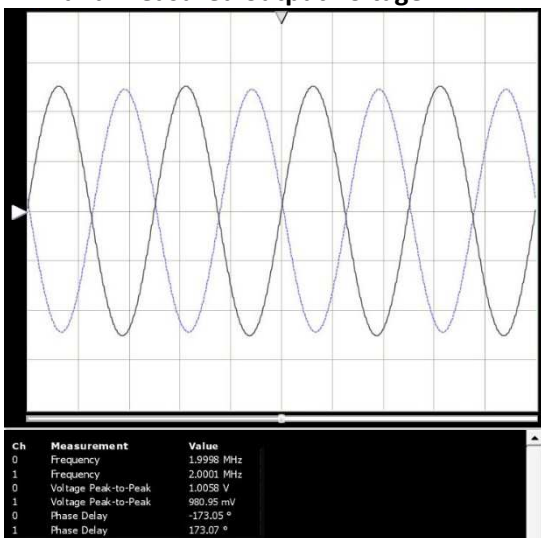

F= 2MHz, R_{LOAD}=980Ω, V_{OUT}=980.95^{mVp-p},

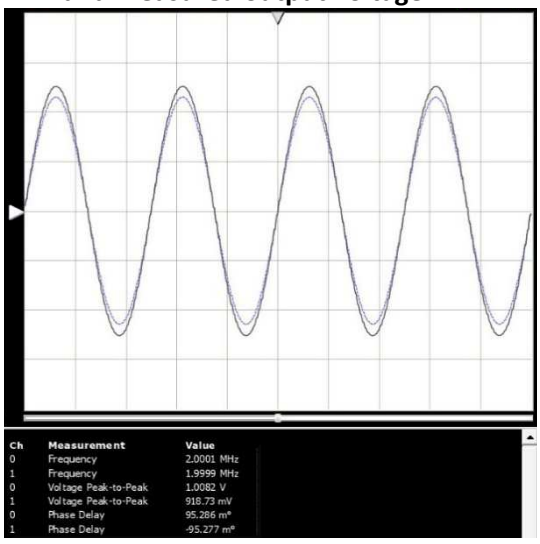

F= 2MHz, R_{LOAD}=918Ω, V_{OUT}=918.73^{mVp-p},

phase delay of 6.95° between input signal 1^{Vp-p} and measured output voltage

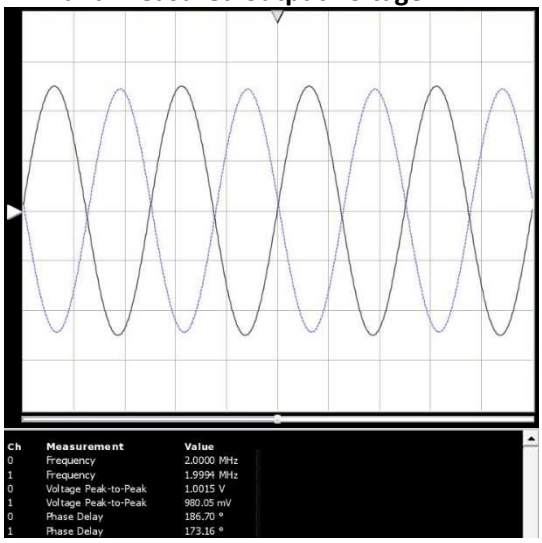

F= 2.5MHz, R_{LOAD}=980Ω, V_{OUT}=980.05^{mVp-p}, phase delay of 6.70° between input signal 1^{Vp-p} and measured output voltage

phase delay of 95m° between input signal 1^{Vp-p} and measured output voltage.

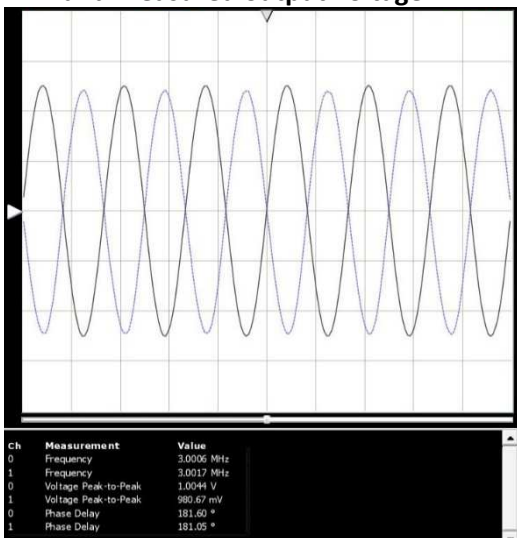

F= 3MHz, R_{LOAD}=980Ω, V_{OUT}=980.67^{mVp-p}, phase delay of 1.60° between input signal 1^{Vp-p} and measured output voltage

Figure 84 shows snapshots of the oscilloscope as displays the input signal (reference signal) produced by the function generator and the output voltage signal measured the load voltage when the sweeping started from 1MHz and ended at 3MHz frequency range and amplitude of the input sine wave signal set 1^{Vp-p}.

6.5.4. Using the OCCII-GIC circuit to cancel a dummy stray capacitance of the current source

We also tested the improved Howland current source with a dummy stray capacitance to show the application of OCCII-GIC circuit in other EIT systems with a higher stray capacitance. We used a dummy stray capacitance parallel with the existing stray capacitance of this system for a total stray capacitance equal to 225pF, that means instead of stray capacitance of 33.8pF (as expected for AZ1 EIT system) an extra dummy capacitance added in parallel with a grounded load to then test the behaviour of the system. We estimated the stray capacitance equal to C_{STRAY}=225pF. Appendix-E shows the output voltage of two different loads are attached to two current sources without using the OCCII-GIC circuit, with this stray capacitance.

Table 14 shows the value of the C_1, R_3 and R_4 that were used to cancel the stray capacitance equal to 225pF for the sample frequency point 1MHz to 3MHz. We utilized a fix value for the R_4 and C_1 and just changed the value of R_3 in the OCCII-GIC circuit.

TABLE 14 VALUES OF COMPONENTS USED IN OCCII-GIC CIRCUITS FOR DIFFERENT FREQUENCY POINTS (1MHZ TO 3MHZ) TO CANCEL THE STRAY CAPACITANCE.

Frequency	C_1(pF)	R_3(Ω)	R_4(Ω)	$C_{EXPECTED\text{-}STRAY}$(pF)
1MHz	300pF	679.2Ω	552.63Ω	225pF
1.25MHz	300pF	434.7Ω	552.63Ω	225pF
1.5MHz	300pF	301.9Ω	552.63Ω	225pF
1.75MHz	300pF	221.8Ω	552.63Ω	225pF
2MHz	300pF	169.8Ω	552.63Ω	225pF
2.5MHz	300pF	108.7Ω	552.63Ω	225pF
3MHz	300pF	75.5Ω	552.63Ω	225pF

The value of the digital-pot Y_4, dummy capacitance equal to 160pF (simulating the stray capacitance of the different EIT system) and Y_1 are fixed and only the value of the digital-pot Y_3 is changed from the full size to low during frequency change.

Figure 85 shows the results that we achieved during these tests when connected to two different loads and try to cancel the stray capacitance of the 225pF at different frequency points.

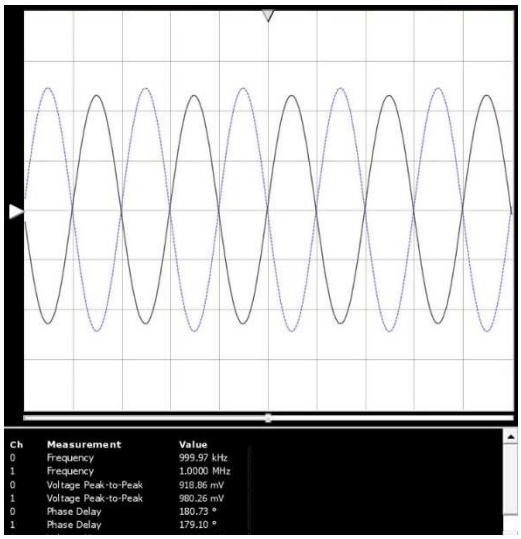

F= 1MHz, $R_{LOAD\text{-}1}$=918Ω, $R_{LOAD\text{-}2}$=980Ω $V_{OUT\text{-}1}$=918.86$^{mVp\text{-}p}$, $V_{OUT\text{-}1}$=980.26$^{mVp\text{-}p}$ with phase diff. =180^{o}, and phase delay=730^{o}m.

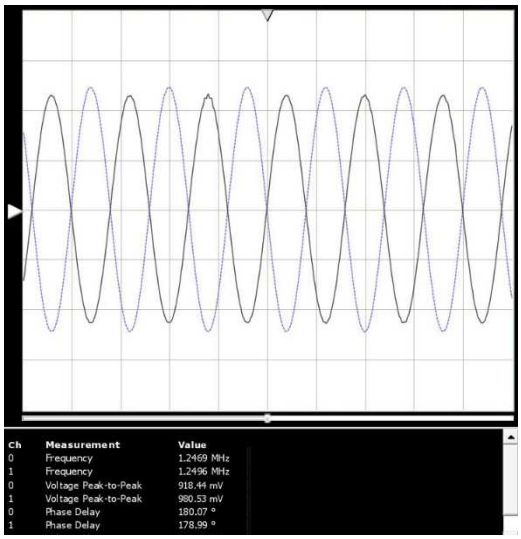

F= 1.25MHz, $R_{LOAD\text{-}1}$=918Ω, $R_{LOAD\text{-}2}$=980Ω $V_{OUT\text{-}1}$=918.44$^{mVp\text{-}p}$, $V_{OUT\text{-}1}$=980.53$^{mVp\text{-}p}$ with phase diff. =180^{o}, and phase delay=70m^{o}.

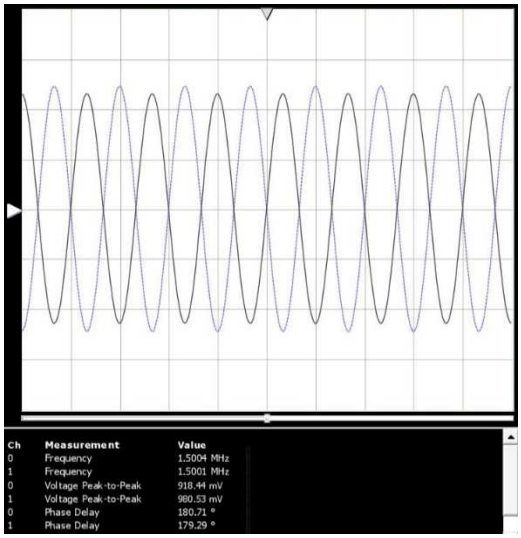

F= 1.5MHz, R_{LOAD-1}=918Ω, R_{LOAD-2}=980Ω V_{OUT-1}=918.44^{mVp-p}, V_{OUT-1}=980.53^{mVp-p} with phase diff. =180^{o}, and phase delay=710m^{o}.

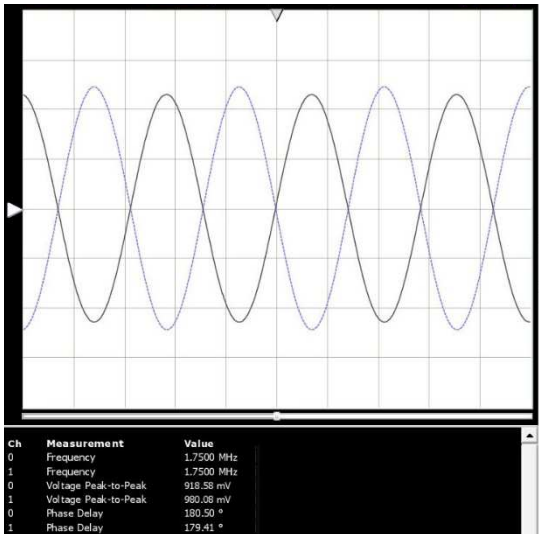

F= 1.75MHz, R_{LOAD-1}=918Ω, R_{LOAD-2}=980Ω V_{OUT-1}=918.58^{mVp-p}, V_{OUT-1}=980.08^{mVp-p} with phase diff. =180^{o}, and phase delay=500m^{o}.

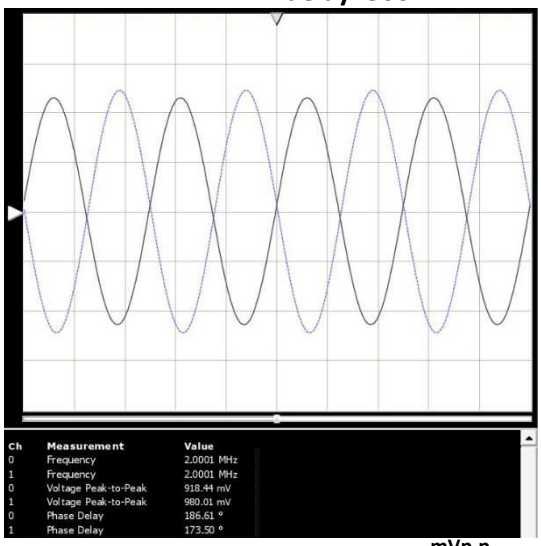

F= 2MHz, R_{LOAD-1}=918Ω, R_{LOAD-2}=980Ω V_{OUT-1}=918.44^{mVp-p}, V_{OUT-1}=980.01^{mVp-p} with phase diff. =180^{o}, and phase delay=6.610^{o}.

Figure 85 shows snapshots of the oscilloscope as display two output voltage measured with two different loads attached to two current sources with 180 out of phase when the sweeping frequency started from 1MHz and ended at 2MHz frequency range with steps of 250kHz and amplitude of input sine wave signal set 1^{Vp-p}.

6.5.5. Using the OCCII-GIC circuit to cancel a stray capacitance of the current mirror current source

We used a single load and connected to a mirrored current source structure and tried to cancel the stray capacitance of the system. We tested for two different

loads (R_{LOAD-1} =730Ω and R_{LOAD-2}=1048Ω) to measure the voltage measurement gain, as are shown in Figure 86 and Figure 87.

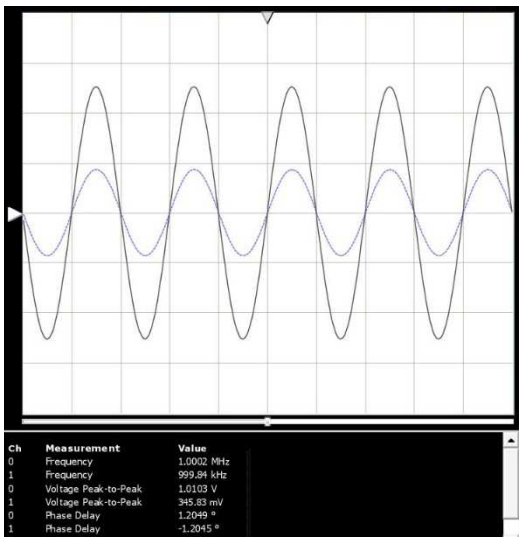

F= 1MHz, R_{LOAD}=730Ω, measured with differential measurement with a gain V_{OUT}^{+}=345.83^{mVp-p}, phase delay =1.2^{o} between the input signal 1^{Vp-p} and output voltage measurement for the current mirror structure with a phase diff. =0^{o}.

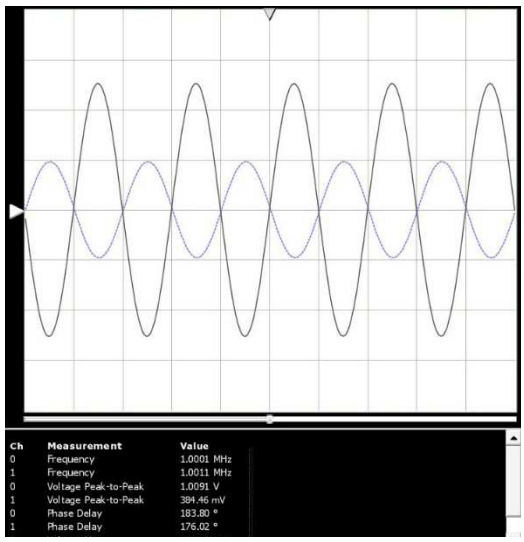

F= 1MHz, R_{LOAD}=730Ω, measured with differential measurement with a gain V_{OUT}^{-}=384.46^{mVp-p}, phase delay =3^{o} between the input signal 1^{Vp-p} and output voltage measurement for the current mirror structure with a phase diff. =180^{o}.

$V_{OUT}=(V_{OUT}^{+}+V_{OUT}^{-})$

$\therefore V_{OUT}=(345.83mV+384.46mV)\times gain=730.29mV$

Figure 86 shows snapshots of the oscilloscope as display reference signal amplitude of the input sine wave signal set 1^{Vp-p} and output voltage measured for a resistor load equal to 730Ω from a mirrored current source structure with 180 degrees out of phase when using a differential voltage measurement with a fixed gain at 1MHz frequency point.

Same test with a resistor load equal to 1048Ω:

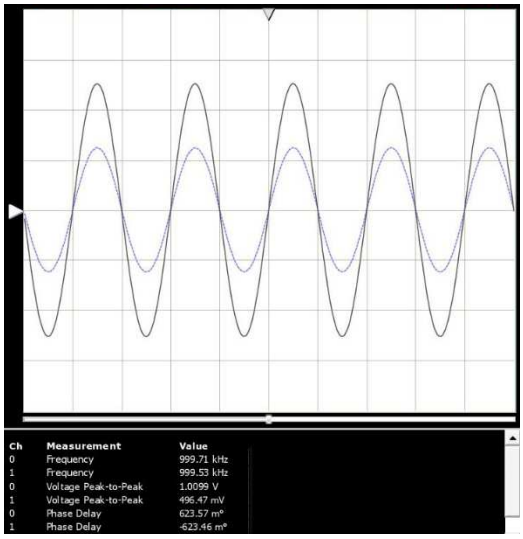

F= 1MHz, R_{LOAD}=1048Ω, measured with differential measurement with a gain V_{OUT}^{+}=496.47^{mVp-p}, phase delay =623.57m^{o} between the input signal 1^{Vp-p} and output voltage measurement for the current mirror structure with a phase diff. =0^{o}.

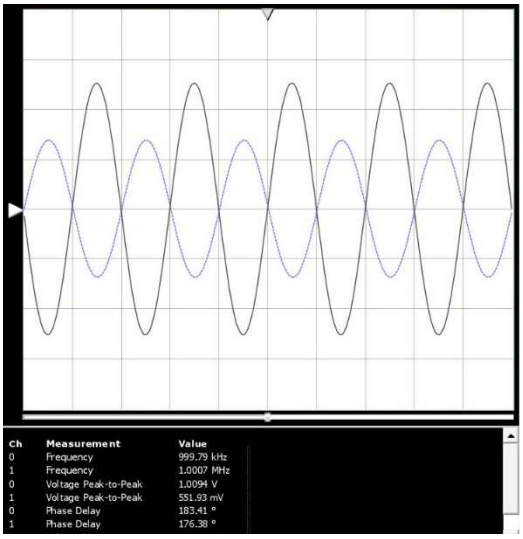

F= 1MHz, R_{LOAD}=1048Ω, measured with differential measurement with a gain V_{OUT}^{-}=551.93^{mVp-p} phase delay =3^{o} between the input signal 1^{Vp-p} and output voltage measurement for the current mirror structure with a phase diff. =180^{o}.

$V_{OUT}=(V_{OUT}^{+}+V_{OUT}^{-})$

$\therefore V_{OUT}(496.47mV+551.93mV)=1048.4mV$

Figure 87 shows snapshots of the oscilloscope as display reference signal amplitude of the input sine wave signal set 1^{Vp-p} and output voltage measured for a resistor load equal to 1048Ω from a mirrored current source structure with 180 degrees out of phase when using a differential voltage measurement with a fixed gain at 1MHz frequency point.

6.6. Maximum load measurement:

We have tested the current sources in regard to the maximum load that can be measured with these two current sources.

1st case: improved Howland current source:

The power-Supply Rejection Ratio (+PSRR) of the operational amplifier OP656 of the improved Howland current source is (+PSRR) +V_S = +4.5Vdc to +5.5Vdc, and (–PSRR) –V_S = –4.5Vdc to –5.5Vdc.

Thus the theoretical the maximum output voltage of the load (Gain) would be around 5V, in regard to output current (1mA) the load will be maximum around 5kΩ.

I measured the DC power supply at the OP656 (+/-Vs pins), directly connected the probe to power supply pins and it was around +/-4.8Vdc and it showed the maximum load to be a 4.37kΩ load (V_{OUT}=4.37V) the output clipped. On the other hand, when the power of op amp is around +/-3.7Vdc, the output load will clip at a load of around 2.5kΩ load. Figure 88 shows the output voltage of the current source when it attached a 4.37kΩ load resistor and the power supply of the OP656 is around +/-4.8Vdc.

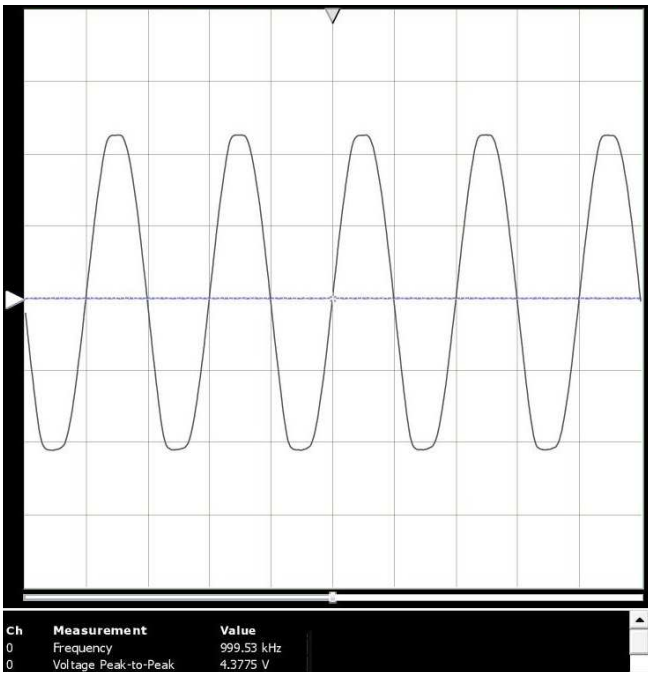

Figure 88 the maximum load that can be measured by the improved Howland circuit is around 4kΩ as tested at 1MHz

2nd case: current conveyor current source:

The power supply rails of the AD844 are +/-15Vdc (with power supply operating range is +/-4.5Vdc to +/-18Vdc) (Data Sheet-AD844S 2009). The internal structure of the output stage transistors of the AD844 uses bipolar collectors, so the output voltage can be obtained (cannot be saturated) until it is a few millivolts from that of the supply rail voltage, this because of limitation of the op amp output stage structure. Thus the output voltage on the load must certainly be less than 30V (+/-15Vdc). I tested the output voltage up to 24.98V with a load of 14.9kΩ and visually, using an oscilloscope, it does not go into saturation or clipping, but when increasing the output voltage by increasing the load to 15kΩ it is saturated. Figure 89 (a) shows a

test of a current conveyor current source for a resistance load of 14.95kΩ with an input signal (reference signal) of $2^{Vp\text{-}p}$, the output voltage up to 24.98V does not go into saturation. It is worth noting that the current conveyor current source has an attenuation of current output thus the output current is $1.67^{mAp\text{-}p}$ instead of ideally 2mAp-p, therefore $1.67^{mAp\text{-}p}$ × 14.95kΩ= $24.96^{Vp\text{-}p}$. However, the current conveyor current source with a load of 15kΩ saturates at a frequency of 100 kHz as shown in Figure 89 (b).

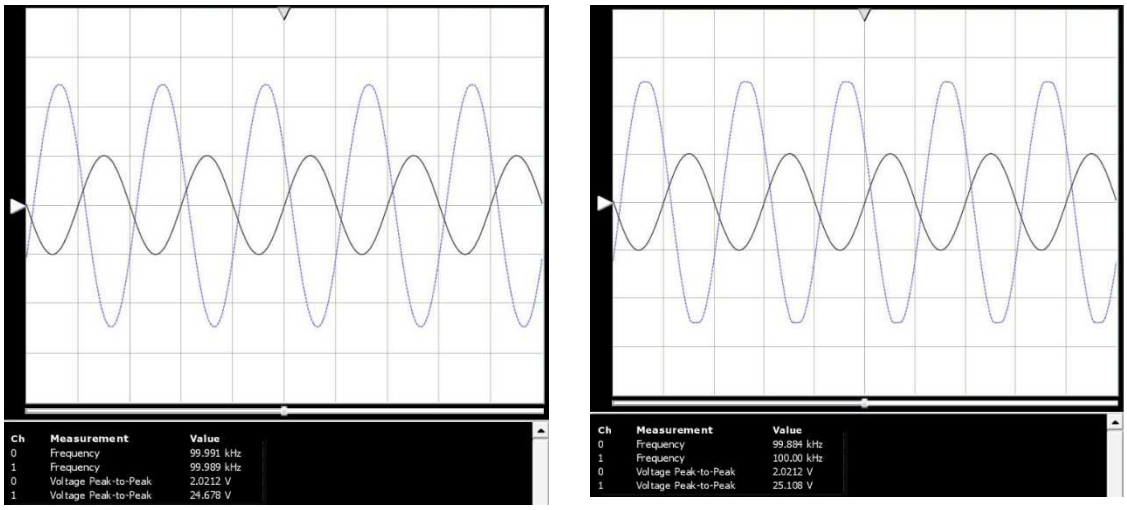

Figure 89 the output voltage of the current conveyor current source with two loads of (a) 14.9kΩ with output voltage of 24.67V which is not saturated and (b) 15 kΩ with output voltage of 25.1V which is saturated at 100kHz.

We created a mirror current source structure by using two current sources 180 degrees out of phase and two OCCII-GIC circuits connected to act as inductors to cancel capacitance. We simulated the OCCII-GIC circuits only with a difference in the component value for R_4 placed in OCCII-GIC but the C_1 and R_3 are kept equal in component values. We presumed a tolerance value of less than <%10 in R_4 resistors placed in the OCCII-GIC circuits (i.e. $R_{4,\ 0\ PHASE}$=1300Ω, $R_{3,\ 180\ PHASE}$=1350Ω) and preserved R_3 and C_1 values equivalent (i.e.$R_{3,\ 0\ \&\ 180\ PHASE}$=97, and $C_{1,\ 0\ \&\ 180\ PHASE}$ =300pF) with a 1kΩ dummy load and a dummy stray capacitance of 160pF. We observed a sharp decrease (impact) in the output current curve at the expected frequency point as shown in the Figure 90.

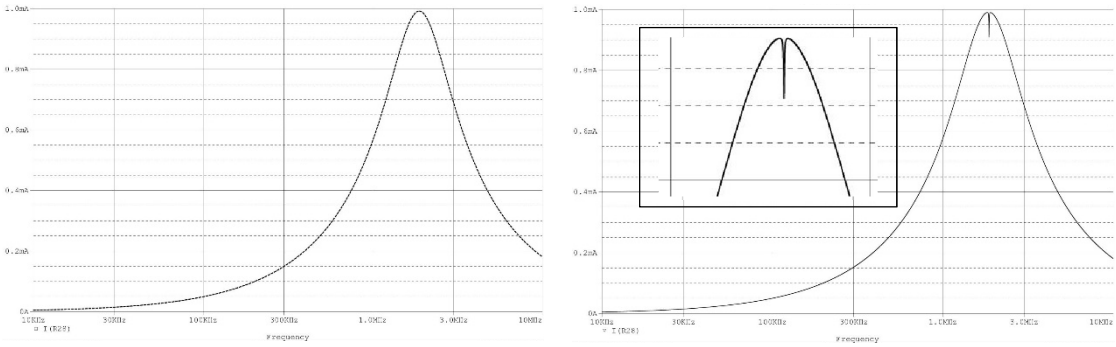

Figure 90 the output current signal of the mirror current source with attached OCCII-GIC circuits. The left output current curve obtained when using two identical OCCII-GIC circuits with the same values of R_3, R_4 and C_1. The right output current curve is obtained when using the same values for R_3 and C_1 but different values of R_4 (i.e. 1300Ω and 1350Ω).

Although, it is possible to have a different value of the stray capacitance in each branch of the mirror current source structure. By using different component values of R_3, R_4 and C_1 in the OCCII-GIC circuit, we can produce a corresponding inductance to cancel this capacitance but finally it needs to match and make two similar RLC circuits since this relies on LC resonance.

The simulation results confirm that we can use a single digital-pot in place of R_4 in the OCCII-GIC structure. This works better than using two digital-pots in place of R_3 and R_4 for multi-frequency systems as the OCCII-GIC is affected by the high pin capacitance of a digital-pot used instead of R_3. Therefore, the best solution is to use a single digital-pot in place of R_4 and to keep R_3 as a fixed resistor if we want an expected useful high frequency bandwidth of 1MHz to 3MHz for output impedance more than 1MHz, although this idea depends on the value of stray capacitance in the design that we want to cancel since that relies on LC resonance.

6.7. Measuring the output impedance of the current source under test:

The output impedance of the current source under test, and that with a capacitance cancelling circuit, has been treated as consisting of the parallel combination of an output resistance, R_O, and output capacitance, C_O i.e. $Z_O=R_O||Zc_o$. When the current source is delivering current into a resistive load Z_O needs to be large with respect to the load in order to not affect the measurements unduly. This means

Ro and Zc_o need to be large with respect to the load at all frequencies. At low frequencies the impedance of R is the main effect on the AC voltage on the resistive load, thus R_O. At high frequencies $Zc_o = 1/jwc_o$ must be large with respect to the load resistance thus Co must be small (See Figure 91 and Figure 92).

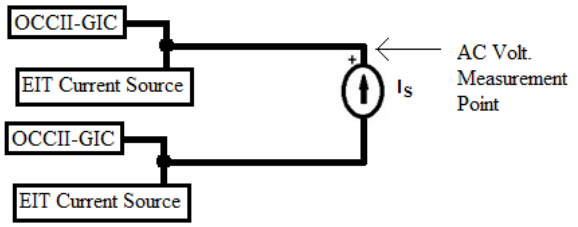

Figure 91 Perfect current source connected to the output point of the current source and measuring the AC voltage

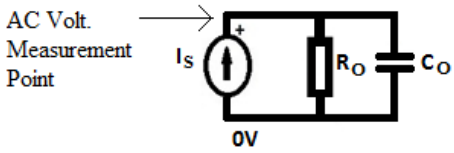

Figure 92 Perfect AC current source with R_O and C_O and measuring the AC voltage

Two different approaches, in simulation and in practice, of measuring the output impedance Z_O, have been used:

One (see Figure 91), earth the input and measure the output voltage when the output is driven by an AC current source.

Two (see Figure 92), drive the input with a voltage and using the fact that the circuit delivers a constant current dependent on the input voltage and the only load on the output is Z_O, measure the output voltage and deduce Z_O, alternatively add a known load R and deduce Z_O where Z_O is in parallel with R.

Any results of a swept AC analysis simulation need to be confirmed with a transient simulation at different frequencies. If a transient simulation shows that the output is centered near and around 0^V and is not clipping, at the start of the simulation, then an AC analysis is probably valid. If not then a load resistor connected to 0V to center the output and eliminate clipping by reducing the output must be used. In this case, the output impedance (Z_O) is found by considering the output impedance in parallel with this load.

6.7.1. Simulating the first method

We set the input drive to zero, inject 1mA with a perfect AC current source into the output and measure the amplitude and phase of the output. This will give a characteristic shape when the output voltage amplitude and phase are plotted against frequency. Then to find the output resistance and capacitance that these plots

indicate, we drive with an identical perfect AC source a parallel earthed resistor, $R_{EXP,}$ and capacitor, C_{EXP} and change the R_{EXP} and C_{EXP} values until the shapes of the amplitude and phase plots match. If a load resistor was used to bring the output near 0V then the output impedance is found by considering the output impedance in parallel with this load.

6.7.2. In practicing the first method

A very high input impedance and high frequency AC voltage probe and a very high output impedance and high frequency AC source are needed. Both exist in the OrCAD package but are hard to realize in practice, especially the AC source. A practical AC source that will not grossly affect the measurements needs to have output impedance that is much greater than the expected output impedance to be measured and an output capacitance much less than the expected output capacitance. A supporting company, Sensatech Research (Thomas Bach 2014), provided suitable high input impedance, $>10^{11}\Omega$ and <0.1fF, and high frequency, >10MHz, probes and high output impedance and high frequency AC sources, for taking the practical measurements.

6.7.3. Simulating the second method with no load if possible

We drive the input with a voltage and use the fact that we have a circuit that has a transfer ratio of 1V/mA with little phase angle driving Z_O only, measure the output voltage. This gives us a simple method to confirm the circuit is working correctly at different frequencies and loads. Since the circuit designed is working correctly as a constant current generator of 1mA, if we drive the input with 1V AC, a 1kΩ load should have 1V AC across it and a 2kΩ load should have 2V AC across it. This needs to be confirmed at frequencies > 1MHz. Thus we can confirm that the voltage on the load follows the transfer ratio of 1V/mA correctly and the phase error is small.

6.7.4. Practicing the second method

Only a very high input impedance and high frequency AC voltage probe is needed. At low frequency the output resistance is the output voltage divided by 1mA.

For example, if a 1V AC input drive gave an output voltage of 100V AC this must mean the output impedance is 100kΩ.

The output impedance found with an AC analysis does not take into consideration the effect of the rail voltage of the circuits used. At best the active devices used will have a maximum input and output voltage equal to their rail voltage. A transient analysis will show these effects. As the active devices in the OCCII-GIC cannot give 100V AC at their output or accept it on their input then this is not a practical method as it stands. The input drive voltage of the AC constant current generator must be reduced in order to use this principle to measure the output impedance.

Looking closely at the components used in the OCCII-GIC, we soon see some practical limitations. The Texas Instruments OPA656 operational amplifier is used in both the Howland source and in the OCCII-GIC. This device is powered from +/-5V rails and is not rail-to-rail input or output. The maximum positive input voltage is typically +2.05V and the maximum negative input voltage is -3.9V according to the data sheet (Data Sheet-OPA656 2008). Thus used in the Howland source if the load is approximately 1.05kΩ the output will be near clipping as the current from the output first flows through a 1kΩ resistor in series with the output IC pin before getting to the load and feedback resistors. We need to reduce the input drive to around 0.5mV in order to make our signal small enough so that we do not have output clipping in the Howland, thus allowing us to practically measure the output impedance. This gives us an AC current source output of 0.0005 mA and an expected voltage across a 3MΩ resistor of 1.5V ($3*10^6$Ω × 0.0005mA = 1.5V). This method used as a simple method to measure the output impedance of the current source both in simulation and in practice.

When used in the OCCII-GIC its input will be at or near clipping when a perfect source is driving an output impedance of approximately 2.05kΩ. This causes an input near the maximum input before distortion of the OPA656 used in the first stage of the OCCII-GIC. For calibration for example a near perfect 1MΩ resistor has been made by using two in series 0.5 MΩ +/-0.1% tolerance resistors, suspended in air, thus reducing its parallel stray capacitance to an estimated 0.1pF across the pair.

6.8. To validate the performance of the current source

A plot of the output impedance versus frequency is provided as shown in Figure 93. We assign the resulting maximum values of R_O and Z_O when minimizing the output capacitance C_O of the circuit. In the case of the improved Howland current source, we maximized the output resistance of the current source by using the digital-pot inside the improved Howland current source (in place of R_3), and eliminated the total output capacitance by adjusting the digital-pot inside the OCCII-GIC (in place of Y4). The output impedance is influenced by the both digital-pots in the improved Howland source and the OCCII-GIC, so we used the MCU to achieve the maximum output impedance of the circuit. In the case of the current conveyor current source, the digital-pots in OCCII-GIC are adjusted to eliminate the total output capacitance C_O = 3fF (femto-Farad), thus, an output impedance of 1MΩ at the 3MHz frequency point has been achieved. Although a phase shift is present in the current output signals and it needs to be computed as a part of the measurement data when producing the image.

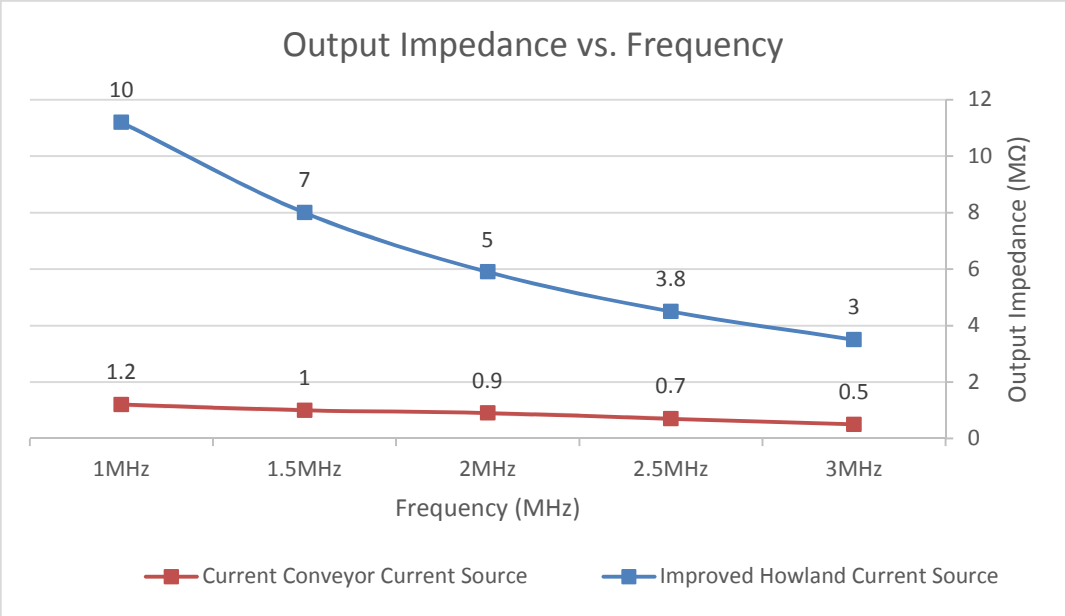

Figure 93 A result of the output impedance (Z_o) when combining the current sources with OCCII-GIC over the frequency range of 10kHz to 3 MHz

In reality it is possible to achieve much better output impedance of the EIT system since the total value of stray capacitance (C_{STRAY}) is less than <30pF in AZ1 EIT system (as this includes the on/off capacitance of the drive multiplexers). We are able

to operate on the variable frequency bandwidth between 1MHz to 3MHz with an output impedance of more than 1MΩ. The results show that the output impedance is 10MΩ at 1MHz, and stays above 500kΩ at 3MHz frequency.

6.9. Evaluate phantom

As a first step, we connected the actual E-phantom to the EIT board by using the 85 electrodes (INGUN Electrode GKS-100 224 130A 2000A) for plug-in connection. The electrode shape and characteristic are shown in Figure 67 which has less than 20mΩ contact resistance (DATA SHEET-INGUN 2004). Thus, it would be a great direct connection between the EIT board electrode nodes and E-phantom board electrode nodes. Since, these electrodes are spring loaded and we used them to fit this connection. Also these electrodes are exactly the same as the electrodes used for the image reconstruction. Figure 94 shows the connection between the EIT board and E-phantom board.

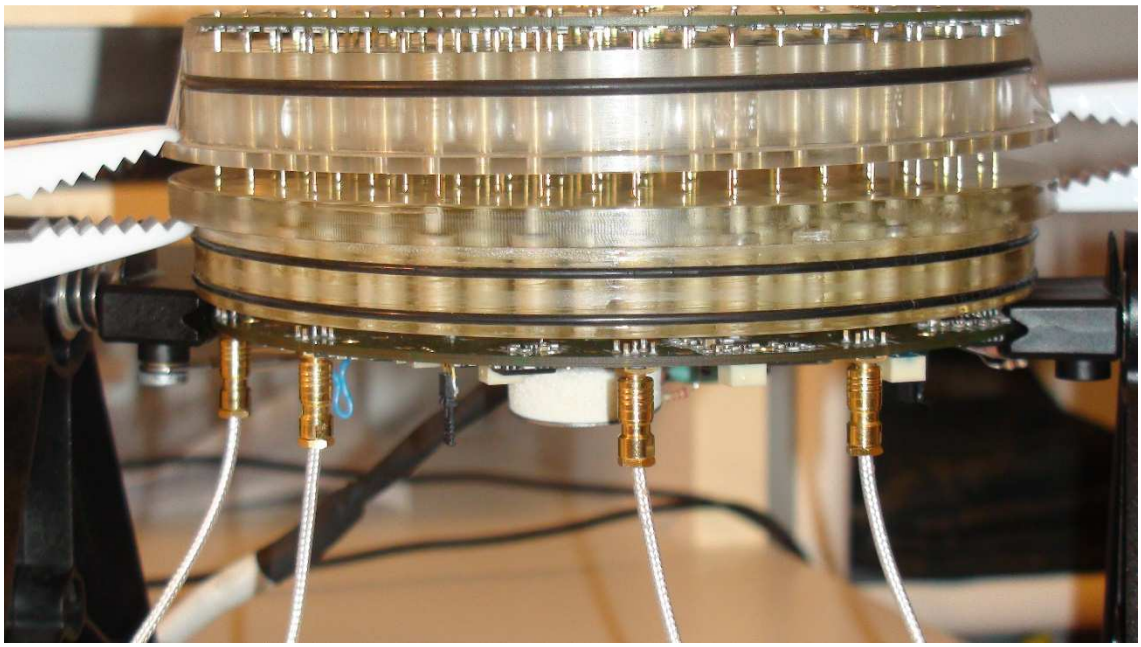

Figure 94 shows the connection between the EIT board at the bottom and the E-phantom board at the top by using 85 electrodes.

In the 2nd step, the E-phantom and the RSC circuit models are simulated in a PSpice OrCAD simulation. The theoretical result of the impedance measurements has been found by solving the Cole-Cole equation. Figure 95 shows the impedance curve of

three different tissues at different frequencies. The phantom simulation is based on evaluating how the E-phantom (consisting of 1200 resistors), performs as a simulation model of the saline conductive medium, 0.5mS/cm conductivity.

RSC modules are inserted into the medium as a target to simulate different tissues. The measurement results are fed to an inverse reconstruction algorithm. The RSC models are used to simulate the electrical properties of tissues inside a medium where the complex conductivity differs from the conductivity of the medium (Qiao, Wang et al. 2012). The theoretical and experimental impedance spectra for the Carcinoma, Fat, and Stroma tissues with the real, imaginary and relaxation frequency are shown in Figure 95.

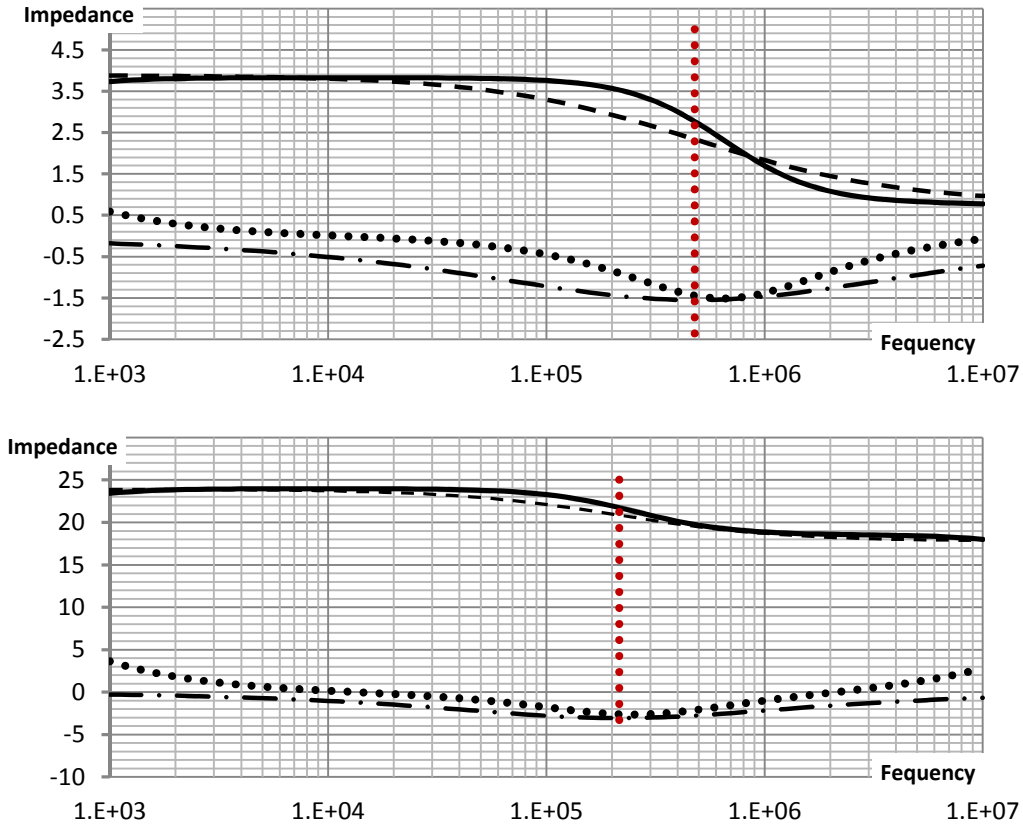

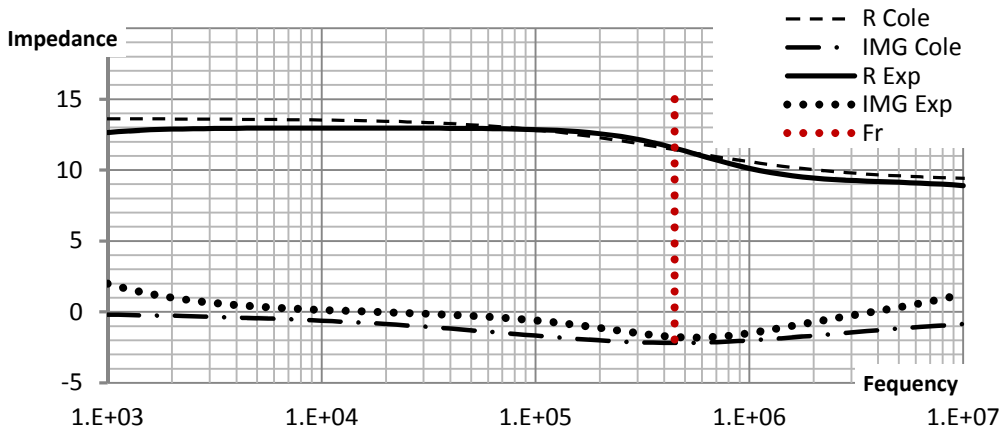

Figure 95 Theoretical and experimental impedance spectra for (a) Carcinoma, (b) Fat, and (c) Stroma, Real, Imaginary and Relaxation Frequency (F_r)

The real and imaginary curves of the impedance of Carcinoma, Fat and Stroma tissues are used to find the different properties of these tissues, namely: R_0, R_∞ and Fr. In general, these curves are compared to the theoretical and experimental results of the EIT system, since the objective is to find the actual behaviour of the system.

We have evaluated the phantom accompanied by a simulation analysis process of the EIT structure, keeping in mind the need for the most effective use of the RSC models in order to best evaluate the tissue properties.

This simulation work has led to the development of a resistive phantom simulation design whose values are found using the FEM mesh phantom method. The resistive phantom is primarily employed to be connected instead of using a physical phantom to assess the performance of an EIT system with multi-frequency input signals. As localized conductivity perturbations are produced by this electronic mesh phantom, it can be used to evaluate the performance of the EIT algorithms for image reconstruction. Tests and simulations were performed on the EIT system to indication the Cole-Cole dispersion data and conductivity perturbations perform on the EIT system.

As the next step in evaluating the resistive phantom system, we constructed a tomography image based on the AZ1 EIT system. Figure 96 shows the image reconstruction based on a simulation program that consisted of the whole EIT system and resistive E-phantom with effects using inserted RSC models. Five frequencies were

used in the measurement sequence from 30 kHz to 3MHz (30 kHz, 100 kHz, 300 kHz, 1 MHz and 3 MHz frequency points, respectively) with an injected current intensity of 2mA peak to peak for this image reconstruction scheme. Figure 96 shows the image reconstruction based on a tissue simulation program that has included an RSC model between 17 and 5 electrodes (9 O'clock).

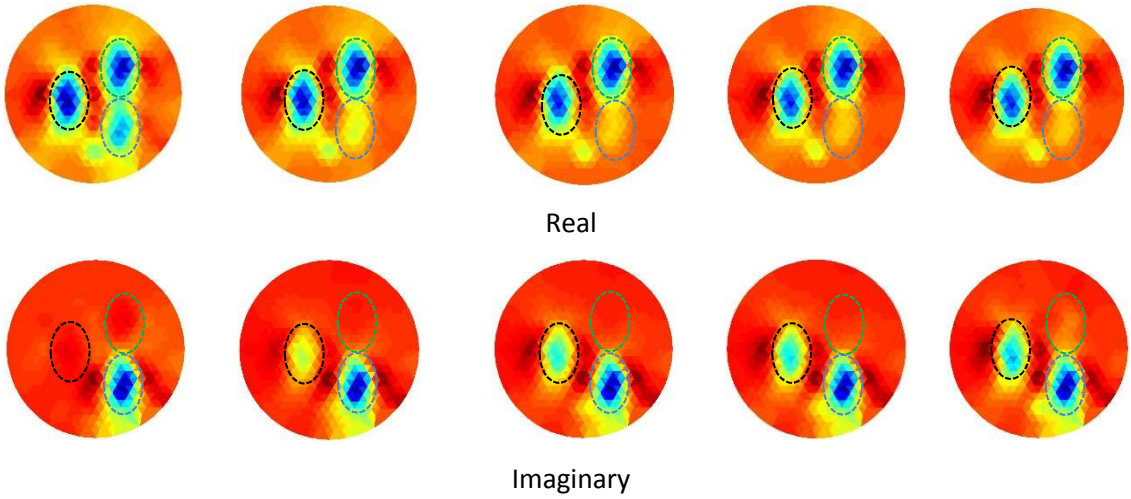

Figure 96 the real and imaginary part of frequency-difference images of an E-phantom within three RSC models RSC-1: placed at 17-5 (9 o'clock with black dotted line) for carcinoma tissue, RSC-2: placed at 15-21 (2 o'clock with green dotted line) for stroma tissue, and RSC-3: 19-30 (5 o'clock with blue dotted line) for fat tissue from 30 kHz to 3 MHz respectively

In this section we present a comparative image that is produced by removing the back projection image. If we take the image without any RSC model is the back projection data, then remove this data from the image during the reconstruction process this will produce the final image that is showing the electrical properties of an RSC model inserted between two electrodes. Figure 97 shows the image of the EIT system when we remove the back projection image. This image is produced from using the simulation program to simulate the E-phantom and RSC model at 3MHz frequency.

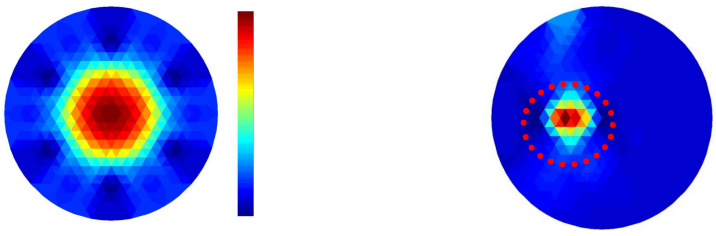

Figure 97 the left figure displays the image as a raw data and the right figure shows after removal of back projection at 3MHz with an RSC model of Carcinoma between electrodes e_{17} - e_5 (9-clock). The Carcinoma tissue has a cubic shape with the dimensions of 10mm(W)*10mm(L)*10mm(H), and the RSC value of R=202Ω,S=0.6Ω,C=695pF

6.10. System evaluation

The total data set for the Sussex EIT system comprises of 1416 measurements. This measurement was repeated 1000 times and the data analyzed statistically using the following equations for SNR and Accuracy.

$$SNR = 20 \log \frac{\left| \frac{1}{n} \sum_{i=1}^{n} v_i \right|}{\sqrt{\frac{1}{n-1} \sum_{n=1}^{n} (v_i - \bar{v})^2}} \quad 59$$

where v_i denotes the i[th] measurement, $\bar{v}$, the average of v_i.

The accuracy is calculated from the following equation:

$$A_i = \left[1 - \left| \frac{\frac{1}{n} \sum_{i=1}^{n} v_i - v_i^t}{v_i^t} \right| \right] \times 100 \quad 60$$

where v_i^t denotes the theoretical value for the i[th] measurement.

We measured SNR and accuracy as shown in Figure 98 and Figure 99 where the measurement index increases from 1 to 1416.

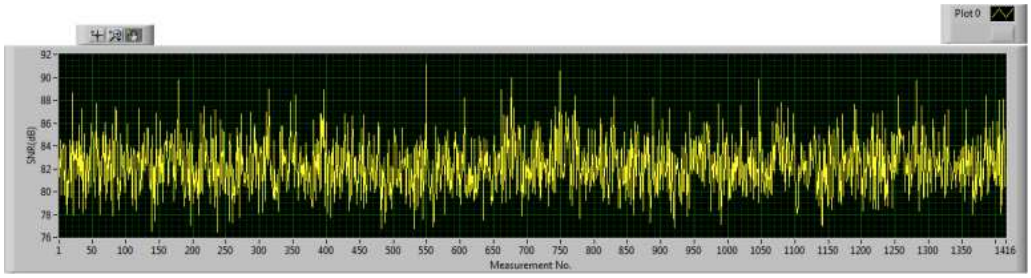

Figure 98 SNR- Measurement no. of the 1416 measurements of the pure conductivity on 2D planar

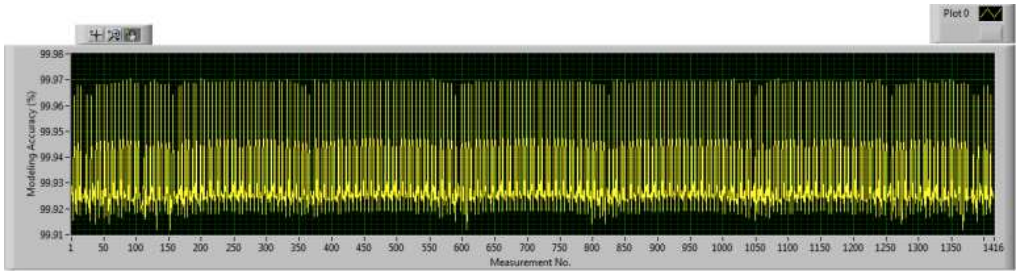

Figure 99 Modelling Accuracy – Measurement no. of the 1416 measurements of the pure conductivity on 2D planar

The average SNR of 82.28dB with the maximum SNR of 91.06dB and minimum SNR of 76.42dB are achieved. An average modelling accuracy of 99.47% with max and min value of 99.97 and 99.91 are achieved.

Chapter 7 General discussion and conclusion

7.1. General discussion

We designed the high performance and low current distribution power system with a low current effect to minimize their effect on the analogue circuits. Our results have shown it is advantageous to have an accurate on-board power supply. These supplies +/-5Vdc for the op amps, MUXs and +/-15Vdc for the current conveyors. Our results show that this is especially important for the OPA656 op amp as reducing the power rails reduces the maximum output voltage of the load. This means for a 1mA current source that the maximum load that can be driven is reduced. We also used ferrite beads to block the high-frequency energy coming back through the supply, thus decreasing the minimum noise in the power supply lines of the op amps. Using an on-board stable power supply for the EIT board is an advantage compared to other EIT systems that use an external power supply circuit for convenience and minimum noise reasons. The power isolation also designed and used protection circuits for patient safety.

We used a single sinewave input in the AZ1 EIT system that produced by signal generator. We created two 180 degrees out of phase current sources and routed these sources to the electrodes using multiplexers. We used a cascading method with two stages of drive multiplexers in series in each current source channel to minimize the total on/off capacitance of the multiplexers thus the minimum total stray capacitance

involved with a current source. Although using multiplexer produces on/off capacitance associated with stray capacitance, using a single voltage source input and signal calibration system probably achieves more stable repetitive results than using multi-source techniques.

Developing analogue circuits are required by simulating the complete circuits and using the system noise with all specific component effects. We developed circuits via methods incorporating system protection and system shielding in analogue circuit design and the PCB prototype.

Due to new developments in electronics packaging and system design such as redesigning the power supply system when considering the system noise and improving the addressing control based on a micro-controller the performance of the system has been improved.

In regard to current source performance at high frequency in an EIT system, the output resistance and capacitance of the current source and parasitic capacitances especially in multiplexers used to route the current to electrodes reduce the output impedance of the current source. This degrades the ability to produce good spatial resolution. When these unwanted capacitances are cancelled, a higher output impedance current source can be achieved. In order to do this, a GIC (i.e. Gyrator) or NIC circuits used in parallel with a current source circuit is a common solution when the GIC circuit is tuned for each frequency point. However, GICs composed of two op-amps and five passive components as a solution in EIT systems does not have an ideal performance for multi-frequency systems. For this reason the more complicated OCCII-GIC circuit has been used to cancel the stray capacitance of the design. This method utilises two OCCII-GIC circuits combined with two 180 degrees out of phase current sources. Each OCCII-GIC circuit produces a variable inductance in parallel with the RC circuit created by the current source joined with the source and parasitic capacitances. This inductor circuit is used to cancel unwanted capacitances of the current source at different frequency points, thus created a RLC circuit that relies on an LC resonance condition, which increases the output impedance of the current source and improve the spatial resolution of the impedance images in the EIT system.

The simulation results show the need to make two identical RLC circuits in order to cancel the stray capacitance in the mirror current source structure. Although, it is possible to have a different value of the stray capacitance attached to each branch, it needs to match and create two similar RLC circuits in order to produce an equal LC resonance condition otherwise it would produce a sharp decrease in current at the peak frequency point on the output current signal.

In our case the value of stray capacitance for both branches are equal, therefore we need to keep both OCCII-GIC circuits with exactly the same component values in order to produce exactly the same value of inductance to cancel the unwanted capacitances involved with each current source at a specific frequency point. However, in regard to our experience the best solution would be first to use a calibration process to realize the maximum output impedance for each of the branches when minimizing the total capacitances then creating a fully mirrored current source structure and measured the result.

The simulation and experimental results are interpreted to draw conclusions about the system. Due to improvements in the system design such as the power supply, considering the system noise, improving the shielding system and protection circuits for patient safety, we obtained an EIT system with good performance and minimum noise effects. Our findings confirm that OCCII-GIC circuit based on active components is a similar method to common GIC with two op amps and five passive components to cancel the stray capacitance but it achieves much better results and works for the frequency range up to 3MHz. Our results suggest that conditioning the current source of the EIT system based on using the OCCII-GIC circuit to cancel unwanted capacitance effects for improving spatial resolution of the impedance images is a valuable approach. The simulation and experimental results showed that it delivered a multi frequency EIT system based on tuneable frequency points with acceptable output impedance for different loads. The AZ1 EIT system has been tested and achieved a high SNR and modelling accuracy of the output voltage signal. Experimentally the goal was to try to make the circuit give a maximum output impedance at high frequencies with minimum phase shift and gain characteristics

compared to the reference signal. This is achieved when we are able to remove the effect of capacitances including those produced by the digital-pots. Although there is a limit on changing the load capacitance in the current source with OCCII-GIC as well as using GIC or NIC. Because the LC resonance condition will be changed (the value of inductance depends on the value of capacitance) this caused instability in the current source.

Comparison of the criteria used by Ross (Ross, Saulnier et al. 2003b) and Oh et al. (Oh, Lee et al. 2007) shows a similar method to cancel the stray capacitance by producing inductance using different circuits based on active components and digital-pots to produce a multi-frequency system establishing a system that works at frequencies up to 500kHz. In order to compare the performance of the current source combined with general GIC (composed of two op amp and five passive components as shows in Figure 13) based on Ross (Ross, Saulnier et al. 2003b) and Oh et al. (Oh, Lee et al. 2007) studies on the theoretical phase, simulating their circuits (the improved Howland current source and GIC structure) to produce a variable grounded inductor with the ability to adjust within the frequency range from 100Hz to 1MHz and achieve an output impedance much less than 500kΩ within the desired frequency range.

Since the passive components for the current source and general GIC structure are available with a tolerance and each passive component (e.g. resistor) in reality is paralleled with an estimated capacitance of 0.3pF of the SMD resistor on the PCB board, also the operational voltage amplifiers are affected by the common-mode and differential input impedance, which is undetermined in their study - the total output impedance of the current source circuit is significantly reduced. Additionally, the capacitance of the digital-pots is unspecified in their model, when using a digital-pot naturally produced parallel grounded capacitors in the high and low pins and a wiper with a variable resistor that are used in place of R_3 in the improved Howland current source and Z_5 in place of GIC structure, which also directly reduced the entire current source output impedance, therefore based on our achievements and results, we suggested an alternative GIC circuit based on active components to add to the current sources that are employed in EIT systems at high frequencies.

Our results confirm that AZ1 EIT system has been implemented with the OCCII-GIC as a stray capacitance cancellation method to improve the system performance and increased the frequency bandwidth of the system in comparison to other EIT systems. We have considered all the individual effects in the simulation circuits and prepared circuits with very similar behaviour to experimental conditions to achieve the similar experimental results. This helps us to understand and improve the performance results, which are much closer to the simulation results. This also helps us to consider the result of the OCCII-GIC structure and confirm that it works for the frequency range above 1MHz (We found it is possible to achieve an output impedance of 1MΩ at high frequency) and effectively would produce an impedance image when assessing the performance of the system using an E-phantom based on an RSC model of different tissue characteristics.

The OCCII-GIC configuration works with the current source and employs digital-pots to tune the circuit at each frequency point. The goal was to tune in order to achieve a system with high output impedance especially at higher frequencies. Our findings confirm that the OCCII-GIC circuit produces high output impedance that can be achieved over a limited bandwidth compared to the common GICs (i.e. Antoniou 1969) which consist of two op amp and five passive components. Using active components, such as a current conveyor which is a current-sense circuit compared to the operational amplifier used in common GICs which is a voltage-sense circuit with limitations such as frequency dependence and finite gain. Also the OCCII-GIC circuit built with less passive components (i.e. a capacitance and two resistors), achieves a stable current at high frequency, with much higher output impedance compared to other current sources using common GICs as a capacitance cancellation method which are designed and recommended by other EIT research groups (Ross 2003a, Oh, Lee et al. 2007).

It is worth noting that the frequency bandwidth will be narrow by moving the frequency points from 1MHz to 3MHz, since the maximum output impedance would be achieved at the peak point. So, it would be the best if able to achieve the maximum accurate value of variable resistor to obtain the maximum output impedance at the

certain frequency point, thus we used resistor trimmers (manual potentiometers) parallel and series with digital-pots to be able to calibrate the current source with OCCII-GIC circuits and achieve a calibration table for different frequency points.

The improved system is a planar 85 electrode channel, with multi frequency operation from two independent sources (current-based and voltage-based). We built and tested for the different EIT systems current sources, as the major current sources used in the EIT systems are based on improved Howland current source and Current Conveyor current source to confirm the OCCII-GIC is a method that will work in reality.

It is designed to operate in the frequency range from 10kHz up to 3MHz with an output impedance of a few GΩ over the desired frequency bandwidth but in regard to the electrical package limitation the combination of the OCCII-GIC with the improved Howland current source has not achieved the output impedance of a few GΩ at high frequency points (500kΩ at high frequency). However, we achieved acceptable output impedance for the frequencies between 1MHz to 3MHz. We designed an OCCII-GIC with two digital-pots to operate at the multi-frequency. Each digital-pot has been placed in the system with the minimum capacitance effect and these effects were considered in the simulation system and during the experimental tests. Thus we claim that the improved bandwidth based on a stray capacitance cancellation method increased the spatial resolution and operating frequency, hence improving the performance of the system although there are limitations with the appearance of a phase shift in the output current signals and DC offsets. The negative issue that we found with this approach was the effect of capacitances produced by the digital-pots, which affected the output impedance of the current sources. Using digital-pots we were able to remove the effect of parasitic capacitance produced by the current source and multiplexers when changing the LC resonance point but the capacitance of the pins of the digital-pots has an impact at high frequency.

We built an EIT system based on a planar 85-electrode channel and using an MCU for addressing control between 85 electrodes by using a cascade method for DRV MUXs. The on/off capacitance of the switching channel becomes very low (around

20pF) for each current injection branch, thus increasing the operating frequency and frame rate of the system when comparing it with the previous Sussex EIT systems. We used a single source method compared to semi/fully parallel source methods that use more than one source to connect to a single or a group of channels to stop the capacitance effect of DRV MUXs, but with the cascading method there is a possible method to reduce these capacitance effects and take advantage of the single source such as more convenience in the calibration process.

The capacitance cancellation method presented in this research is essentially used to facilitate high accuracy current injection for the multi-frequency EIT systems. Although, we simulated the current source combined with OCCII-GIC to cancel the C_{STRAY} with increment frequency point of 200 kHz, however, in reality we used only around 7 frequency points.

When comparing the current-based and voltage-based current sources, we found that the improved Howland current source has much better output impedance and less output capacitance compared to the current conveyor current source. Our results show that output impedance of the improved Howland current source combined with OCCII-GIC is much higher than the current conveyor current source combined with OCCII-GIC. However, the maximum load that can measured with the improved Howland current source is much lower than the current conveyor current source although it also depends on the DC power supply rails.

The calibration data of the EIT system are necessary to expand the resolution of reconstructed images because the measurement data that was obtained from the subject associated with the noise. This produces a much more complex system especially in multi frequency systems which have different phase and gain. AZ1 EIT system included an auto calibration process (as a voltage measurement system calibration) to measure the differential and common-mode gains with the effect of on-resistor of the multiplexers based on a few dummy resistor and calibration lines. This calibration process was controlled by the MCU and the measured values used as part of the calibration table. The calibration data was achieved when using dummy loads connected to different pair of electrodes and measuring the output voltage via

differential voltage measurement. Thus we were able to connect all electrodes one by one and measure the response voltage as the calibration data. Therefore, we were able to measure the effect of all drive and receive channels with this auto calibration process. Then, this calibration data was used in the image processing data, and used with the raw data to compare with the image data. This calibration process also combined with an electronic mesh phantom to fully assess the performance of the EIT system. Thus we obtained an EIT system with the channel assessment and acquired calibration data for each channel.

We used an 85 planar electrode plate, which placed on the bottom of the cylindrical measurement volume. The 85 electrodes fitted on the PCB as a circular planar array in order to achieve close electrode contact to the current source and minimize the noise and stray capacitance of the EIT system. Most EIT systems use cables to inject current or /and to collect measurement data; whilst the AZ1 EIT system is a planar structure with a single board of current injection, electrode plate and voltage measurement systems that able to inject the current signals and measure the voltage signals with minimum noise. The performance of the AZ1 EIT system is not dependent on the type and length of any cables.

The long term plan is to make available this innovative EIT system with its good on-board power supply, good high frequency current sources with capacitance cancellation method, drive and receive multiplexers, voltage measurement with calibration circuits, PGA, and an addressing control subsystems for 85 electrodes all fitted on a single circular board with an 83mm radius available in the market for all other EIT research groups at a minimum cost.

In EIT systems, assessment, validation of the performance and calibration of systematic errors in the electrical field generated inside of the interrogated volume is important. Our objective was to present and build an E-phantom for calibration, assessment and validation of the AZ1 EIT system performance in the *in vivo* conduction. Evaluation of the AZ1 EIT system has been assessed using a realistic E-Phantom, which is created and evaluated based on the RSC model of the different conductivities in breast tissue. We designed a dynamic mesh phantom that is capable

of imitating a generalized homogeneous medium. The planar E-phantom was also designed based on the FEM method to evaluate the system performance. We connected the E-phantom to the EIT board to assess the performance of the EIT system by the use of electrodes which have less than 20mΩ contact resistance with a length of 3.84cm. The EIT board electrodes are the same electrodes that are used to produce the breast tissue image, the phantom thus characterised the same effects that are produced during the *in vivo* conditions for reconstructing the conductivity image of the breast. Therefore, we can confirm that this phantom obtained the same results and it is therefore realistic for the *in vivo* condition to assess the performance of the EIT system. The EIT board directly connected to the E-phantom and produced raw data of 1416 measurement combinations then the calibration data was added to produce an image. Therefore, we used the calibration data and E-phantom assessments to be able to measure the SNR and model the accuracy of the AZ1 EIT system.

This E-phantom used a MCU to be able to produce a conductive perturbation in 6 places, which is used to produce different images that can be used to evaluate the image reconstruction software. The E-Phantom design improved its features by using the RSC model, where we considered the capacitance effects of the different tissues at the different frequencies by solving the Cole-Cole equation. This enables the evaluation of the different conductivity values of the tissue. We performed the E-phantom with three different tissue values as mentioned in Table 11, the results show that the system is able to specify the different tissue characteristics and the performance features of the EIT system. The RSC models the EIT system with different tissue characteristics placed between 85 electrodes to obtain the impedance spectra of these tissues. The full cycle of the Cole-Cole model can be achieved with this EIT system for the tissues that have a relaxation frequency around 1MHz as the AZ1 EIT system can operate up to 3MHz. This E-phantom is able to imitate all the electronic characteristics of the physical environment of a breast inside a cylindrical insulated container that has been described in the mesh phantom principles section. This phantom can be used for 2D and 3D calibration process. However, this phantom only emulates a 10mm thick layer with highest sensitivity of a saline conductive medium,

which can only emulate an impedance distribution representative of a breast tissue in saline with this thick layer of conductive medium. This E-phantom is designed for the planar structure. However, it can be used to assess the performance of the other EIT systems with any measurement structure, at any frequency and any amplitude range of the signal. Although, the variations in electrode-saline contact impedance are not accounted for by the E-phantom as it bypasses the electrolytic interface. We have not considered the other types of errors initiating from electrode contact impedances, electrode size and shape, and the effect of the subject position that generates systematic errors in the reconstructed images.

The preliminary results have demonstrated that the E-phantom can be very effective as a clinical prototype for QA assessment and future certification. The purpose of the phantom is intended for system validation and performance testing during all phases of the clinical trials: pre-trial, during trial and future clinical derivatives. The E-phantom will also be a useful research tool for EIT researchers, as altering the location and distribution of the impedivity is readily achieved.

Thus, a novel E-phantom designed, simulated and measured a desired SNR and modelling accuracy of the AZ1 EIT system, it also enables representation of the different tissue characteristics based on different RSC models.

7.2. Conclusion and future work

In order to decrease the unwanted capacitance effects in EIT systems, different GIC circuits have been designed, simulated and tested. Our aim is to assess most experimental results using the current source with OCCII-GIC circuit presented in the AZ1 EIT system. The AZ1 EIT system has been implemented with the OCCII-GIC as a stray capacitance cancellation method improving the system performance and increasing the frequency bandwidth of the system. The new EIT system is a planar 85 electrode board with multi-frequency channels with two independent sources (current-based and voltage-based) and designed to operate over a narrow frequency range from 10kHz up to 3MHz with an output impedance of a gigaohm to more than >

500kΩ at maximum frequency, in regard to existence of stray capacitance and electrode contact impedance sensitivity variations in geometry.

AZ1 EIT has been implemented for the clinical application that has been tested in the instrumentation and sensor laboratory at the Sussex University. A new feature of the GIC based on current conveyors has been presented with current based and voltage based source topologies. As previously described, it can be used as an inductor circuit to eliminate the effects of the stray and output capacitances of the current source. The performance of the OCCII-GIC has been computed with phase and magnitude errors. This capacitance cancellation technique is capable of working with other existing EIT sources. The study results of the OCCII-GIC are based on the active device with a current feedback loop, thus it is feasible to tune over a wide range of parameters. This is a significant change in the design compared to the general GIC methods used to ameliorate the constraints caused by passive components and op amp limitations.

Finally, AZ1 EIT circuit boards have been designed to install in the Sussex EIT system for the clinical trials, with numerous mechanical systems that have been installed on the clinical bed to produce the whole EIM test procedure.

In future work we intend to extend the capability of The AZ1 EIT system using (i) FPGA for signal generation, DAS and addressing control, (ii) combination of voltage and current source in a single platform, and (iii) extend the mesh phantom include the effects of the permittivity of the solution and electrode size and shape.

7.2.1. FPGA system overview Design a Digital waveform Generator based on FPGA

The FPGA design consists of independent parts: an implementation of the signal generation, a modulator, the matched filter and the ADC clock modules. The task defined is the design of a digital waveform generator using an FPGA and feeding this to the DAC with high stability and multi-frequency. For this aim the designed system uses 16-Bit DAC at 100 MSPS, via a passive band-pass filter with a zero degrees phase shift to have a smooth signal. By division of the 40 MHz or any other value of the

main clock of the FPGA the frequency of the signal can be changed. We are using digital phase sensitive demodulation (Digital-PSD) within the FPGA for synchronization between the data acquisition system (DAS) and signal generation, demodulation and changing the amplitude of the signal. We could therefore measure phase (the waveform data) with a shifter and then add a multiplying DAC to change the amplitude.

System consisting two main parts: signal generator and the data acquisition module. Regarding this design, we will design a system based on FPGA use in the DAS and signal generators related to the hardware specification that has been defined. This task comprises the following:

- Sine and Cosine waveforms with multi-frequencies for feeding to ADC
- Full spectrum of sampling signals to ADC
- Full spectrum of sampling signal from DAC as part of DAS measurement system
- Generation a DDSs (direct digital synthesizers)
- Generation a D-PSD (digital phase sensitive demodulation)
- Communication between FGPA and MCU
- Feed pattern to DACs
- Feed Cosine to DAC
- FGPA Implementation
- Digital matched filter structure
- Define sampling rate
- Produce clock for ADC
- Demodulation

7.2.2. The feasibility study of voltage source implementations

A voltage source can be implemented using a high-speed, wideband op amp as an alternative for the excitation system in EIT. A voltage source with high precision is inexpensive and simply can be implemented for the excitation system in EIT to resolve the current source problems.

The proposed technique is based on using a voltage source and measuring the actual voltage on an electrode connected to a reference impedance to confirm that the electrode voltage is known.

In this case little current will be injected into the target by the electrodes and thus the receiving electrodes will measure small voltages that suffer from noise. This can limit the ability to see deeply into the target. Also for safety reasons the current injected by the voltage method must be restricted if the target is alive, such as in breast cancer tomography. However, restrictions on the amount of bandwidth, high component count and complexity of analogue circuitry suggests that the voltage source method in EIT systems may be better than the current source as used in ACT4 and the Dartmouth group EIT system.

The existence of errant stray capacitance in parallel with the load causes undesired effects using both the voltage and current source methods. The voltage source method is also affected by the on-resistance of any multiplexers used in the signal path, as these form, with the undesired stray capacitances, low pass RC filters so any driving voltage will be altered in amplitude and phase by the time it reaches the electrode.

If we connect a known reference impedance to the electrode and measure the current injected by the driving voltage fixed in amplitude and phase before any multiplexers, we can measure the errors in amplitude and phase from the driving voltage. We can then apply correcting amplitudes and phases to the driving voltage source so that the amplitude and phase are what they would be without any RC effects. For safety reasons we must limit the current injected before it passes through a multiplexer to an electrode by using a small resistor in the signal line and measuring the voltage across it with a differential amplifier. In the current delivery method if we measure the voltage on each electrode pad with known calibrating impedance on the PCB, we have a similar way to measure errors caused by stray capacitances. The proposed voltage source schematic with feedback loop and the current measurement system is simulated in Figure 100. This method is able to analyse the effect of on-

resistance produced by MUXs. The result is a closed loop current system, which is only dependent on biological load.

Also, a calibration method is required in order to determine the CMRR of the differential amplifiers. The circuitry is designed to achieve a bandwidth of greater than 10MHz over a wide range of loads in the presence of load capacitance. Preliminary simulation results are obtained to found the bandwidth performance of the system in order to verify the practical implementation of the voltage source. Thus, we would utilize the voltage source on this board in order to achieve a multi-frequency system up to 10MHz with an acceptable SNR and accuracy. The calibration methods are also performed before and during data acquisition. We will employ an on board Microcontroller for tuning sources and selecting input and measuring channels. This research presents an innovative multi frequency EIT system based on current source and voltage source topologies. The simulation of the EIT system shows it should be useable at frequencies above 10MHz. Figure 100 shows a schematic diagram of a voltage source with DRV and REC MUXs, measurement subsystem based on a four-electrode method of the AZ1 EIT system.

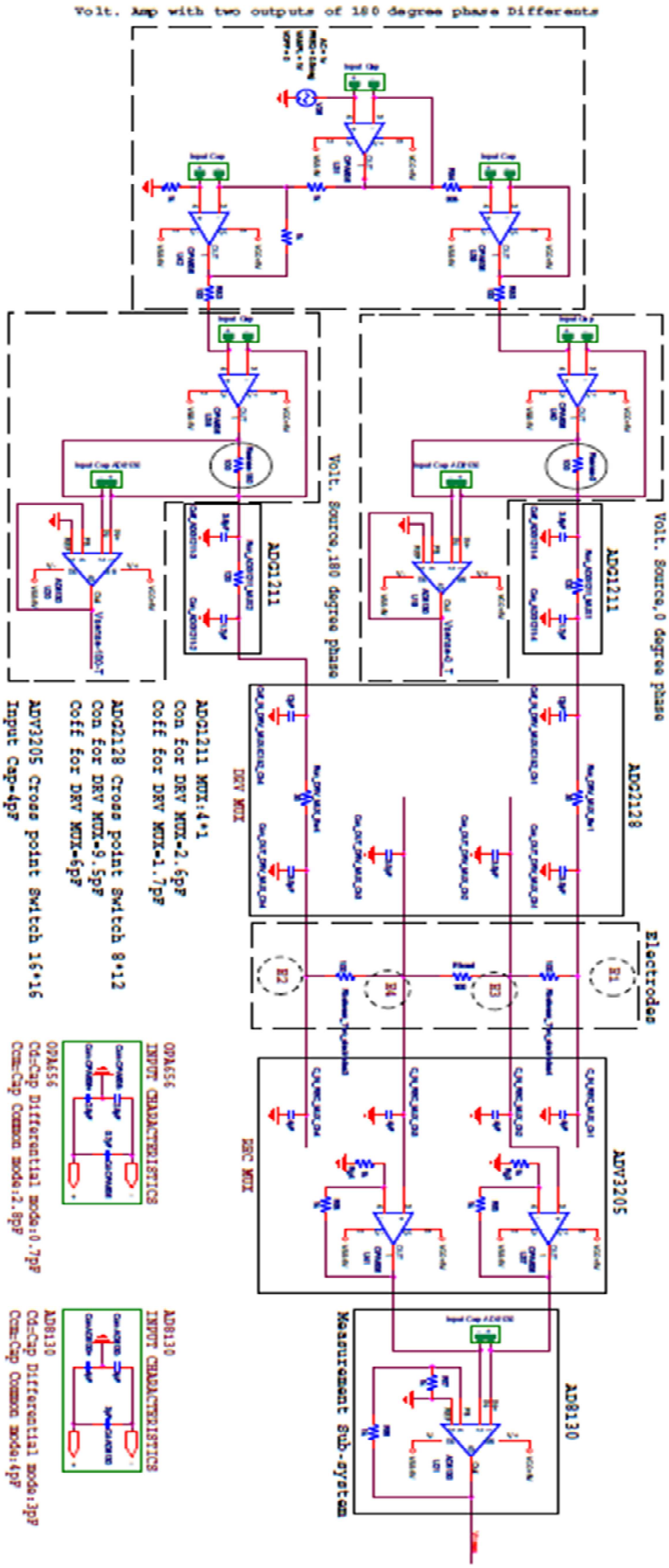

Figure 100 A schematic of a voltage source with DRV and REC MUXs, measurement subsystem.

7.2.3. The effect of electrode in the Mesh phantom design

We intend in future work to extend the capability of using this phantom so it is more accurate at high frequency. This means we intend to include the effects of the permittivity of the solution. This probably means every resistor of an improved E-phantom will have a capacitor across it or capacitor in series with a resistor. At high frequencies this will cause a phase shift across the original resistors and also make the amplitude of the impedance less. Including permittivity in the mesh will be a more complicated use of FEM as each element will be complex, i.e. the admittance element matrix will have real and imaginary parts.

In future work we intend to take into consideration the effect of electrode size and shape and to simulate some of the effects of the 3-D nature of the homogenous medium, container and target as opposed to the present 2-D simulation.

References

ABUELMA'ATTI, M. and TASADDUQ, N., 1999. New negative immittance function simulators using current conveyors. *Microelectronics Journal,* **30**(9), pp. 911-915.

ABUELMA'ATTI, M.T., 2000. Comment on'Active simulation of grounded inductors with CCII s and grounded passive elements'. *International journal of electronics,* **87**(2), pp. 177-181.

ADLER, A., GRYCHTOL, B. and BAYFORD, R., 2015. Why is EIT so hard, and what are we doing about it? *Physiological Measurement,* **36**(6), pp. 1067.

AMERICAN CANCER SOCIETY, 04/15, 2015-last update, Basic Cancer [Homepage of American Cancer Society], [Online]. Available: http://www.cancer.org [04/20, 2015].

AMMARI, H., 2008. *An introduction to mathematics of emerging biomedical imaging Modalities.* Berlin Heidelberg: Springer.

ANTONIOU, A., 1969. Realisation of gyrators using operational amplifiers, and their use in RC-active-network synthesis, *Proceedings of the Institution of Electrical Engineers* 1969, IET, pp. 1838-1850.

BARBER, D. and BROWN, B., 1984. Applied potential tomography. *Journal of Physics E: Scientific Instruments,* **17**(9), pp. 723.

BARBER, D., BROWN, B. and FREESTON, I., 1984. Imaging spatial distributions of resistivity using applied potential tomography—APT, *Information Processing in Medical Imaging* 1984, Springer, pp. 446-462.

BAXTER, G., JONES, V., MILNES, V., ODUKO, J.M., PHILLIPS, V., SELLARS, S. and VEGNUTI, Z., 9/1, 2014-last update, Guidance notes for equipment evaluation and protocol for user evaluation of imaging equipment for mammographic screening and assessment, NHSBSP Equipment Report 1411 [Homepage of NHS Cancer Screening Programmes], [Online]. Available: www.gov.uk/phe [12/1, 2014].

BAYFORD, R., 2006. Bioimpedance tomography (electrical impedance tomography). *Annu.Rev.Biomed.Eng.,* **8**, pp. 63-91.

BERA, T.K., 2014. Bioelectrical Impedance Methods for Noninvasive Health Monitoring: A Review. *Journal of Medical Engineering,* **2014**.

BINDU, G.N., ABRAHAM, S.J., LONAPPAN, A., THOMAS, V., AANANDAN, C.K. and MATHEW, K., 2006. Active microwave imaging for breast cancer detection. *Progress In Electromagnetics Research,* **58**, pp. 149-169.

BIOLEK, D., 1995. Novel signal flow graphs of current conveyors, *Circuits and Systems, 1995., Proceedings., Proceedings of the 38th Midwest Symposium on* 1995, pp. 1058-1061 vol.2.

BOND, E.J., LI, X., HAGNESS, S.C. and VAN VEEN, B.D., 2003. Microwave imaging via space-time beamforming for early detection of breast cancer. *Antennas and Propagation, IEEE Transactions oon,* **51**(8), pp. 1690-1705.

BOWRON, P. and STEPHENSON, F.W., 1979. *Active filters for communications and instrumentation.* McGraw-Hill.

BRAGOS, R., BLANES, P., RIU, P. and ROSELL, J., 1995. Comparison of current measurement structures in voltage-driven tomographic systems, *Innovations in Instrumentation for Electrical Tomography, IEE Colloquium on* 1995, IET, pp. 8/1-8/3.

BRAGOS, R., ROSELL, J. and RIU, P., 1994. A wide-band AC-coupled current source for electrical impedance tomography. *Physiological Measurement,* **15**(2A), pp. A91.

BROWN, B., 2003. Electrical impedance tomography (EIT): a review. *Journal of medical engineering & technology,* **27**(3), pp. 97-108.

BROWN, B. and SEAGAR, A., 1987. The Sheffield data collection system. *Clinical Physics and Physiological Measurement,* **8**(4A), pp. 91.

BRUUN, E. and OLESEN, O.H., 1992. Conveyor implementations of generic current mode circuits. *International journal of electronics,* **73**(1), pp. 129-140.

CANCER RESEARCH UK, 04/20, 2015-last update, What is cancer? [Homepage of Cancer Research UK], [Online]. Available: http://www.cancerresearchuk.org [04/20, 2015].

CANCER RESEARCH UK, 2014c. *UK Cancer Incidence (2011) by Country Summary, Jan.* CS_DT_INCCOUNTRIES. UK: Cancer Research.

CANCER RESEARCH UK, 16/04, 2014b-last update, Breast Cancer (C50), Average Number of New Cases per Year and Age-Specific Incidence Rates, Females, UK, 2009-2011 [Homepage of Cancer Research UK], [Online]. Available: http://www.cancerresearchuk.org/cancer-info/cancerstats/types/breast/incidence/uk-breast-cancer-incidence-statistics [1/12, 2014].

CANCER RESEARCH UK, 27/11, 2014a-last update, Beast Cancer (C50) Five-Year Relative Survival by Stage, Women Aged 15-99 Years, Former Anglia Cancer Network, 2002-2006 [Homepage of Cancer Research UK], [Online]. Available: http://www.cancerresearchuk.org/cancer-info/cancerstats/types/breast/survival/breast-cancer-survival-statistics#source6 [1/12, 2014].

CASAS, O., ROSELL, J., BRAGÓS, R., LOZANO, A. and RIU, P., 1996. A parallel broadband real-time system for electrical impedance tomography. *Physiological Measurement,* **17**(4A), pp. A1.

CHEREPENIN, V., KARPOV, A., KORJENEVSKY, A., KORNIENKO, V., MAZALETSKAYA, A., MAZOUROV, D. and MEISTER, D., 2001. A 3D electrical impedance tomography (EIT) system for breast cancer detection. *Physiological Measurement,* **22**(1), pp. 9.

CHOI, M.H., ISAACSON, D., SAULNIER, G.J. and NEWELL, J.C., 2003. An iterative approach for applying multiple currents to a body using voltage sources in electrical impedance tomography, *Engineering in Medicine and Biology Society, 2003. Proceedings of the 25th Annual International Conference of the IEEE* 2003, IEEE, pp. 3114-3117.

COLE, K.S. and COLE, R.H., 1942. Dispersion and absorption in dielectrics II. Direct current characteristics. *The Journal of chemical physics,* **10**(2), pp. 98-105.

COLE, K.S. and COLE, R.H., 1941. Dispersion and absorption in dielectrics I. Alternating current characteristics. *The Journal of chemical physics,* **9**(4), pp. 341-351.

COOK, R.D., SAULNIER, G., GISSER, D.G., GOBLE, J.C., NEWELL, J. and ISAACSON, D., 1994. ACT3: A high-speed, high-precision electrical impedance tomograph. *Biomedical Engineering, IEEE Transactions on,* **41**(8), pp. 713-722.

COURTESY OF THE NATIONAL CANCER INSTITUTE, 4/23, 2015-last update, Getting Your Mammogram Results [Homepage of NIH Turning Discovery Into Health], [Online]. Available: http://www.cancer.gov/cancertopics/types/breast/understanding-breast-changes [4/26, 2015].

DATA SHEET-3269W, 2011. *3269 - 1/4 " Square SMD Trimpot, Trimming Potentiometer.* Trimpot. Bourns.

DATA SHEET-AD8114, 2005a. *Buffered Analog Crosspoints Array, Low Cost, 225 MHz, 16×16 Crosspoint Switches.* Rev. B. Analog Devices.

DATA SHEET-AD8130, 2005b. *Voltage Measurement, Low Cost, 270 MHz Differential Receiver Amplifier.* Rev. C. Analog Devices.

DATA SHEET-AD844S, 2009. *Current Conveyor, Monolithic Op Amp, 60 MHz, 2000 V/ms, with Current Feedback Amplifiers.* REV. C. Analog Devices;.

DATA SHEET-ADG1211, 2012a. *Analog Switches Multiplexers, Low Capacitance, Low Charge Injection, iCMOS, Quad SPST Switches.* Rev. B. Analog Devices.

DATA SHEET-ADG2128, 2012b. *Analog Switches Multiplexers, I^2C CMOS, 8 X 12 Analog Switch Array with Dual/Single Supplies.* Rev. D. Analog Devices.

DATA SHEET-ADV3205, 2011. *Buffered Analog Crosspoints Array, 60 MHz, G = +2, 16 ×16 Buffered Analog Crosspoint Switch.* Rev 0. Analog Devices;.

DATA SHEET-FT232R, 2010. *USB to serial UART interface, USB UART IC, FTDI chip.* FT_000053. Future Technology Devices International Limited.

DATA SHEET-INGUN, 2004. *INGUN GKS-100 224 130A 2000E, Test Probes,* Catalog 2003/04. Ingun.

DATA SHEET-OPA656, 2008. *Operational Amplifier, Wideband, Unity Gain Stable FET-Input,* SBOS196G,. Texas Instruments Inc.;.

DATA SHEET-OPA657, 2008b. *OPERATIONAL AMPLIFIER,1.6GHz, Low-Noise, FET-Input, OPA657, Rev. E.* SBOS197E. Texas Instruments Inc.

DATA SHEET-PIC18F87K90, 2010. *Family, 64/80-Pin, High-Performance Microcontrollers with LCD Driver and nanoWatt XLP Technology.* DS39957B. Microchip Technology Inc.

DATA SHEET-RESISTIVE PRODUCT, 2015. *Precision Thin Film Chip Resistor, tolerances to ±0.01%.* RNCF Series. Stackpole Electronics, Inc.

DATA SHEET-X9C102, 1996. *E2POT Nonvolatile Digital Potentiometer.* 3863-2.4 2/12/99 T2/C0/D0 SH. Xicor Inc.

DE MARCELLIS, A. and FERRI, G., 2011. *Analog circuits and systems for voltage-mode and current-mode sensor interfacing applications.* 2011 edn. Netherlands: Springer.

ELORANTA, P., 2004. Current Conveyors, History, Theory, Applications and Implementation. *Postgraduate Course in Electronic Circuit Design II, Helsinki University of Technology,* .

FABRIZI, L., MCEWAN, A., OH, T., WOO, E. and HOLDER, D., 2009. A comparison of two EIT systems suitable for imaging impedance changes in epilepsy. *Physiological Measurement,* **30**(6), pp. S103.

FANG, Q., MEANEY, P.M., GEIMER, S.D., STRELTSOV, A.V. and PAULSEN, K.D., 2004. Microwave image reconstruction from 3-D fields coupled to 2-D parameter estimation. *Medical Imaging, IEEE Transactions on,* **23**(4), pp. 475-484.

FEAR, E.C., LI, X., HAGNESS, S.C. and STUCHLY, M.A., 2002. Confocal microwave imaging for breast cancer detection: Localization of tumors in three dimensions. *Biomedical Engineering, IEEE Transactions on,* **49**(8), pp. 812-822.

FERLAY, J., SOERJOMATARAM, I., ERVIK, M., DIKSHIT, R., ESER, S., MATHERS, C., REBELO, M., PARKIN, D., FORMAN, D. and BRAY, F., 2014. GLOBOCAN 2012 v1. 0, Cancer Incidence and Mortality Worldwide: IARC CancerBase No. 11 [Internet]. Lyon, France: International Agency for Research on Cancer. c2013 [cited 2013 Oct 17]. *globocan.iarc.fr/Default.aspx.Accessed,* .

FERLAY, J., SOERJOMATARAM, I., DIKSHIT, R., ESER, S., MATHERS, C., REBELO, M., PARKIN, D.M., FORMAN, D. and BRAY, F., 2015. Cancer incidence and mortality worldwide: sources, methods and major patterns in GLOBOCAN 2012. *International Journal of Cancer,* **136**(5), pp. E359-E386.

FERRI, G., GUERRINI, N., ROMANATO, R., SCOTTI, G. and TRIFILETTI, A., 2007. CCII-based high-valued inductance simulators with minumum number of active elements, *Circuit Theory and Design, 2007. ECCTD 2007. 18th European Conference on* 2007, IEEE, pp. 440-443.

FHAGER, A., HASHEMZADEH, P. and PERSSON, M., 2006. Reconstruction quality and spectral content of an electromagnetic time-domain inversion algorithm. *Biomedical Engineering, IEEE Transactions on,* **53**(8), pp. 1594-1604.

FRANCO, S., 2014. *Design with operational amplifiers and analog integrated circuits.* 4th edn. New York, USA: McGraw-Hill.

GAGNON, H., COUSINEAU, M., ADLER, A. and HARTINGER, A.E., 2010. A resistive mesh phantom for assessing the performance of EIT systems. *Biomedical Engineering, IEEE Transactions on,* **57**(9), pp. 2257-2266.

GAGNON, H., HARTINGER, A.E., ADLER, A. and GUARDO, R., 2008. A phantom for assessing the performance of EIT systems, *EIT Conf. 2008 (Dartmouth, NH, USA)* 2008.

GAGNON, H., SIGMEN, Y., HARTINGER, A.E. and GUARDO, R., 2009. An active phantom to assess the robustness of EIT systems to electrode contact impedance variations, *Proceedings of the International Conference on Biomedical Applications of Electrical Impedance Tomography (EIT'09)* 2009.

GIFT, S.J., 2004. New simulated inductor using operational conveyors. *International journal of electronics,* **91**(8), pp. 477-483.

GISSER, D., ISAACSON, D. and NEWELL, J., 1988. Theory and performance of an adaptive current tomography system. *Clinical Physics and Physiological Measurement,* **9**(4A), pp. 35.

GOHARIAN, M., SOLEIMANI, M., JEGATHEESAN, A., CHIN, K. and MORAN, G.R., 2008. A DSP based multi-frequency 3D electrical impedance tomography system. *Annals of Biomedical Engineering,* **36**(9), pp. 1594-1603.

GRIFFITHS, H., 1995. A Cole phantom for EIT. *Physiological Measurement,* **16**(3A), pp. A29.

GRIFFITHS, H., 1988. A phantom for electrical impedance tomography. *Clinical Physics and Physiological Measurement,* **9**(4A), pp. 15.

HAHN, G., BEER, M., FRERICHS, I., DUDYKEVYCH, T., SCHRÖDER, T. and HELLIGE, G., 2000. A simple method to check the dynamic performance of electrical impedance tomography systems. *Physiological Measurement,* **21**(1), pp. 53.

HAHN, G., JUST, A., DITTMAR, J. and HELLIGE, G., 2008. Systematic errors of EIT systems determined by easily-scalable resistive phantoms. *Physiological Measurement,* **29**(6), pp. S163.

HARTOV, A., MAZZARESE, R.A., REISS, F.R., KERNER, T.E., OSTERMAN, K.S., WILLIAMS, D.B. and PAULSEN, K.D., 2000. A multichannel continuously selectable multifrequency electrical impedance spectroscopy measurement system. *Biomedical Engineering, IEEE Transactions on,* **47**(1), pp. 49-58.

HENDERSON, R.P. and WEBSTER, J.G., 1978. An impedance camera for spatially specific measurements of the thorax. *Biomedical Engineering, IEEE Transactions on,* (3), pp. 250-254.

HIGASHIMURA, M.F., 1987. Novel method for realising lossless floating immittance using current conveyors. *Electronics Letters,* **23**(10), pp. 498-499.

HOLDER, D.S., 2005. *Electrical impedance tomography: methods, history and applications.* first edn. Bristol: Institute of Physics Publishing.

HUBER, N., BÉQO, N., ADAMS, C., SZE, G., TUNSTALL, B., QIAO, G. and WANG, W., 2010. Further investigation of a contactless patient-electrode interface of an Electrical Impedance Mammography system, *Journal of Physics: Conference Series* 2010, IOP Publishing, pp. 012166.

HUMPHREY, L.L., HELFAND, M., CHAN, B.K. and WOOLF, S.H., 2002. Breast cancer screening: a summary of the evidence for the US Preventive Services Task Force. *Annals of Internal Medicine,* **137**(5_Part_1), pp. 347-360.

HWANG, E.S., KINKEL, K., ESSERMAN, L.J., LU, Y., WEIDNER, N. and HYLTON, N.M., 2003. Magnetic resonance imaging in patients diagnosed with ductal carcinoma-in-situ: value in the diagnosis of residual disease, occult invasion, and multicentricity. *Annals of surgical oncology,* **10**(4), pp. 381-388.

ISAACSON, D., MUELLER, J. and SILTANEN, S., 2003. Biomedical applications of electrical impedance tomography. *Physiological Measurement,* **24**(2), pp. 1-1.

IZUMORI, A., TAKEBE, K. and SATO, A., 2010. Ultrasound findings and histological features of ductal carcinoma in situ detected by ultrasound examination alone. *Breast Cancer,* **17**(2), pp. 136-141.

JOSSINET, J., 1998. The impedivity of freshly excised human breast tissue. *Physiological Measurement,* **19**(1), pp. 61.

KHAN, A.A., BIMAL, S., DEY, K. and ROY, S., 2002. Current conveyor based R-and C-multiplier circuits. *AEU-International Journal of Electronics and Communications,* **56**(5), pp. 312-316.

KHAN, I.A. and ZAIDI, M.H., 2003. A novel generalized impedance converter using single second generation current conveyor. *Active and passive electronic components,* **26**(2), pp. 91-94.

KOPANS, D.B., 1998. *Atlas of Breast imaging.* 2nd edn. Philadelphia: Lippincott-Raven.

LEE, C.H., DERSHAW, D.D., KOPANS, D., EVANS, P., MONSEES, B., MONTICCIOLO, D., BRENNER, R.J., BASSETT, L., BERG, W. and FEIG, S., 2010. Breast cancer screening with imaging: recommendations from the Society of Breast Imaging and the ACR on the use of mammography, breast MRI, breast ultrasound, and other technologies for the detection of clinically occult breast cancer. *Journal of the American college of radiology,* **7**(1), pp. 18-27.

LI, D., MEANEY, P.M. and PAULSEN, K.D., 2003. Conformal microwave imaging for breast cancer detection. *Microwave Theory and Techniques, IEEE Transactions on,* **51**(4), pp. 1179-1186.

LI, X., HAGNESS, S.C., VAN VEEN, B.D. and VAN DER WEIDE, D., 2003. Experimental investigation of microwave imaging via space-time beamforming for breast cancer detection, *Microwave Symposium Digest, 2003 IEEE MTT-S International* 2003, IEEE, pp. 379-382.

MALTRON INTERNATIONAL, 1/1, 2012-last update, Maltron Sheffield MK 3.5 [Homepage of Maltron International Ltd], [Online]. Available: http://www.maltronint.com/eit/msmk35.php [02/25, 2015].

MARTINSEN, O.G. and GRIMNES, S., 2008. *Bioimpedance and bioelectricity basics.* 2nd edn. Great Britain: Academic press.

MAUNDY, B., GIFT, S. and ARONHIME, P., 2007. Realization of a GIC using hybrid current conveyor/operational amplifier circuits, *Circuits and Systems, 2007. MWSCAS 2007. 50th Midwest Symposium on* 2007, IEEE, pp. 163-166.

MCEWAN, A., CUSICK, G. and HOLDER, D., 2007. A review of errors in multi-frequency EIT instrumentation. *Physiological Measurement,* **28**(7), pp. S197.

MCEWAN, A., ROMSAUEROVA, A., YERWORTH, R., HORESH, L., BAYFORD, R. and HOLDER, D., 2006. Design and calibration of a compact multi-frequency EIT system for acute stroke imaging. *Physiological Measurement,* **27**(5), pp. S199.

MEANEY, P.M., FANNING, M.W., LI, D., POPLACK, S.P. and PAULSEN, K.D., 2000. A clinical prototype for active microwave imaging of the breast. *Microwave Theory and Techniques, IEEE Transactions on,* **48**(11), pp. 1841-1853.

MEANEY, P.M., FANNING, M.W., RAYNOLDS, T., FOX, C.J., FANG, Q., KOGEL, C.A., POPLACK, S.P. and PAULSEN, K.D., 2007. Initial clinical experience with microwave breast imaging in women with normal mammography. *Academic Radiology,* **14**(2), pp. 207-218.

MEANEY, P., FANG, Q., DEMIDENKO, E. and PAULSEN, K., 2005. Error analysis in microwave breast imaging: Variance stabilizing transformations. *Proceedings of ICONIC,* .

MEDICINENET, I., 2010-last update, Picture 26. Breast Anatomy. Available: http://www.medicinenet.com/image-collection/breast_anatomy_picture/picture.htm [03/1, 2015].

METHERALL, P., BARBER, D., SMALLWOOD, R. and BROWN, B., 1996. Three dimensional electrical impedance tomography. *Nature,* **380**(6574), pp. 509-512.

MIYAKAWA, M., ISHIDA, T. and WATANABE, M., 2004. Imaging capability of an early stage breast tumor by CP-MCT, *Engineering in Medicine and Biology Society, 2004. IEMBS'04. 26th Annual International Conference of the IEEE* 2004, IEEE, pp. 1427-1430.

MOVVA, S., 2013-last update, A Visual Guide to Breast Cancer. Available: http://www.webmd.com/breast-cancer/ss/slideshow-breast-cancer-overview [03/1, 2015].

MUÑOZ, D.R., BERGA, S.C. and ESCRIVÁ, C.R., 2005. Current loop generated from a generalized impedance converter: a new sensor signal conditioning circuit. *Review of scientific instruments,* **76**(6), pp. 066103.

OFFICE FOR NATIONAL STATISTICS (ONS), 19/6/2014. *Cancer Statistics Registrations, England (Series MB1).* 43,2012. England: Cancer Statistics Registrations.

OH, T.I., LEE, K.H., KIM, S.M., KOO, H., WOO, E.J. and HOLDER, D., 2007. Calibration methods for a multi-channel multi-frequency EIT system. *Physiological Measurement,* **28**(10), pp. 1175.

OH, T.I., WI, H., KIM, D.Y., YOO, P.J. and WOO, E.J., 2011. A fully parallel multi-frequency EIT system with flexible electrode configuration: KHU Mark2. *Physiological Measurement,* **32**(7), pp. 835.

OSTERMAN, K., KERNER, T., WILLIAMS, D., HARTOV, A., POPLACK, S. and PAULSEN, K., 2000. Multifrequency electrical impedance imaging: preliminary in vivo experience in breast. *Physiological Measurement,* **21**(1), pp. 99.

PEASE, R.A., 2008. A comprehensive study of the Howland current pump. *National Semiconductor.January,* **29**.

PENHOET, E.E., PETITTI, D.B. and JOY, J.E., 2005. *Saving Women's Lives:: Strategies for Improving Breast Cancer Detection and Diagnosis.* 1st edn. National Academies Press.

POPLACK, S.P., TOSTESON, T.D., WELLS, W.A., POGUE, B.W., MEANEY, P.M., HARTOV, A., KOGEL, C.A., SOHO, S.K., GIBSON, J.J. and PAULSEN, K.D., 2007. Electromagnetic Breast Imaging: Results of a Pilot Study in Women with Abnormal Mammograms 1. *Radiology,* **243**(2), pp. 350-359.

PRAKOBNOPPAKAO, S., CHIPIPOP, B., SURAKAMPONTORN, W. and WATANABE, K., 2002. Design of a Current-Mode CCII-Based Bandpass Filter from Immittance Function Simulator using Commercial Available CCII (AD844), *ITC-CSCC: International Technical Conference on Circuits Systems, Computers and Communications* 2002, pp. 743-746.

QIAO, G., WANG, W., DUAN, W., ZHENG, F., SINCLAIR, A.J. and CHATWIN, C.R., 2012. Bioimpedance analysis for the characterization of breast cancer cells in suspension. *Biomedical Engineering, IEEE Transactions on,* **59**(8), pp. 2321-2329.

QIAO, G., WANG, W., WANG, L., HE, Y., BRAMER, B. and AL-AKAIDI, M., 2007. Investigation of biological phantom for 2D and 3D breast EIT images, *13th International Conference on Electrical Bioimpedance and the 8th Conference on Electrical Impedance Tomography* 2007, Springer, pp. 328-331.

QURESHI, T., CHATWIN, C., HUBER, N., ZARAFSHANI, A., TUNSTALL, B. and WANG, W., 2010. Comparison of Howland and General Impedance Converter (GIC) circuit based current sources for bio-impedance measurements, *Journal of Physics: Conference Series* 2010, IOP Publishing, pp. 012167.

ROBINSON, J., 2008. New CCII current conveyor. *Application Notes,* **4198**, pp. 1Y6.

ROSS, A.S., SAULNIER, G., NEWELL, J. and ISAACSON, D., 2003b. Current source design for electrical impedance tomography. *Physiological Measurement,* **24**(2), pp. 509.

ROSS, A.S., 2003a. *An adaptive current tomograph for breast cancer detection, Ph.D. dissertation*, Dept. Elect. Eng., Rensselaer Polytechnic Institute, Troy, NY, USA.

RUBÆK, T., MEANEY, P.M., MEINCKE, P. and PAULSEN, K.D., 2007. Nonlinear microwave imaging for breast-cancer screening using Gauss–Newton's method and the CGLS inversion algorithm. *IEEE Transactions on Antennas and Propagation,* **55**(8), pp. 2320-2331.

SAULNIER, G.J., ROSS, A.S. and LIU, N., 2006. A high-precision voltage source for EIT. *Physiological Measurement,* **27**(5), pp. S221.

SCHNALL, M.D., 2003. Breast MR imaging. *Radiologic clinics of North America,* **41**(1), pp. 43-50.

SCHNEIDER, I., KLEFFEL, R., JENNINGS, D. and COURTENAY, A., 2000. Design of an electrical impedance tomography phantom using active elements. *Medical and Biological Engineering and Computing,* **38**(4), pp. 390-394.

SCHWAN, H.P., 1963. *Detection of biological impedances.* New York Academic Press: Physiological Techniques in Biological Research.

SEDRA, A. and SMITH, K.C., 1970. A second-generation current conveyor and its applications. *IEEE Transactions on Circuit Theory,* **17**(1), pp. 132-134.

SEDRA, A.S. and BRACKETT, P.O., 1978. *Filter theory and design: active and passive.* Matrix Pub.

SEDRA, A.S. and ROBERTS, G.W., 1990. Current conveyor theory and practice. *Analogue IC design: the current-mode approach,* .

SEMENOV, S., 2009. Microwave tomography: review of the progress towards clinical applications. *Philosophical transactions.Series A, Mathematical, physical, and engineering sciences,* **367**(1900), pp. 3021-3042.

SEOANE, F., BRAGÓS, R., LINDECRANTZ, K. and RIU, P., 2008. Current source design for electrical bioimpedance spectroscopy. *In: Encyclopedia of Healthcare Information Systems.,* , pp. 359-367.

SHAKTOUR, M. and BIOLEK, D., 2008. FLOATING GIC AND ITS IMPLEMENTATION. *IMAPS CS International Conference,* .

SHEINGOLD, D.H., 1964. Impedance & admittance transformations using operational amplifiers. *Lightning Empiricist,* **12**(1), pp. 7.

SIM TECHNIKA, 2008-last update, MEIK III machine . Available: http://www.impedance.ru/en/product_hist.html [02/23, 2015].

SREE, S.V., NG, E.Y., ACHARYA, R.U. and FAUST, O., 2011. Breast imaging: A survey. *World journal of clinical oncology,* **2**(4), pp. 171-178.

SZE, G., 2012. *Detection of breast cancer with electrical impedance mammography, Ph.D. dissertation*, University of Sussex.

TESCHNER, E. and IMHOFF, M., 2011. Electrical Impedance Tomography: The realization of regional ventilation monitoring. *Drager Medical GmbH,* .

THOMAS BACH, 2014. *Capacitive Sensing Solutions.* Sensor applications. UK: Sensatech Research.

TRANSSCAN TSCAN-2000, 1/27, 2000-last update, T-Scan Impedance Imaging of the Breast is Safe and Effective [Homepage of TransScan], [Online]. Available: http://www.imaginis.com/t-scan/t-scan-impedance-imaging-of-the-breast-is-safe-and-effective [02/23, 2015].

U.S. FOOD AND DRUG ADMINISTRATION, 2002-last update, TransScan T-Sca 2000-P970033. Available: http://www.accessdata.fda.gov/scripts/cdrh/cfdocs/cfTopic/pma/pma.cfm?num=p970033 [02/23, 2015].

VIRNIG, B.A., SHAMLIYAN, T., TUTTLE, T.M., KANE, R.L. and WILT, T.J., 2009. Diagnosis and management of ductal carcinoma in situ (DCIS).

VISHAY, 12/13, 2013-last update, Surface Mount Glass GF1 Passivated Rectifier [Homepage of Vishay], [Online]. Available: www.vishay.com; [1/4, 2015].

WAN, Y., NEGISHI, M. and CONSTABLE, R.T., 2013. A feasibility study of magnetic resonance driven electrical impedance tomography using a phantom. *Physiological Measurement,* **34**(6), pp. 623.

WANG, W., BRIEN, M., GU, D. and YANG, J., 2007a. A comprehensive study on current source circuits, IFMBE, ed. In: *13th International Conference on Electrical Bioimpedance and the 8th Conference on Electrical Impedance Tomography*, 29th Augest - 2nd September 2007a, Springer, pp. 213-216.

WANG, W., TUNSTALL, B., CHAUHAN, D. and MCCORMICK, M., 1998. The design of De Montfort Mk2 electrical impedance mammography system, *Engineering in Medicine and Biology Society, 1998. Proceedings of the 20th Annual International Conference of the IEEE* 1998, IEEE, pp. 1042-1043.

WANG, W., WANG, L., QIAO, G., PRICKETT, P., BRAMER, B., TUNSTALL, B. and AL-AKAIDI, M., 2007b. Study into the repeatability of the electrode-skin interface utilizing electrodes commonly used in Electrical Impedance Tomography, *13th International Conference on Electrical Bioimpedance and the 8th Conference on Electrical Impedance Tomography* 2007b, Springer, pp. 336-339.

WANG, W., TANG, M., MCCORMICK, M. and DONG, X., 2001. Preliminary results from an EIT breast imaging simulation system. *Physiological Measurement,* **22**(1), pp. 39.

WEBSTER, J.G., 1990. *Electrical impedance tomography.* 1st edn. Bristol: Adam Hilger.

WILSON, A., MILNES, P., WATERWORTH, A., SMALLWOOD, R. and BROWN, B., 2001. Mk3. 5: a modular, multi-frequency successor to the Mk3a EIS/EIT system. *Physiological Measurement,* **22**(1), pp. 49.

WTOREK, J., STELTER, J. and NOWAKOWSKIM, A., 1999. Impedance mammograph 3D phantom studies. *Annals of the New York Academy of Sciences,* **873**(1), pp. 520-533.

XIAOLIN ZHANG, WEI WANG, SZE, G., BARBER, D. and CHATWIN, C., 2014. An Image Reconstruction Algorithm for 3-D Electrical Impedance Mammography. *Medical Imaging, IEEE Transactions on,* **33**(12), pp. 2223-2241.

YASIN, M., BÖHM, S., GAGGERO, P.O. and ADLER, A., 2011. Evaluation of EIT system performance. *Physiological Measurement,* **32**(7), pp. 851.

YBARRA, G.A., LIU, Q.H., YE, G., LIM, K.H., LEE, J., JOINES, W.T. and GEORGE, R.T., 2007. Breast imaging using electrical impedance tomography (EIT). *Emerging Technology in Breast Imaging and Mammography, American Scientific Publishers,* .

YERWORTH, R.J., BAYFORD, R., CUSICK, G., CONWAY, M. and HOLDER, D.S., 2002. Design and performance of the UCLH Mark 1b 64 channel electrical impedance tomography (EIT) system, optimized for imaging brain function. *Physiological Measurement,* **23**(1), pp. 149.

YORKEY, T.J., WEBSTER, J.G. and TOMPKINS, W.J., 1987. Comparing reconstruction algorithms for electrical impedance tomography. *Biomedical Engineering, IEEE Transactions on,* (11), pp. 843-852.

ZARAFSHANI, A., HUBER, N., BÉQO, N., TUNSTALL, B., SZE, G., CHATWIN, C. and WANG, W., 2010. A flexible low-cost, high-precision, single interface electrical impedance tomography system for breast cancer detection using FPGA, *Journal of Physics: Conference Series* 2010, IOP Publishing, pp. 012169.

ZOU, Y. and GUO, Z., 2003. A review of electrical impedance techniques for breast cancer detection. *Medical engineering & physics,* **25**(2), pp. 79-90.

Appendices and Functional Parts

Appendix-A: Calculation of maximum total current of Power supply

Maximum total current of Howland current source plus GIC circuits for +5V rail:

*3*16.3mA (three voltage amplifiers for two different branch voltages are 180 degrees out of phase)*
+ 1×3mA (one DCP is active mode)
+ 1×500µA (one X9C102 is in standby mode)
*+ 2*16.3mA (two Howland Amplifiers)*
*+ 4*16.3mA (four GIC's Amplifiers)*
= 150.2mA

Maximum total current of Howland current source plus GIC circuits for -5V rail:

*3*16.3mA (three voltage amplifiers for two different branch voltages are 180 degrees out of phase)*
*+ 2*16.3mA (two Howland Amplifiers)*
*+ 4*16.3mA (four GIC's Amplifiers)*
=146.7mA

Maximum total current of Howland current source plus OC I circuits for +5V rail

*3*16.3mA (three voltage amplifiers for two different branch voltages are 180 degrees out of phase)*
+ 1×3mA (one DCP is active mode)
+ 1×500µA (one X9C102 is in standby mode)
*+ 2*16.3mA (two Howland's Amplifiers)*
*+ 6*16.3mA (six OCCII's Amplifiers)*
+ 2×3mA (two DCP is active mode)
+ 2×500µA (two X9C102 is in standby mode)
=189.8mA

Maximum total current of Howland current source plus OC I circuits for -5V rail

*3*16.3mA (three voltage amplifiers for two different branch voltages are 180 degrees out of phase)*
*+ 2*16.3mA (two Howland's Amplifiers)*
*+ 6*16.3mA (six OCCII's Amplifiers)*
= 179.3mA

Maximum total current of Howland current source plus OC II circuits for +5V rail

*6*16.3mA (six OCCII's Amplifiers)*
+ 2×3mA (two DCP X9C102 is active mode)
+ 2×500µA (two DCP X9C102 is in standby mode)
=104.8mA

Maximum total current of Howland current source plus OC II circuits for -5V rail

*6*16.3mA (six OCCII's Amplifiers)*
+ 2×3mA (two DCP X9C102 is active mode)
+ 2×500µA (two DCP X9C102 is in standby mode)
=104.8mA

Maximum total current of Current Mirror mode for +5V rail

*3*16.3mA (three voltage amplifiers for two different branch voltages are 180 degrees out of phase)*
*+ 2*16.3mA (two feedback loop's Amplifiers)*
= 81.5mA

Maximum total current of Current Mirror mode for -5V rail

*3*16mA (three voltage amplifiers for two different branch voltages are 180 degrees out of phase)*
*+ 2*16mA (two feedback loop's Amplifiers)*
= 81.5mA

Maximum total current of Common part includes MUXs and Measurement for +5V rail

*8*20µA (8 ADG2128 used for supporting 85 electrodes)*
*+ 1*50mA (Six ADV3205 modules are used, only one is in active output mode)*
*+ 5*35mA (Six ADV3205 modules are used, 5 are in disable output mode)*
*+ 1*13mA (Six ADV3205 modules are used, all use DV_{CC} digital voltage level)*
*+ 1*10.6mA (one Differential single added amplifier)*
+ 1×3mA (one DCP is in active mode used in PGA)
= 251.22mA

Maximum total current of Common part includes MUXs and Measurement for -5V rail

*8*20µA (8 ADG2128 used for supporting 85 electrodes)*
*+ 1*50mA (Six ADV3205 modules are used, only one is in active output mode)*
*+ 5*35mA (Six ADV3205 modules are used, 5 are in disable output mode)*
*+ 1*10.6mA (one Differential single added amplifier)*
= 235.22mA

Maximum total current of Howland current source plus GIC circuits for +15V rail:

= 0mA

Maximum total current of Howland current source plus GIC circuits for -15V rail:

=0.mA

Maximum total current of Howland current source plus OC I circuits for +15V rail

*4*7.5mA (four AD844 are used for two different branch voltage are 180 degrees out of phase)*
=30mA

Maximum total current of Howland current source plus OC I circuits for -15V rail

*4*7.5mA (four AD844 are used for two different branch voltage are 180 degrees out of phase)*
=30mA

Maximum total current of Howland current source plus OC II circuits for +15V rail

*2*7.5mA (two AD844 are used for two different branch voltage are 180 degrees out of phase)*
=15mA

Maximum total current of Howland current source plus OC II circuits for -15V rail

*2*7.5mA (two AD844 are used for two different branch voltage are 180 degrees out of phase)*
=15mA

Maximum total current of Current Mirror mode for +15V rail

*2*7.5mA (two AD844 are used for two different branch voltage are 180 degrees out of phase)*
= 15mA

Maximum total current of Current Mirror mode for -15V rail

*2*7.5mA (two AD844 are used for two different branch voltage are 180 degrees out of phase)*
= 15mA

Maximum total current of Common part includes MUXs and Measurement for +15V rail

*2*380µA (two ADG1211 used for supporting 8 ADG2128 second stage of 85 electrodes)*
= 720µA

Maximum total current of Common part includes MUXs and Measurement for -15V rail

*2*380µA (two ADG1211 used for supporting 8 ADG2128 second stage of 85 electrodes)*
= 720µA

Appendix-B: SUBHOST Software Port Usage v4.00

1. SUBHOST PIC 18F65K90 TQFP
2. PIC package is used TQFP64
3. DATA DIRECTION REGISTERS

Letter	Number	Direction	Name	Description	Note
RA	0	OUT	CE/3	IC 26 – Enable OF MUX ADV3205	Enable Low, Must be low to clock-in and latch data, Connected to Electrodes
	1	OUT	CHPOT(5)	Digital-POT, Channel Select POT IC46:CS	-
	2	OUT	CHPOT(11)	Digital-POT, Channel Select POT IC22:CS	-
	3	OUT	CHPOT(2)	Digital-POT, Channel Select POT IC54:CS	-
	4	OUT	CE/1	IC 4 – Enable OF MUX ADV3205	Enable Low, Must be low to clock-in and latch data, Connected to Electrodes
	5	OUT	CHPOT(3)	Digital-POT, Channel Select POT IC45:CS, Digital-POT, Channel Select POT IC67:CS	-
	6	IN/OUT	CLKOUT	Crystal Clock Out	-
	7	IN/OUT	CLKIN	Crystal Clock In	-
RB	0	OUTPUT	CE/2	IC 3 – Enable OF MUX ADV3205	Enable Low, Must be low to clock-in and

					latch data Connected to Electrodes
	1	OUTPUT	A1	OUTPUT SELECT OF MUXS; IC 3,4,25,26,40,41- ADV3205 Enable	Connected to all ADV3205 Output address lines
	2	OUTPUT	A2	OUTPUT SELECT OF MUXS; IC 3,4,25,26,40,41- ADV3205 Enable	Connected to all ADV3205 Output address lines
	3	OUTPUT	A3	OUTPUT SELECT OF MUXS; IC 3,4,25,26,40,41- ADV3205 Enable	MSB, Connected to all ADV3205 Output address lines
	4	OUT	CHPOT(15)	Digital-POT, Channel Select POT IC61:CS	-
	5	OUT	IN1_180phase	ADG1211, IC80:IN1, SW1, for 180 phase	-
	6	IN	PGC	PIC Programming Clock	-
	7	IN	PGD	PIC Programming Data	-
RC	0	OUT	D1	INPUT SELECT OF MUX ADV3205	Connected to all ADV3205 Input address lines
	1	OUT	D0	INPUT SELECT OF MUX ADV3205	LSB, Connected to all ADV3205 Input address lines
	2	OUT	D2	INPUT SELECT OF MUX ADV3205	Connected to all ADV3205 Input address lines
	3	OUT	D3	INPUT SELECT OF MUX ADV3205	MSB, Connected to all ADV3205 Input address lines
	4	OUT	D4	INPUT SELECT OF MUX ADV3205	Output enable

	5	OUT	IN4_180phase	ADG1211, IC80:IN4, SW4, for 180 phase	-
	6	OUT	TXX1, P2	PC USB Serial Transmit	-
	7	IN	RXX1, P1	PC USB Serial Receive	-
RD	0	OUT	UPDATE/	UPDATE ALL MEASURMENT MUXs IC 3,4,25,26,40,41- ADV3205 Enable	Enable (Transparent) Low. Allows serial register to connect directly to switch matrix. Data latched when high.
	1	OUT	A0	IC 3,4,25,26,40,41- ADV3205 Enable	LSB, Connected to all ADV3205 Output address lines
	2	OUT	CE/5	IC 41 – Enable OF MUX ADV3205	Enable Low, Must be low to clock-in and latch data Connected to Electrodes
	3	OUT	INC-	IC 35,23,30,31,44,54,56,57,45,46,61 – Digital-POT INC-	-
	4	OUT	CHPOT(9)	Digital-POT, Channel Select POT IC30:CS	-
	5	OUT	UP/DWON	IC 35,23,30,31,44,54,56,57,45,46,61 – Digital-POT Up/Down	-
	6	OUT	RESET/	RESET ALL MEASURMENT MUXs IC3,4,25,26,40,41– ADV3205 And IC27,5,42,52,55,68,91,104-ADG2128 Active Low Logic Input, Reset Input MUXs	ADV3205: Disable Outputs, Active Low ADG2128: Active Low Logic Input. When this pin is low, all switches are open, and appropriate registers are cleared to 0.
	7	OUT	CHPOT(7)	Digital-POT, Channel Select POT IC23:CS	-
RE	0	OUT	CHPOT(14)	Digital-POT, Channel Select POT IC72:CS	-
	1	IN	Analogue input	AN0	-

	2	IN	Analogue input	AN1	-
	3	OUT	IN3_0phase	ADG1211, IC79:IN3, SW3, for 0 phase	-
	4	OUT	IN1_0phase	ADG1211, IC79:IN1, SW1, for 0 phase	-
	5	OUT	IN4_0phase	ADG1211, IC79:IN4, SW4, for 0 phase	-
	6	OUT	CE/6	IC 40 – Enable OF MUX ADV3205	Enable Low, Must be low to clock-in and latch data, Connected to Electrodes
	7	OUT	IN2_0phase	ADG1211, IC79:IN2, SW2, for 0 phase	-
RF	1	OUT	CHPOT(1)	Digital-POT, Channel Select POT IC44:CS	-
	2	OUT	SCL	Digital-Input, Serial Clock Line	Open drain input that is used in conjunction with SDA to clock data into the device, External pull-up resistor required
	3	OUT	SDA	Digital I/O	Bidirectional open drain data line, External pull-up resistor required
	4	OUT	CHPOT(4)	Digital-POT, Channel Select POT IC56:CS	-
	5	OUT	CE/4	IC 25 – Enable OF MUX ADV3205	Enable Low, Must be low to clock-in and latch data, Connected to Electrodes
	6	OUT	CHPOT(6)	Digital-POT, Channel Select POT IC57:CS	-
	7	OUT	IN3_180phase	ADG1211, IC80:IN3, SW3, 180 phase	-
RG	0	OUT	CHPOT(10)	Digital-POT, Channel Select POT IC35:CS	-

	1	OUT	CLK	ADV3205, IC3,4,25,26,40,41:pin97	-
	2	OUT	IN2_180phase	ADG1211, IC80:IN2, SW2, for 180 phase	-
	3	OUT	CHPOT(8)	Digital-POT, Channel Select POT IC31:CS	-
	4	OUT	CHPOT(12)	Digital-POT, Channel Select POT IC65:CS	-
	5	IN	MCLR/	Master Clear (input) or programming voltage (input) of PIC.	This pin is an active-low Reset to the device.

Appendix-C: modify improved Howland current source

We made a few improvements in the improved Howland current source by adding resistor and capacitors as shown in Figure 101. The results show the output capacitance has been reduced with these modifications.

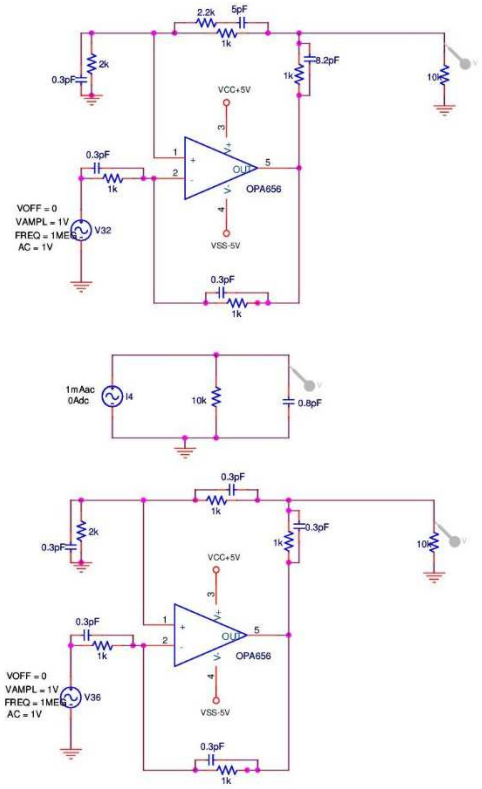

Modify improved Howland current source

Perfect current source

Improved Howland current source

(a)

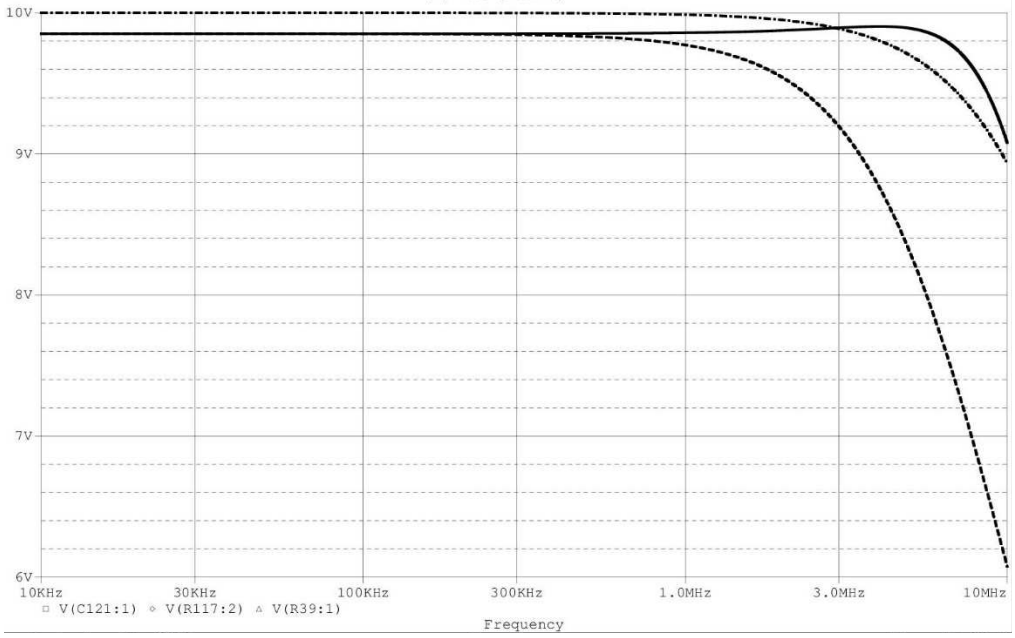

(b)

Figure 101 shows (a) a modified current source schematic, (b) the output capacitance result from this modify schematic when comparing improved Howland current source output voltage shows a dashed line curve (---), modify the schematic shows a dotted line curve (….) and perfect current source shows a line (___).

Appendix-D: Output signal of the current conveyor current source

The output current and phase delay curves achieved when the current conveyor current source is compared with the reference input signal with 180^{o} out of phase and with a R_{LOAD}=813.6Ω, as shown in Figure 102. Although, there is an α gain (I_{TZ}= αI_X) in reality between the R_X placed in the current conveyor current source ($I_X=\frac{V_{IN}}{R_X}=\frac{I_{TZ}}{\alpha}$) and the output voltage signal. Therefore, the V_{OUT}=767^{mVp-p}.

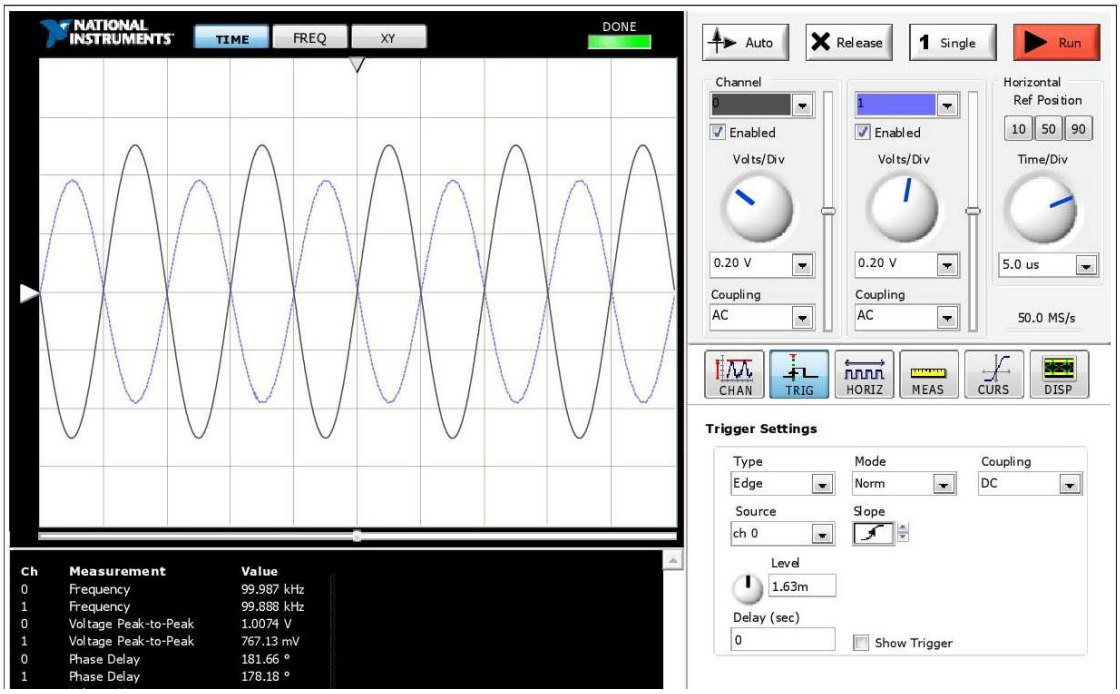

Amplitude:0.5V (1^{Vp-p}) black curve, F=100kHz, phase different=180^{o}, probe (x10), R_{LOAD}=813.6Ω and there is a gain equal to 0.93 bule curve Ch:0.2v/div and probe 1MΩ, and Trigger 0V and Time base of 10MS/s (5us/Div)

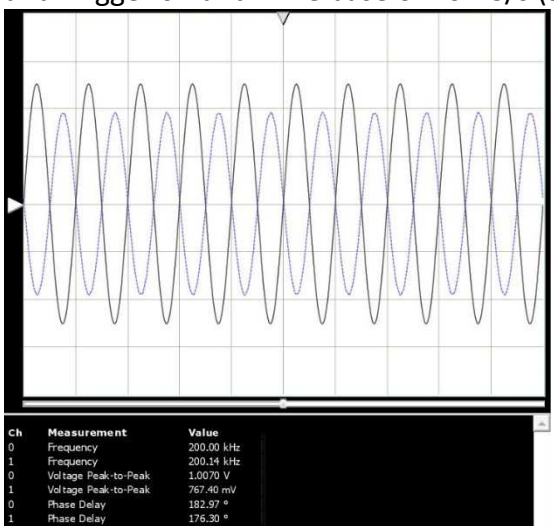

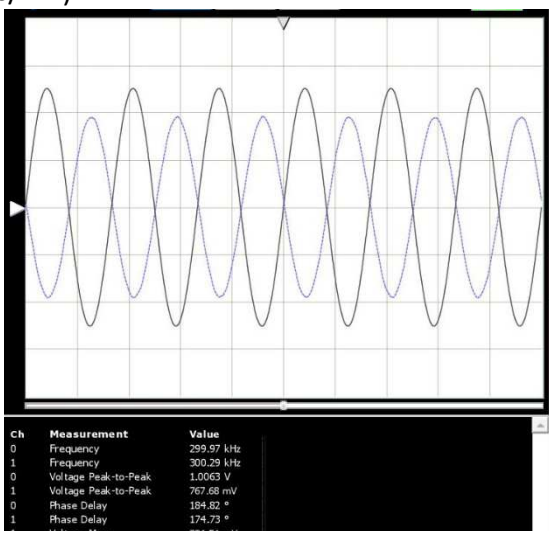

@ 200 kHz, R_L=813.6Ω, V_L=767.40^{mVp-p}, with a gain of 0.93, and phase delay with input signal +2^o

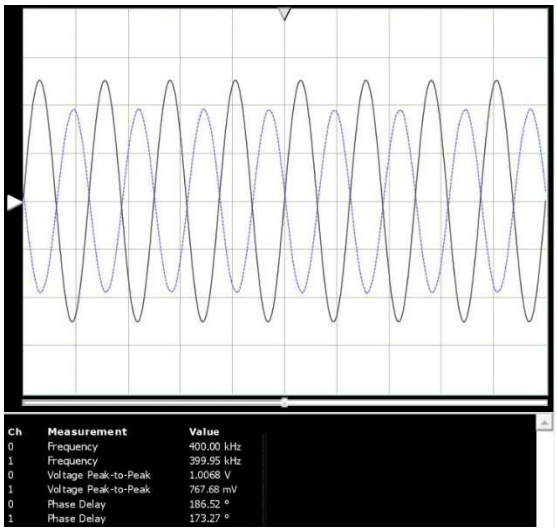

@ 300 kHz, R_L=813.6Ω, V_L=767.68^{mVp-p}, with a gain of 0.93, and phase delay with input signal +4^o

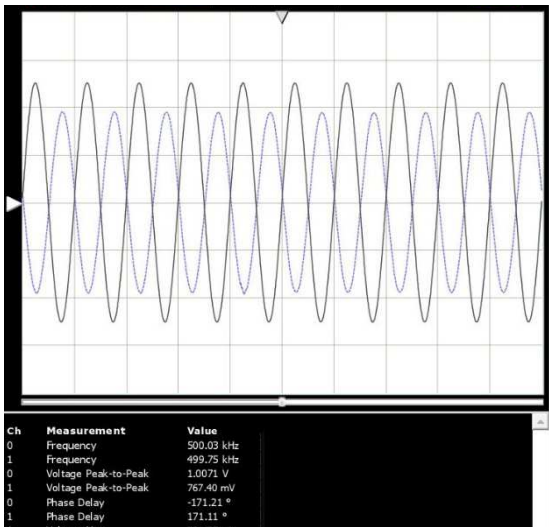

@ 400 kHz, R_L=813.6Ω, V_L=767.68^{mVp-p}, with a gain of 0.93, and phase delay with input signal +6^o

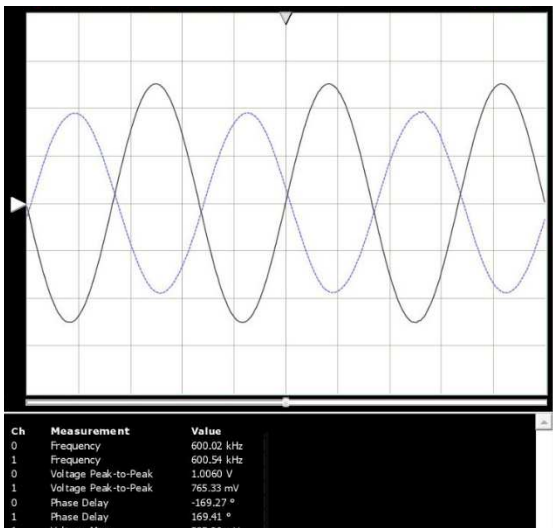

@ 500 kHz, R_L=813.6Ω, V_L=767.40^{mVp-p}, with a gain of 0.93, and phase delay with input signal +9^o

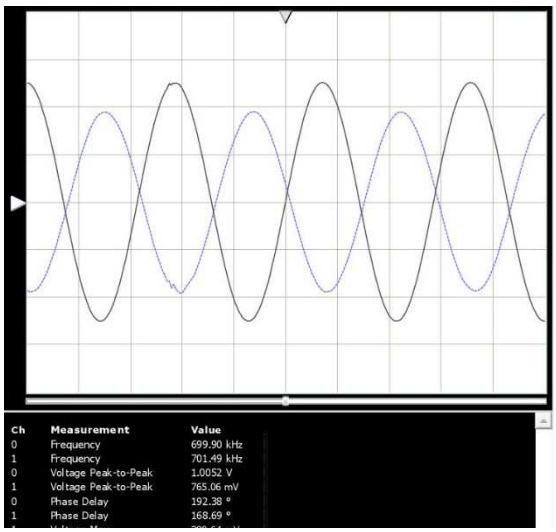

@ 600 kHz, R_L=813.6Ω, V_L=765.33^{mVp-p}, with a gain of 0.93, and phase delay with input signal +11^o

@ 700 kHz, R_L=813.6Ω, V_L=765.06^{mVp-p}, with a gain of 0.93, and phase delay with input signal +12^o

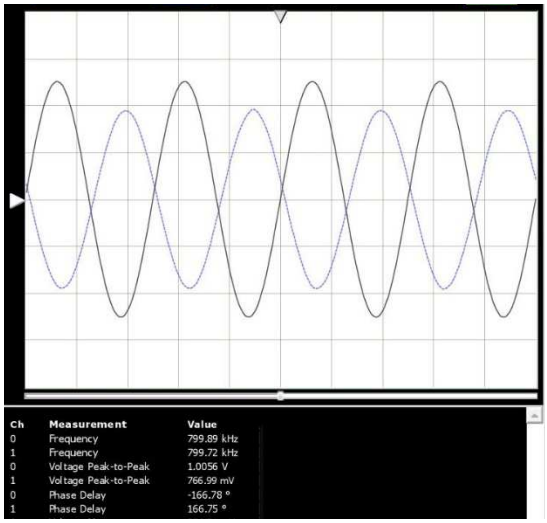

@ 800 kHz, R_L=813.6Ω, V_L=766.90^{mVp-p}, with a gain of 0.93, and phase delay with input signal +14^{o}

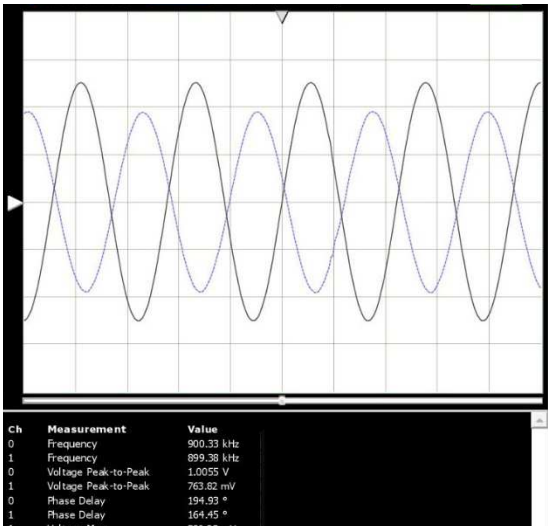

@ 900 kHz, R_L=813.6Ω, V_L=763.82^{mVp-p}, with a gain of 0.93, and phase delay with input signal +15^{o}

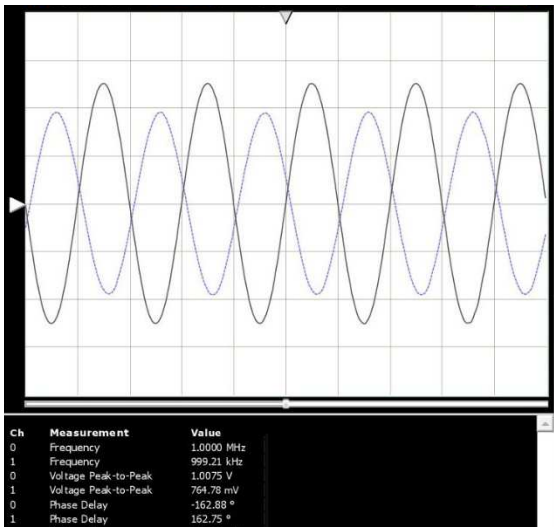

@ 1MHz, R_L=813.6Ω, V_L=764.78^{mVp-p}, with a gain of 0.93, and phase delay with input signal +18^{o}

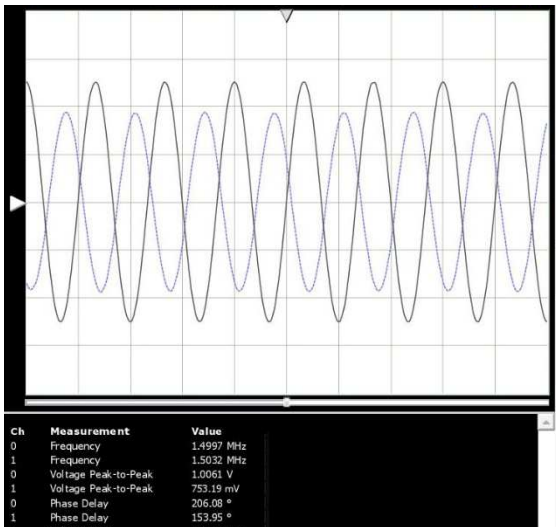

@ 1.5MHz, R_L=813.6Ω, V_L=753.19^{mVp-p}, with a gain of 0.93, and phase delay with input signal +26^{o}

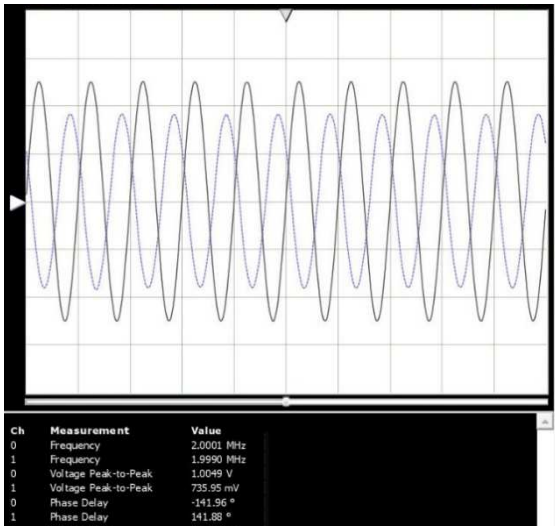

@ 2MHz, R_L=813.6Ω, V_L=735.95^{mVp-p}, with a gain of 0.93, and phase delay with input signal +39^o

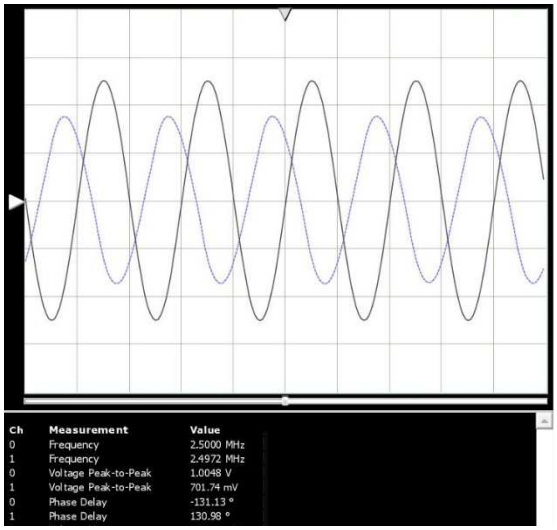

@ 2.5MHz, R_L=813.6Ω, V_L=701.74^{mVp-p}, with a gain of 0.93, and phase delay with input signal +50^o

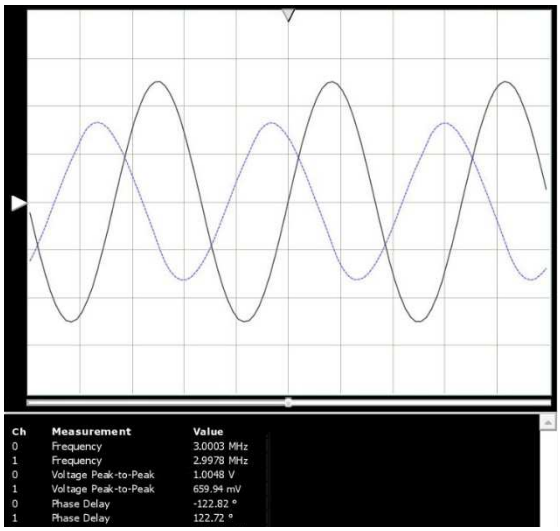

@ 3MHz, R_L=813.6Ω, V_L=659.94^{mVp-p}, with a gain of 0.93, and phase delay with input signal +58^o

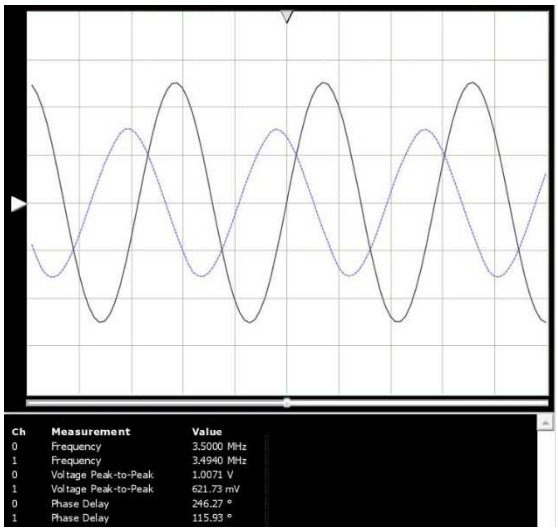

@ 3.5MHz, R_L=813.6Ω, V_L=621.73^{mVp-p}, with a gain of 0.93, and phase delay with input signal +66^o

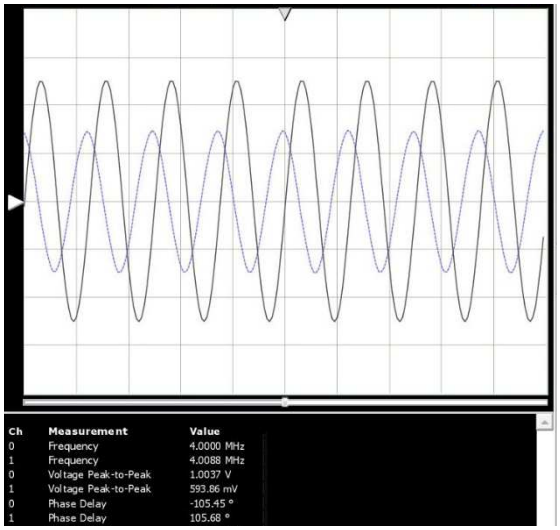

@ 4MHz, R_L=813.6Ω, V_L=593.86^{mVp-p}, with a gain of 0.93, and phase delay with input signal +75^{o}

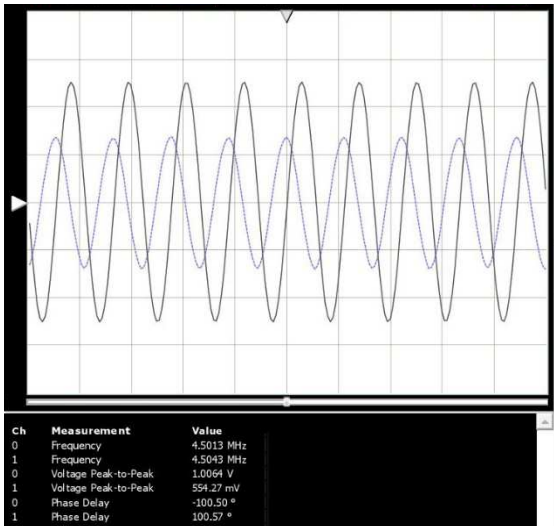

@ 4.5MHz, R_L=813.6Ω, V_L=554.27^{mVp-p}, with a gain of 0.93, and phase delay with input signal +80^{o}

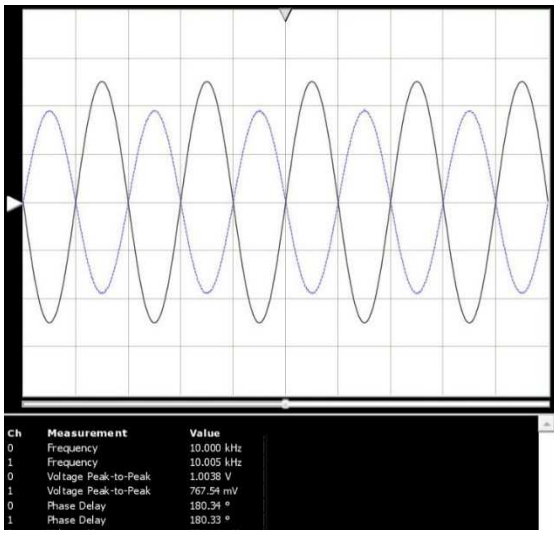

@ 10 kHz, R_L=813.6Ω, V_L=767.54^{mVp-p}, with a gain of 0.93, and phase delay with input signal +0^{o}

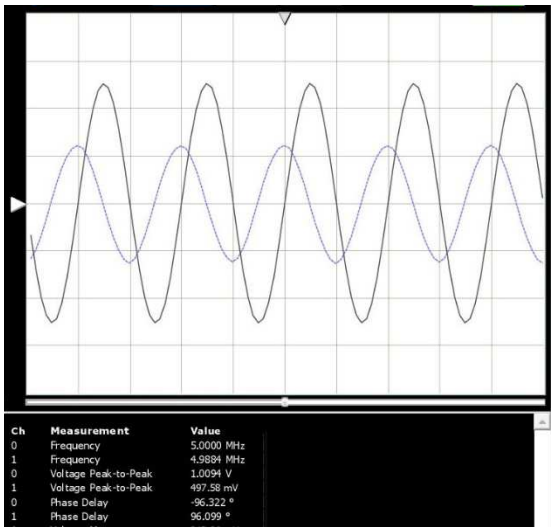

@ 5MHz, R_L=813.6Ω, V_L=497.58^{mVp-p}, with a gain of 0.93, and phase delay with input signal +104^{o}

Figure 102 snapshots of the oscilloscope that shows the input reference signal and the output signal of the load voltage on the scope when connecting to an current conveyor current source for sweeping the frequency start from 100kHz to 1MHz with steps of 100kHz, 1MHz to 5MHz with steps of 500kHz and amplitude of the input sine wave is set for1^{Vp-p}.

Appendix-E: Output signal of two current sources with 180^{o} out of phase

These curves were achieved when two different loads were attached to the two current sources to measure two different loads with a 180 degree phase difference, as shown in Figure 103. The actual load resistors are equal to $R_{LOAD\text{-}0\ phase}$ = 918Ω and $R_{LOAD\text{-}180\ phase}$ =977Ω. We measured the output of the two current sources with 180 degrees out of phase based on the Sussex EIT system structure. Although, we achieved a small phase shift between these two output signals during these tests. As we expected based on the simulation results the range of output current would be $1^{mAp\text{-}p}$ at 50 kHz dropped to around $750^{uAp\text{-}p}$ at 5MHz with a phase diff. equal to 180^{o}).

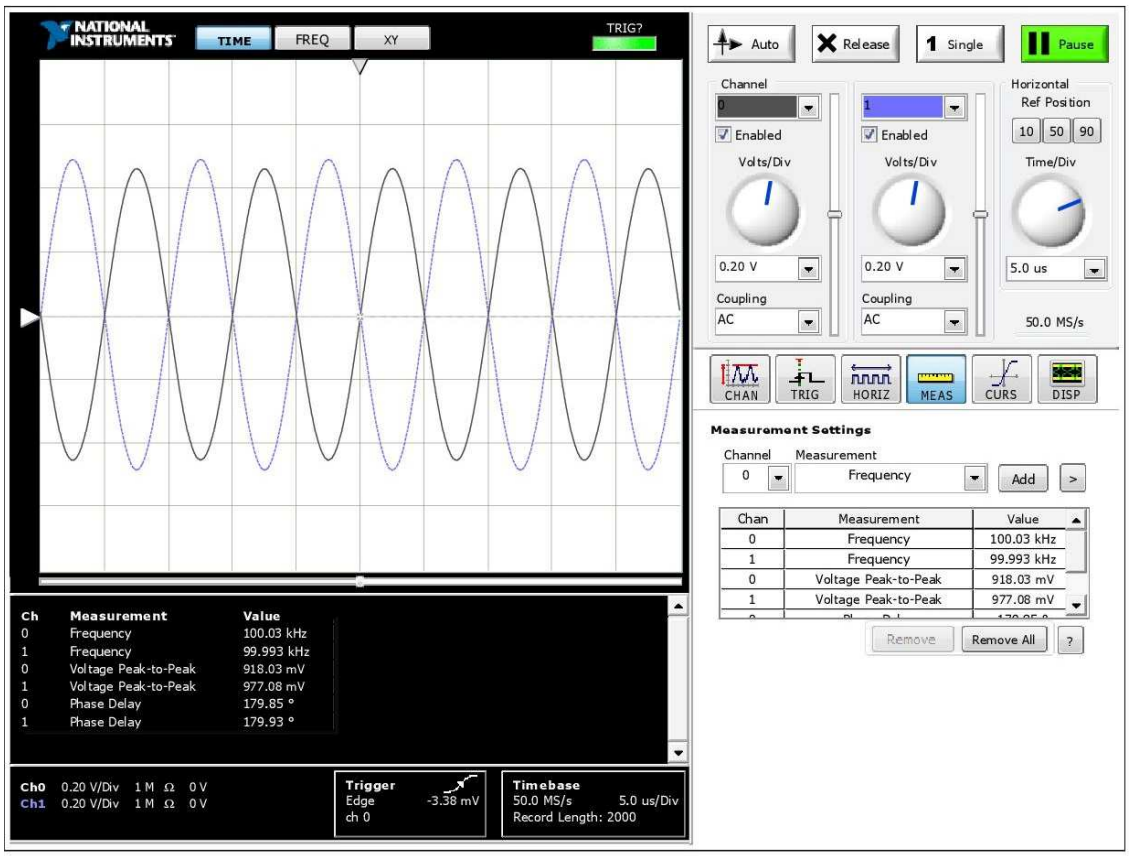

Amplitude:0.5V, F=100kHz, phase different=180^{o}, probe (x10), R_{LOAD}=918Ω and 977 Ω, Ch:.5v/div and probe 1MΩ, 0V and Trigger 0V and Time base of 10MS/s (5us/Div)

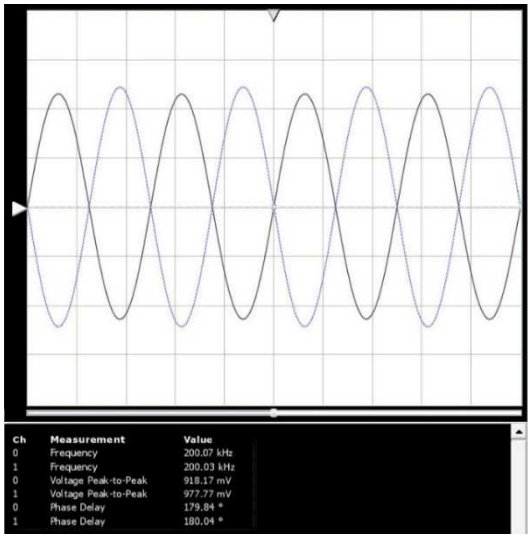

F= 200 kHz, R_{LOAD-1}=918Ω, R_{LOAD-2}=977Ω V_{OUT-1}=918.17^{mVp-p}, V_{OUT-1}=977.77^{mVp-p} with phase diff. =180^{o}

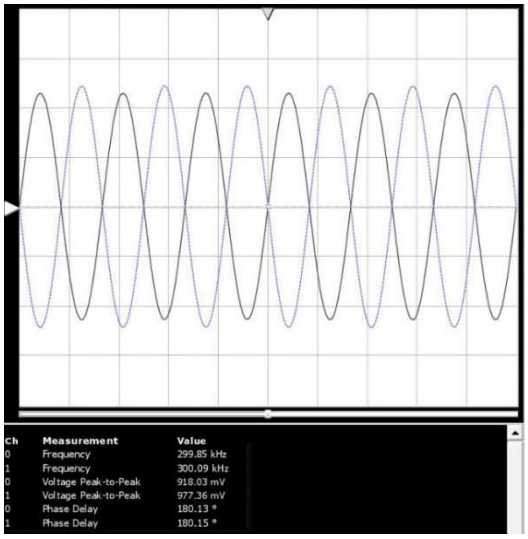

F= 300 kHz, R_{LOAD-1}=918Ω, R_{LOAD-2}=977Ω V_{OUT-1}=918.03^{mVp-p}, V_{OUT-1}=977.36^{mVp-p} with phase diff. =180^{o}

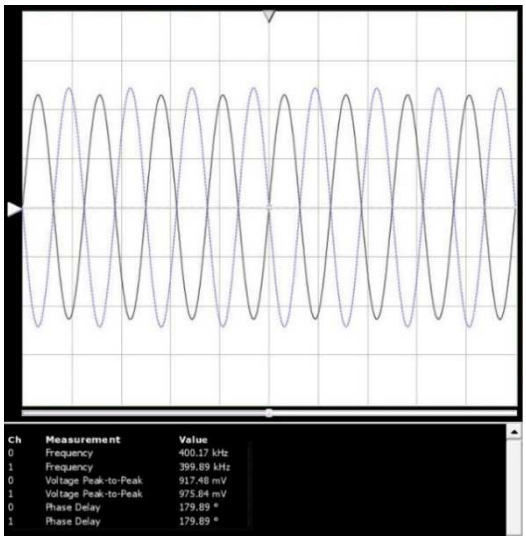

F= 400 kHz, R_{LOAD-1}=918Ω, R_{LOAD-2}=975.84Ω V_{OUT-1}=917.48^{mVp-p}, V_{OUT-1}=977.77^{mVp-p} with phase diff. =180^{o}

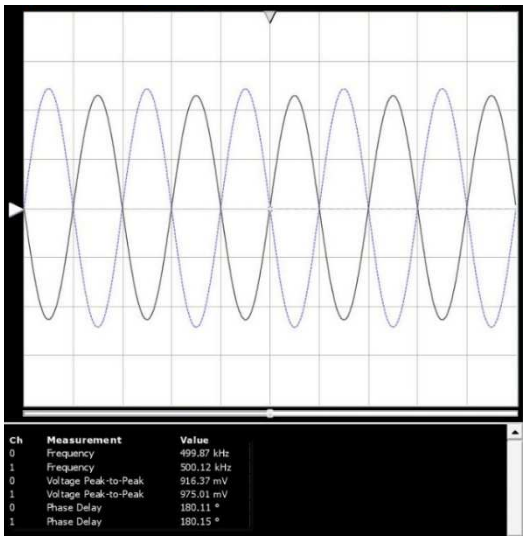

F= 500 kHz, R_{LOAD-1}=918Ω, R_{LOAD-2}=977Ω V_{OUT-1}=916.37^{mVp-p}, V_{OUT-1}=975.01^{mVp-p} with phase diff. =180^{o}

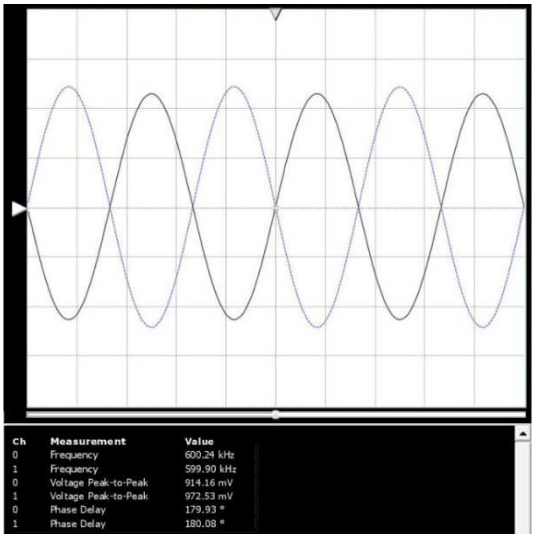

F= 600 kHz, R_{LOAD-1}=918Ω, R_{LOAD-2}=977Ω V_{OUT-1}=914.16^{mVp-p}, V_{OUT-1}=972.53^{mVp-p} with phase diff. =180^{o}

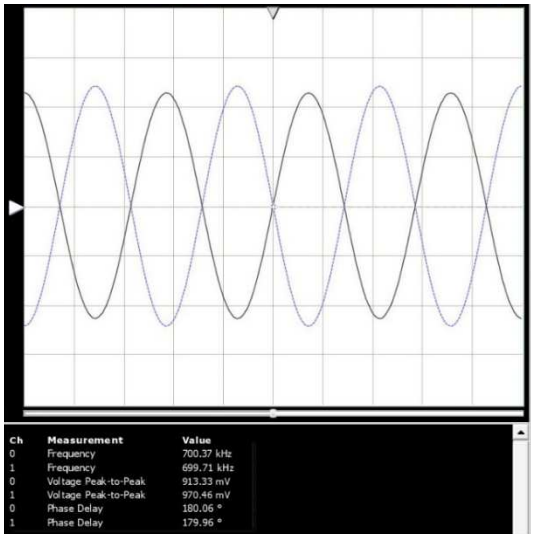

F= 700 kHz, R_{LOAD-1}=918Ω, R_{LOAD-2}=977Ω V_{OUT-1}=913.33^{mVp-p}, V_{OUT-1}=970.46^{mVp-p} with phase diff. =180^{o}

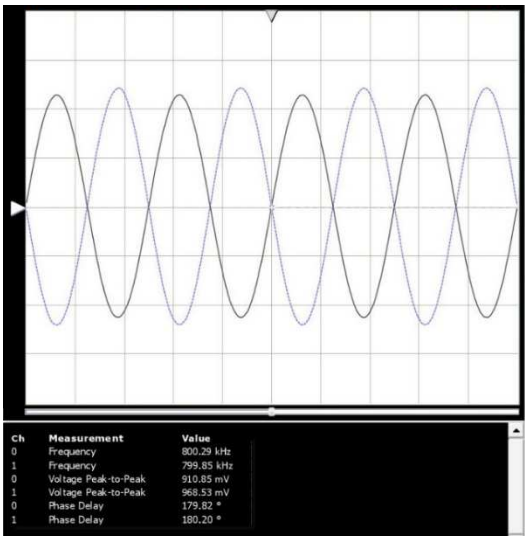

F= 800 kHz, R_{LOAD-1}=918Ω, R_{LOAD-2}=977Ω V_{OUT-1}=910.85^{mVp-p}, V_{OUT-1}=968.53^{mVp-p} with phase diff. =180^{o}

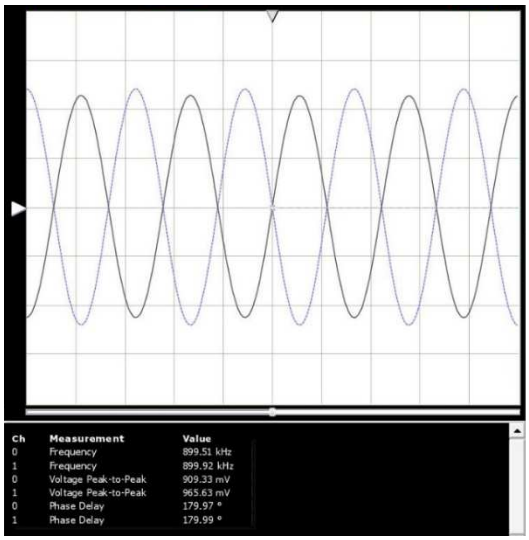

F= 900 kHz, R_{LOAD-1}=918Ω, R_{LOAD-2}=977Ω V_{OUT-1}=909.33^{mVp-p}, V_{OUT-1}=965.63^{mVp-p} with phase diff. =180^{o}

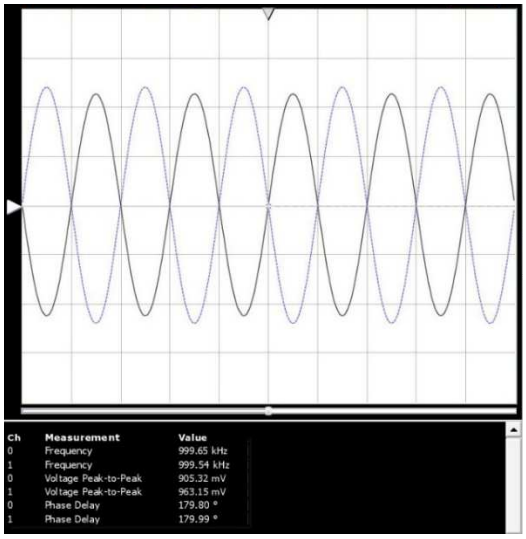

F= 1 MHz, R_{LOAD-1}=918Ω, R_{LOAD-2}=977Ω V_{OUT-1}=905.32^{mVp-p}, V_{OUT-1}=963.15^{mVp-p} with phase diff. =180^{o}

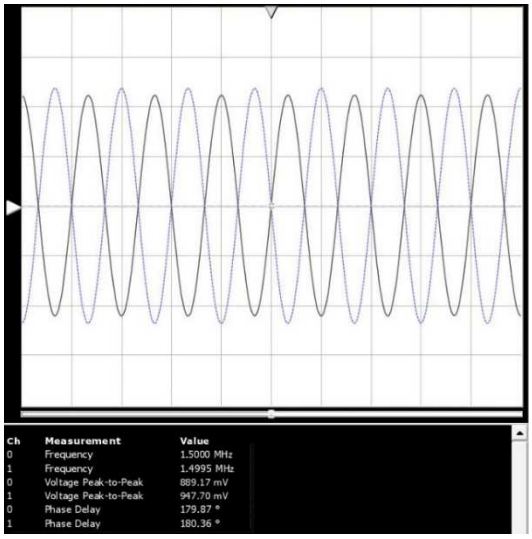

F= 1.5 MHz, R_{LOAD-1}=918Ω, R_{LOAD-2}=977Ω V_{OUT-1}=809.17^{mVp-p}, V_{OUT-1}=947.70^{mVp-p} with phase diff. =180^{o}

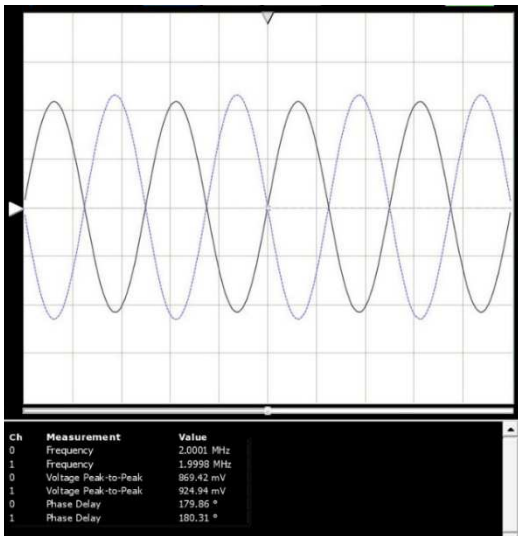

F= 2 MHz, R_{LOAD-1}=918Ω, R_{LOAD-2}=977Ω V_{OUT-1}=869.42^{mVp-p}, V_{OUT-1}=924.94^{mVp-p} with phase diff. =180^{o}

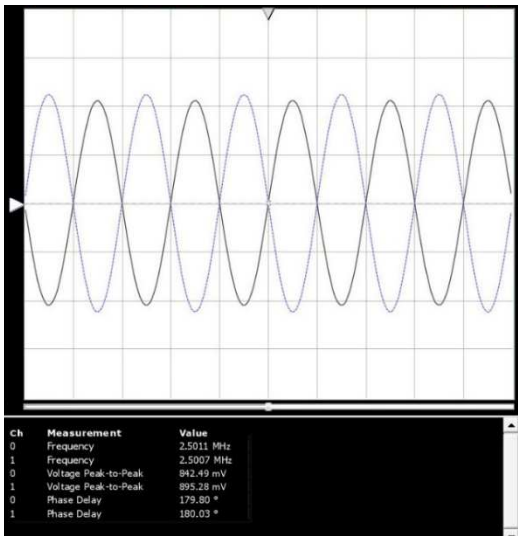

F= 2.5 MHz, R_{LOAD-1}=918Ω, R_{LOAD-2}=977Ω V_{OUT-1}=842.49^{mVp-p}, V_{OUT-1}=895.28^{mVp-p} with phase diff. =180^{o}

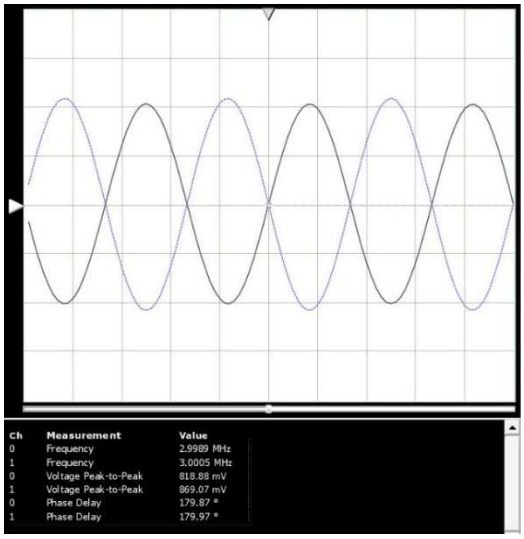

F= 3 MHz, R_{LOAD-1}=918Ω, R_{LOAD-2}=977Ω V_{OUT-1}=818.88^{mVp-p}, V_{OUT-1}=869.07^{mVp-p} with phase diff. =180^{o}

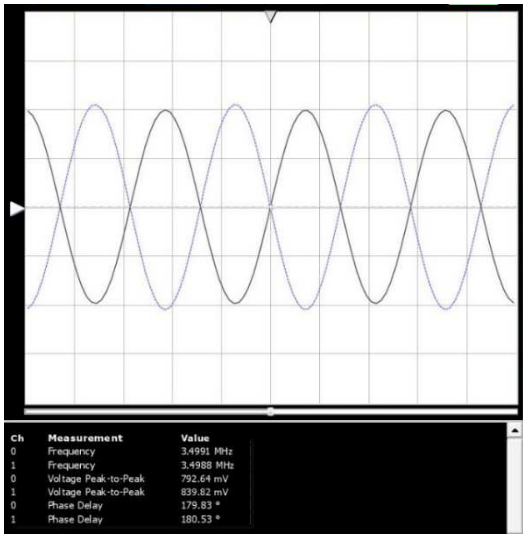

F= 3.5 MHz, R_{LOAD-1}=918Ω, R_{LOAD-2}=977Ω V_{OUT-1}=792.64^{mVp-p}, V_{OUT-1}=839.82^{mVp-p} with phase diff. =180^{o}

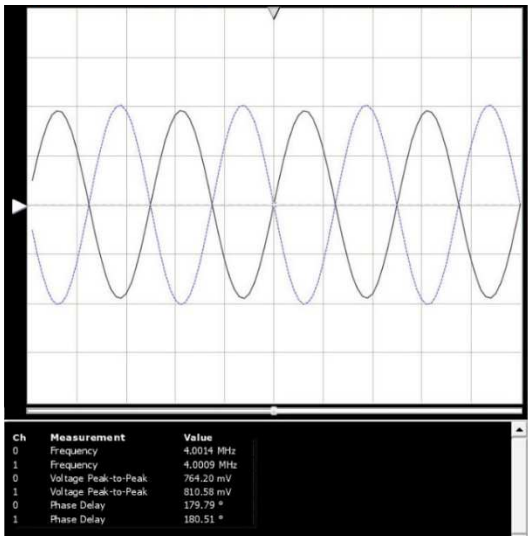

F= 4 MHz, R_{LOAD-1}=918Ω, R_{LOAD-2}=977Ω V_{OUT-1}=764.20^{mVp-p}, V_{OUT-1}=810.58^{mVp-p} with phase diff. =180^{o}

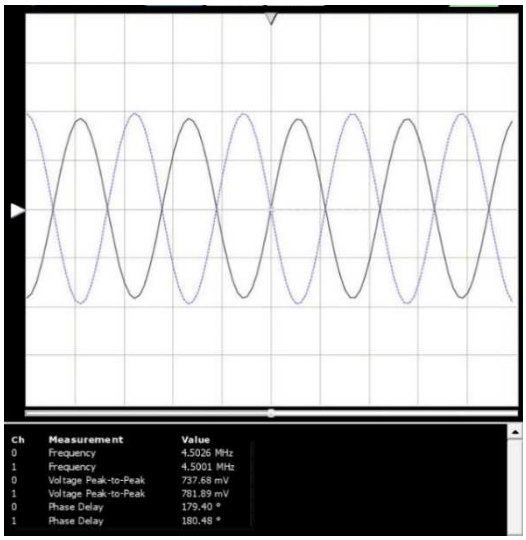

F= 4.5 MHz, R_{LOAD-1}=918Ω, R_{LOAD-2}=977Ω V_{OUT-1}=9737.68^{mVp-p}, V_{OUT-1}=781.89^{mVp-p} with phase diff. =180^{o}

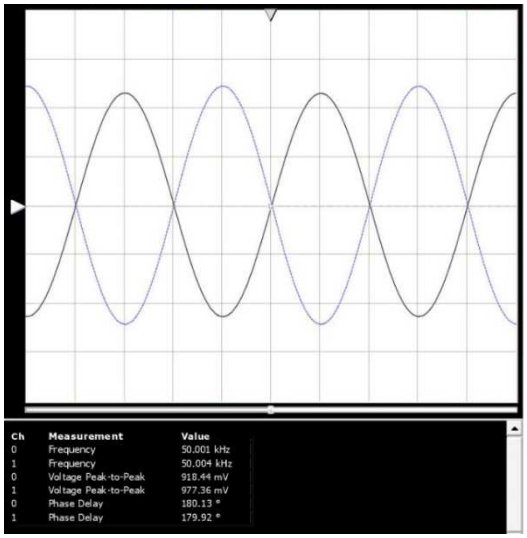

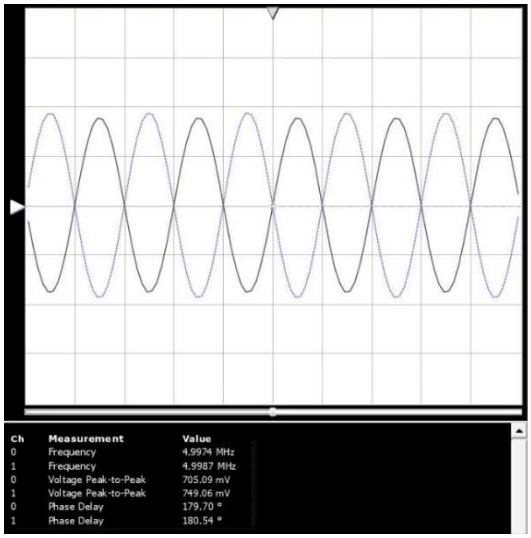

F= 50 kHz, R_{LOAD-1}=918Ω, R_{LOAD-2}=977Ω V_{OUT-1}=918.44^{mVp-p}, V_{OUT-1}=977.36^{mVp-p} with phase diff. =180^{o}

F= 5 MHz, R_{LOAD-1}=918Ω, R_{LOAD-2}=977Ω V_{OUT-1}=705.09^{mVp-p}, V_{OUT-1}=749.06^{mVp-p} with phase diff. =180^{o}

Figure 103 snapshots of the oscilloscope that shows the output signal of the load voltages on the scope when connecting to two current sources for sweeping the frequency starting from 100kHz to 1MHz with steps of 100kHz, and 1MHz to 5MHz with steps of 500kHz and amplitude of the input sine wave is set for1^{Vp-p}.